Fakulteit Ingenieurswese, Bou-omgewing & IT

Faculty of Engineering, Built Environment & IT

Evaluation of the Performance of Briquettes as Potential Feed Material to the Rotary Kiln Electric Furnace at Barro Alto, Brazil

By

Johnny Obakeng Mogalanyane

Submitted in fulfilment of the
requirements for the degree of

Master in Metallurgical Engineering

Supervisors: Professor Andrie Garbers-Craig
Professor Natasia Naudé

UNIVERSITEIT VAN PRETORIA
UNIVERSITY OF PRETORIA
YUNIBESITHI YA PRETORIA
Denkleiers • Leading Minds • Dikgopolo tša Dihlalefi

ABSTRACT

The Barro Alto nickel laterite deposit, characterized by three main ore types (West, East, and Plain), employs a processing plant equipped with two 185 m rotary kilns and six-in-line rectangular electric arc furnaces. This study investigated the impact of briquetting of the ferronickel ore, premised on the minimization of fine particles in the rotary kiln, as well as improving charge permeability in the furnace and overall process safety. ISO standard tests for iron ore pellets were used to evaluate the physical and metallurgical properties of briquettes prepared under different conditions.

Briquetting tests were conducted on screened nickel laterite ore (−6.3 mm and −12.5 mm) at moisture contents of 16% and 24% and cured under closed and open conditions. Results revealed that, at a briquette ore top size of −6.3 mm and 16% moisture content, the average green briquette compressive strength was 559 N and the drop number was 19.1; however, an increase in moisture content to 24% had a detrimental effect on green both briquette compressive strength and yield. At a briquette ore top size of -6.3 mm and a 16% moisture content, an average green briquette yield of 85.2% was reported .Increasing the moisture content proved to have a detrimental effect on the green briquette yield, with an average green briquette yield of 67.7% reported at a moisture content of 24%.

Size degradation resulting from reduction indicated that the degree of disintegration of the briquettes ($RDI_{-0.5mm}$) increased with an increase in moisture content for briquette ore top sizes of −6.3 mm and −12.5 mm. For the −6.3 mm briquette ore top size, $RDI_{-0.5mm}$ increased from 1.76% at 16% moisture to 3.33% at 24% moisture content.

The ISO 8371 test method was used to evaluate decrepitation of briquettes on entry into the rotary kiln. Results indicated that moisture significantly influenced decrepitation compared with curing conditions. For the −6.3 mm briquette ore top size, the average decrepitation index was 0.33% at 16% moisture content; this increased to 0.61% at 24% moisture content. For the −12.5 mm briquette ore top size, the decrepitation index was 2.34% at 16% moisture content and 1.96% at 24% moisture content.

The degree of reduction was evaluated using the ISO 4695 test method. At 16% moisture content, the average iron reduction was 33.4% under open and closed curing conditions for −6.3 mm briquette ore top size and 39.9% for −12.5 mm briquette ore top size; at 24% moisture content, the average iron reduction was 27.6% for −6.3 mm briquette ore top size and 36.9% for −12.5 mm briquette ore top size.

A tumble index of 95.5% was reported at 16% moisture content under open curing conditions at briquette ore top size of -6.3 mm. At briquette ore top size of -12.5 mm the tumble index dropped significantly to 40.3%. The results indicated that the tumble index is significantly affected by the particle size distribution, a similar trend was also observed under closed curing conditions. At 16% moisture content under closed curing conditions a tumble index of 91.4% was reported at briquette ore top size of -6.3 mm and 40.7% at briquette ore top size of -12.5 mm

Based on the findings of the test programme, optimal structural integrity and process stability can be achieved using briquettes produced at an ore top size of −6.3 mm, with a moisture content of 16%, and cured under open conditions.

Key words: Nickel laterite ore, Ferronickel, Briquette, Moisture content, Curing conditions, Physical properties, Metallurgical properties

PLAGIARISM DECLARATION

Full Names	Johnny Obakeng Mogalanyane
Student number	04338502
Topic of work	Master’s Thesis – Evaluation of Briquettes as Potential Feed Material to the Electric Arc Furnace at Barro Alto, Brazil

Signature of author

Date: 09/01/2025

ACKNOWLEDGEMENTS

I would like to thank my supervisors, Professor N. Naudè and Professor A.M. Garbers-Craig, at the Department of Materials Science and Metallurgical Engineering, for their support, supervision, and guidance during the course of my study. I wish to also thank Anglo American for their continued financial and technical support throughout my studies, particularly the team at Value-In-Use, led by Jacques Muller. English language technical editing of a draft of this thesis was carried out by Professor K.C. Sole. To my daughter, Rorisang, I hope that when you come across this work someday, it will inspire you to achieve even greater heights. To my siblings—Refilwe, Thabo, Pearl, and Mo—you have been my unwavering source of strength and motivation. To my parents, your love, patience, and support have been a true blessing, sustaining me through every challenge.

TABLE OF CONTENTS

LIST OF TABLES

LIST OF FIGURES

LIST OF ABBREVIATIONS

AI	Abrasion index
BEI	Backscattered electron image
DoE	Design of experiments
DI	Decrepitation index
EDS	Energy-dispersive X-ray spectroscopy
kPa	Kilopascal
kt/a	kilo tonnes per annum
LME	London Metal Exchange
Mass%	Mass percentage
MPa	Megapascal
Mt	Million tonnes
PSD	Particle size distribution
RDI	Reduction disintegration index
RI	Reducibility index
SEM	Scanning electron microscopy
TI	Tumble index
USA	United States of America
XRD	X-ray diffraction
XRF	X-ray fluorescence

1. Introduction

1.1. Barro Alto deposit

Barro Alto mine is wholly owned and operated by Anglo American. The mine is situated in Goias region of Brazil, which is within close proximity (150 km) of Anglo American's Codemin nickel mine. The mine is 18 km from Barro Alto town. Figure 1 shows the geographical location of Barro Alto. The project is situated in the central western part of Brazil, which is an area characterized by good infrastructure, with easy access to roads, rail, and power. The strategic location of this deposit offers several advantages, particularly with respect to ease of access to the raw material, labour, and power.

The Barro Alto deposit was first discovered in 1960. Exploration work commenced in 1970, followed by the first feasibility study in 1988 (Anglo-American, 2009). Anglo American acquired the mineral rights to the deposit in 2002 and the mining operation commenced in 2004. At commencement, the mined ore was fed to the then-existing Codemin plant. Construction of the plant commenced in 2007, after the project was approved in 2006. A summary of the project history is graphically presented in Figure 2.

Distances from Barro Alto	
Codemin	150 km
Brasília	170 km
Anápolis	200 km
Goiânia	230 km
Santos	1 200 km`

Figure 1: Geographical location of Barro Alto project (Anglo-American, 2009)

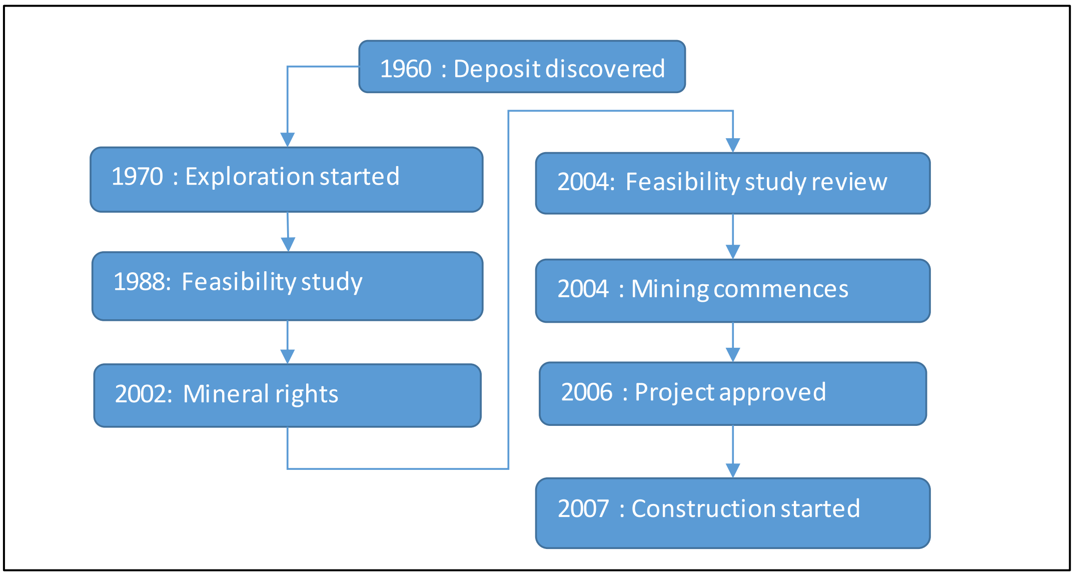

Figure 2: Summary of project history (Anglo-American, 2009)

The Barro Alto deposit is a *nickel laterite ore body* that consists of three main ore types that occur in six different areas, illustrated in the cross-sectional view in Figure 3. The ore types are classified into three categories based on the Ni and Fe contents and SiO_2/MgO ratios (Ratié et al., 2018).

- Plain type ore: 1.3 mass% Ni; 21 mass% Fe; SiO_2/MgO 1.7
- East type ore: 1.6 mass% Ni;15 mass% Fe; SiO_2/MgO 1.6
- West type ore: 1.8 mass% Ni; 19 mass% Fe; SiO_2/MgO 3.1

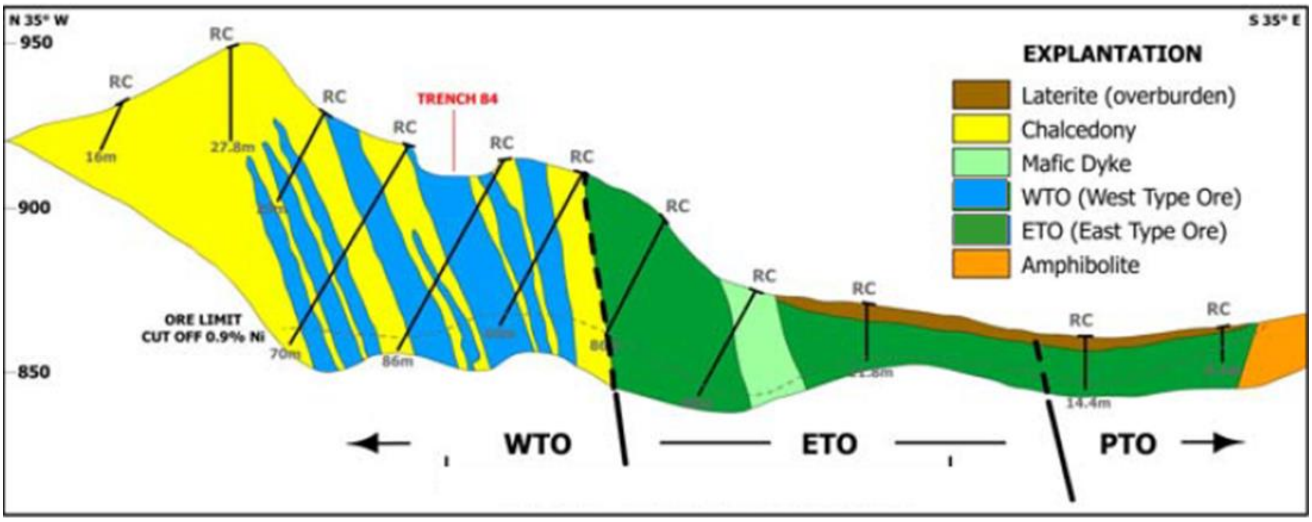

Figure 3: Barro Alto geology (Anglo-American 2009)

Known nickel deposits in Brazil account for 350 × 10^6 t ore, with a reported average nickel grade of 1.50% (Barros de Oliveira et al., 1992). The ore bodies are scattered throughout the country and are mostly associated with ultramafic complexes (Barros de Oliveira et al., 1992). In Brazil, there is a greater prevalence of silicate ores over oxidized ores, with the main nickel-containing minerals being serpentine, smectite, garnierite, and goethite. With respect to nickel production, Brazil has key resources of 4 × 10^6 t nickel, all of which is from lateritic deposits. Only two sulfide deposits are known in the country: Americano do Brasil and Fortaleza de Minas.

1.2. Nickel ores

Nickel is a hard and ductile metal with high resistance to corrosion and oxidation. In its first major application in 1820, nickel was used in an alloy of nickel, copper, and zinc called German silver (Crundwell et al., 2011). It was only in 1857 that nickel had its first major use, when the United States of America (USA) introduced a one-cent coin that was made of a copper–nickel alloy.

In 1950, Monypenny observed that nickel was among the most important elements that improved the properties of high-chromium stainless steels. In the following years, nickel assumed even greater importance. In 1969 alone, nickel stainless ingot production in the USA exceeded 1 Mt and the nickel contained in stainless steel was well over 100 000 t (Bernstein and Peckner, 1977).

There was sharp increase in the use of nickel in the twentieth century, largely driven by growth in the stainless-steel industry as a result of industrialization and urbanization programmes of developing nations. The demand for nickel rose from 1.1 Mt in 1999 to 1.3 Mt in 2009, at an average compound growth rate of 2% per annum. The highest offtake of nickel was experienced in 2006, when demand reached the order of 1.4 Mt (Anglo American, 2009). Global consumption of nickel by region is presented in Figure 4. Table 1 presents 2021 global nickel consumption by category.

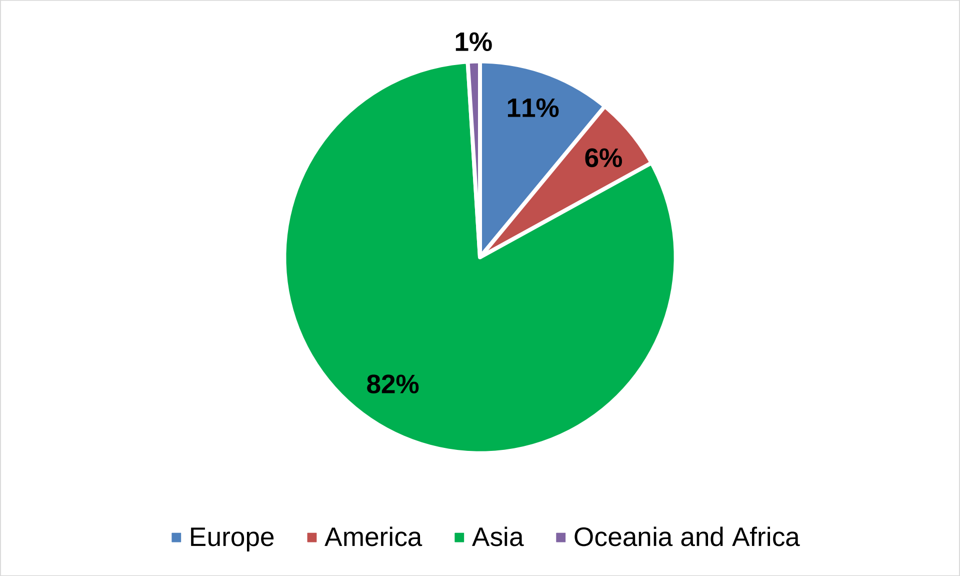

Figure 4: Global nickel consumption by region (International Nickel Study Group, 2021)

Table 1: Nickel consumption by category (International Nickel Study Group, 2021)

Category	Proportion of total consumption, %
Stainless steel	69
Batteries	13
Alloys	7
Electroplating	5
Special steels	5
Other	1

1.2.1.Nickel market analysis

The London Metals Exchange (LME) regulates the price of nickel, which is the world centre for trading of industrial metals. The pricing of *ferronickel* is derived from the average LME price of nickel metal. The price of nickel, illustrated in

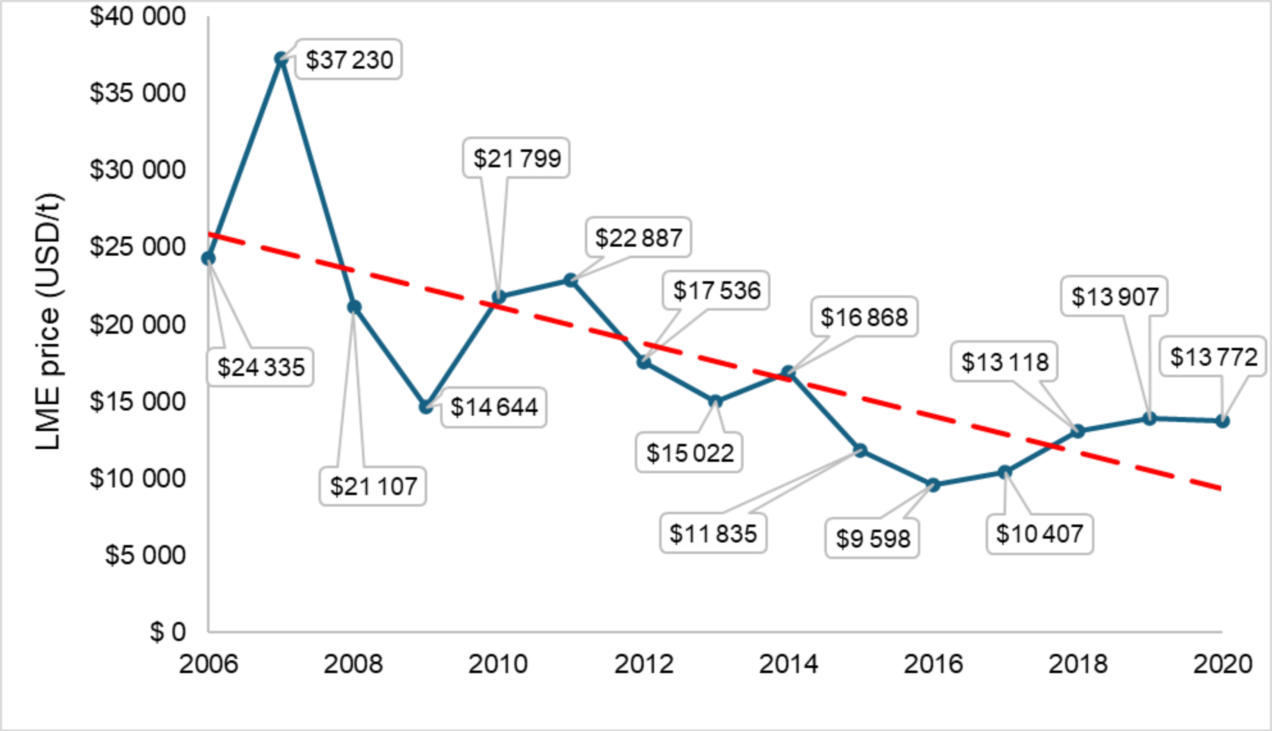

Figure 5: Nickel price from 2006 to 2021 (International Nickel Study Group, 2021)

, has increased since 2005. In 2007, a spike in the nickel price was experienced, mainly due to demand outstripping the supply (Crundwell et al., 2011). In the first quarter of 2011, the nickel market experienced a shortfall of 33 kt, primarily due to the delay in launching of new projects: as a consequence of the shortfall, the average nickel price was 5% higher in 2011 than in 2010. The price comparison between 2019 and 2020 is presented in Table 2.

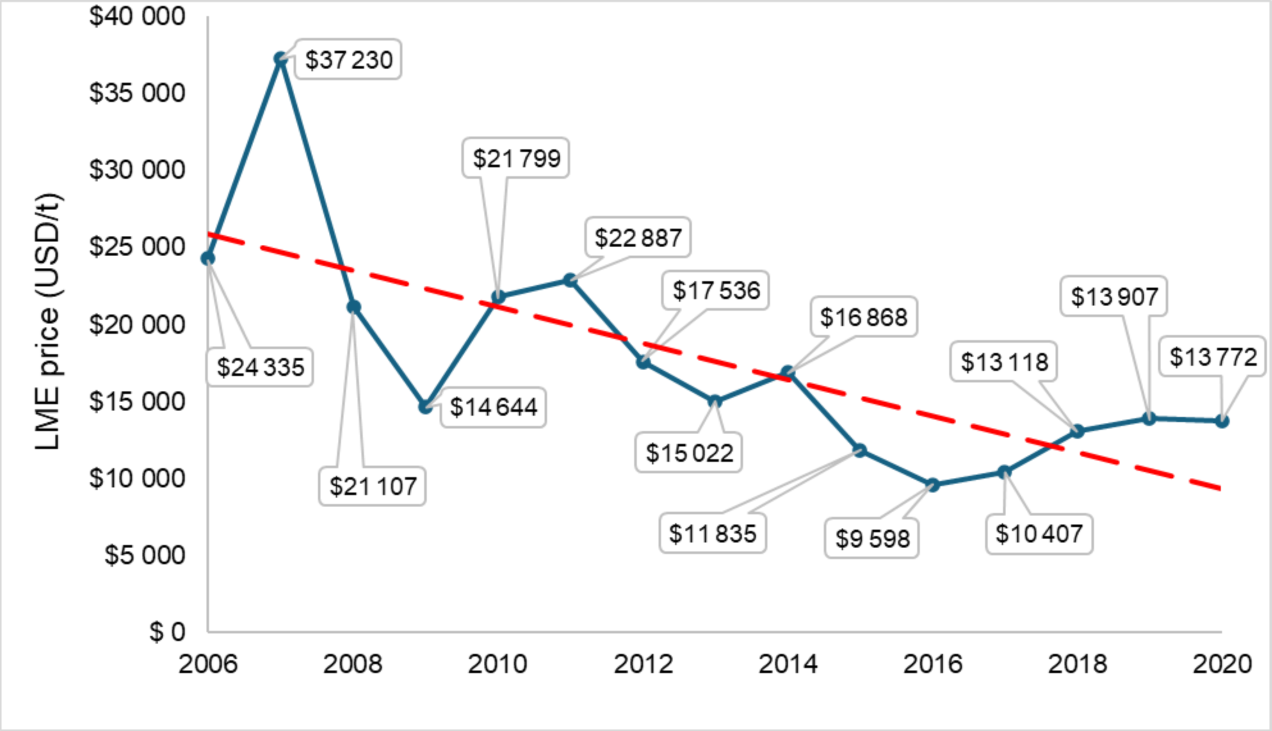

Figure 5: Nickel price from 2006 to 2021 (International Nickel Study Group, 2021)

Table 2: Nickel price (International Nickel Study Group, 2021)

Average nickel price, USD/t	2019	2020
Average market price (LME, cash)	13 907	13 772

Nickel ore deposits can be classified into three distinct groups: the sulfides, *laterites,* and deep-sea manganese nodules. The primary source of nickel has traditionally been the sulfide deposits, mainly due to the ease of recovery associated with these deposits. It is anticipated that 60% of the world's nickel resources are found as laterites, illustrated in Figure 6 (International Nickel Study Group, 2021).

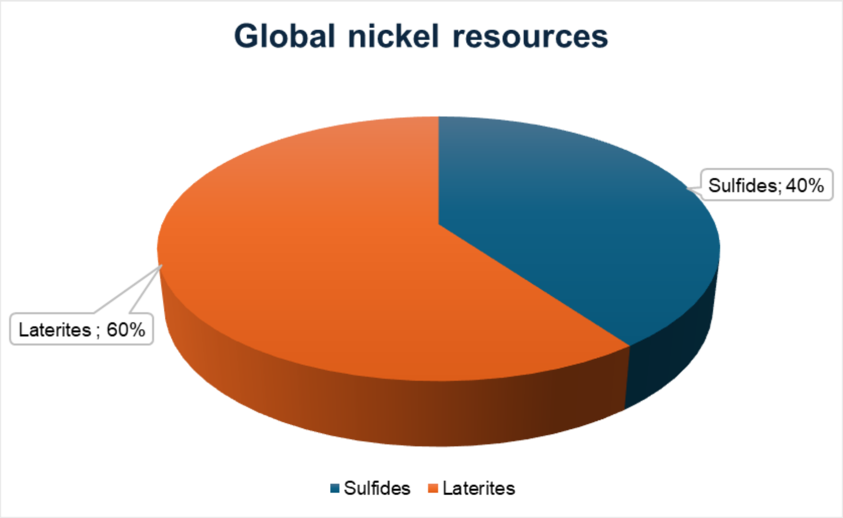

Figure 6: Global nickel resources (International Nickel Study Group, 2021)

Nickel laterite ore bodies offer the following advantages over sulfides (Li, 1999):

- Larger reserves;
- Superior grade;
- Significantly lower operational costs because sulfide ores bodies occur in hard rock and are consequently characterized by high mining costs;
- Lower environmental impact (sulfur dioxide emission regulations make production of nickel from sulfide ore bodies less favourable);
- The advancement of new technologies, aimed at increasing byproduct revenue, make laterite-based nickel production more economically favourable.

Figure 7 shows past nickel production from sulfide and laterites, and future predictions.

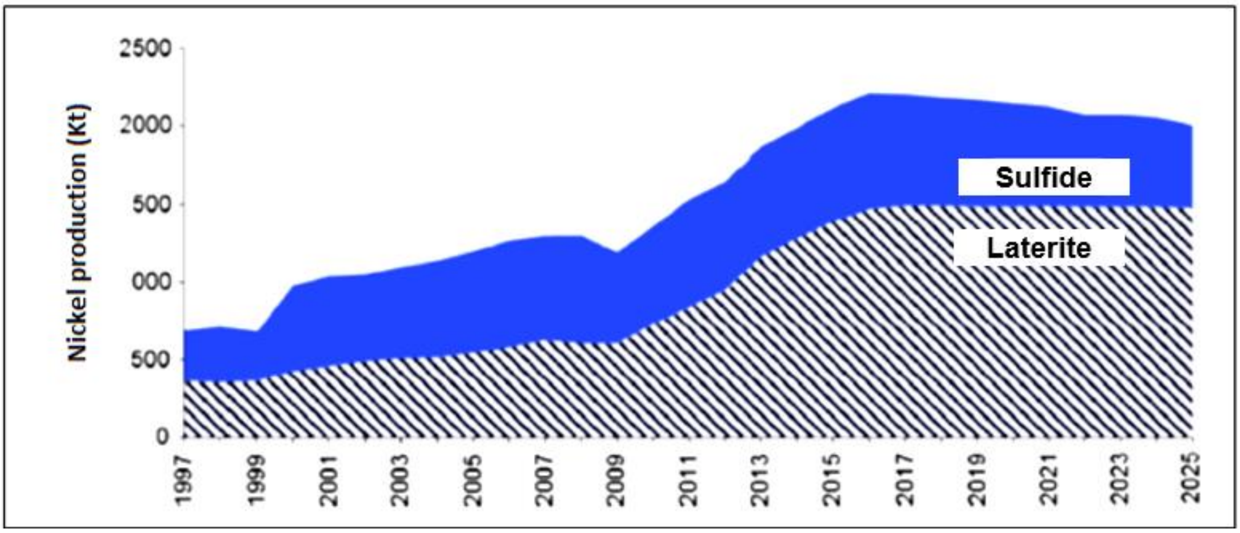

Figure 7: Historical nickel production and future predictions (Oxley et al., 2016)

1.3. Mineralogy of nickel laterites

Laterite ore bodies originate from mafic and ultramafic igneous rocks. They are associated with high iron and magnesium contents. Nickel laterite formation involves dissolution of the original minerals, movement of the elements in solution, and precipitation of some elements in another location (Li, 1999).

Nickel laterite ore bodies can be classified into five different zones according to their mineral composition. The thickness of each zone differs, depending on the location. The five different nickel laterite zones are (Li, 1999):

- **Iron-capping zone**: This zone occurs mainly at the top of the nickel laterite deposit. One of its main characteristics is that it has undergone the greatest degree of weathering, so most nickel in this zone has already been leached. Owing to the significantly lower nickel grades, this zone is considered as a discard during the mining operation.

- **Limonite zone**: The limonite zone occurs below the iron-capping zone and is characterized by a high degree of weathering, fine grain size, and low nickel grade. The mineralogical and chemical composition is uniform throughout the limonite zone, with goethite being the primary phase that hosts most of the nickel.

- **Transition/intermediate zone**: This zone occurs between the limonite and saprolite zones, owing to the relative difficulty in separating the two zones.

- **Saprolite zone**: The saprolite zone is characterized by nickel-rich mineral phases, such as serpentine, and has heterogeneous chemical and mineralogical compositions.

- **Bedrock zone**: The bedrock zone represents the original rock prior to the start of the laterization process. The main minerals in the parent rock are serpentine and olivine.

While the chemical and mineralogical compositions of laterites mainly differ due to different climatic regions in which they occur, laterites can be classified into two main groups: limonites and serpentine laterites.

Limonitic ore consists mainly of hydrated ferric oxide and quartz, whereas serpentinic ore consists mainly of hydrated magnesium silicate, in which the magnesium is usually replaced by iron and nickel (Li, 1999). The most prominent minerals occurring in nickel laterites are presented in Table 3.

Table 3: Prominent minerals in nickel laterites (Li, 1999)

Dominant phase	Formula	Ni, %
Limonite zone		
Goethite	(Fe,Al,Ni)OOH	0.5–1.5
Asbolite lithiophorite cryptomelane	Mn, Fe, Co, Ni oxides	1–10
Intermediate zone		
Nontronite	$(Ca,Na,K)_{0.5}(Fe^{3+},Ni,Mg,Al)_4(Si,Al)_8O_{20}(OH)_4$	0–0.5
Quartz	SiO_2	0
Saprolite zone		
Nickeliferous serpentine	$(Mg,Fe,Ni)_3Si_2O_5(OH)_4$	1-10
Garnierite	$(Ni,Mg)_3Si_4O_{10}(OH)_2$	10-24
Bedrock zone		
Olivine	$(Mg,Fe,Ni)_2SiO_4$	0.25
Orthopyroxene	$(Mg,Fe)SiO_3$	0.25
Serpentine	$Mg_3Si_2O_5(OH)_4$	0.25

1.4. Extraction of nickel laterites

Depending on the required final product, nickel laterites can be processed either via hydro- or pyrometallurgical routes to produce nickel metal. The key processes that have been adopted over the years for the processing of nickel laterites are presented in Table 4.

Table 4: Nickel laterite processing -Technology advancement (Li, 1999)

Year	Process description
1889	Matte smelting of silicate
1943	Reduction roast–ammonia leach of laterite ore
1958	Electric furnace smelting to ferronickel
1959	Pressure leaching of oxide ores with sulfuric acid
1974	Reduction roast and electric furnace smelting

The general nickel production routes from laterites are summarized in Figure 8. Nickel produced from laterite ore bodies is energy-intensive, so it is critical that pre-reduction be conducted to yield high-grade ferronickel (Li, 1999). Pre-reduction minimizes the requirements for refining, thus reducing overall energy requirements. One major requirement for the pre-reduction stage is to reduce as much of the nickel as possible to maximize nickel recovery, whilst reducing as little of the iron as possible to obtain a more valuable high-grade product (Li, 1999).

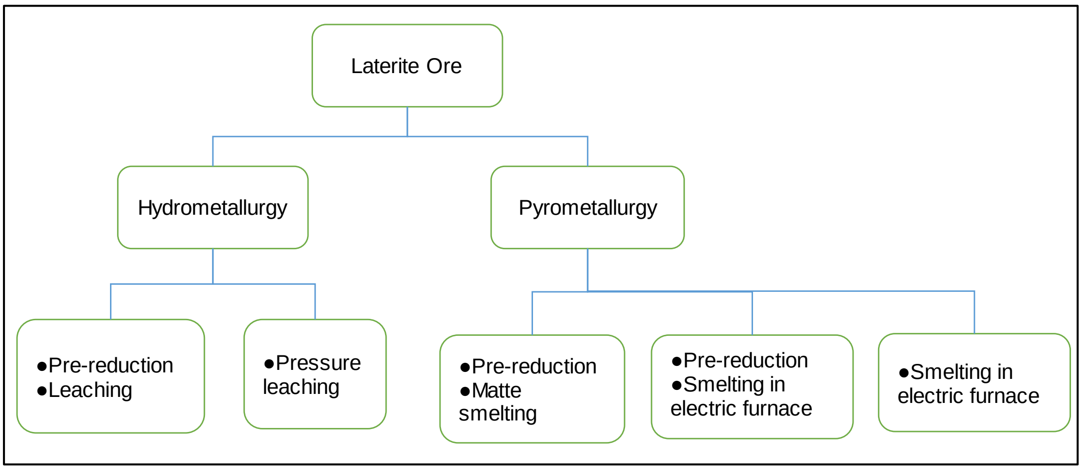

Figure 8: Processes for nickel production from laterites (Li, 1999)

1.5. Barro Alto operation

The Barro Alto plant is designed to treat 2.4 Mt of dry ore per annum, with an average production of 36 kt/a nickel when the plant reaches full production. Over the first five years of production, the plant is expected to produce 41 kt/a of nickel. Anglo American expects that the Barro Alto plant at full operation will bring its total nickel production to 61 kt/a, which excludes nickel production from the Anglo Platinum operations.

The Barro Alto nickel ore reserve and mineral resource statements are presented in Tables 5 and 6, respectively. As of 2022, the reserve statement indicated a total nickel ore reserve of 42.9 Mt at a grade of 1.29% nickel with a total of 554 kt contained metal. The mineral resource statement indicated a total of 9.3 Mt of nickel associated with 111 kt nickel metal at a grade of 1.19%.

On the basis of the mineral resource statement, ore reserve statement, cost per tonne of metal produced, and its contribution to the group's overall nickel production, the Barro Alto deposit is a strategic asset to the Anglo American group.

Table 5: Barro Alto nickel ore reserve statement (Anglo American, 2022)

		Tonnes		Grade		Contained metal	
	Classification	2022	2021	2021	2022	2022	2021
Nickel ore reserve		Mt	Mt	% Ni	% Ni	kt	kt
	Proved	10.2	12.7	1.39	1.40	142	178
	Probable	32.8	35.5	1.26	1.26	413	448
	Total	42.9	48.2	1.29	1.30	554	626

Table 6: Barro Alto nickel mineral resource statement (Anglo American, 2022)

		Tonnes		**Grade**		**Contained Metal**	
Nickel mineral resource	Classification	2022	2021	2022	2021	2022	2021
		Mt	Mt	% Ni	% Ni	kt	kt
	Measured	2.5	2.5	1.15	1.15	29	29
	Indicated	10	10	1.08	1.08	108	108
	Measured and indicated	12.5	12.5	1.09	1.09	137	137
	Inferred (in LOM*)	5.5	5.5	1.33	1.33	73	73
	Inferred (ex LOM)	3.8	3.8	100	100	38	38
	Total inferred	9.3	9.3	1.19	1.2	111	111

* LOM: Life of mine

The following definitions are provided in accordance with the reserve/resource statements (Anglo American, 2022):

- Ore reserve: This refers to the part of the *measured or indicated resource* that can be economically processed. Ore reserve can be classified into two categories; namely, proven reserve and probable reserve.
- Proven reserve: This refers to the *measured mineral resource* that can be economically mined.
- Probable reserve: This refers to the part of *the indicated mineral resource* than can be economically mined.
- Mineral resource: This is the content of the material that is of economic significance. Mineral resources can be classified into three categories; namely, inferred, indicated, and measured.

An economically viable project should have 40 kt/a nickel capacity, which requires an 800 kt nickel deposit with a life of mine (LOM) of 20 years (Dalvi et al., 2004). The Barro Alto operation meets these requirements, with a 41 kt/a capacity for the first five years, an LOM of 26 years, and total reserve of 123 Mt.

The Barro Alto process flow sheet is presented in Figure 9. The plant employs the rotary kiln –electric arc furnace route to process the ore, with two 185 m rotary kilns and two six-in-line rectangular electrical furnaces. The process is energy-intensive, with an annual electrical power consumption of 1.4 million MWh. The process is nevertheless profitable, with a capital intensity of USD 50.1/kg.

The process route begins with size reduction using a sequence of primary, secondary, and tertiary crushers. The crushed material is stockpiled to create a constant feed to the plant and to homogenize the feed material. There should be as little variance as possible in the feed material. A reclaimer is used to feed the material into a dryer. Drying takes place in a rotating dewatering kiln, which reduces the moisture content to approximately 22%, depending on the operation. The dried material is screened for top-size control prior to stockpiling. The dewatered ore is fed to the upper end of the rotating kiln with coal and recycled pelletized dust from the calcination kiln.

The combined material is treated through calcination kilns to remove any excess moisture, producing a completely dry and partially reduced ore. Nickel and iron are reduced in electric arc furnaces and collected as an alloy; MgO, SiO_2, and Al_2O_3 are collected in the slag.

The four main features of the plant are (Figure 9):

- Dewatering;
- Calcination;
- Electric arc furnace smelting;
- Metal refining.

Studies are currently underway at Anglo American to consider briquetting as an alternative form of agglomerating the ore. Preliminary indications are that briquetting would offer the following advantages (Brujin, 2019):

- Increase process safety and stability by reducing gas build-up;
- 3 kt/a increase in nameplate capacity;
- 5% lower plant electricity consumption.

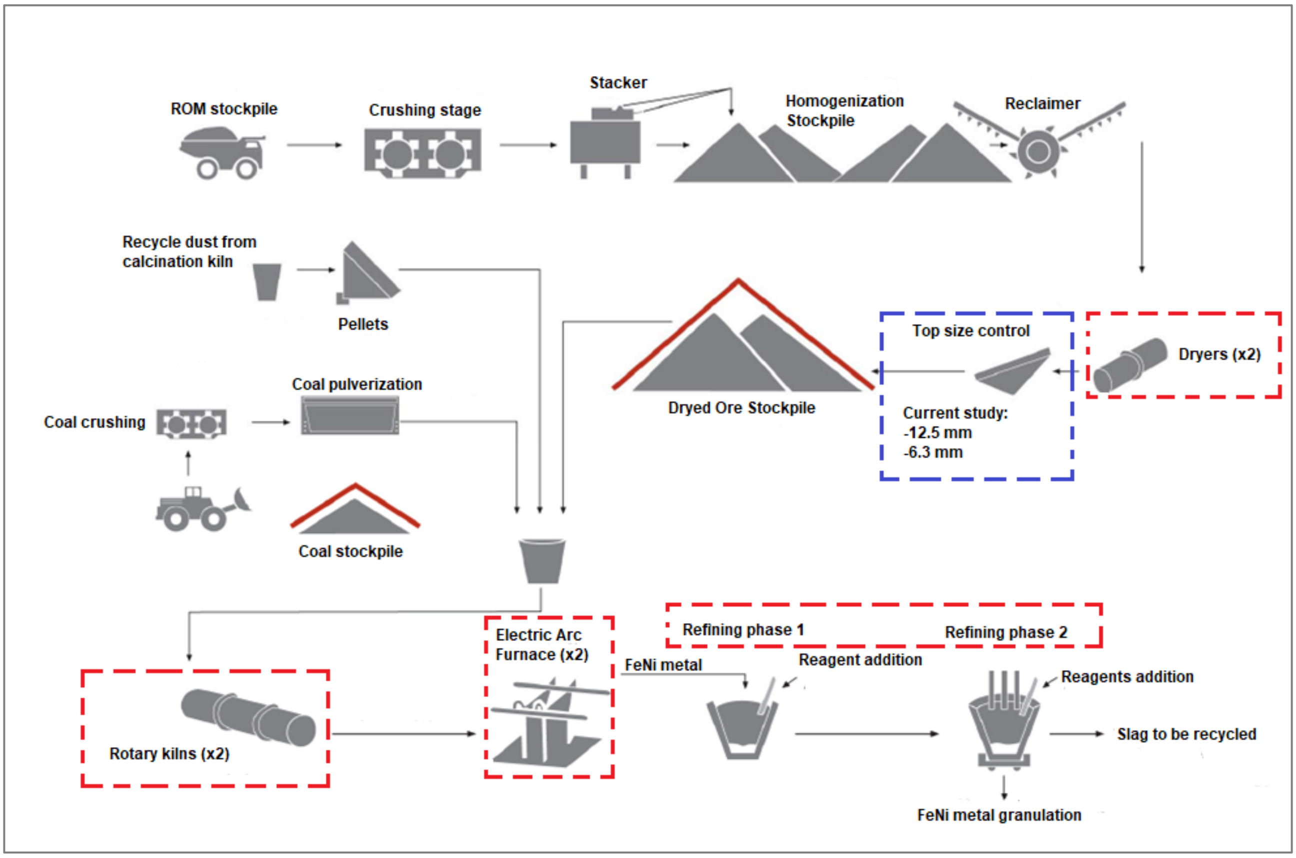

Figure 9: Barro Alto process flow sheet (Anglo-American, 2009)

1.6. Briquetting

Briquetting as a method of agglomeration of fines generated during the steel and iron-making process was first discovered in the nineteenth century. The first recorded successful industrial briquette application was in Finland in 1989. This involved agglomeration of fine magnetite ore without the use of any binder and with an energy consumption of 5 kWh, producing 1 t briquettes (Kurunov and Bizhanov, 2018). This was considered a success because the briquettes were successfully further treated in a blast furnace.

Technological advancement of the briquetting process has been relatively slow. This has led to other agglomeration techniques, such as sintering and pelletization, becoming preferred. In comparison with these agglomeration techniques, briquetting offers the advantage of elimination of the grinding phase (Vining et al., 2017), which lowers overall energy requirements and could, in turn, increase overall productivity.

Briquetting as an agglomeration method consists of three main technologies: vibro-pressing, roller pressing, and stiff extrusion (Kurunov and Bizhanov, 2018). Vibro-pressing was first used in the USA, followed by Russia, for waste processing and agglomeration of fine ore and concentrates.

Anglo American's Barro Alto industrial complex is committed to sustainability-driven strategic goals, which include a focus on reducing carbon dioxide (CO_2) emissions from existing thermal applications. The viability of using hydrogen as a replacement for fossil fuels in thermal processes depends on several factors, including the source of hydrogen and local economic conditions, such as raw material costs, electricity prices, and the prevailing cost of incumbent fossil fuels (Brosig et al., 2023).

In 2021, Vale initiated load tests on its iron briquette plant at the Turabao Unit in Brazil. According to Vale, the adoption of briquettes could lead to a substantial reduction in greenhouse gas emissions, potentially achieving up to a 10% reduction compared with the traditional blast furnace process. This reduction is attributed to elimination of the carbon-intensive sintering stage. Additionally, Vale asserted that use of briquettes reduces emissions of particulates and harmful gases, such as sulfur dioxide (SO_x) and nitrogen oxides (NO_x), as well as the need for water in the production process (Vale, 2023).

Anglo American has set a specific target to reduce greenhouse gas emissions by 30% by 2030 (Anglo-American, 2022). Given the positive findings from Vale's research, it is conceivable that utilization of briquettes could be instrumental in helping Anglo American achieve its greenhouse gas reduction goals.

1.6.1. Binderless agglomeration

The mechanism of binderless agglomeration is primarily due to application of excessive pressure on the solid particles, which causes the formation of common surface areas between the individual grains, thus minimizing the voids. Individual grains are held together by van der Waals forces (Koerner and MacDougall, 1983). Van der Waals forces are, however, typically weak, requiring that the surface area between individual particles be considerable to produce briquettes of sufficient strength.

Binderless compaction relies primarily on machine roll pressure to ensure that a uniform surface area is formed between individual grains. Coarse particles would require substantially greater pressure than compaction of fine particles. Whilst fine particles require substantially less pressure to compact without a binder, this can give rise to degassing difficulties (Koerner and MacDougall, 1983).

An optimum particle size thus exists between the relative proportions of fine and coarse particles in a sample to allow fine particles to fill the interstices and minimize the crushing energy/force required for the coarse particles. Binderless compaction is limited to certain material types: compaction of elastic and hard brittle material is often impractical.

1.6.2. Agglomeration with a binder

A binder is any material that facilitates cohesion of particles. In view of this definition, binders may be classified into the following generic categories (Koerner and MacDougall, 1983):

Matrix binders: These types of binders promote the formation of a continuous matrix between particles. Asphalt is a typical matrix binder.
Film binders: These types of binders originate from solutions. A water solution of starch is a typical example of a film binder.
Chemical binders: As the name suggests, chemical binders depend on a chemical reaction to be effective, either between solid particles and the binder or between binder components.
Lubricant binders: The mechanism of lubricant binders relies on reduction of interparticulate consolidation friction. Lubricant binders may either be solids or liquids, examples of which include oil, water, starch, and talc.

The choice of binder is largely dependent on process economics; however, in general, the selection of the most suitable binder is determined by optimum particle size, temperature, and mixing (Koerner and MacDougall, 1983).

1.7. Hypothesis

The hypothesis for this study is as follows:

> Briquettes of comparable physical and metallurgical properties to those obtained at Anglo American (Value-in-Use) pilot-plant campaign programme can be produced from Barro Alto ferronickel ore plant feed screened at −6.3 mm and −12.5 mm at ore moisture contents of 16% and 24%.

1.7.1.Research objectives

The following objectives were identified for the study:

- Evaluate the effect of particle size distribution (PSD) on performance of briquettes;
- Evaluate the effect of moisture content on performance of briquettes;
- Evaluate the effect of curing conditions on performance of briquettes;
- Using the results obtained, determine optimum conditions with respect to briquette production and performance.

Evaluation of the briquette performance was based on the following International Standards Organisation (ISO) tests:

- Crushing strength (ISO–4700);
- Tumble strength and abrasion index (ISO–3271);
- Decrepitation index (ISO–8371);
- Reduction disintegration index (ISO–4696–1);
- Rotary kiln simulation using a Linder furnace (Non–standard test).

It was envisaged that the outcomes of these tests would yield better understanding of briquette performance, particularly in relation to moisture content, PSD, and curing conditions. Furthermore, it was suggested that production of briquettes would improve charge permeability of the electric arc furnaces, thereby improving process safety, stability, and overall metal extraction.

1.8. Thesis organization

This thesis is structured into five key areas according to the following chapters:

Chapter 2: This chapter presents the literature study. The literature study includes various agglomeration methods and briquetting technologies. Process parameters, which affect the quality of briquettes, are discussed. These include briquetting pressure, machine roll speed, curing methods, PSD, and the effect of moisture content. Mineralogy of nickel laterite ores is also discussed.

Chapter 3: This chapter presents the experimental methodology. The principle of Design of Experiments (DoE) was adopted and is discussed in detail, including the briquette test programme and experimental design. A stepwise methodological approach to briquette production is presented.

Chapter 4: This chapter focuses on the exoperiments that were conducted in the study.

Chapter 5: This chapter focuses on findings from the study. Results discussed include ore feed characterization and PSD analysis. Results obtained from the ISO tests are presented and discussed. These include compressive strength, tumble index (TI), abrasion index (AI), reducibility index (RI), decrepitation index (DI), reduction disintegration index (RDI), and Linder furnace tests.

Chapter 6: This chapter draws conclusions on findings from the test programme. Optimum briquetting conditions are presented. Results from the optimum conditions are compared with those obtained from the Anglo American (Value-In-Use) pilot-plant programme.

Chapter 7: This chapter discusses future work.

2. Literature review

2.1. Agglomeration methods

The modern economy requires that waste generation be minimized in every production process, whenever possible. This requires retreatment of production ‘waste’ from one operation to the next to avoid any waste being rejected from the production process. Waste-free operations are those wherein the production waste generated from one process can be used in other subsequent processes. The food, chemical, timber, and mining industries generate considerable amounts of fine waste material: rational economic use of such material requires pressing/compaction and briquetting.

In ferroalloy applications, a significant amount of dust is generated in gas cleaning of furnaces. Dust emissions from ferroalloy furnaces occur at a rate of 8–30 kg/t of ferroalloy (Kurunov and Bizhanov, 2018). In the production of silicomanganese, the dust contains 21.0–34.3 mass% manganese oxide, while that from ferromanganese production contains 30–35 mass% manganese oxide (Kurunov and Bizhanov, 2018).

The use of fines without any prior agglomeration as feed into an electric arc furnace would adversely affect furnace performance, leading to lower productivity, decreased charge permeability, and reduced metal extraction. The combined effects of large quantities of fines generated in the processing of ferroalloys and depletion of high-grade ores are key drivers for the need for prior agglomeration. Four methods have been established for the agglomeration of iron ore fines: sintering, pelletizing, nodulizing, and briquetting (Eisele and Kawatra, 2003).

2.1.1. Sintering

In the sintering process, iron-containing fines are combined with a solid fuel and their combination is ignited on a travelling grate. The burning fuel increases the temperature of the bed to 1300–1480°C, which sinters the fines into a porous material suitable for use in a blast furnace (Eisele and Kawatra, 2003). Bonding between the particles is caused by partial melting and recrystallization.

2.1.2. Pelletizing

Pelletizing has widely been used to produce iron pellets that exhibit properties required for feed into a blast furnace. In the production of pellets, fine ore particles are mixed with a binder and balled using a pelletizing disc to form green pellets.

To produce pellets with high physical strength and the metallurgical characteristics required for handling and transportation, the green pellets are heated at elevated temperature (1000–1300°C (Nheta et al., 2018). According to Eisele and Kawatra (2003), production of pellets requires a suitable binder, sufficient moisture, and a fine PSD to allow particles to pelletize.

2.1.3.Nodulizing

In the nodulizing process, fine ore particles are fed to a rotary kiln and heated to temperatures just below their melting point. The charge is tumbled in the kiln, which causes nodules to form. The nodules are bonded together by the liquefied part of the partially melted fines. Advantages of nodulizing are that it has high tolerance limits with regards to feed moisture content and PSD, and yields high-strength nodules (Eisele and Kawatra, 2003).

2.1.4.Briquetting

Briquetting ranks amongst the oldest forms of agglomeration methods. It involves compression of finely divided material under pressure, sometimes using binders to enhance the agglomeration. During the briquetting process, fines are pressed into lumps of regular shapes using either rolls, extruders, or punches (Eisele and Kawatra, 2003).

Pressing refers to the mutual displacement of particles, followed by their packing under the influence of an external load that is equivalent to or greater than the load at the limit of plasticity of the material (Drzymala, 1993). In the pressing of an elastoplastic material, an increase in the pressing force/pressure is associated with an increase in the durability of the bonds between particles, as a result, the overall strength of the briquette increases. For an elasto-brittle material, an increase in the pressing force/pressure may lead to breakage at the materials' point of contact and hence a reduction in the overall compressive strength of the briquette.

2.2. Briquetting technologies

2.2.1.Vibro-pressing briquetting

Vibro-pressing briquetting technology was first introduced in 1970. In its first application, this technology was used for agglomeration of agricultural raw material (Kurunov and Bizhanov, 2018). Vibro-pressing produces briquettes at relatively low pressures, in the region of 0.02–0.1 MPa, and a frequency of 30–70 Hz.

Typical vibro-pressing briquetting equipment has a maximum capacity of 30 t/h of briquettes (Kurunov and Bizhanov, 2018). This technology produces briquettes with relatively low mechanical strength. Such briquettes are not transportable via conveyor belts.

2.2.2.Extrusion briquetting

Extrusion as a method of agglomerating iron ore fines was first practised in the 1950s. In its first application, a hydrated mixture of iron ore fines and bentonite was placed in a chamber and then extruded through a die, producing cylindrical briquettes (Kurunov and Bizhanov, 2018). Extrusion briquetting is mainly used to produce dense, spherical agglomerates with good integrity. The largest particle size achieved by this technology is 5 mm. The process involves four main steps (Kurunov and Bizhanov, 2018):

- Mixing particles with a liquid binder, in a process referred to as granulation.
- Compaction of the mixture at a density close to the saturation density of the ore and binder mixture, which allows for release of entrapped air. This is the extrusion stage.
- Breaking down of the extrudate into smaller rods, which are rounded on a horizontal rotating friction plate.
- Drying of the pellets.

Extrusion devices can be classified based on their feeding mechanism into either ram feeding or gravity feeding. The type of extruder will generally affect the quality of the formed pellets/granules. High-pressure frontal extruders produce high-density hard pellets, whilst radial extruders yield moderate-density pellets, and dome extruders produce the lowest density pellets. The primary advantage of extrusion as method of briquetting in comparison with roller pressing and vibro-pressing is that it offers better quality pellets, reduced binder consumption, and the ability to agglomerate wet materials (Kurunov and Bizhanov, 2018).

The main criteria for determining whether a material is amenable to extrusion is its plasticity, which is a characteristic that ensures that the material can be successfully pushed through the holes in the die.

2.2.3.Roller-press briquetting

At inception, roller-press technology was primarily used for briquetting of fine iron ore particles and metallurgical waste. In general, roll-press briquetting is limited to pillow- or egg-shaped agglomerates/briquettes.

Spherically shaped briquettes are not possible with this type of machine because this would require a hemispherical pocket, which would encourage sticking. A roller-press briquetting machine consists of two pairs of rollers and an outer steel cover. Particles pass through the gap between the two rotating rollers under either gravity feed or screw feeding. Roller feeding mechanisms are illustrated in Figure 10. The feeding mechanism is an important aspect in the briquetting process: it is required to achieve uniform and continuous flow of material, so as to fill the nip between the rollers so that briquettes formed are homogenous (Kleinebudde, P. and Knop, K. 2007).

According to Johanson’s theory, it is generally accepted that there are three distinct regions of material behaviour in roller-press briquetting, as illustrated in Figure 11: the slip, nip, and release regions (Souihi, 2014). Particle compaction takes place near the region characterized by minimal gap width between the rollers (Souihi, 2014). The particles first go through the slip region, which is characterized by particles slipping at the surface of the rollers. The behaviour of a material in the slip region depends on the wall friction and inter-particle friction of the feed powder (Kleinebudde, P. and Knop, K. 2007). The nip region begins at the roll angle α (nip angle), when the wall velocity of the particles is equal to the velocity of the rollers. Particles are drawn into the smallest gap between the rollers, where they are compressed. With an increase in the nip angle, the maximum pressure applied in the nip region increases, and the roller gap and roller speed decrease. The release region begins at a point where the roller gap width begins to increase again. After being released, the briquetted material may increase in size owing to elastic recovery, which results in larger strip thickness in comparison with the roller gap.

Roller compaction technology is a continuous process; however, it can also be operated in batch or semi-batch mode. It offers the following advantages, in comparison to vibro-pressing and extrusion briquetting (Kleinebudde, P. and Knop, K. 2007):

- Production of briquettes of uniform consistency with regards to shape, density, and size;
- Dust reduction and improved safety by minimising operator exposure;
- Increases bulk density, which facilitates material handling and transportation.

A comparison of the different briquetting technologies is presented in Table 7.

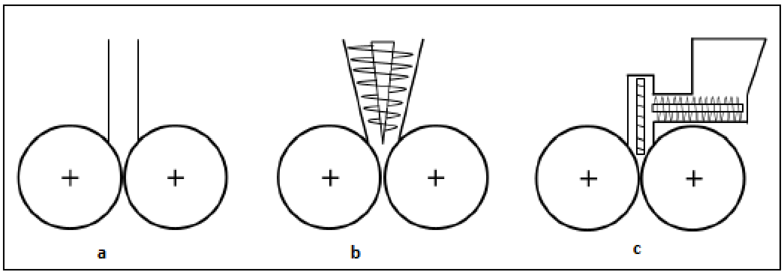

Figure 10: Different feeding mechanisms: (a) gravity, (b) single screw, (c) double screw (Souihi, 2014)

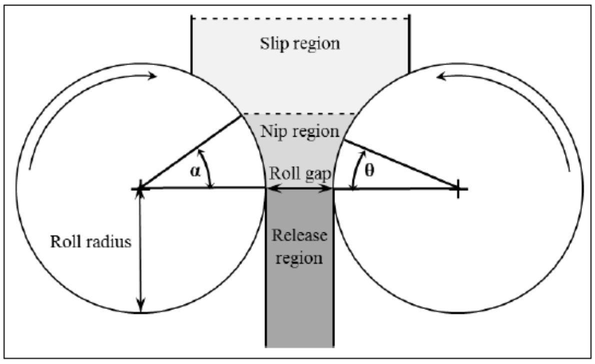

Figure 11: Roll compaction process, indicating the different zones of material behaviour (Souihi, 2014)

Table 7: Comparison of briquetting technologies (Kurunov and Bizhanov, 2018)

Parameter	**Briquetting type**		
	Vibro-press	Roller-press	Extruder
Maximum capacity, t/h	30	50	100
Cement binder content, %	8–10	15–16	3–9
Thermal processing of raw material	80°C (16–20 h)	–	–
Shape of briquettes	Cylinder	Pillow	Any shape
Dimensions, mm	80 × 80	30 × 40 × 50	5–35
Moisture content of charge, %	< 5	< 10	8–15

ZEMAG 01 roll-press briquetting machine was utilized in this study. This is the same equipment as used in the pilot-plant campaign tests at Anglo American (Value-In-Use). A schematic diagram of the ZEMAG-01 is illustrated in Figure 12. The specifications are:

- Roller diameter: 415 mm
- Pressing track width: 140 mm
- Total pressing force: 640 kN
- Roller speed: 4.5–10 rpm
- Driving power: 15 kW
- Number of tamping worms: 1
- Worm speed: 30–120 rpm

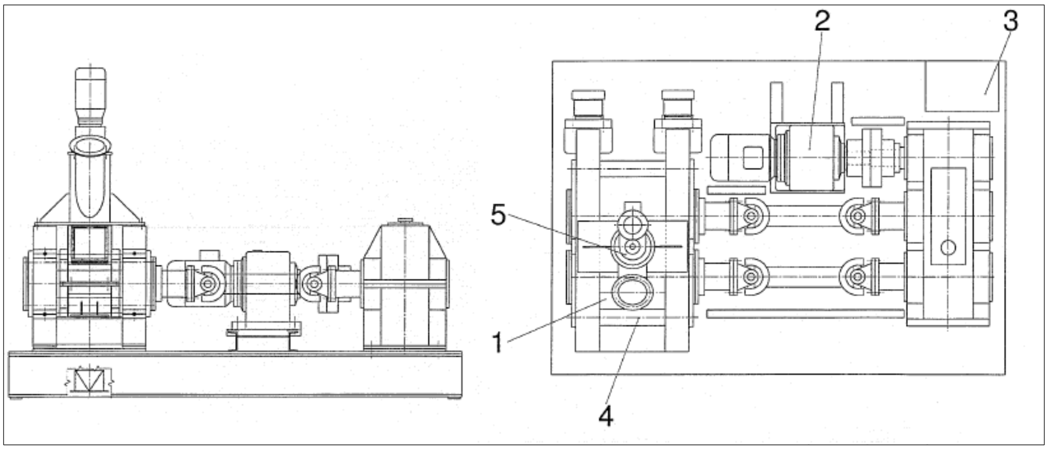

Figure 12: ZEMAG-01 briquetting machine: 1) rolls with bearing, 2) drive, 3) hydraulic system, 4) roll housing, 5) tamping worm (Weber and Schroder, 2002).

2.3. Process parameters

Several parameters affect the performance and quality of briquettes. These may be grouped into machine/equipment properties and ore properties. Machine properties include machine roller speed and roller pressure; ore properties include PSD, moisture content, and curing conditions (Vining et al., 2017 and Sun et al., 2014).

2.3.1. Briquetting pressure

Pressure application by the briquetting rollers allows for different mechanisms to be prevalent, depending on the pressure. At elevated pressures, interparticle bonding is more prevalent (Kaliyan and Morey, 2009). A study of compaction behaviour of oak sawdust indicated that increasing the pressure increased abrasive resistance, impact resistance, and compressive strength of the resultant agglomerates (Kaliyan and Morey, 2009). The effect of briquetting pressure on compressive strength of the resultant agglomerates, as determined in the above study, is presented in Table 8. Durability and compressive strength increased with an increase in the forming pressure. At low pressures, contact between particles is insufficient to result in high compressive strength owing to relatively larger gaps between the particles. At elevated pressures, gaps between the larger particles are filled by fine particles, thereby increasing contact area and enhancing the formation of mechanical interlocking between particles (Sun et al., 2014).

Table 8: Effect of pressure on quality and strength of densified product (Kaliyan and Morey, 2009)

Feed material	Forming pressure,	Durability of product,	Compressive strength,
	MPa	%	MPa
Oak saw dust	34	Not available	25
	69	93.3	28
	103	94	45
	138	98.3	49
Pine saw dust	34	Not available	25
	69	71.2	35
	103	91.7	44
	138	93.2	45

2.3.2.Machine roll speed

The maximum stress on the briquettes depends on the roller diameter. In general, greater stresses are produced on larger diameter rollers (larger machines). It is critical that the roller drive produces constant torque and equal velocity of the two roller shafts to prevent wear of rollers and shearing forces that might fracture the briquettes (Kleinebudde, P. and Knop, K. 2007).

Vining et al. (2017) studied the effect of machine roller speed on green briquette yield at different moisture contents for Australian hematite–goethite iron ore fines. The results indicated that the briquettes produced at a roller speed of 12 rpm were weak and poorly formed and the yield was low (Vining et al., 2017). It was concluded that optimum roller speeds of 4.5–10 rpm were sufficient to produce briquettes of satisfactory quality.

2.3.3.Curing conditions

Drying, by definition, refers to the process by which water is removed from a body by application of heat. Classification of drying can be based on the prevalent method of heat transfer (radiation, convection, or conduction). The movement of moisture can be slow during a drying process, because the liquid needs to diffuse through structural obstacles caused by the molecular configuration (Cardoso et al., 2003). This can, however, be overcome by application of different drying techniques that employ different heat- and mass-transfer mechanisms.

The mechanism of drying by evaporation can be separated into three distinct stages: high-rate stage, falling-rate stage, and low-rate stage (Han and Zhou, 2013). The high-rate stage is characterised by evaporation at the surface of the body and is primarily limited by atmospheric conditions (vapour pressure, wind velocity, etc.).

Qiu and Ben-asher (2010) stated that drying is primarily characterized by adequate supply of water to the surface and is controlled by the energy available at the surface in the high-rate stage of evaporative drying. The falling-rate stage only commences once surface moisture has been depleted. It is characterized by movement of evaporation from the surface to the sub-surface, resulting in the formation of a dry surface layer. This stage ends when there is minimal liquid water movement and only a vapour flux through the solid pores (Qiu and Ben-asher, 2010). Sub-surface evaporation is primarily dependent on properties of the body that is being dried.

One of the conditions required for continued evaporation from a solid body is that the vapour pressure in the environment over the evaporating body should remain lower than that at the surface (Qiu and Ben-asher, 2010). The rate of evaporation of water from a body is directly proportional to the vapour pressure (Fisher, 2020).

2.3.4.Particle size distribution

PSD is one of the key ore parameters that affects the quality of a formed briquette. The effect of PSD on compressive strength is illustrated in Figure 13. Compressive strength increases with an increase in the proportion of material less than 125 µm, i.e., an increase in compressive strength with a decrease in particle size. Finer particles allow for an increased contact area between particles. This, in turn, forms stronger bonds between particles, thereby increasing the compressive strength. Additionally, the distance between particles is shortened with finer particles, which increases the intensity of the forces between particles, leading, in turn, to an increase in compressive strength (Sun et al., 2014).

As a result of the forces between particles, force chains are formed in a briquette, the length of which is dependent on the number of contact forces and particle size. In comparison with larger particles, finer particles result in longer force chains, which increases the compressive strength (Sun et al., 2014). Finer particles usually absorb more moisture than larger particles, thus undergoing a higher degree of conditioning, while larger particles may act as fissure points that may result in cracks and fracture (Kaliyan and Morey, 2009). Although fine particles may result in more durable briquettes, fine grinding is undesirable due to a higher cost of production. A key observation made by Kaliyan and Morey (2009) was that decreasing the average size of rice husks from 5.14 mm to 4.05 mm increased the durability of briquettes from 84.1% to 95% at a pressure of 31.2 MPa.

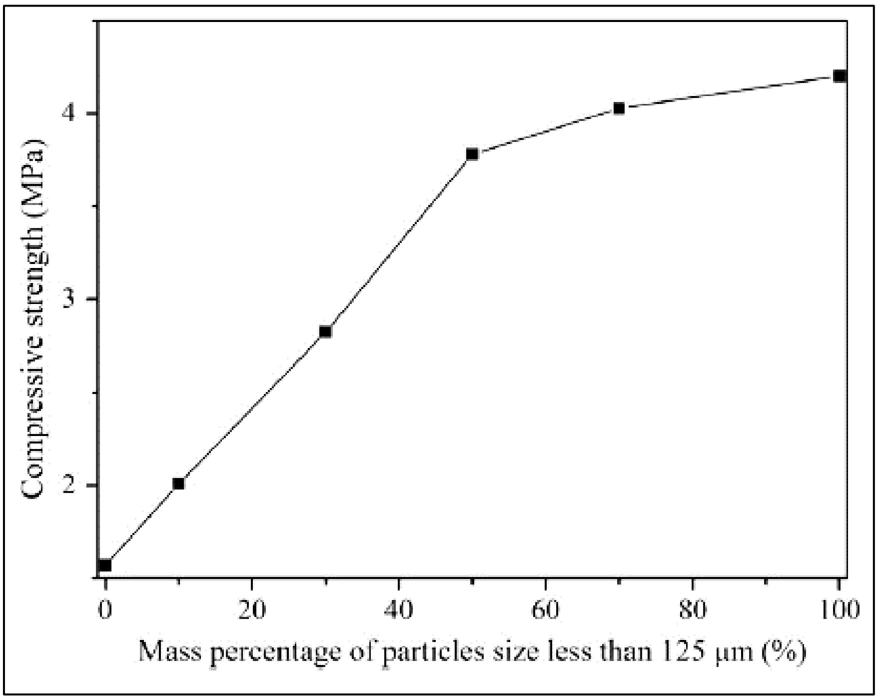

Figure 13: Effect of particle size on compressive strength of coal at moisture content of 27.51% (Sun et al., 2014)

2.3.5.Effect of moisture content

2.3.5.1.Compressive strength

Various studies have indicated that the strength of ores is compromised in the presence of water. Several mechanisms have been proposed to explain this phenomenon, including (Van Eeckhout et al., 1976) fracture energy reduction and pore water pressure.

Fracture energy reduction: This mechanism has been widely used to describe the effect of reduction in the compressive strength of the ore with an increase in moisture content. The Griffiths fracture criteria is used to explain this mechanism, according to Equation 1 (Van Eeckhout et al., 1976):

$$\boldsymbol{\sigma_t} = \sqrt{(\boldsymbol{2E\gamma/\pi C_0})} \qquad \mathbf{1}$$

where σ_t (Pa) is tensile stress required to cause a crack; E is Young's modulus of elasticity; γ is surface energy; C_0 one-half initial crack length.

An increase in moisture content has been found to decrease the surface energy due to physical absorption. A decrease in surface energy leads to a reduction in fracture strength, so the strength of the ore will also decrease. This phenomenon is referred to as the Rhebinder effect.

Pore water pressure: Under conditions of increasing moisture content, if the fluids in a particle pore are pressurized as the particle is compressed, an outward pressure gradient is created (Van Eeckhout et al., 1976). This lowers the strength of the ore. The pore pressure is controlled by the effective stress, which affects the strength of ore with interconnecting pores.

2.3.5.2.Degree of reduction

The effect of moisture content on the degree of reduction was studied by Murakami et al. (2009), Larssen and Tangstad (2022), and Li (1999). Murakami et al. (2009) stated that the specific surface area of an ore increases with an increase in moisture. Ores with higher moisture content are therefore expected to exhibit a higher degree of reduction. The results noted, however, a decrease in the degree of reduction for ores with higher moisture content. Larssen and Tangstad (2022) evaluated the reduction behaviour of Comilog (Gabon) and Nchawning (South Africa) ores with different moisture contents and stated that ores with higher moisture content will exhibit a higher concentration of water vapour in industrial operation. According to Li (1999)**,** the presence of water vapour has a detrimental effect on metal extraction.

2.4. Binding mechanisms

The mechanisms by which binding of agglomerates occur are discussed by Pietsch(2008). These mechanisms are divided into five major groups, as discussed in the following subsections.

2.4.1.Solid bridges

Solid bridges are prevalent at elevated temperatures and can be formed by sintering, chemical reaction, or hardening binders (Pietsch, 2008). Figure 14 illustrates the different mechanisms by which solid bridges may be formed. At points of contact, a solid bridge may develop owing to diffusion of molecules between particles. Sinter bridges are formed when the temperature in a system rises above two-thirds of the melting temperature, resulting in diffusion of atoms or molecules at points of contact. The formation of solid bridges by chemical reaction of hardening binders is primarily dependent on materials involved and their properties (Pietsch, 2008).

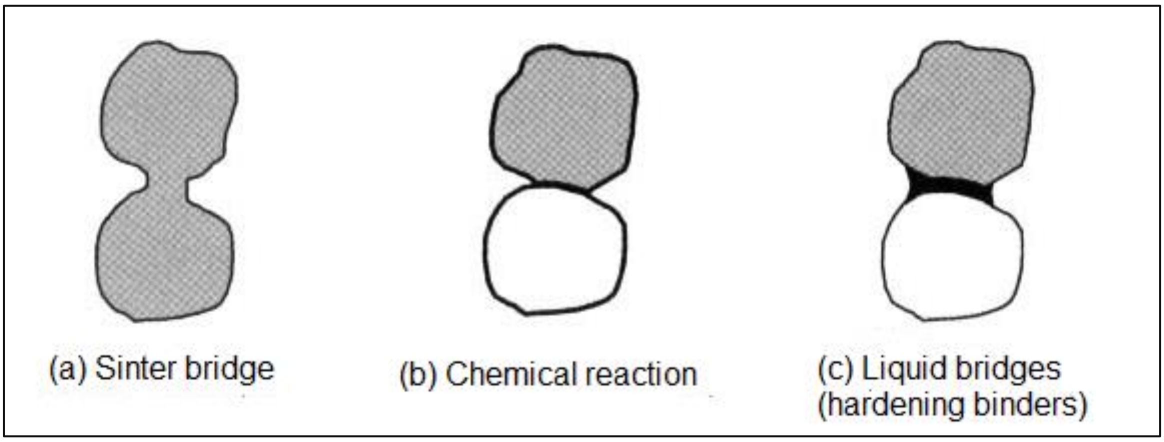

Figure 14: Illustration of different solid bridges (Pietsch, 2008)

2.4.2.Interfacial forces and capillary pressure

These mechanisms are common in wet agglomeration applications. Agglomerates are bonded by liquid bridges at contact points between particles. Capillary pressure and interfacial forces may create strong bonds in liquid bridges. These bonds may disappear if the liquid evaporates, and no other mechanism is dominant. Liquid bridges develop either from free water or capillary condensation, and are a precondition for the formation of solid bridges (Janwong, 2012). If the pores between particles are filled with a liquid and a concave meniscus develops at the ends of the pore on the surface of the system, a negative capillary pressure will form in the interior, resulting in agglomeration (Janwong, 2012). The interfacial forces and capillary pressure mechanisms are illustrated in Figure 15.

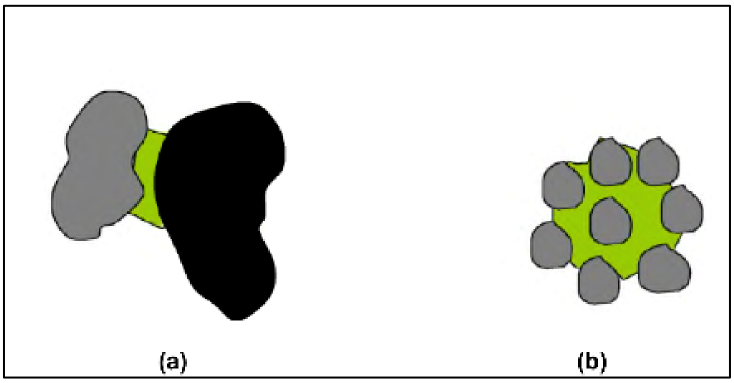

Figure 15: Liquid bridges between particles. (a) Two particles bonded by liquid bridge (b) agglomerates bonded by capillary pressure (Janwong, 2012)

2.4.3.Attractive forces between solid particles

This mechanism relies on electrostatic, magnetic, or van der Waals forces to cause solid particles to stick together. The magnitude of the forces between particles is very high at close distances between particles: with an increase in the interparticle distance, the magnitude of the forces also decreases (Janwong, 2012).

The prevalence of this mechanism increases with decreasing particle size. The most significant binding mechanisms in this category are molecular, electric, and magnetic forces (Pietsch, 2008).

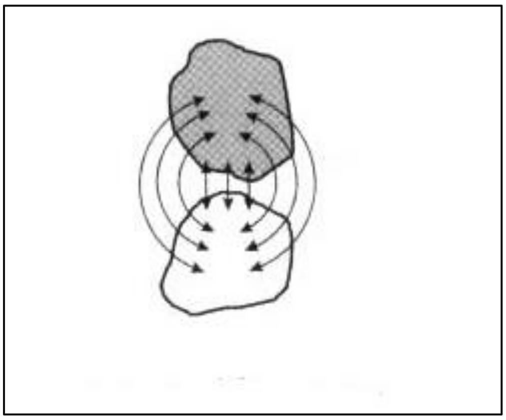

Figure 16: Attractive forces between solid particles (Pietsch, 2008)

2.4.4.Form-closed bonds (Interlocking)

Interlocking bonds typically occur if the particulate solids have the shape of fibres, threads, or lamellae that twist and bend about each other or entangle during agglomeration, resulting in ‘form-closed’ bonds (Pietsch, 2008). Interlocking bonds require that a compression or shear force must always act on the system to enhance the bonds. The strength of the agglomerates is a function of the type of interaction and material properties (Janwong, 2012). Interlocking bonds between particles are graphically illustrated in Figure 17.

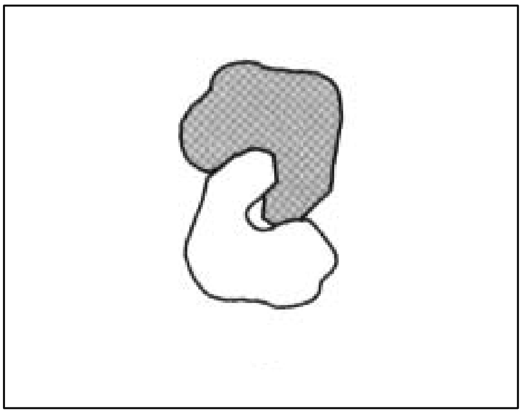

Figure 17: Interlocking bonds between particles (Pietsch, 2008)

2.4.5.Adhesion and cohesion forces

Adhesion and cohesion forces occur at solid–liquid interfaces in the presence of viscous binders, such as bitumen, pitch, and tar. Application of such binders results in adhesion forces at the solid–binder interface and cohesion forces within the viscous material (Pietsch, 2008).

2.5. Binders and binder systems

Briquetting can be performed either with or without a binder. Binders play a significant role in the production of briquettes. The quality of the binder directly affects the quality and performance of the briquette. Binders act with moisture in the ore and ore particles, thus affecting the capillary forces and viscous forces that bind particles together (Halt and Kawatra, 2013). Different types of binders are required for different applications.

Selection of an appropriate binder is crucial to the economic and technical feasibility of the final agglomerate/briquette/pellet. Binders may be categorized on the basis of the dominant mechanism that induces strength. There are five main grouping of binder systems: inactive film, chemical film, inactive matrix, chemical matrix, and chemical reaction (Koerner et al., 1983). Selection of a binder can be affected by several factors, including the required strength, cost of agglomeration, application, and final product shape.

Some binders undergo changes in their characteristics when heated or cured. A classical example of this is lignosulfonate: at ambient temperatures, lignosulfonates are hydrophilic; however, they become irreversibly insoluble on heating to temperatures in excess of 205°C (Koerner et al., 1983). It follows that a binder needs to be compatible with the end use of the agglomerate. Different binding systems are discussed below.

2.5.1. Inactive film binding system

This mechanism relies on the surface tension of the liquid, which pulls the particles together. Water is a typical example of an inactive film binding system, owing to the strength of its surface tension and its ability to wet particles, thereby acting as a lubricant. This mechanism requires that each particle is either coated with the binder or is sufficiently wet prior to agglomeration: thorough mixing prior to agglomeration improves effectiveness of the binder.

2.5.2. Chemical film binding system

Chemical film binders create a thin coating on the particles to be agglomerated. The thin layer of coating is set by a chemical reaction (Koerner and MacDougall, 1983). A key advantage of chemical film binders is the relatively short curing period required, resulting in waterproof agglomerates. Sodium silicate is a typical example of a chemical film binder, which on application can be set by addition of dilute acid to the fine particles to be agglomerated.

2.5.3. Inactive matrix binding system

This binding system requires that the particles be arranged in a continuous matrix with the binding material. It is the effectiveness of the continuous matrix formed between the particles and the binder that determines the performance of the agglomerates produced.

2.5.4. Chemical matrix and chemical reaction binding system

This system that relies on a chemical reaction between two binder components (Koerner and MacDougall, 1983). Lime and molasses are an example of a chemical matrix binding system. This binder may be used with either agitative agglomeration or briquetting. When using lime and molasses as a binder, it is important that curing takes place at relatively low temperature, because the reaction toward calcium sucrose is slowed at elevated temperatures.

2.6. Mineralogy of laterite ores

Laterite soils are produced as a result of either tropical or subtropical weathering. Three grades of laterite soils were originally identified on the basis of the silica–alumina (SiO_2/Al_2O_3) ratio: ratios less than 1.33 were considered true laterites; between 1.33 and 2.00 were considered to be lateritic soils; ratios greater than 2.00 were considered to be non-lateritic tropically weathered soils (Gidigasu, 1976). The presence of iron in laterite soil is of great significance, so a new definition was later proposed that incorporates iron to define the three different laterite soil grades: $(SiO_2)/(Al_2O_3 + Fe_2O_3)$.

The Barro Alto mine is situated within the Barro Alto complex, forming a 35 km arc extending from southwest to northeast. Its primary mineral resource consists of saprolite covered by laterites, which includes sequences of serpentinized dunites and pyroxenes (Bolaños-Benítez et al., 2021). Ratié et al. (2018) studied the nickel distribution in samples collected from the Barro Alto complex, and confirmed the presence of serpentine, chlorite, talc, smectite, goethite, magnetite, and quartz. Selivanov et al. (2020) studied the thermal properties of nickel laterite ores from the Ural deposit (Russia), and confirmed that the ore constituted of serpentine minerals (lizardite), talc, and chlorites with impurities that included chromium-containing spinel and quartz. Rhamdhani et al. (2009) studied the microstructure and phase characterisation of nickel laterite ore from Yabulu refinery (Queensland, Australia) and identified the main mineral constituents as goethite (iron oxide), serpentine, quartz, olivine, magnetite, and chromite. Traces of pyroxenes, gibbsite, diopside, and forsterite were also observed.

The mineral groups associated with laterite deposits are discussed in the following sections.

2.6.1.Olivine group: forsterite

The (Mg,Fe) olivines form a complete solid solution between forsterite (Mg_2SiO_4) and fayalite (Fe_2SiO_4) (Deer et al., 1966). In iron-rich olivines, there is minimal replacement of (Mg, Fe) by either Mn or Ca, whilst in Mg-rich olivines, nickel and chromium are commonly present. Olivines are susceptible to hydrothermal alteration, with serpentization being the most prevalent form of olivine alteration. The products of Mg-rich olivine alteration include lizardite, chrystolite, antigorite, brucite, talc, and carbonates.

2.6.2.Pyroxene group: enstatite and diopside

The pyroxene mineral group includes both monoclinic and orthorhombic minerals, and can be subdivided into three main groups and two minor sub-groups. The main groups are (Deer et al., 1966):

- Magnesium-iron rich pyroxene: enstatite, ferrosilite
- Calcium pyroxene: diopside
- Sodium pyroxene: jadeite

Structurally, the chemical formula of the pyroxene may be expressed as $M_2M_1T_2O_6$, where T is Si, Al; M1 is Al, Cr, Fe^{3+}, Ti, Fe^{2+}, or Mg; M_2 is Ca, Na, Mn, or Fe^{2+}.

2.6.2.1.Enstatite

Enstatite occurs in three distinct structural forms: orthoenstatite, protoenstatite, and clinoenstatite. The three different polymorphs are stable at different temperatures(Deer et al., 1966). Protoenstatite is most stable at temperatures between 1000°C and 1300°C: at 1550°C, it decomposes to forsterite and liquid. Protoenstatite melts at temperatures of 1559°C and 101.3 Kpa to form forsterite and liquid in the Mg_2SiO_4–SiO_2 system.

In the MgO–SiO_2–H_2O system, enstatite crystallizes at temperatures above 700°C and is stable in the presence of water at temperatures below 900°C (Deer et al., 1966). Clinoenstatite is the most stable polymorph at temperatures below 566°C. Orthoenstatite is stable at intermediate temperatures.

2.6.2.2.Diopside

There is complete solid solution between $CaMgSi_2O_6$ and $CaFeSi_2O_6$ in the diopside–hedenbergite series. Although aluminium is present in the minerals of this series, Si and Al replacement only occurs up to 10%. Magnesium-rich members of this series are characterized by high manganese content. Both diopside and hedenbergite are characterized by the metamorphosis of calcium-rich sediments: diopside is prevalent in the relatively early stages of the mineral sequence.

2.6.3.Amphibole group: hornblende

Hornblendes exhibit the formula $(Na,K)_{0–1}Ca_2(Mg,Fe^{2+},Fe^{3+},Al)_5Si_{6–7.5}Al_{2–0.5}O_{22}(OH)_2$, and belong to the amphibole group of minerals. The general formula of amphiboles may be presented as $A_{0–1}B_2C_5T_8O_{22}(OH,F)_2$. The predominant cations, which may occupy each structural site, are (Deer et al., 1966):

- A: Na and K
- B: Na, Ca, Mg, Fe^{2+}, Mn, Li
- C: Mg, Fe^{2+}, Al, Fe^{3+}, Mn, Zn, Cr, Ti, Li
- T: Si, Al

Various authors have studied changes in hornblende on heating. Rosenbusch and Wülfing (1885) observed that a dark green hornblende turned red when heated and exhibited strong absorption. Schneider (1891) demonstrated an increase in pleochroism with an increase in absorption upon heating, and further claimed, based on chemical analysis of the heated hornblende, that no ferrous iron was present. Hornblendes were heated in carbon dioxide by Graham (1926**)**, who concluded that the resulting changes (optical properties) were identical with those observed when heating in air. De Angelis et al. (2015) stated that the thermal stability boundary for hornblendes is in the region of 880–900°C.

The changes in optical properties exhibited by hornblendes upon heating have been variously explained: Takeshi (1929) attributed this effect to oxidation of ferrous to ferric iron; Kozu et al. (1927) claimed that the changes are a result of inversion; Graham (1926) attributed the changes to dehydration. Barnes (1930) undertook a study of fourteen hornblende samples that were heated to 850°C over a period of 3 h to ensure that the changes proceeded to completion. The results indicated that the changes in the optical properties of hornblende on heating were directly proportional to changes in the iron content.

Barnes (1930) further asserted that oxidation is the key reaction that drives the changes in the optical properties of hornblende on heating.

Barnes (1930) reviewed chemical analyses of hornblende samples from Renfrew and Lanark (Canada) prior to and after thermal treatment. The results confirmed the oxidation of ferrous to ferric iron; however, this was only true for iron-rich hornblendes.

De Angelis et al. (2015) stated that the properties of amphibole on heating have only been studied in relatively few experiments, so no tool exists to estimate their time-scale conversion as a result of heating. As stated, hornblende is characterized by the formula $(Na,K)_{0–1}Ca_2(Mg,Fe^{2+},Fe^{3+},Al)_5Si_{6–7.5}Al_{2-0.5}O_{22}(OH)_2$, while its high-temperature alliteration product is characterized by the formula $NaCa_2Mg_2Fe^{3+}{}_3[O_2|Al_2Si_6O_{22}]$. This suggests that the alteration of hornblende may be presented by:

$$NaCa_2(Mg_2Fe^{2+}Fe^{3+}{}_2Al_2)Si_6O_{22}(OH)_2 \rightarrow NaCa_2(Mg_2Fe^{3+}{}_3Al_2)Si_6O_{22} + H_2O\ (g) \qquad \textbf{2}$$

2.6.4. Mica group: talc and chlorite

Minerals belonging to the mica group have significant variation in their chemical and physical properties; however, they are all characterized by plate-like morphology. Structurally, micas can be described according to the following chemical formula: $X_2Y_{4–6}Z_8O_{20}(OH,F)_4$, where X = K, Na, Ca; Y = Al, Mg, Fe, Mn, Cr, Ti, Li; Z = Si, Al, Fe^{3+}, Ti.

2.6.4.1. Talc

There is generally little variation in the chemical composition of talc. Al or Ti may substitute for Si while Mn, Al, or Fe (Fe^{2+}, Fe^{3+}) may substitute for Mg. Talc undergoes thermal decomposition at 800°C to yield enstatite and cristobalite according to (Deer et al., 1966):

$$Mg_3Si_4O_{10}(OH)_2 \rightarrow 3\ MgSiO_3 + SiO_2 + H_2O \qquad \textbf{3}$$

The occurrence of talc is primarily dependent on the availability of sufficient magnesium; however, if sufficient Al, Ca, or K are also present, the formations of chlorite, tremolite, or phlogopite are favoured. The occurrence of talc is usually accompanied by serpentine and olivine. The addition of silica, removal of magnesia, or addition of CO_2 can lead to the conversion of serpentine to talc (Deer et al., 1966).

Liu et al., (2014) studied the thermal decomposition of talc, reporting that its decomposition to enstatite and amorphous silica commenced at 800°C and peaked at 895°C. Pyatina et al. (2018) stated that talc transforms into enstatite and amorphous silica at temperature ranges of 800–840°C (Pyatina et al., 2018).

2.6.4.2.Chlorite

Minerals of the chlorite group are characterized by a layered structure, similar to that of talc. Chlorites are characterized by the composition: $(M^{2+,}M^{3+})_{12}Si_{8-x}M^{3+}{}_{x}O_{20}(OH)_{16}$, with x in the range 1–3, where (Deer et al., 1966) M^{2+} = Mg, Fe, Mn, Zn and M^{3+} = Al, Fe, Cr.

The dissociation of clinochlore at temperatures between 600 to 750°C at P_{H2O} of 0.3 GPa to form forsterite, cordierite, and a spinel is given by:

$$5\ Mg_2Al_4Si_3O_{10}(OH)_8 \rightarrow 10\ Mg_2SiO_4 + Mg_2Al_4Si_5O_{18}.nH_2O + 3\ MgAl_2O_4 + (20-n)H_2O \qquad \mathbf{4}$$

Cordierite may either be formed as an anhydrous silicate or may consist of 1.80 mass% H_2O, depending on the pressure, as indicated in Figure 18. The solid line indicates the reaction yielding anhydrous cordierite, while the dotted line indicates that involving cordierite with 1.8 mass% H_2O. At pressures above 0.3 GPa, the thermal decomposition temperature of clinochlore increases to 875°C. The decomposition products include enstatite or garnet instead of cordierite.

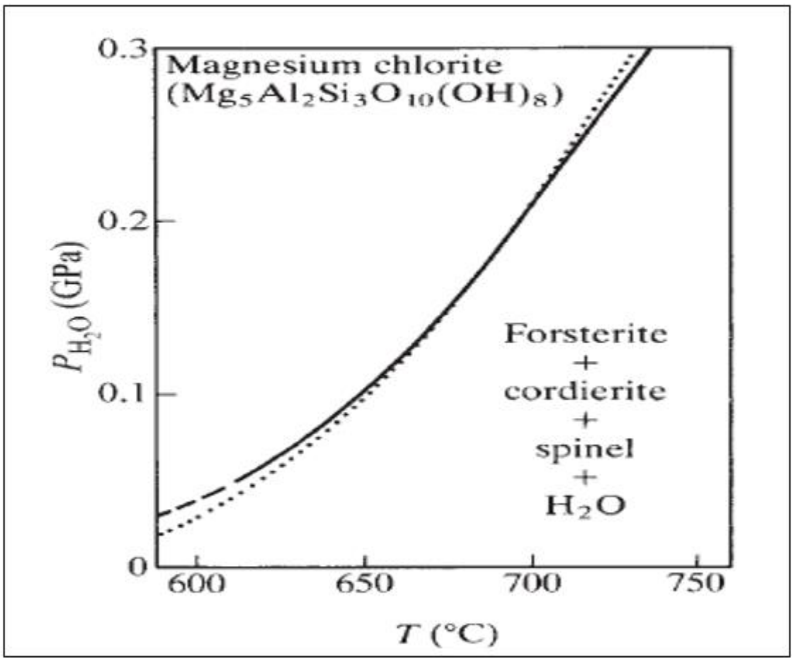

Figure 18: Dissociation curve for the reaction of clinochlore (Cho, 1986)

A kinetic study of clinochlore conducted by Cho (1986) concluded that its decomposition may be presented by:

$$1.11Mg_5Al_2Si_3(OH)_8 \rightarrow (Mg_{4.89}Al_{1.11})(Si_{2.89}Al_{1.11})O_{10}(OH)_8 + 0.264Mg_2SiO_4 + 0.044Mg_3Si_4O_{10}(OH)_2 + 0.396H_2O \qquad \textbf{5}$$

The reaction takes place at 670°C and a pressure of 200000 KPa. Cho (1986) further stated that more detailed studies are required to conclusively characterize the reaction governing the transformation of clinochlore.

2.6.5.Serpentine: lizardite

There are three main forms of serpentine minerals: lizardite, antigorite, and chyrsotile, all characterized by the composition $Mg_3Si_2O_5(OH)_4$. Lizardite is the most common (Deer et al., 1966). There is very little variation in the chemical composition of the serpentine-group minerals, which have the general stoichiometry $H_4Mg_3Si_2O_9$. The main substitutions that occur are that of Si by Al, Mg, and Al, and of Fe^{2+} by Fe^{3+}. Al substitution yields a range of solid solutions between serpentine and amesite. Serpentine minerals undergo thermal decomposition at 600°C in air, forming an olivine according to (Deer et al., 1966):

$$2\ Mg_3Si_2O_5(OH)_4 \rightarrow 3\ Mg_2SiO_4 + SiO_2 + 4H_2O \qquad \textbf{6}$$

Selivanov et al. (2020) stated that lizardite decomposes into forsterite and enstatite on heating, according to:

$$(Mg,Fe,Ni)_3Si_2O_5(OH)_4 \rightarrow (Mg,Fe,Ni)SiO_3 + (Mg,Fe,Ni)_2SiO_4 + 2H_2O \text{ (at 500–700ºC)} \qquad \textbf{7}$$

On further heating to 1100°C, forsterite, enstatite, and maghemite were identified. Crystallization of amorphous enstatite was reported at 824°C, according to:

$$2\ (Mg,Fe,Ni)SiO_3 \rightarrow (Mg,Fe,Ni)_2Si_2O_6 \qquad \textbf{8}$$

2.6.6.Silica minerals: quartz

Quartz occurs in different polymorphs at different temperatures. The three main crystalline forms of SiO_2 (quartz, tridymite, cristobalite) are characterized by different crystal structures, with each being dominant in a well-defined area of stability under equilibrium conditions. The different polymorphs of quartz and their temperature ranges are (Deer et al., 1966):

- α-quartz: Stable at temperatures of 573°C and atmospheric pressure;
- β-quartz: Stable between 573 and 870°C;
- α-tridymite: May exist at atmospheric temperatures up to 117°C;
- β-tridymite: Melts at 1670°C and may exist above 117°C; is stable at 870–1470°C;
- α-cristobalite: Exists at atmospheric temperatures and at temperatures between 200 and 275°C;
- β-cristobalite: Is stable from 1470–1713°C.

The chemical composition of quartz is usually close to 100% SiO_2; however, analyses that indicate small amounts of other oxides could be due to inclusion of minerals or owing to liquid infillings in cavities. Substitution of Al^{3+} for Si^{4+} may take place; this is usually accompanied by the introduction of alkali ions: Li^+ or Na^+.

2.6.7. Hematite: α-Fe_2O_3

Hematite is relatively easily distinguishable from magnetite and ilmenite due to its brown-red colour. It is primarily found as a product of weathering of iron-bearing minerals. In metamorphic rocks, hematite is formed due to the metamorphism of magnetite, siderite, and hydrated iron oxides (Deer et al., 1966).

Whilst the ideal chemical composition of hematite is Fe_2O_3, small amounts of MnO and FeO may be found. At 800°C, TiO_2 (rutile) may enter the α-Fe_2O_3 structure, thereby forming a complete solid solution between hematite and ilmenite above 1050°C. Hematite decomposes to Fe_3O_4 on heating in air in the region of 1390°C (Deer et al., 1966).

2.6.8. Spinel group: magnetite

The spinel group of minerals can be divided into three different series, depending on which trivalent ion is present. Classification of the different spinel groups is presented in Table 9.

Table 9: Spinel group minerals classification (Deer et al., 1966)

	Spinel series (Al)	**Magnetite series (Fe^{3+})**	**Chromite series (Cr^{3+})**
Mg^{2+}	Spinel	Magnesioferrite	Magnesiochromite
Fe^{2+}	Hercynite	Magnetite	Chromite
Zn^{2+}	Gahnite	Franklinite	-
Mn^{2+}	Galaxite	Jacobsite	-
Ni^{2+}	-	Trevorite	-

Trace amounts of Al^{3+} substitute for Fe^{3+} in magnetite ($Fe^{2+}Fe_2{}^{3+}O_4$), whilst Ca (in low concentrations), Mn^{2+}, and Mg^{2+} replace Fe^{2+}. A significant amount of Ti^{4+} can enter the magnetite structure. A continuous solid solution series exists between magnetite and ulvospinel (Fe_2TiO_4). Common replacements/substitutions that occur in magnetite include Cr^{3+} and V^{3+} for Fe^{3+}, while Ni^{2+}, Co^{2+}, Zn^{2+} Mg^{2+}, Mn^{2+}, and Ca^{2+} (low concentrations) may replace Fe^{2+}. At 1452°C, magnetite may contain up to 30% Fe_2O_3: this will convert to hematite on cooling.

2.6.9.Hydroxides: goethite

Goethite primarily occurs as a weathering product of iron-containing minerals, such as siderite, magnetite, and pyrite. Goethite transforms to either magnetite or hematite by dehydroxylation (Deer et al., 1966). The most common substituent ion is aluminium, with Al^{3+} replacing up to a third of the Fe^{3+} ions in some samples given by the formula; Al_x Fe_{1-x} OOH (Deer et al., 1966).

An increase in temperature is associated with increase in sample mass loss due to dehydroxylation, which leads to an increase in the Fe content of the material (Shobhana and Ratnakar, 2017). Magnetite and hematite transform to wustite by the reduction process. The phase-transformation temperature of goethite to hematite is at 350–400°C. Wustite transforms to metallic iron in the presence of a reducing agent.

2.6.10.Summary of phase decompositions in laterites

Decomposition of the following phases is expected, as discussed by various authors:

- Clinochlore decomposes between 600–750°C, forming forsterite, spinel, and cordierite(Cho, 1986).
- Forsterite decomposes above 1000°C under hydrogen pressure ≥ 2.5 GPa (Efimchenko et al., 2019)
- Lizardite decomposes between 500–700°C, forming amorphous enstatite and forsterite, with enstatite crystallizing at 824°C (Selivanov et al., 2020).
- Quartz exhibits polymorphic transformations between 573–1713°C (Deer et al., 1966).
- Enstatite undergoes polymorphic transformations between 566–1550°C (Smyth, 1974).

- A calcium magnesium silicate is expected in the reduced nickel laterite ore (Rhamdhani et al.,2009).
- Hornblendes undergo changes upon heating due to the oxidation of ferrous to ferric iron, resulting in the formation of oxyhornblende, an alteration product (Barnes, 1930), (Deer et al.,1966), (De Angelis et al. 2015), (Pichler and Schmitt-Riegraf, 1997**)**.

2.7. Nickel ore processing

Nickel is primarily used in production of stainless steel and high-temperature alloys. An increase in demand for stainless steel has resulted in an increase in ferronickel production. In 2011, 60% of nickel was extracted from sulfide ores, even though the laterites account for 70% of world nickel resources (Xuewei et al., 2013). The depletion of nickel sulfide ores has focused more attention on laterite processing. An overview of extraction of nickel from laterite and sulfide ores is illustrated in Figure 19.

The extraction of nickel laterites can be summarized into two main processes: smelting (pyrometallurgy) and acid leaching (hydrometallurgy). The choice of process is largely dependent on the chemistry and mineralogy of the host rock. Limonite and smectite ores are characterized by high iron content, while saprolites are characterized by high MgO content. The applicable extraction route for limonite and smectite ores is acid leaching to produce nickel metal, while saprolite ores are subjected to smelting to produce ferronickel.

The rationale behind each of the different extraction processes is further substantiated by the economics of the process. The efficiency of goethite dissolution in hot sulfuric acid, precipitation of iron as hematite or goethite, and the lower MgO content make limonite and smectite economically favourable for high-temperature acid leaching.

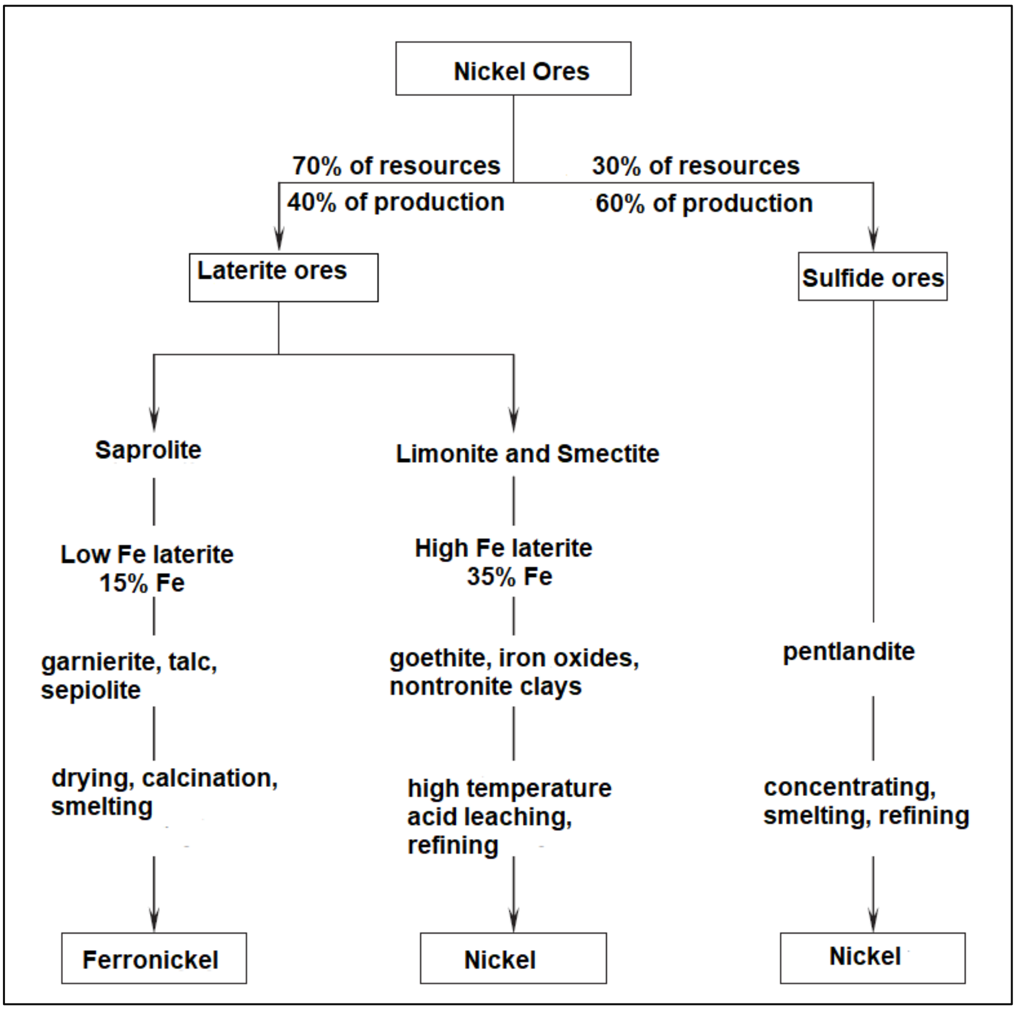

Figure 19: Nickel extraction from laterite and sulfide ores (Crundwell et al., 2011)

The high MgO content associated with saprolite would invariably lead to high acid consumption if subjected to acid leaching. The iron content of this host rock is relatively low in comparison with that of limonite and smectite, and, for this reason, saprolites are subjected to smelting to produce a nickel-rich ferronickel. The required cut-off grades are 1.3% Ni for pressure acid leach and 1.7% Ni for smelter extraction process (Dalvi et al., 2004).

2.8. Pyrometallurgical extraction of nickel laterite ores

Pyrometallurgical extraction of nickel laterites is appropriate for saprolitic ores. The process involves drying and calcination in a rotary kiln, followed by smelting in an electric arc furnace. Depending on the final product required, sulfur could be added to the kiln to produce matte. The final nickel product is dependent on electrical conditions in the furnace and the slag characteristics.

Ores with low-melting-point slags are better suited for matte production, whilst ores with high melting-point slags are suited for ferronickel production (Dalvi et al., 2004). The pyrometallurgical extraction process is characterized by high energy requirements.

An overview of the pyrometallurgical extraction of nickel laterites is presented in Figure 20. The process consists of the following key steps:

- Ore upgrading;
- Calcination and dewatering;
- Smelting;
- Refining.

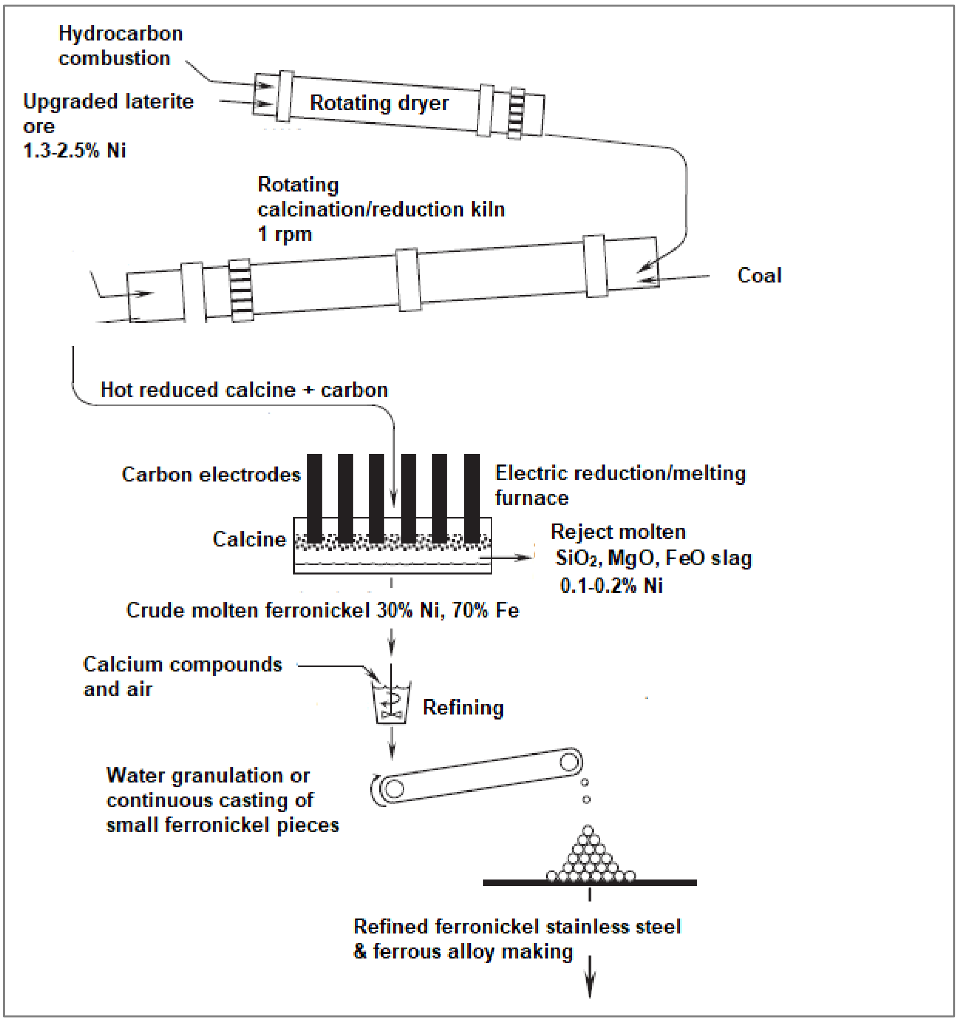

Figure 20: Overview of the pyrometallurgical extraction of nickel laterites (Crundwell et al., 2011)

2.8.1. Ore upgrading

Ore upgrading is a crucial step in the extraction process. The logic behind the upgrading of laterites is that less material (by volume) needs to be transported per tonne of nickel (Crundwell et al., 2011). Reduction in the volume of material being handled by the crushing circuit, smelter, or leach circuit leads to lower energy requirements and lower reagent consumption, whilst increasing the production rate. The combined effect is a lower production cost. The overall process economics are reliant on the extent of upgrading. The main shortcoming of ore upgrading is the unintended loss of nickel in the rejected material from the upgrading plant.

Table 10 presents different nickel laterite upgrading techniques used at operating mines. The principle of upgrading is based on the different mineralogical properties. Laterized minerals are softer than unlaterized minerals such as olivine that contain significantly lower nickel content (Crundwell et al., 2011). Laterized minerals can therefore be separated from unlaterized minerals by crushing and milling to the correct size to produce fine particles characterized by high nickel content and reject coarse particles characterized by low nickel content.

Table 10: Nickel laterite ore upgrading methods used by different mines (Crundwell et al., 2011)

Mine	Nickel in ore, %	Nickel in upgraded ore, %	Method of upgrading
Ravensthorpe, Australia	1.0	2.0	Scrubbing in rotating rotary scrubbers and attritioners
			Separate small Ni-rich particles from large Ni-lean particles in slurry by screen, hydrocyclones, and spirals
			Rejected particles are > 75 um
Faclondo, Dominican Republic	1.2	1.4	Ore treated through wobbler feeders and a ball mill
			Product is screened: particles larger than 10 000 μm are rejected to tailings
Nepoui and Tiebaghi, New Caledonia	1.8	3.0	Ore slurried with water
			Small Ni-rich particles separated from large Ni-lean particles by screening, cyclones, and filters
			Small low-density particles are richer in Ni than large dense particles
			Particle size is < 50 μm
Coral Bay, Philippines	1.26	1.5	Ore is screened, washed, and rescreened several times
			Only −2 mm particles are sent for leaching

2.8.2.Calcination and dewatering

Laterite deposits are primarily formed by weathering of peridotite rocks. Percolation of water through the weathered material takes place. This water contains organic acids and carbon dioxide (Crundwell et al., 2011). The percolated water dissolves the silica, magnesium, nickel, and iron.

Laterites occur mainly in tropical regions, which implies they are associated with relatively high moisture content, whether as run-of-mine (ROM) or in upgraded form. Excess moisture has adverse effects on both ore handling and process safety: if the moisture content is too high, the ore becomes prone to sticking on the conveyor belts and may lead to an explosion in the furnace; in contrast, if the moisture content is too low, excessive dust formation can occur. The moisture content should be accurately controlled to allow for a safe process and efficient handling of the material. Two main processes are used for adjusting the moisture content: dewatering and calcination (Crundwell et al., 2011).

2.8.2.1.Dewatering kiln

Dewatering kilns are designed to produce dried upgraded ore with specified moisture content at a specified rate. This is achieved by adjusting parameters such as feed rates of the ore and fuel (Crundwell et al., 2011). The principle of operation of a dewatering kiln is as follows. Upgraded wet ore is introduced into the kiln. Combustion gas and hot air are simultaneously fed to the kiln at a temperature of 800°C (Crundwell et al., 2011). The gas and ore travel in the same direction in the rotating kiln. Water evaporation is the primary reaction in the dewatering kiln, as characterized by:

$$H_2O(l) \rightarrow H_2O(g);\ \Delta H = 2260\ \text{kJ/kg}\ H_2O \qquad \textbf{9}$$

The operational mechanism of the kiln allows for the ore to be equally exposed to the hot air, thereby allowing uniform evaporation of water. This is achieved by the cascading motion of ore in the kiln using lifters.

Table 11 presents details of three laterite dewatering kilns currently operational for different deposits. The kilns produce moderately dry ore with moisture content of approximately 20%, allowing for ease of material handling (dust minimization and non-sticking).

Table 11: Three laterite ore dewatering kiln operations (Crundwell et al., 2011).

Parameter	Codemin, Brazil	Cerro Matoso, Columbia	PT Antam, Indonesia
Type and number of dryers	One rotary dryer	Two rotary dryers	Two rotary dryers
Outside diameter × length, m	3.4 × 22	5.1 × 45	3.2 × 30
Capacity, t/h dry ore	104	Max. 200 each	50 each
Ore moisture in, %	25–27	22-30	30
Ore moisture out, %	23–24	10-12	22
Fossil fuel type	Fuel oil	Natural guess	Pulverized coal
Dust production, % of ore feed	0.5	4	3
Dust destination	Recycle to dryer	To calcination kilns	Recycle to dryer
Dryer product destination	To calcination kilns	To calcination kilns	Screening, hammer milling, then calcination kiln

2.8.2.2.Calcination kiln

The dewatering kiln produces a moderately dry ore with moisture content of approximately 20%. Introducing ore with this moisture content directly into an electric arc furnace could lead to an explosion. A calcination kiln is introduced to further treat the partially dry ore from the dewatering kiln for removal of excess moisture. Nickel reduction is initiated in the calcination kiln: a portion of the nickel is reduced to a metallic state and Fe^{3+} minerals are reduced to Fe^{2+} minerals. The calcination kiln produces a product for ferronickel smelting at a temperature of 900°C.

The product from the dewatering kiln is introduced into the rotating calcination kiln at the upper end if the kiln. The kiln is typically 185 m in length and rotates at a speed of 1 rpm (Crundwell et al., 2011). The reducing gas and energy are introduced at the lower end of the kiln, which allows for counter current flow of the ore and reducing gas. Combustion of hydrocarbons introduced at the lower end of the kiln produces the required reducing gas for heating and drying of the ore and partial reduction of nickel- and iron-containing minerals. The reactions in the calcination kiln are as follows (Crundwell et al., 2011):

- Water evaporation (20% moisture in ore from the dewatering kiln):

$$H_2O(l) \rightarrow H_2O(g). \qquad \textbf{10}$$

- Decomposition of laterite minerals to oxides and $H_2O(g)$ at 700°C:

$$Ni_3Mg_3Si_4O_{10}(OH)_8(s) \rightarrow 3NiO(s) + 3\,MgO(s) + 4\,SiO_2(s) + 4\,H_2(g); \qquad \textbf{11}$$

$$2FeOOH(s) \rightarrow Fe_2O_3(s) + H_2O(g). \qquad \textbf{12}$$

- Oxide reduction by the coal and reducing gases at 800°C:

$$C(s) + NiO(s) \rightarrow CO(g) + Ni(s); \qquad \textbf{13}$$

$$CO(g) + NiO(s) \rightarrow CO_2(g) + Ni(s); \qquad \textbf{14}$$

$$CO_2(g) + C(s) \rightarrow 2CO(g); \qquad \textbf{15}$$

$$CO(g) + Fe_2O_3(s) \rightarrow CO_2(s) + 2FeO(s); \qquad \textbf{16}$$

$$H_2(g) + Fe_2O_3(s) \rightarrow H_2O(g) + 2FeO(s). \qquad \textbf{17}$$

The calcination kiln produces a partially reduced, completely dry ore (at a temperature of 900°C), as well as dust-containing offgas. The offgas is primarily composed of CO_2, H_2O, and N_2 at a temperature of 250°C (Crundwell et al., 2011). Dust from the offgas is pelletized and recycled to the calcination kiln. Temperature control of the product from the calcination kiln is crucial: above 900°C, nickel and iron oxides fuse with SiO_2 to form unreactive silicates (Crundwell et al., 2011).

Typical compositions of the product from the calcination kiln are presented in Table 12. Table 13 presents detail of various laterite calcination kilns currently operational for different deposits. The kilns produce partially reduced ore for feed into an electric arc furnace and dust-containing offgas for recycling.

Table 12: Calcination kiln product (Crundwell et al., 2011)

Component	Product, mass%
Coal	2
Ni	1.5–3 (25% as metal, 75% as oxide)
Co	0.4–0.08 (20% as metal, 80% as oxide)
Fe	15 (5% as metallic iron, 95% as FeO)
SiO_2	40
MgO	25
Al_2O_3	1

Table 13: Operational calcination kilns (Crundwell et al., 2011)

Parameter	Codemin, Brazil	Cerro Matoso, Columbia	PT Antam, Indonesia
Equipment type and number	Two rotary kilns	Two rotary kilns	Two rotary kilns
Outside diameter × length, m	3.6 × 70	6.1 × 185; 6.1 × 135	4 × 90; 4.2 × 90
Capacity, t/h dry ore	40 each kiln	165 each kiln	32; 35
Fuel type	Heavy oil	Natural gas	Pulverized coal
Discharge temperature, ºC	900	800-850	800–1000
Fuel consumption / t ore	52 kg	50–55 Nm^3	115 kg
Reductant	Wood chips	Anthracite	Anthracite coal
Average reductant consumption	180 kg	50–60kg	67 kg
Dust production, % of ore feed	20	12; 22	8
Dust destination	Recycled to kiln	Extruded and fed to kiln	Pelletized and fed to kiln

2.8.3.Smelting

Ferronickel ore mined at Barro Alto is processed in six-in-line rectangular electric arc furnaces (Anglo-American, 2009). Six electrodes, connected in pairs, are set in line along the centre of the furnace. Metal and slag tap holes are located on opposite ends of the furnace wall, with the metal tap holes located at a lower elevation. Figure 21 illustrates a schematic view of a section through a six-in-line furnace (Mc Dougall, 2013).

The base plate of the furnace is usually flat and is cooled by forced air ventilation. The sidewalls are fitted with copper cooling elements with essential water passages that are set into the refractory lining. These provide capacity to remove heat fluxes through the sidewalls. The copper coolers can be classified into two types: shallow-cooled and deep-cooled. In shallow-cooled coolers, the copper element is located inside the furnace, but the water passages are located on the outside of the furnace; in deep-cooled coolers, both the copper elements and water passage are located inside the furnace. Heat exchangers or cooling towers are used to cool the water. The cooling water system is operated in a closed circuit. Feed material from the rotary kiln is introduced into the furnace through feed chutes. A batch feeding mechanism is used. To control the feeding intervals, the height of the feed piles in the furnace is continuously monitored. Metal is periodically tapped from the tap holes, which are located 700–1000 mm below the slag tap holes into a refractory-lined launder that discharges into a ladle. The tap hole blocks are water-cooled copper elements into which refractory of the tapping channel is set (Mc Dougall, 2013).

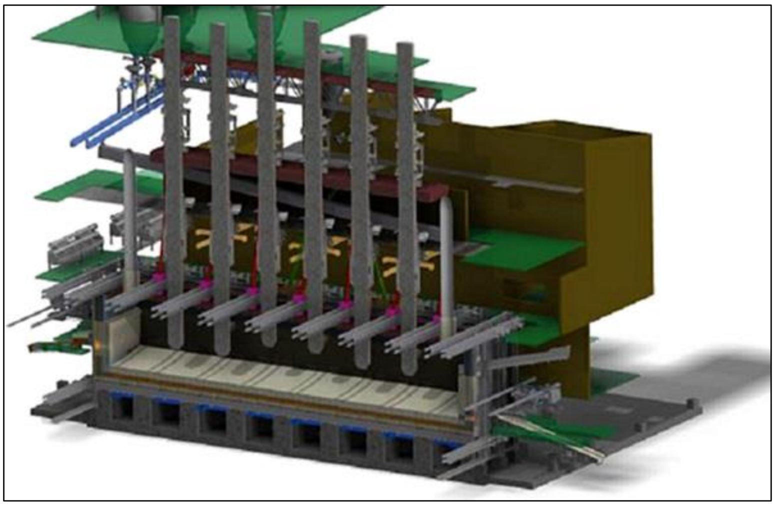

Figure 21: Cross-section through rectangular six-in-line furnace (Mc Dougall, 2013)

Smelting converts the hot calcine from the calcination kiln into hot molten ferronickel that is suitable for refining. Smelting produces three products at different temperatures (Crundwell et al., 2011):

- Unrefined molten ferronickel: The molten ferronickel consists of nickel with a concentration of 20–40% and iron with a concentration of 60–80%, produced at 1450°C;
- Molten slag, consisting of SiO_2, MgO, and FeO, is produced 1550°C;
- Offgas, containing CO and N_2, is produced at 900°C.

.

The density differential between the slag and molten ferronickel allows for the metal to settle to the bottom of the furnace bath and for the slag to float on top.

The three products are recovered separately: ferronickel metal is tapped through the low tap hole and slag is tapped through the high tap hole. The slag is transferred to waste and the molten metal is sent for refining. Not all the nickel is recovered to ferronickel: approximately 2% is lost to the slag, which typically contains 0.1–0.2% nickel (Crundwell et al., 2011). It is critical to minimize losses of nickel to the slag.

Ferronickel furnaces typically have a capacity of producing 250 t/d of molten ferronickel a day and 3700 t/d of molten slag, with an estimated energy consumption of 500 kWh/t feed material (Crundwell et al., 2011).

The reactions in the electric arc furnace are as follows (Crundwell et al., 2011):

- Nickel reduction to metallic nickel:

$$NiO(s) + C(s) \rightarrow Ni(l) + CO(g). \quad \textbf{18}$$

- Iron reduction to metal:

$$FeO(s) + C(s) \rightarrow Fe(s) + CO(g). \quad \textbf{19}$$

- Molten ferronickel formation:

$$Ni(l) + Fe(s) \rightarrow (Ni, Fe)(l). \quad \textbf{20}$$

- Molten slag formation:

$$2MgO(s) + SiO_2(s) \rightarrow \overset{\text{(In molten slag)}}{2Mg(l) + SiO_4(l)} \quad \textbf{21}$$

Reduction behaviour of a saprolitic (garnieritic) nickel laterite was studied by Yang et al. (2019), with the objective of determining ideal conditions for selective reduction of nickel. The ore was reduced with gas containing 60 vol.% CO and 40 vol.% CO_2 at 740°C for a period of 60 min (Yang et al., 2019). The study revealed that a ferronickel alloy was formed owing to reduction of the metal oxides; however, the degree of reduction was largely dependent on the temperature and CO concentration. Back-scattered electron images (BSI) of the pre-reduced ore are presented in Figure 22. Ferronickel alloy particles were only visible at nano-scale size and their analysis by energy-dispersive spectroscopy (EDS) was inconclusive (Yang et al., 2019). Prominent phases identified in the pre-reduced ore were (1) wustite, (2) modified chlorite, (3) olivine, (4) pyroxene, (5) talc, and (6) quartz.

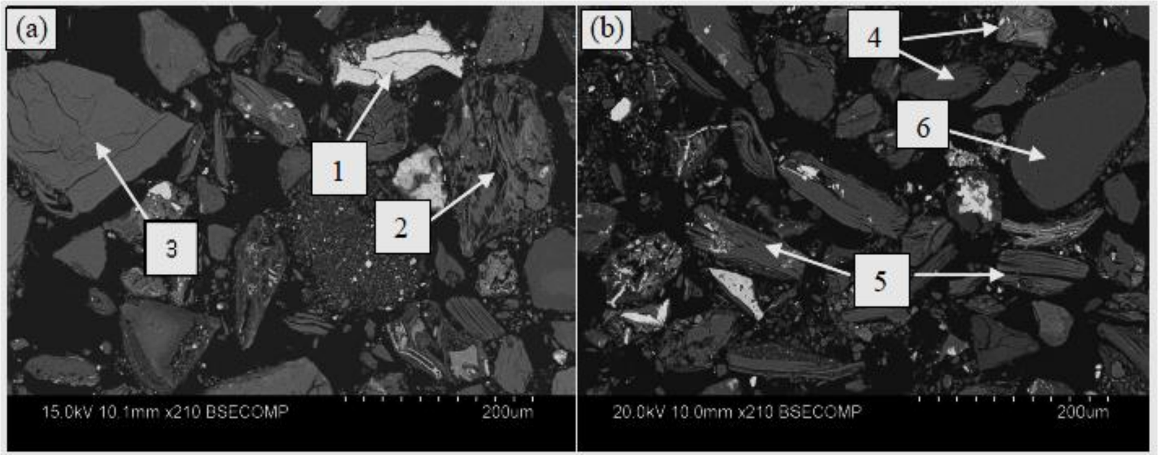

Figure 22: Back-scattered electron micrograph of a pre-reduced laterite ore (Yang et al., 2019)

The most critical factors in the reduction of laterite ores are temperature and reducing gas composition. According to Li (1999), a reducing gas containing a mixture of 90% H_2O and 10% H_2 or 75% CO_2 and 25% CO will result in desired high extraction of nickel from typical laterite ores at 900°C.

However, different types of lateritic ores require different conditions: when H_2 is used for limonitic ores, the optimum temperature range is between 550°C and 850°C; for serpentinic ores, the optimum temperature is between 550°C and 650°C.

2.8.4.Refining

The ferronickel product from the electric arc furnace typically contains impurities. These are known to affect the strength, corrosion resistance, and toughness of the ferrous alloys. Typical impurity elements include phosphorus, sulfur, cobalt, carbon, chromium, and silicon.

Phosphorus and sulfur are key impurities that have a detrimental effect on ferronickel metal: removal of these impurities is imperative to the metallurgical performance of the ferroalloys. Additionally, market constraints regarding maximum allowable impurity levels drive their removal. London Metal Exchange (LME) pricing considers several factors, including shape and form of the metal, grade, and purity. Higher level of impurities in the ferronickel would demand a higher price discount, which, in turn, affects the process economics.

2.8.5.Removal of impurities from ferronickel

2.8.5.1.Sulfur removal

Calcium carbide is used for removal of sulfur from the molten ferronickel, as characterized by (Crundwell et al., 2011):

$$S(l) + CaC_2(s) \rightarrow 2C + CaS\ (l). \qquad \textbf{22}$$

2.8.5.2.Phosphorus removal

Lime and oxygen are used in the removal of phosphorous from ferronickel, as represented by Reaction 2.15 (Crundwell et al., 2011). The molten slag is removed by decanting.

$$2P(l) + 5O(g) + 4CaO(s) \rightarrow (CaO)_4P_2O_5\ (l) \qquad \textbf{23}$$

3. Experimental procedures

3.1. Briquette performance

Several standard tests have been developed by the International Standards Organisation (ISO) to evaluate the quality of iron ore lump, pellets, and sinter; however no standard tests exist for evaluating performance of ferronickel briquettes (Iljana, 2017). An iron ore feed material is characterized by chemical composition, PSD, crushing strength, reduction disintegration index (RDI), reducibility index (RI), and decrepitation index (DI) (Iljana, 2017). To evaluate the quality of the produced ferronickel briquettes, standard ISO tests procedures for iron ore pellets were used in this study. Table 14 presents a summary of these tests.

Table 14: International Standards Organisation tests for iron ore used in this study

Standard	Test ID	
ISO 4700	Compressive strength	CS
Anglo American (Value-In-Use) in-house standard	Drop number testing	DN
ISO 3271	Tumble strength	TI
	Abrasion index	AI
ISO 4695	Reducibility index	RI
ISO 8371	Decrepitation index	DI
ISO 4696-1	Reduction disintegration index	RDI
Non-standard test	Rotary kiln simulation	Linder furnace

3.2. Experimental design

The Design of Experiments (DoE) approach was adopted for the current study. According to the theory of DoE, valid conclusions can be drawn from experiments with natural fluctuations, such as temperature, soil conditions, and rainfall, in the presence of identified variables. The identified variables ordinarily lead to systematic biases in a group of results (Goupy, 1993).

One of the main objectives in a DoE study is to formulate a strategy that should (Goupy, 1993):

- Give the desired results as quickly as possible;
- Avoid conducting unnecessary experiments;
- Ensure that results are as precise as possible;
- Allow for the experiments to progress without any delays;
- Provide a model and optimization of the phenomena studied.

Such a strategy is considered effective when it takes into consideration three key areas of knowledge acquisition: regular acquisition of results, selection of best experimental strategy, and interpretation of results. This strategy is schematically presented in Figure 23.

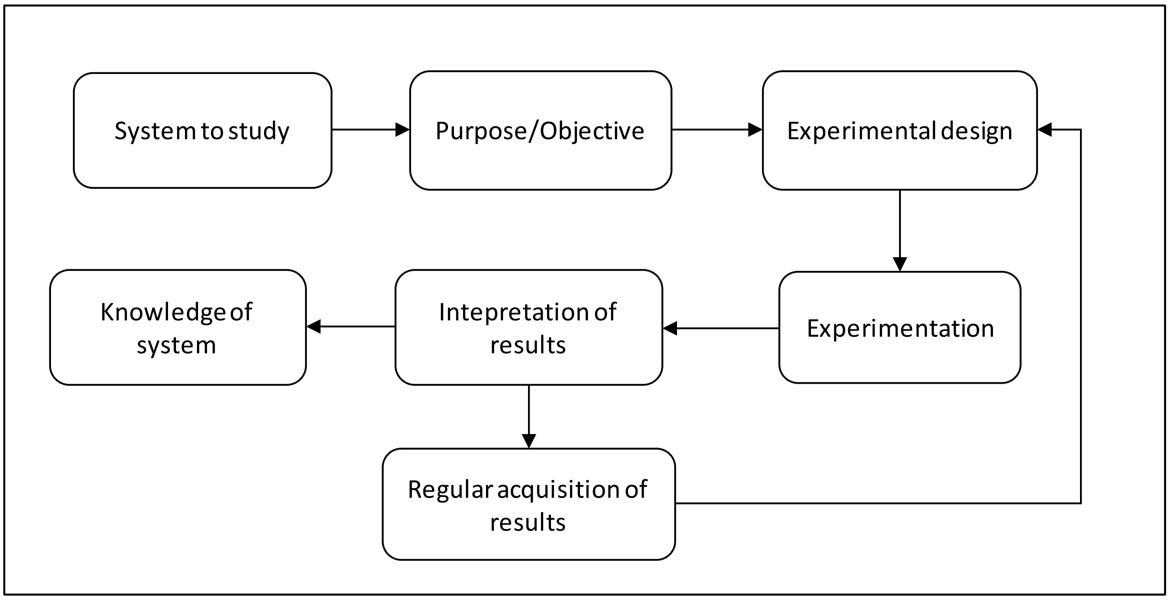

Figure 23: Experimental strategy (Goupy, 1993)

3.3. Principles of DoE

The experimental design methodology allows for values of all factors to be varied in each experiment. This forms the basis for a factorial design approach, wherein the factors evaluated may be quantitative or qualitative. Two-level factorial design, although the simplest, is extensively used because it may be applied to many situations as either complete or fractional designs. The two-level factorial is characterized by the following equation (Antony, 2014):

$$Y = n^k, \qquad \textbf{24}$$

where Y is the number of experiments required; k is the number of factors to be evaluated; n is the level of factors to be evaluated. A two-level factorial design approach was used for the current study.

In factorial experimentation, the effects due to each factor and their combinations are estimated. Each factor affecting briquette performance was evaluated at two levels. Applying the two-level factorial to three factors, the number of briquetting tests required are:

$$Y = 2^3 = 8 \text{ (briquette production tests)},$$

where the three k are moisture content, ore top size, and curing conditions.

3.4. Briquetting test programme

Figure 24 presents a flow diagram of the test programme. The study commenced with characterization of the feed ore, following which screening was carried out to produce bulk −12.5 mm and −6.3mm feed ore top sizes for briquetting studies. The bulk -12.5mm and -6 3 mm samples were split into representative samples for the test campaign.

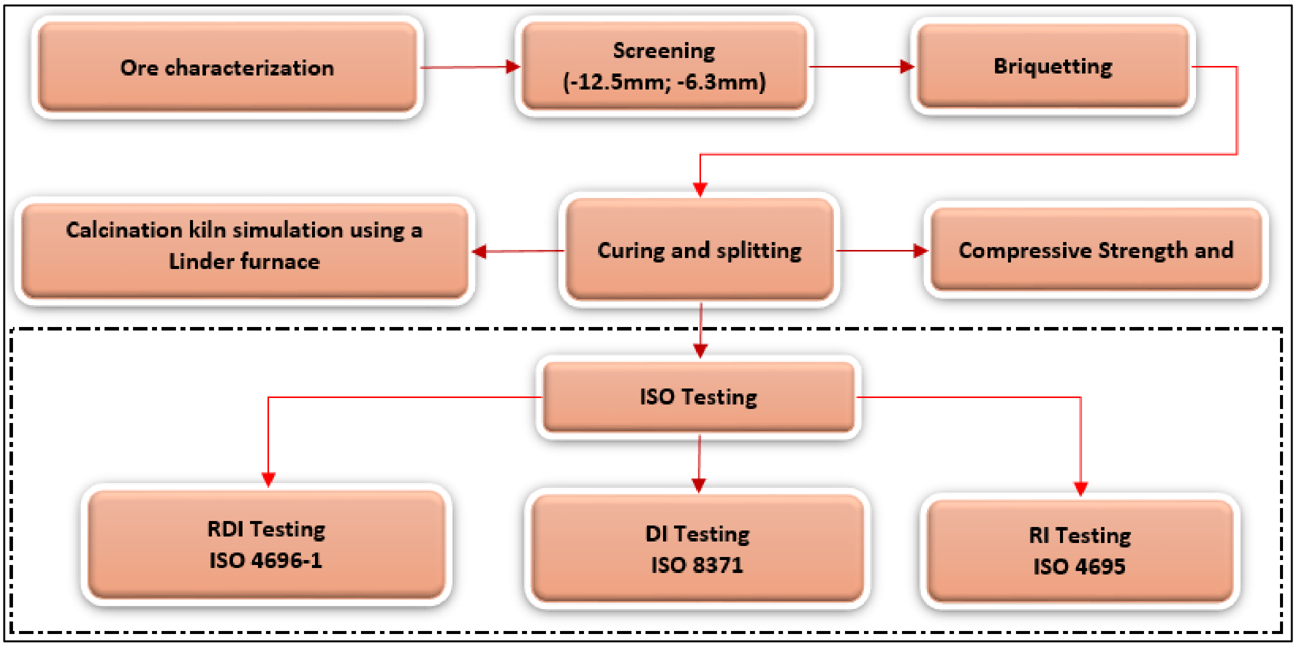

Figure 24: Test programme flow diagram

3.5. Test parameters

The main variables that affect performance of briquettes are machine roller speed, ore moisture content, PSD, briquetting pressure, density, and basicity (Vining et al., 2017; Sun et al., 2014). PSD analysis was conducted on the plant feed material. The results suggested that briquettes can be produced from he ore screened at −6.3 mm; therefore this top size was chosen for briquette production. However, owing to the heterogeneity of the sample, provision was made to also evaluate the performance of briquettes produced with a coarser top size of −12.5 mm. The following parameters were investigated for briquettes with top sizes of −6.3 mm and −12.5 mm: moisture content; curing condition.

3.5.1. Moisture content

Moisture contents of 16% and 24% were selected for the test programme because these values are typical for operating nickel laterite plants: Loma de Niquel, Venezuela, operates at moisture content of 15%, whilst Pacific Metal Co., Japan, operates at moisture content of 24% (Crundwell et al., 2011).

3.5.2. Curing conditions

Barro Alto plant is situated in the state of Goias, Brazil. The average relative humidity ranges from 57.9% during August to October to 85.2% in the period December to February (Lima et al., 2012). The average rainfall ranges from 0–128.7 mm^3 for April to August and 70.9–287.5 mm^3 for September to March (Cardoso et al., 2003).

Preliminary water-immersion tests indicated that green briquettes completely disintegrated in the presence of water. Preliminary relative humidity tests indicated average moisture absorptions of 8.23% and 8.69% at 54% and 80% relative humidity over a period of 7 d, respectively. Green briquettes were not subjected to RI, DI, RDI, or Linder furnace testing.

To preserve the structural integrity of the briquettes, preliminary tests indicated that it was important that the curing conditions either be optimized or set at the most economic level to maintain process economics. The duration and nature of curing ultimately affects mechanical properties of the briquettes. In evaluating the effects of curing conditions on briquette performance, two conditions were proposed: open curing and closed curing. Open-cured briquettes were placed on a tray and allowed to cure in the open atmosphere; closed-cured briquettes were placed in a sealed container and allowed to cure in a closed environment. The open-curing method aimed to simulate conditions under which briquettes are stockpiled and cured in the open atmosphere; the closed-curing method aimed to simulate conditions where briquettes are stockpiled and cured in closed silos. The study was limited to curing conditions and did not include the effect of pressure on the briquettes.

The objective of these tests was to evaluate the effect of curing time and curing method on strength development of the briquettes. This is particularly useful with regard to determining the duration for which briquettes can be stockpiled and their performance on transportation and loading on to the conveyor belts. Curing times of 2, 4, 8, 24, 48, 72, and 96 h were evaluated, which are consistent with the Anglo American (Value-In-Use) in-house pilot-plant curing standard.

3.6. Test matrix

3.6.1. Briquette production

The two-level factorial method requires categorization of the levels to be investigated into high (+) and low (−) levels. Designation of the levels allows for formulation of the test matrix. These are presented in Tables 15 to 17.

The factors are moisture content, top particle size, and curing conditions (Table 15). The test matrix was constructed in an order that allowed for evaluation of combinations of all three factors (Tables 16 and 17).

Table 15: Test level designation

Moisture, %		Particle size, mm		Curing	
–	+	−	+	−	+
16	24	−6.3	−12.5	Open	Closed
Low level	High level	Low level	High level	Low level	High level

Table 16: Test matrix

Test number	Moisture	Particle size	Curing
1	−	−	−
2	+	−	−
3	−	+	−
4	+	+	-
5	−	−	+
6	+	−	+
7	−	+	+
8	+	+	+

Table 17: Test matrix: Operational levels

Test number	Moisture, %	Particle size, mm	Curing
1	16	−6.3	Open
2	24	−6.3	Open
3	16	−12.5	Open
4	24	−12.5	Open
5	16	−6.3	Closed
6	24	−6.3	Closed
7	16	−12.5	Closed
8	24	−12.5	Closed

3.7. Analysis of results

DoE principles allow for the analysis of each of factor and their interactions. Mathematically, the most significant factor affecting briquette performance and their optimum interactions can therefore be determined. Evaluation of the factors was conducted using a statistical software package (Minitab). Main and interaction plots were used in analysis of the results.

3.7.1. Main-effect plots

The main-effects plot was used to evaluate the response values at each level. This plot was used to accurately compare the prominence of the effects of the different factors. The magnitude of a response is either positive (+) or negative (−), where the sign indicates whether the response value increases or decreases; the magnitude indicates of the strength of the response (Goupy, 1993).

Operating lines are constructed connecting the points for each specific variable relative to a reference line, the steepness of which indicates the significance of the process parameter on the measured response: the steeper the slope, the more prominent is the factor is on the measured response (Goupy, 1993).

3.7.2. Interaction plots

Interaction plots are useful in analysing the response of two factors at all combinations of their settings, either high (+) or low (−) level. The plot indicates whether an interaction exists between the factors. Operating lines are constructed for each process parameter. Parallel operating lines indicate that there is no interaction; non-parallel operating lines indicate the presence of an interaction between the two parameters on the measured response.

3.7.3. Analysis of variance

To assess whether differences between measured responses are statically significant at different factor levels, the p-value, which is factor specific, was compared with the significance level to assess the null hypothesis. The null hypothesis states that the measured responses are all equal. The significance level, given by an alpha value (α) of 0.05 (95% confidence interval), was used as the test statistic. The test statistics were set as follows:

- Null hypothesis: All measured responses are the same;
- Alternative hypothesis: Not all measured responses are the same;
- Significance level (α): 0.05.

Test criteria:

- p-value ≤ α: This indicates that the difference between some measured responses are statistically significant and that the null hypothesis can be rejected;

- p-value > α: The differences between the measured responses are not statistically different and thus the null hypothesis cannot be rejected.

4. Experimental

4.1. Sample preparation

Samples of ore were received from Barro Alto, packaged in 200 L drums, as shown in Figure 25. The ore was dried to constant mass on a drying pan at 105°C, to average moisture contents of 3.10%. The drying pad with ore is illustrated in Figure 26. The ore was screened at −6.3 mm and −12.5 mm. Four batches of each size fraction were removed by rotary splitting. PSD analysis was conducted for the −6.3 mm and −12.5 mm top size samples.

Figure 25: As-received sample

Figure 26: Ore drying pad at 105°C

4.2. Feed characterization

X-ray fluorescence (XRF) analysis of the as-received sample and by size distribution (assay by size) was carried out using the Malvern Panalytical Axios FAST (Malvern Panalytical) to determine chemical compositions. The crystalline phase compositions of the ore were determined by X-ray diffraction (XRD) analysis, using a PANalytical X'Pert Pro powder diffractometer in θ–θ configuration with an X'Celerator detector and variable divergence and fixed receiving slits with Fe-filtered Co-Kα radiation ($\lambda = 1.78\text{x}10^{-6}$ mm).

For the determination of amorphous content, 20% SiO_2 (99% pure; Aldrich) was added to the samples. The samples were prepared for XRD analysis using a back-loading method. The backloading method consists of pressing the opposite side of the sample which is being analysed, with minimal interference in the distribution of crystals and thereby reducing the effect of preferred orientation (Da Silva et al., 2011).

The relative phase amounts (mass% of crystalline phase) were estimated using the Rietveld method (Autoquan software, Meyer Instruments, United States of America).

Scanning electron microscopy (SEM) was used to observe the morphology of the samples, while the elemental compositions of the phases were identified through back-scattered electron imaging (BEI) employing an energy-dispersive spectrometer (EDS). Pulverized samples were mounted in resin, then ground, polished, and gold coated for analysis. The elemental composition was measured using XRF.

4.3. Moisture content determination

A representative aliquot was removed from each sample batch reserved for briquette production by rotary splitting and subjected to initial moisture content analysis using a MB-90-OHAUS moisture content analyser (Figure 27).

Figure 27: MB-90-OHAUS moisture content analyser

The aliquot was evenly placed on the sample pan, the cover closed, and the initial sample mass recorded. The sample was then heated using halogen heating to 200°C and the mass continuously measured as a function of time.

The analysis was terminated when the mass loss remained constant (mass change of < 1 mg) for 60 s. The difference between the initial and final masses were used to calculate the inherent moisture content.

Inherent moisture content refers to mechanically entrained water in a sample; loss on ignition (LOI) refers to the determination of organic and carbonate constituents and water bound in the crystal structure of a sample.

The analysed inherent moisture (initial sample moisture) was used to calculate the required water addition to attain the test moisture contents according to the following equations:

$$m_{\text{dry}} = m_0 \times \frac{100 - w_0}{100}; \qquad \mathbf{25}$$

$$m_{\text{wet}} = m_0 \times \frac{100 - w_0}{100 - w_1}; \qquad \mathbf{26}$$

$$w_{\text{req}} = m_{\text{wet}} \times \frac{w_1}{100} - m_0 \times \frac{w_0}{100}, \qquad \mathbf{27}$$

where m_o and m_{dry} are the initial and dry sample (less the inherent moisture) masses (g), respectively; w_o and w_1 are the inherent and desired moisture contents (mass%), respectively; m_{wet} is the sample wet mass (g); w_{req} is the water addition required to achieve desired moisture (g).

The ore and calculated water addition were mixed in an Eirich mixer (Figure 28) for 60 s.

Figure 28: Eirich mixer

4.4. Briquette production

Briquettes were produced at top sizes of −6.3 mm and −12.5 mm, using the ZEMAG-01 roller press and a 20 t hydraulic press, respectively.

4.4.1. Pilot-plant tests (briquette top size −6.3 mm)

Briquetting was carried out using a ZEMAG-01 roller press briquetting machine, illustrated in Figure 29. Ore was fed into the feed hopper and pushed down into the area between the two rollers using the tamping worm. Briquettes were formed by pressing the ore in the gap between the two rollers and collected underneath the roller press. The following machine parameters were used: feed speed of 30 rpm; roll speed of 5.4 rpm; roll pressure of 17500 KPa.

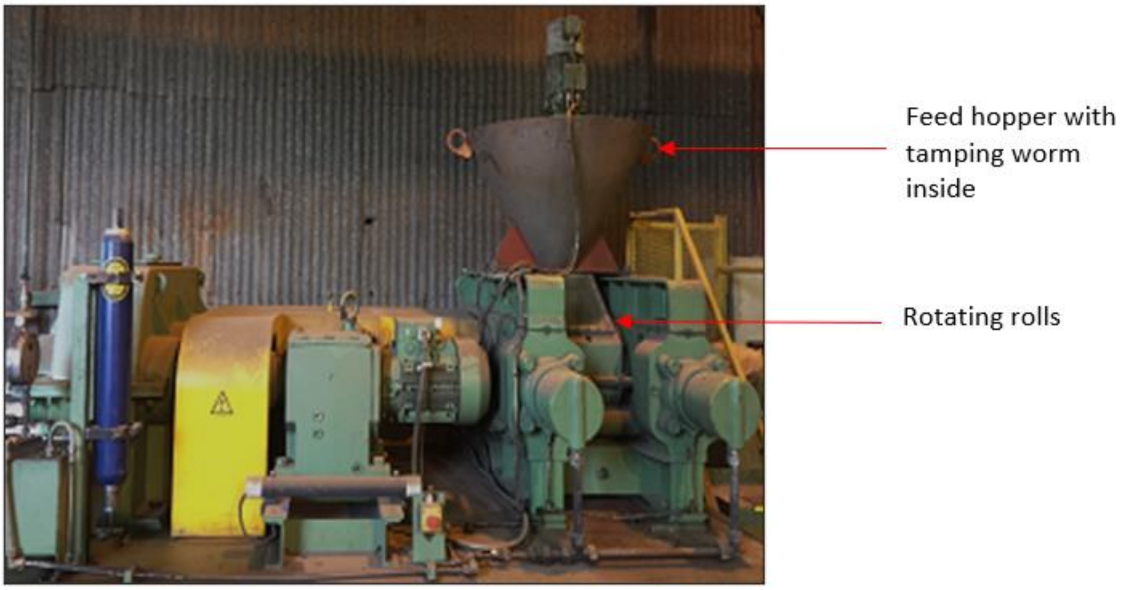

Figure 29: ZEMAG -01 briquetting machine

The briquettes were tumbled on a pelletizing disk (Figure 30) for 30 s to remove edges, following which they were screened at 12 mm, to separate fines and broken briquettes from intact briquettes. The final briquettes had dimensions (W × L × H) of 30 mm × 30 mm × 18 mm (Figure 31).

Figure 30: Removal of edges on a pelletizing disk

Figure 31: Pilot-plant briquettes

4.4.2.Laboratory tests (briquette ore top size −12.5 mm)

Laboratory-scale briquetting was conducted using a 20 t hydraulic press, illustrated in Figure 32. The rig was mounted on a steel frame and consisted of a hydraulic press, gauge lever, and briquetting chamber. The briquette chamber comprised a mould holder, ring, and mould/piston. A batch feeding mechanism was used. The briquettes had dimensions (W × L × H) of 30 mm × 30 mm × 20 mm (Figure 33). The 20-ton press was chosen for the -12.5mm ore top size briquettes due to its versatility in handling different feed ore sizes.

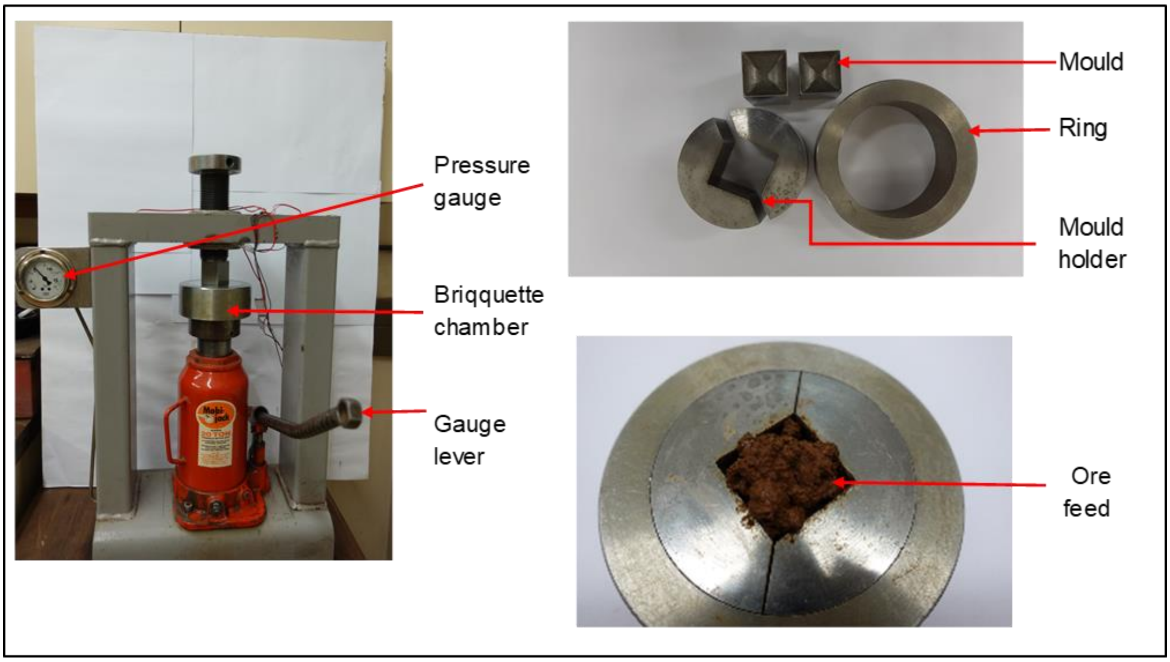

Figure 32: Laboratory-scale briquetting equipment

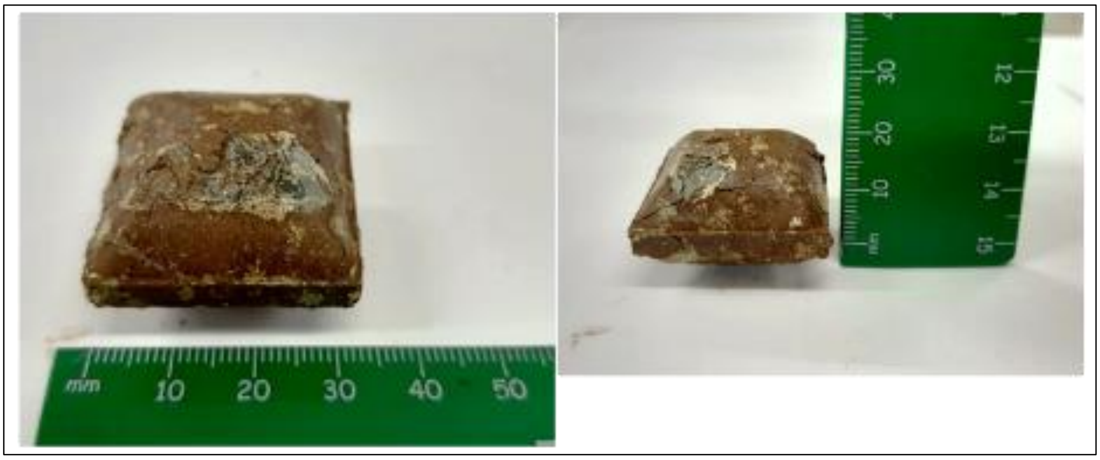

Figure 33: Laboratory-scale briquettes

Both sets of briquettes were allowed to cure for a period of 2 h prior to the ISO and Linder furnace tests. Open and closed curing conditions are illustrated in Figure 34. Closed-cured briquettes were placed in a sealed container; open-cured briquettes were placed on a tray and cured in the open atmosphere.

Figure 34: (a) Open- and (b) closed-cured briquettes

4.5. Green briquette yield

The green briquette yield of each batch was determined according to the following equation:

$$\% \text{ Yield} = 100 \times \frac{m_1}{m_2}, \qquad \textbf{28}$$

where m_1 (g) is the mass of whole briquettes; m_2 is the sample wet mass (g).

4.6. Drop number and compressive strength testing

The drop number test involves dropping a briquette from a height of 1 m onto a steel plate. The drop number is expressed as the average number of drops until breakage.

Determination of the compressive load required to cause breakage of the pellets is detailed in the ISO 4700 test method. Compressive strength tests were conducted using an Instron 3367 machine (Figure 35). The method specifies that a sample be placed on steel panels of a loading unit and compressed at speeds ranging from 10–20 mm/min. The crushing strength is recorded as the maximum load (N) attained in the test. Each test was repeated seven times: the reported crushing load is calculated as the arithmetic average of all measurements. The standard deviation was also recorded.

Tests were conducted on the following briquettes:

- Green briquettes at timed intervals up to 96 h;
- RI test product briquettes;
- Linder furnace test product briquettes.

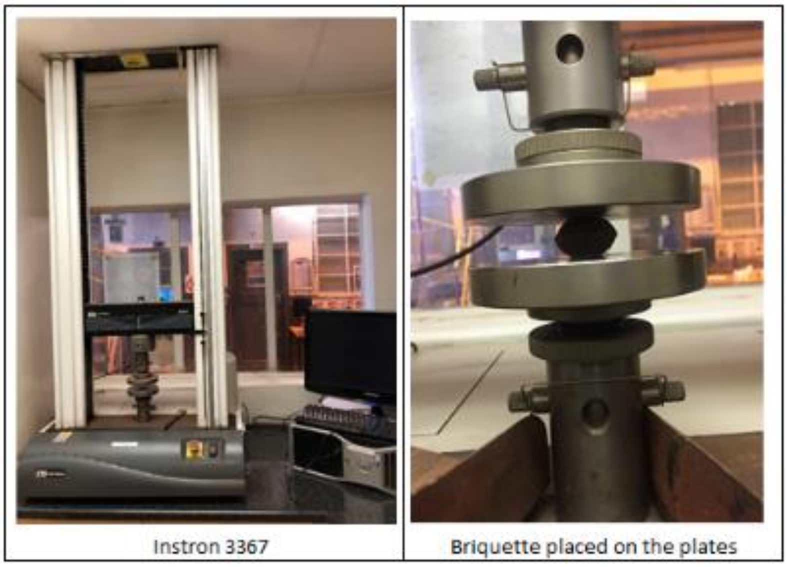
Instron 3367
Briquette placed on the plates

Figure 35: Strength testing (Instron 3367)

4.7. Tumble strength and abrasion index testing

The resistance of iron ore to size degradation by impact and abrasion can be evaluated using the ISO 3271 standard method. The method allows for calculation of both abrasion and tumble indices. The sample is tumbled in a rotating drum for 200 revolutions at a speed of 25 rpm. A schematic diagram of the ISO 3217 test apparatus is presented in Figure 36. On completion of tumbling, the sample was removed from the drum and screened at 6.3 mm and 0.5 mm. The tumble index (TI) is presented as the fraction of mass larger than 6.3 mm. The abrasion index (AI) is presented as the fraction of mass less than 0.5 mm. These indices were calculated as follows:

$$\mathrm{TI} = 100 \times \frac{m_1}{m_0}; \qquad \mathbf{29}$$

$$\mathrm{AI} = 100 \times \frac{m_0-(m_1+m_2)}{m_0}, \qquad \mathbf{30}$$

where m_0 is the mass after reduction, before tumbling, m_1, and m_2 are masses of the fractions retained on the 6.3 mm (+6.3 mm), and 0.5 mm (+0.5 mm) screens, respectively.

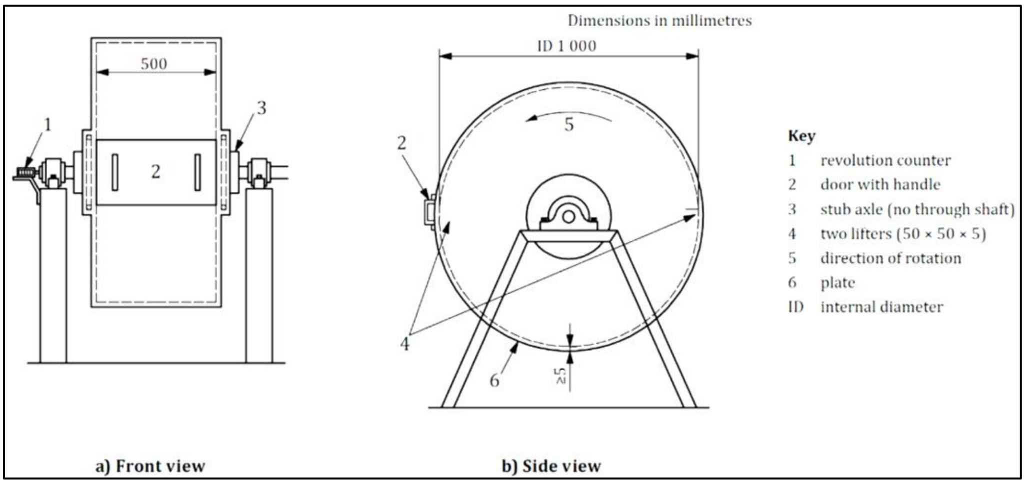

Figure 36: Schematic diagram of ISO 3271 test apparatus (Iljana, 2017)

4.8. Reducibility index testing

The ISO 4695 method is used to evaluate the degree to which oxygen is removed from an ore under conditions dominant in the reduction zone of a furnace. The method specifies that a 500 g sample be isothermally reduced at 900° C using a reducing gas that consists of 20 vol.% CO, 20 vol.% CO_2, and 60 vol.% N_2. The reducing gas flow rate should be maintained at 12.5 L/min during the reducing period. Mass loss of the sample is continually monitored until completion of the test. Table 18 presents the gas and temperature profiles used in the test. The gas composition in the reduction stage had a CO/(CO + CO_2) ratio of 0.5. Figure 38 presents a schematic of the RI test apparatus. Figure 37 shows a cross-section through a briquette after reduction, demonstrating that reaction proceeded throughout the briquette. On completion of the RI test, briquettes were reserved for TI and AI testing.

Table 18: Gas and temperature profiles during reducibility test

Stage	Definition	Temperature, °C	Gas flow rate, L/min	Gas composition	Duration, min
1	Heating	240	6.25	50% N_2	10
2	Drying free moisture	300	6.25	50% N_2	50
3	Calcination	800	6.25	50% N_2	50
4	Reduction	900	12.5	20% CO, 20% CO_2, 60% N_2	76
5	Cooling	< 200	2.5	20% N_2	-

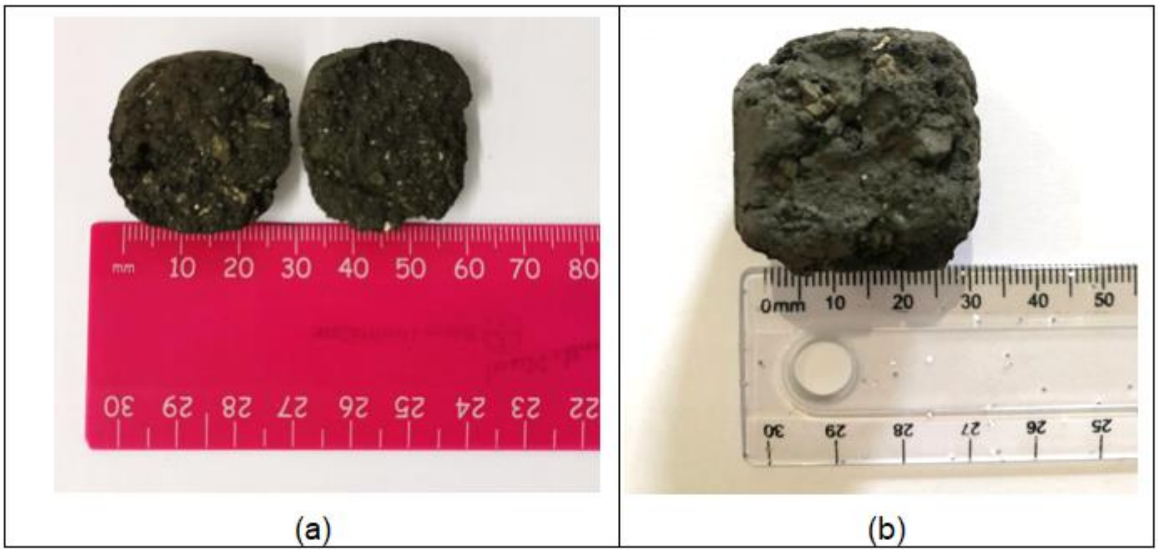

(a) (b)

Figure 37: Cross-sections through (a) −6.3 mm and (b) −12.5 mm briquettes after reduction

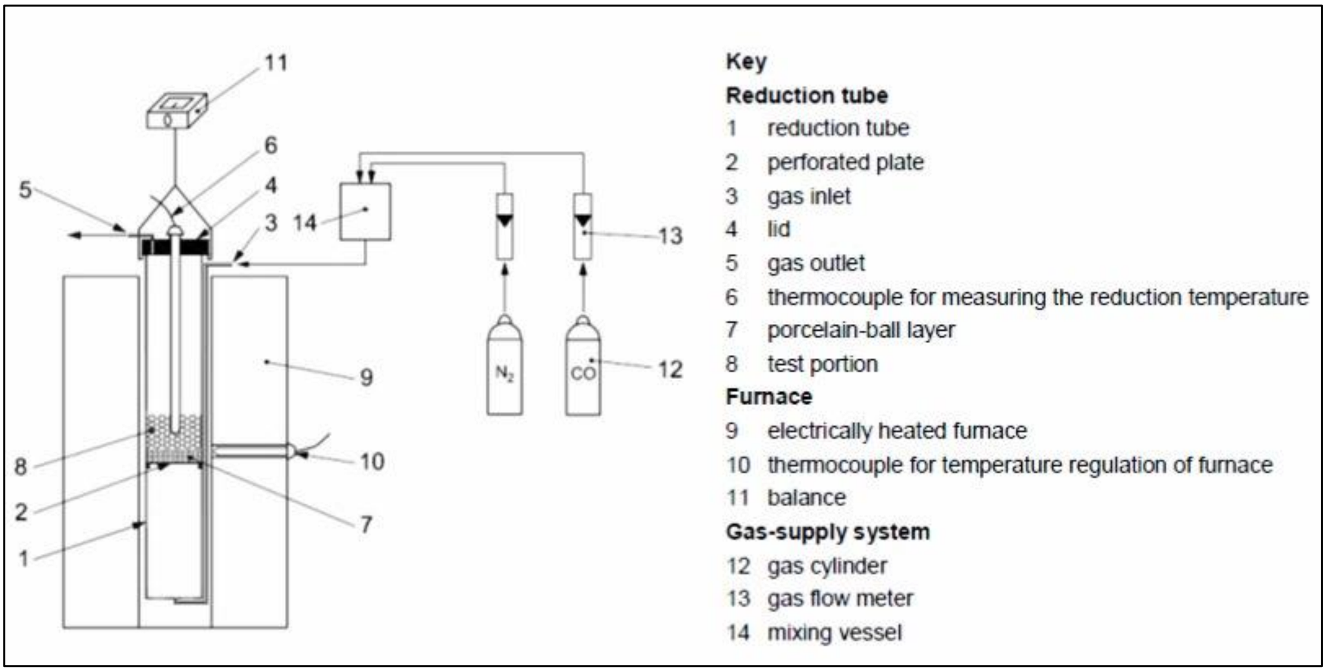

Figure 38: Schematic diagram of ISO 4695 test apparatus used to evaluate reducibility (Iljana, 2017)

For the purpose of the current study, the degree of reduction was derived from the mass loss in the reduction zone and the chemical analysis of hematite (Fe_2O_3) present in the laterite ore. The percentage decrease in degree of reduction per percentage increase in moisture content was calculated according to the following:

$$Decrease\ in\ reduction = \frac{|Red_{16\%} - Red_{24\%}|}{8\%} \times 100 \qquad \textbf{31}$$

where $\text{Red}_{16\%}$ and $\text{Red}_{24\%}$ are the average degrees of reduction at moisture contents of 16% and 24%, respectively.

On completion of the RI test, the briquettes were reserved for TI and AI testing, compressive strength and drop number testing, and chemical and mineralogical analyses.

4.9. Decrepitation index test

The decrepitation index (DI) refers to the breakage of the green briquettes at the point of entry into the rotary kiln. DI is expressed as the mass% of −6.3 mm material on completion of thermal treatment. A 500 g sample was loaded into the DI furnace (Figure 39), which was pre-heated to 700°C. The test was conducted for a period of 90 min, following which the briquettes were removed from the furnace, cooled in air, and the mass recorded. The heat-treated briquettes were screened at 6.3 mm, 3.15 mm, and 0.5 mm.

DI is calculated according to the following equation:

$$\text{DI}_{-6.3\text{mm}} = 100 \times \frac{m_1}{m_2}, \tag{32}$$

where m_1 is the mass of the −6.3 mm size fraction (undersize) and m_2 is the mass of the sample after thermal treatment.

To evaluate the fines generated, the mass% of the fractions passing 3.15 mm and 0.5 mm were also recorded.

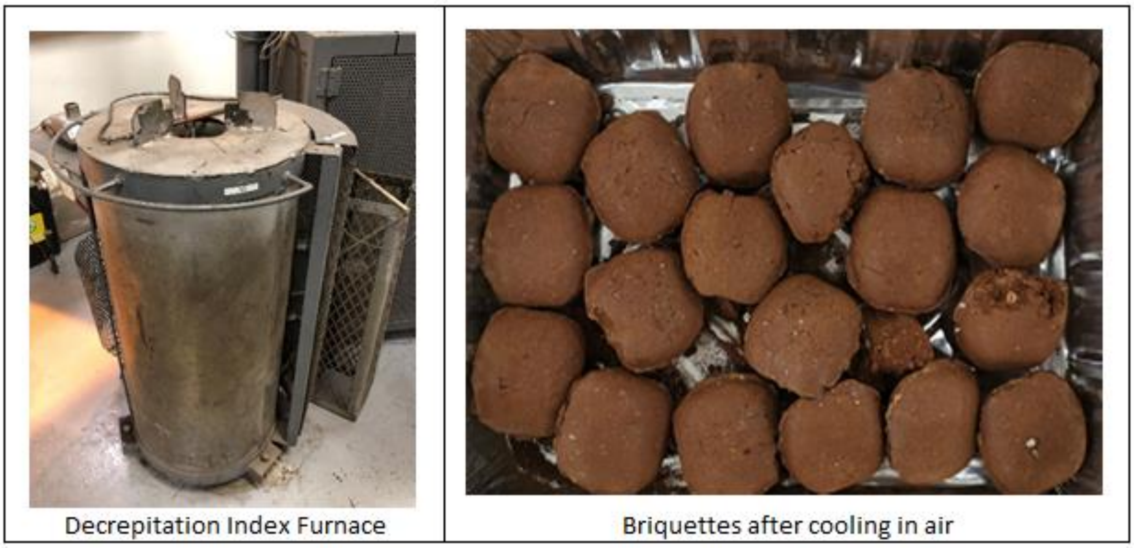

Figure 39: Decrepitation index test furnace and produced briquettes

4.10.Reduction disintegration index test

The ISO 4696-1 test is used for evaluating the degree of size degradation of iron ore when reduced in a CO–CO_2–H_2–N_2 gas mixture under conditions resembling those of the low-temperature reduction zone of a furnace. Hematite has a hexagonal crystal structure with a density of 5.225 g/cm^3, while magnetite has an octahedral crystal structure with a density of 5.220 g/cm^3. The reduction of hematite to magnetite is associated with a change in its volume and crystal structure, thus generating strains and causing crack growth across the matrix, which results in the disintegration of particles (Lu, 2015).

According to the test procedure, a 500 g sample was isothermally reduced at 500°C using a gas composition of 20.0 vol.% CO, 20.0 vol.% CO_2, 2.0 vol.% H_2, and 58.0 vol.% N_2 for a period of 60 min, whilst maintaining a gas flowrate of 20 L/min. The furnace gas composition and temperature profiles are presented in Table 19. Figure 40 presents a schematic of the test apparatus. On completion of reduction, the sample was cooled using N_2. The sample was then tumbled, using a tumble drum with two lifters for 300 revolutions. The samples were screened at 6.3 mm, 3.15 mm, and 0.5 mm and the masses recorded. Reduction disintegration indices (RDI) are calculated as the fractions of +6.3 mm, −3.15 mm, and −0.5 mm material, according to the following equations:

$$\mathrm{RDI}_{+6.3} = 100 \times \frac{m_1}{m_0}; \qquad \mathbf{33}$$

$$\mathrm{RDI}_{-3.15} = 100 \times \frac{m_0-(m_1+m_2)}{m_0}; \qquad \mathbf{34}$$

$$\mathrm{RDI}_{-0.5} = 100 \times \frac{m_0-(m_1+m_2+m_3)}{m_0}; \qquad \mathbf{35}$$

where m_0 is the mass after reduction; m_1, m_2 and m_3 are masses of the fractions retained on the 6.3 mm (+6.3 mm), 3.15 mm (−6.3 mm +3.15 mm), and 0.5 mm (−3.15 mm +0.5 mm) screens, respectively.

Table 19: Gas and temperature profiles of reduction disintegration test

Stage	Temperature, ºC	Gas flow rate, L/min	Gas composition	Duration, min
1	420	20	50% N_2	40
2	420	20	25% N_2	40
3	450	20	25% N_2	20
4	480	20	100% N_2	40
5	500	20	20% CO, 20% CO_2, 58% N_2, 2%H_2	60

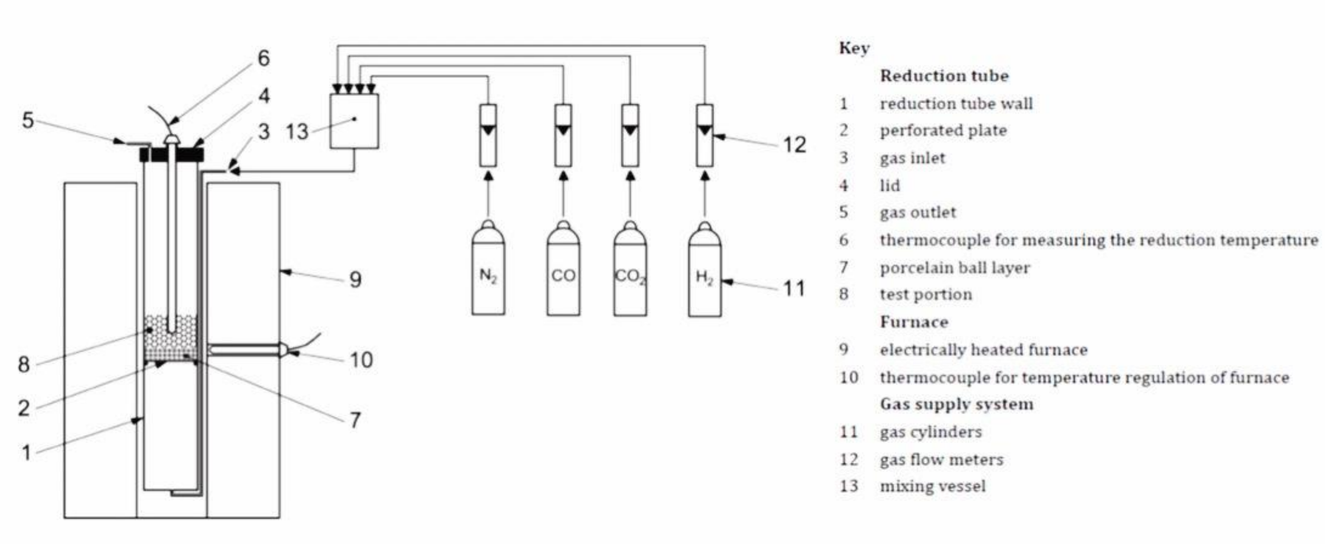

Figure 40: Schematic diagram of ISO 4696 test apparatus (Iljana, 2017)

4.11.Rotary kiln simulation

Production of ferronickel requires the ore to be treated through various stages that allow for a higher material concentration. Ore is fed into a rotary kiln to generate a calcined and pre-reduced product. Handling of the ore is important during the calcination stage because the calcined product is fed directly into an electric arc furnace, where it is melted and further reduced. The calcine needs to have good structural integrity. Linder furnace tests were conducted to simulate conditions in a rotary kiln (Figure 41).

The objective of the tests was to evaluate the degradation of green briquettes when being tumbled, heated, calcined, and reduced. A 2 kg sample was placed in the furnace, which was rotated at 23 rpm, which is equivalent to the rotational speed of a typical 5.75 m diameter calcination kiln. The furnace gas composition and temperature profiles are presented in Table 20. On completion of the tests, the pre-reduced briquettes were screened at 6.3 mm, 3.15 mm, and 0.5 mm to evaluate the degree of degradation.

Table 20: Gas and temperature profile of Linder furnace test

Stage	Definition	Temperature, °C	Gas flow rate, L/min	Gas composition	Duration, min	Speed, rpm
1	Heating	250	25	50% N_2	10	23
2	Drying free moisture	220	25	50% N_2	50	23
3	Calcination	800	25	50% N_2	60	23
4	Reduction	840	50	20% CO, 20% CO_2, 60% N_2	66	23
5	Cooling	< 300	25	20% N_2	-	0

Figure 41: Linder furnace

The overall performance of the briquettes was evaluated against the target responses obtained from a pilot-plant test campaign conducted at Anglo American (Value-In-Use), as presented in Table 21.

Table 21: ISO test target responses (pilot-plant campaign results)

Test type	ISO	Parameter	Target response (Pilot campaign)
Green briquette	ISO-4700	Compressive strength	350–620 N
Reducibility index	ISO-4695	Reduction index	39.3–42.2
		Compressive strength	370–779 (N)
		Drop number	4–10.7
		TI	95.5–96.2%
		AI	2.93–3.57%
Decrepitating index	ISO-8371	DI (% −3.15 mm)	0.083–0.22
Reduction disintegration index	ISO-4696-1	RDI (% −0.5 mm)	1.42–6.02%
		RDI (% −3.15 mm)	1.60–8.95%
		RDI (% −6.3 mm)	1.62–9.98%
Rotary kiln simulation	Non-standard test	% −3.15mm	2.67–5.60%

5. Results and discussion

5.1. Ore characterization

5.1.1. Particle size distribution

The PSD of the nickel laterite ore is presented in Figure 42. The results indicate that at a top size of −6.3 mm, 80.2% of the material was < 3350 µm, whilst 31.0% of the material was < 850 µm. At a top size of −12.5 mm, the results indicate that 69.3% of the material was < 3350 µm, whilst 25.4% of the material was < 850 µm. The −6.3 mm top size comprised a greater proportion (19.1%) of fine particles (−500 µm) in comparison with the −12.5 mm top size (15.2%).

The presence of fine particles at the ore top size of −6.3 mm is significant with regards to the prevailing binding mechanism on briquetting. Additionally, the presence of fine particles has a detrimental effect on furnace performance: fine particles reduce permeability and furnace efficiency, leading to lower metal extractions and increased power consumption (Goenka and Naik, 2013). Fines can also increase gas build-up and thereby compromise process safety and stability (Moreira Alves and de Souza Sales, 2002).

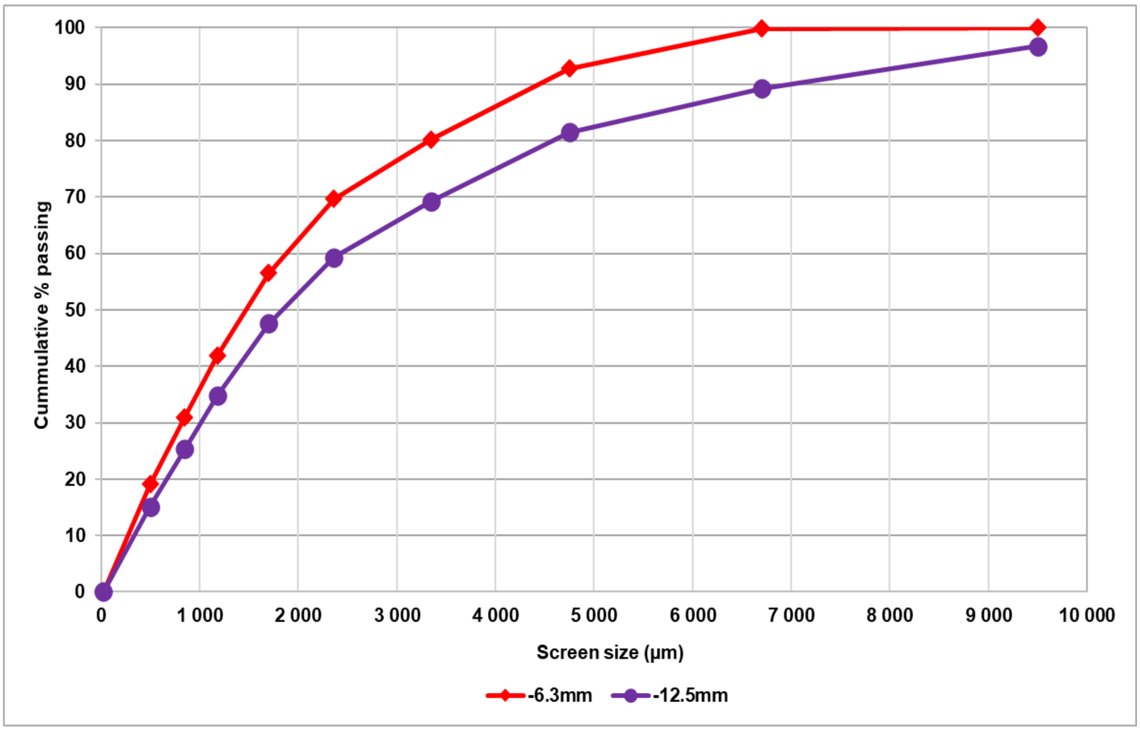

Figure 42: Particle size distribution of as-received ores

5.1.2. Chemical and mineralogical analysis

XRF analysis of the feed sample indicated that the ore contained 2.03 mass% NiO and 17.2 mass% Fe_2O_3. The ore can be considered lateritic, given its average $(SiO_2)/(Al_2O_3 + Fe_2O_3 + Fe_3O_4)$ mass ratio of 2.09. In accordance with the categorization of the laterites given by Janwong (2012), saprolitic laterite ores consist of 0.4–3 mass% Ni, 0.02–1 mass% Co, 10–30 mass% Mg, and 9–25 mass% Fe.

The XRF analysis confirmed that the ore is a saprolitic laterite with 12.1 mass% Fe, 17.2 mass% Mg, and 1.60 mass% Ni. Lu et al., (2013) stated that hydrous magnesia silicates dominate the saprolites, with nickel substituting magnesia to form garnierite $(Mg,Ni)_3Si_2O_5(OH)_4$, without any discrete nickel minerals.

For the ore top size of −6.3 mm, the XRF analysis confirmed that the ore contained 2.15 mass% NiO and an LOI of 12.4 %. Screening resulted in notable upgrading of the ore, with an increase to 5.66% NiO and 27.2% Fe_2O_3, which signified rejection of the nickel-lean minerals. According to Crundwell et al. (2011), the advantage of upgrading lateritic ores using screens is that it offers a comparatively cheap method of rejecting nickel-lean minerals by physical separation in comparison with methods such as leaching.

For the ore top size of −12.5 mm, results indicated that the ore contained 1.93 mass% NiO with an LOI of 11.1%. This is a 4.93 mass% decrease in NiO content and 17.4 mass% decrease in Fe_2O_3 content in comparison with the plant feed. A $(SiO_2)/(Al_2O_3 + Fe_2O_3)$ mass ratio of 2.62 was obtained. The −12.5 mm fraction cannot therefore be classified as a true laterite, but rather as a non-lateritic tropically weathered ore. Table 22 summarises the XRF results; detailed results are presented in Appendix 1.

Table 22: X-ray fluorescence analysis of ore

Component, mass %			
Analyte	ROM*	−6.3 mm fraction	−12.5 mm fraction
SiO_2	41.6	37.6	44.2
Al_2O_3	2.80	4.18	2.67
Fe_2O_3	17.2	21.9	14.2
NiO	2.03	2.15	1.93
MgO	23.0	19.4	28.8
Fe (Total)	12.0	15.3	9.93
Ni (total)	1.60	1.69	1.52
Fe/Ni	7.54	9.07	6.55
$(SiO_2)/(Al_2O_3 + Fe_2O_3)$	2.08	1.44	2.62
LOI	11.0	12.4	11.1

*ROM: run-of-mine (as-received) material

An assay by size analysis was carried out on the ROM sample (Figure 43). The results indicate that both the iron and nickel grades increased with decreasing particle size. At a top size of 26 500 µm, Fe_2O_3, and NiO grades of 8.50% and 1.44% were reported, respectively, whilst at the bottom size of 25 µm, Fe_2O_3 and NiO grades of 27.0% and 2.52% were reported, respectively. Particle size mass distributions were used to calculate grades of 16.8% Fe_2O_3 and 2.00% NiO. Detailed assay-by-size XRF analyses are presented in Appendix 1.

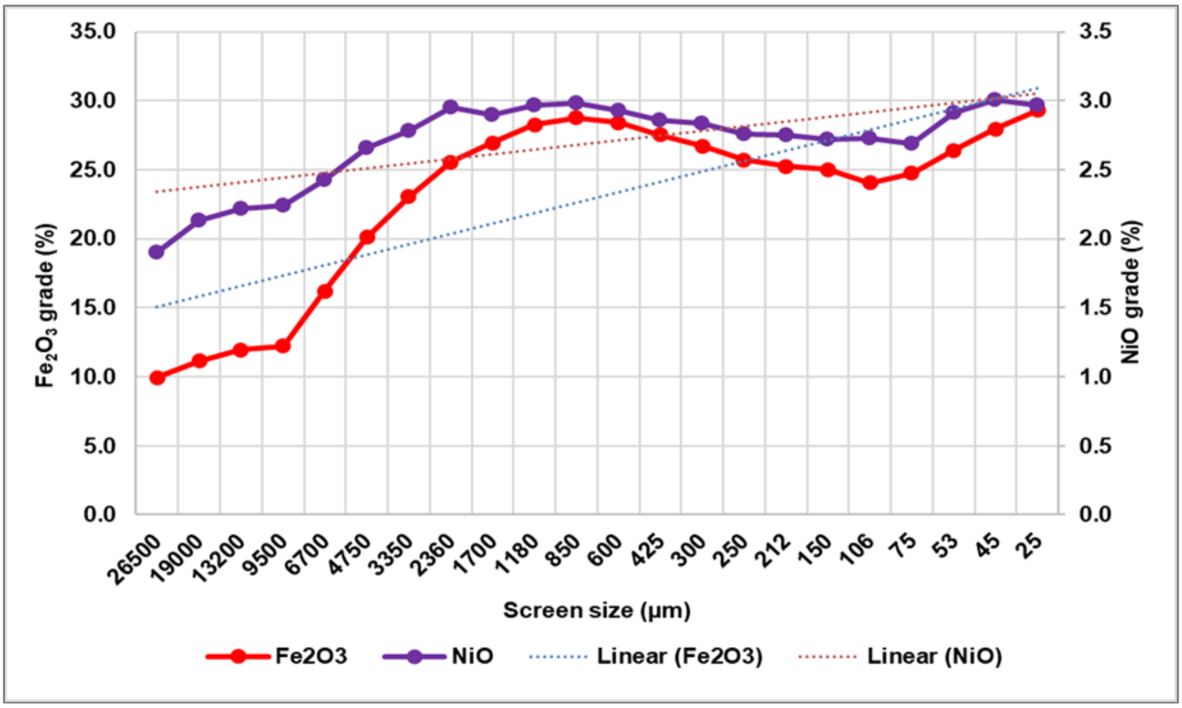

Figure 43: Distributions of major oxide components between different size fractions

Quantitative XRD analyses of the ROM, −6.3 mm, and −12.5 mm feed samples are presented in Table 23. The results indicate that the ore consisted primarily of silicates: lizardite ($Mg_3Si_2O_5(OH)_4$) (a silicate of the serpentine group), quartz (SiO_2) (a framework silicate), and forsterite ($Mg_{1.8}Fe_{0.2}SiO_4$) (a ring silicate of the olivine group). Iron was primarily contained in non-silicate minerals: hematite (Fe_2O_3) and magnetite (Fe_3O_4).

For the ore top size of −6.3 mm, the results indicate an 18.1% reduction in the mass% quartz (11.8% to 9.66%), which is the most common iron-containing gangue mineral. Magnesium-rich olivine (forsterite), which is detrimental to smelting, was also rejected, with the results indicating a 18.7% reduction (6.36% to 5.17%). A (SiO_2)/(Al_2O_3 + Fe_2O_3) mass ratio of 1.44 (Table 22) was obtained, indicating that the upgraded ore was a true laterite, according to the expanded definition (Gidigasu, 1976).

Table 23: Quantitative X-ray diffraction analysis of feed samples

Mineral, mass %			
Mineral	ROM	−6.3 mm fraction	−12.5 mm fraction
Amorphous	34.3	40.7	15.2
Chlorite	6.51	6.53	15.0
Enstatite	1.37	4.14	5.70
Forsterite	6.36	5.17	16.2
Hematite	1.30	2.96	1.30
Hornblende	5.42	6.88	3.10
Lizardite	22.8	18.8	18.0
Magnetite	4.19	5.16	-
Quartz	11.8	9.66	11.3
Talc	5.86	–	14.2

XRF analysis confirmed that the ore was a saprolititc laterite. Gleeson, S.A et al. (2004) confirmed that saprolites are dominated by an amorphous phase. Work by Bolaños-Benítez et al. (2020), which studied the potential release of Cr from solids to surface water and groundwater in a nickel laterite deposit from Barro Alto, also noted the presence of an amorphous phase. Back-scattered electron image (BEI) and X-ray mapping analyses were conducted on the three feed samples. The results are presented in Appendix 2.

Quantitative XRD analyses generated the stoichiometries of prominent phases present in the ore. These stoichiometries were used, together with individual EDS spectrum analyses, to distinguish and calculate the EDS-based stoichiometry for each phase.

The observed phases in the ROM sample included hornblende ($Ca_{1.6}Na_{0.44}K_{0.08}Mg_{3.16}Fe_{1.68}Al_{1.54}Ti_{0.17}Si_{6.76}O_{24}H_{1.98}$), lizardite ($Mg_3Si_2O_5(OH)_4$), quartz ($SiO_2$), and chlorite ($Mg_{11.12}Fe_{0.87}Si_{5.11}Al_{2.88}O_{36}H_{16}$), which are in agreement with the phases identified by quantitative XRD analysis. EDS compositions of the samples and stoichiometries of the observed phases are presented in Appendix 3. For all samples, the chemical composition of quartz was typically close to 100% SiO_2, although EDS analysis indicated the presence of Mg, Al, and Fe. This was likely due to small inclusions of other minerals or liquid infillings in cavities within the quartz (Deer at al., 1966). A spinel-group mineral was also identified for the ore top size of −12.5 mm. The general formula of the spinel-group minerals is $A^{2+}B_2^{3+}O_4$, where A may either be Mg, Fe^{2+}, Zn, Mn, Ni, Co, Cu, or Ge, and B can be Al, Fe^{3+}, Cr, V, or Ti. The stoichiometry and composition of the spinel mineral are presented in Appendix 3.

XRF analysis showed the ore contained an average of 23.7 mass% MgO. In higher MgO laterites, Ni^{2+} readily replaces Mg^{2+} due to similar ionic radii, making the laterites difficult to reduce. EDS analysis confirmed this, showing Ni in chlorite, enstatite, forsterite, and lizardite. The amorphous phase primarily contained magnesium, silica, iron, aluminum, nickel, and chromium, with traces of potassium, calcium, manganese, and rutile. Detailed compositions are in Table 25 and Appendix 3. Amorphous phases are detectable in XRD due to their broad, diffuse peaks, while scanning electron microscopy (SEM) cannot distinguish them as it provides high-resolution surface images without atomic-level structural details. The EDS composition of these phases was determined based on an overall chemical balance.

Table 24: Calculated amorphous phase compositions in feed samples

Analyte	Component mass, %		
	ROM	−6.3 mm	−12.5 mm
MgO	18.80	18.08	44.40
SiO_2	38.49	30.53	25.42
Fe_2O_3	34.00	33.27	21.70
Al_2O_3	0.62	8.23	2.60
NiO	4.13	3.91	1.97
Cr_2O_3	3.24	2.40	1.72
K_2O	0.09	0.09	0.06
CaO	0.09	0.68	1.00
MnO	0.22	1.14	0.63
TiO_2	0.22	0.22	0.09

5.2. Summary of ore characterisation results

The nickel content in laterites can be upgraded by selective mechanical removal of silica and/or by rejecting low-grade constituents. This is ordinarily accompanied by a change in ore chemistry (Dalvi et al., 2004).

Comparison of the XRF analyses comparison between the ROM, −6.3 mm, and −12.5 mm fractions indicated better ore upgrading when screening at −6.3 mm (Table 22). The ROM sample graded 2.03 mass% NiO and 17.2 mass% Fe_2O_3: screening at −6.3 mm and −12.5 mm indicated grades of 2.15 mass% NiO, 21.9%Fe_2O_3 and 1.93 mass% NiO, 14.2 mass% Fe_2O_3, respectively.

The degree to which ores have been laterized may be determined by the $(SiO_2)/(Fe_2O_3 + Al_2O_3)$ ratio (Gidigasu, 1976). The −12.5 mm fraction yielded a ratio of 2.62; the plant feed and −6.3 mm fraction yielded 2.08 and 1.44, respectively. In accordance with the definition presented by Gidigasu (1976), detailed in Section 2.6, the ROM and −12.5 mm fraction may be considered to be non-lateritic tropically weathered ores; the −6.3 mm fraction may be considered to be lateritic.

According to Dalvi et al. (2004), ores suited for production of high-carbon ferronickel are characterized by low Fe/Ni ratios (5–6), whilst low-carbon ferronickel may be produced from saprolitic ores with relatively high Fe/Ni ratio (6–12). Low-carbon ferronickel is a result of mildly reducing conditions in the furnace, which prevents excessive iron reduction and ferronickel that is overly dilute in nickel (Crundwell et al., 2011). The results indicate that briquettes produced at ore top sizes of both −6.3 mm and −12.5 mm are suitable for production of low-carbon ferronickel, with Fe/Ni ratios of 6.55 and 9.07, respectively.

The phases reported by quantitative XRD analysis were largely in agreement with those reported by Rhamdhani et al. (2009), Selivanov et al. (2020), and Yang et al. (2019). The analyses indicated that the −12.5 mm feed constituted 14.2 mass% talc; no talc was observed in the −6.3 mm feed. Talc is the softest mineral on the Mohr’s hardness scale. It is thus reasonable that the presence of talc could lead to a reduction in the briquette compressive strength at −12.5 mm top size. Selivanov et al. (2020) further showed that reduction of nickel and iron from serpentine commences at temperatures above 1250°C.

Based on these findings and the presence of lizardite in both the −6.3 mm and −12.5 mm fractions, it was not expected that either nickel or iron would be reduced because all tests (DI, RI, RDI, and Linder furnace testing) were conducted at temperatures below 1250°C.

Table 25 summarises the partitioning of iron and nickel in the different minerals, as determined by EDS analysis. The averages were calculated from five analysis for each mineral. According to Yang et al. (2019), pyroxene particles generally exhibit a porous structure, with large pores on the surface and in their interior. The generally porous structure of the pyroxenes means that both nickel and iron from these phases are expected to be relatively easily accessible by the gaseous reductant.

EDS analyses indicated 5.43 mass% Fe content in the pyroxene at a top size of −6.3 mm and 7.51 mass% Fe at a top size of −12.5 mm. Comparing the nickel contents, no nickel was reported in the pyroxene phase at −6.3 mm, but 1.72 mass% nickel was reported in −12.5 mm material. This suggests that a higher degree of iron reduction from the pyroxene phase is expected from the larger briquettes.

Both −6.3 mm and −12.5 mm materials had comparable amounts of iron and nickel in the olivine phase (forsterite). Yang et al. (2019) stated that olivines are characterised by a compact and dense structure, which means that the likelihood of nickel and iron reduction from these phases is significantly lower. Elliott et al. (2016) reported that reduction of iron and nickel is easier from pyroxene minerals. These findings suggest that that a higher degree of reduction will be obtained in briquettes produced from ore top size of −12.5 mm, given the marginally higher iron and nickel contents in the pyroxene phase.

Table 25: Average iron and nickel concentrations in main minerals identified in −6.3 mm and −12.5 mm fractions, as determined from energy-dispersive spectroscopy analysis

Phase	**Mineral group**	**−6.3 mm**		**−12.5 mm**	
		Fe, mass%	Ni, mass%	Fe, mass%	Ni, mass%
Enstatite	Pyroxene	5.43	-	7.51	1.72
Forsterite	Olivine	6.27	1.22	6.31	1.32
Hornblende	Amphibole	2.52	-	6.54	2.52
Iron oxide	Oxide	57.5	2.50	67.9	1.95
Lizardite	Serpentine	8.49	1.50	-	-
Quartz	Silica	4.10	-	1.65	-

In comparing mineralogies of feed and reduced laterite ore, Rhamdhani et al. (2009) concluded that the prominent phases on completion of reduction were olivine, magnetite, quartz, and chromite. Minor phases included forsterite, nickeloan, pyroxene, serpentine, Ca–Mg silicate, Fe–Mg–Al silicate, Al-rich olivine, and Al-rich chromite. These authors further reported that the particles in the reduced ore had similar characteristics to those in the feed. On studying the reduction behaviour of garnieritic lateritic nickel ores, Yang et al. (2019) found that the prominent phases in the reduced ore were talc, chlorite, pyroxene, olivine, quartz, and wustite. While it is anticipated that ferronickel alloy particles will form on completion of reduction, Rhamdhani et al. (2009) concluded from SEM observation that it was difficult to distinguish the ferronickel alloy from oxides. Yang et al. (2019) stated that EDS analysis of ferronickel alloy particles on completion of reduction testing was inconclusive, because the particles were of submicron size. Selivanov et al. (2020)**,** however, reported that reduction of metals in the ore, leading to the formation of iron–nickel alloy, was prevalent at temperatures above 1200°C in the presence of a reducing gas.

5.3. Briquette test results

5.3.1. Briquette yield

The green briquette yield was calculated for each batch of briquettes produced using Equation 3.5. At a briquette ore top size of −6.3 mm and 16% moisture content, an average green briquette yield of 85.2% was measured (Appendix 4). Increasing the moisture content proved to have a detrimental effect, with an average green briquette yield of 67.7% at a moisture content of 24%.

At a briquette ore top size of −12.5 mm and moisture content of 16%, an average green briquette yield of 88.4% was measured. Increasing the moisture content had a detrimental effect, with an average green briquette yield of 78.2% for a moisture content of 24%.

5.3.2. Drop number and compressive strength

All briquette batches were subjected to a 2 h curing period, as described by the Anglo American (Value-In-Use) standard method (Section 3.6.2). Drop number and compressive strength measurements were then conducted.

The compressive strength results of the green briquette measured over a 96 h period are illustrated in Figure 44 and Figure 45 for the −6.3 mm and −12.5 mm briquette ore top sizes, respectively. The results indicate improved briquette compressive strength for the ore top size of −6.3 mm.

As stated in Section 2.3.4, compressive strength increases with an increase in the proportion of the fine fraction, given that finer particles allow for increased contact area between particles and hence formation of stronger interparticle bonds. As indicated in Section 4.1.1, the −6.3 mm ore top size consisted of 19.1% −500 µm material, in comparison with 15.2% for the −12.5 mm fraction. Owing to an increased surface area in finer particles, inter particle forces increase, which subsequently enhances strength of the briquettes (Satyananda et al., 2017).

In comparing the briquette compressive strength for each size fraction, the results indicate that the compressive strength increased with decrease in moisture content. As discussed in Section 2.3.5, an increase in moisture content is associated with a decrease in the surface energy due to physical absorption, which causes a decrease in the strength, in a phenomenon referred to as the Rhebinder effect. Figure 45 indicates a significant increase in the briquette compressive strength at 96 h for 16% moisture content under open curing conditions. Using the Grubs test (Aslam, 2020) for outliers at 95% confidence, this data point was determined to be an outlier.

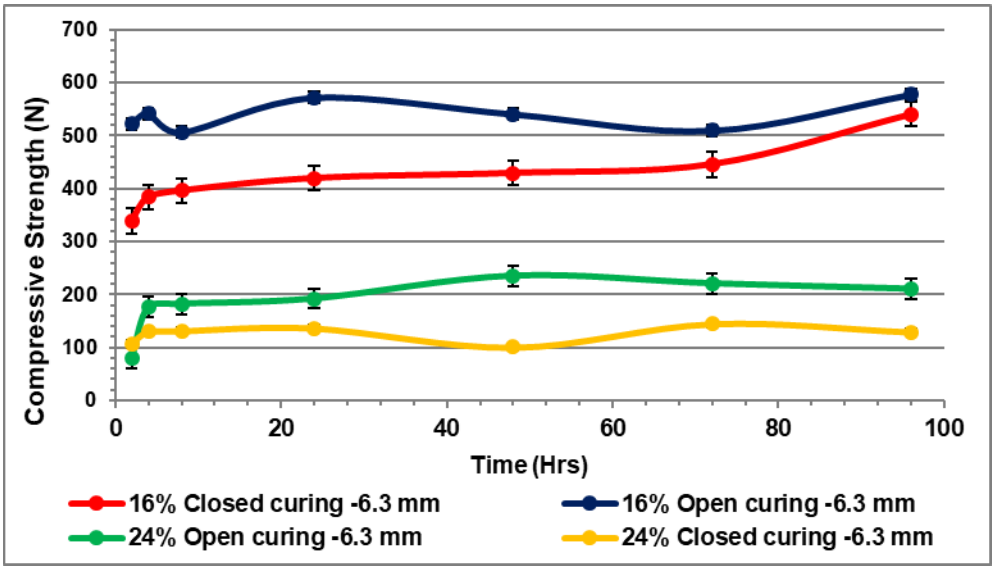

Figure 44: Green briquette compressive strength over 96 h for briquette ore top size of −6.3 mm

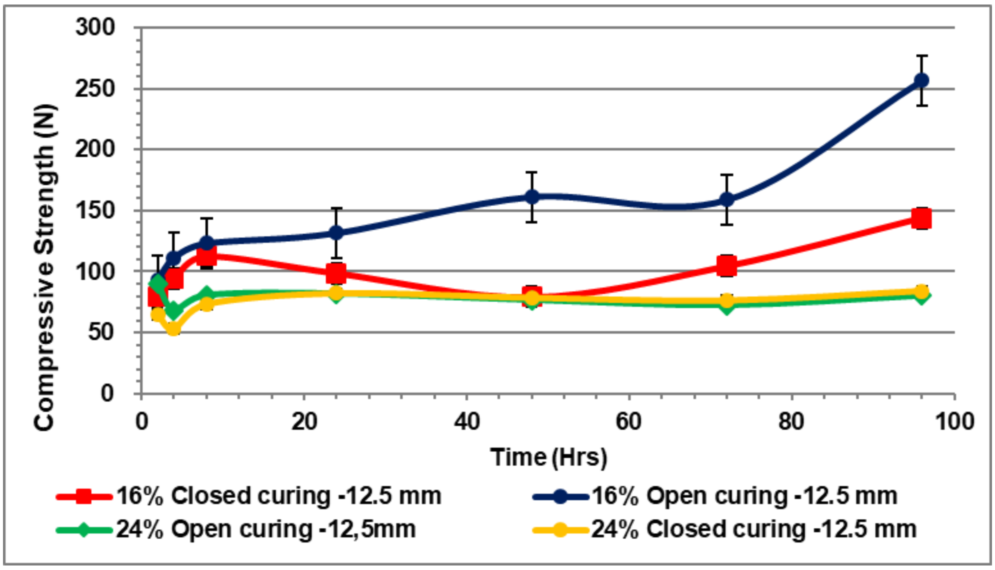

Figure 45: Green briquette compressive strength over 96 h for briquette ore top size of −12.5 mm

Increasing the moisture content had a detrimental effect on both the drop number and compressive strength. These results are presented in Appendix 4.

The green briquette yield and compressive strength results are in agreement with results reported by Vining et al. (2017), who evaluated the performance of briquettes produced from hematite–goethite iron ore. Their results showed that green briquette compressive strength increased with decreasing moisture content. The study further noted that higher briquette yields were associated with improved briquette strength, whilst lower briquette yields were associated with poor briquette strength.

The main-effect plot of green briquette compressive strength is illustrated in Figure 46. The results indicate that moisture content had a far greater significance on compressive strength in comparison with curing condition at a briquette ore top size of −6.3 mm; however, the opposite is true for a briquette ore top size of −12.5 mm.

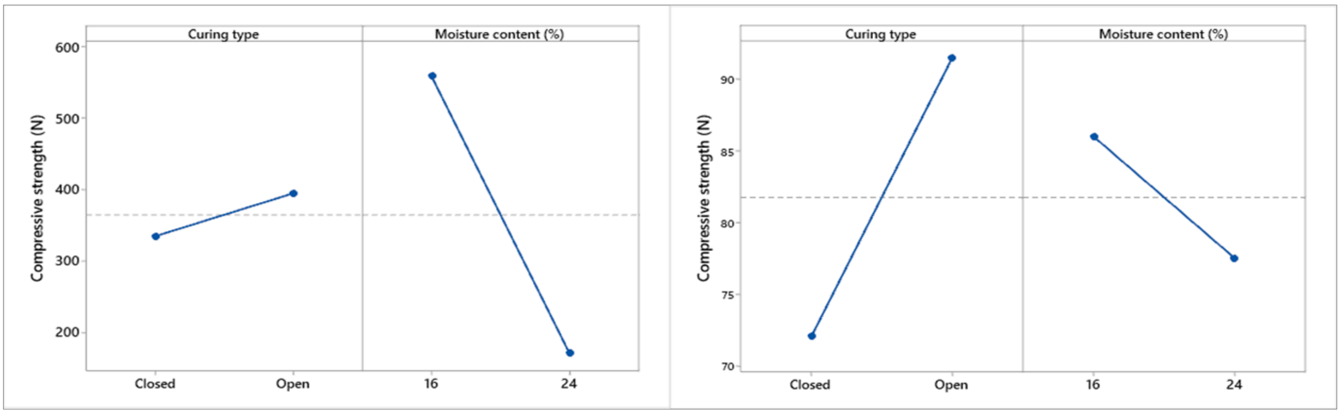

Figure 46: Main-effects plot of green briquette compressive strength, left at briquette ore top size of −6.3 mm and right at a briquette ore top size of −12.5 mm

The interaction plots between moisture content and curing condition on green briquette compressive strength are presented in Figure 47. No interaction existed between these parameters on the green briquette compressive strength for the low top size. The change in average compressive strength from a moisture content of 16% to 24% therefore did not depend on the curing condition. However, for the larger top size, the interaction plot indicates that there is an interaction between moisture content and curing conditions. The degree of interaction is minimal, with only a 35 N difference in briquette compressive strength at 24% moisture content between the closed and open curing conditions.

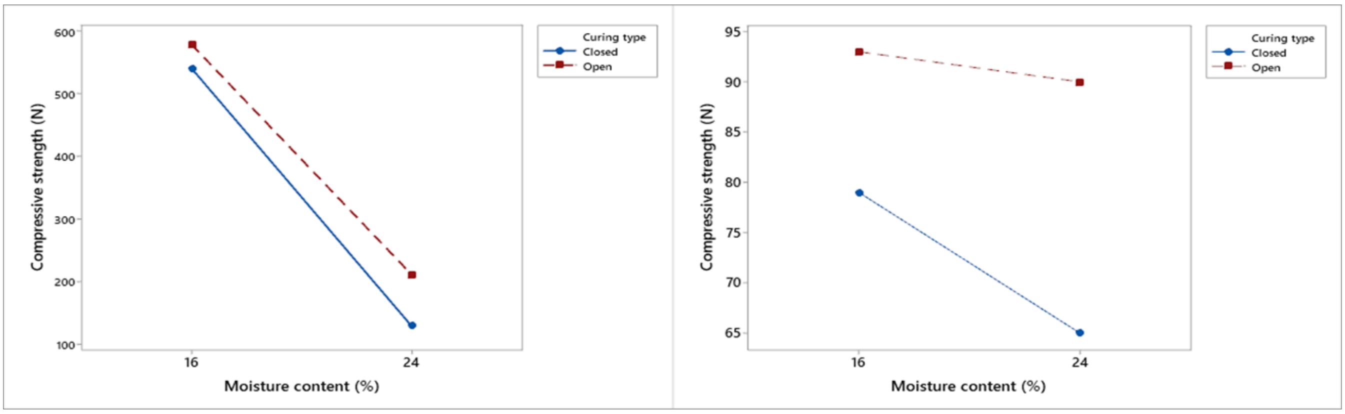

Figure 47: Interaction plot of green briquette compressive strength, left at briquette ore top size of −6.3 mm and right at a briquette ore top size of −12.5 mm

5.3.3.Tumble strength and abrasion index test

Briquettes produced from the top size of −12.5 mm (briquettes produced in the laboratory using the 20 t test rig) disintegrated completely after the TI test (Figure 48).

Figure 48: −12.5 mm briquettes after tumble index test

The TI and AI test results are presented in Table 26, the averages are presented according to moitsure content for both the -6.3mm briquette ore top size and the -12.5mm briquette ore to size. Both indices decreased as the moisture content increased. This trend is consistent with the findings of Li et al. (2022), who studied the effect of moisture content on limonitic nickel laterites and found that increasing the moisture content from 14% to 21% had a beneficial effect on TI, but at moisture contents greater than 21%, the TI deteriorated. Although moisture helps to bind particles together into agglomerates (Section 2.5.1), the results suggest that too much moisture can make agglomerates susceptible to disintegration.

At the briquette ore top size of −6.3 mm, average TI of 93.4% and 87.1% were measured for moisture contents of 16% and 24%, respectively. The corresponding AI values were 4.99% and 6.82%, respectively.

At a briquette ore top size of −12.5 mm, average TI and AI values of 40.5% and 13.4%, respectively, were measured for 16% moisture content. Increasing the moisture content to 24% had a marginal effect on both values: average TI and AI were 41.9% and 14.7%, respectively, which represents 3.46% and 9.70% increases with the increase in moisture content. Detailed results are presented in Appendix 5.

Table 26: Tumble index and abrasion index test results

Briquette ore top size	Moisture, %	Curing condition	TI, % > 6.3 mm	Average TI, moisture specific	AI, % < 0.5 mm	Average AI, moisture specific
−6.3 mm	16	Open	95.5	93.4	3.63	4.99
	16	Closed	91.4		6.35	
	24	Open	89.2	87.1	6.07	6.82
	24	Closed	85.0		7.58	
−12.5 mm	16	Open	40.3	40.5	13.0	13.4
	16	Closed	40.7		13.7	
	24	Open	35.2	41.9	13.1	14.7
	24	Closed	48.5		16.2	

The main-effects and interaction plots of the TI and AI are illustrated in Figure 49 and Figure 50, respectively. The main-effects plot indicates that, at a briquette ore top size of −6.3 mm, the moisture content had a greater significance on the TI than the curing condition (Figure 49). At a briquette ore top size of −12.5 mm, curing conditions had the more significant impact on the TI.

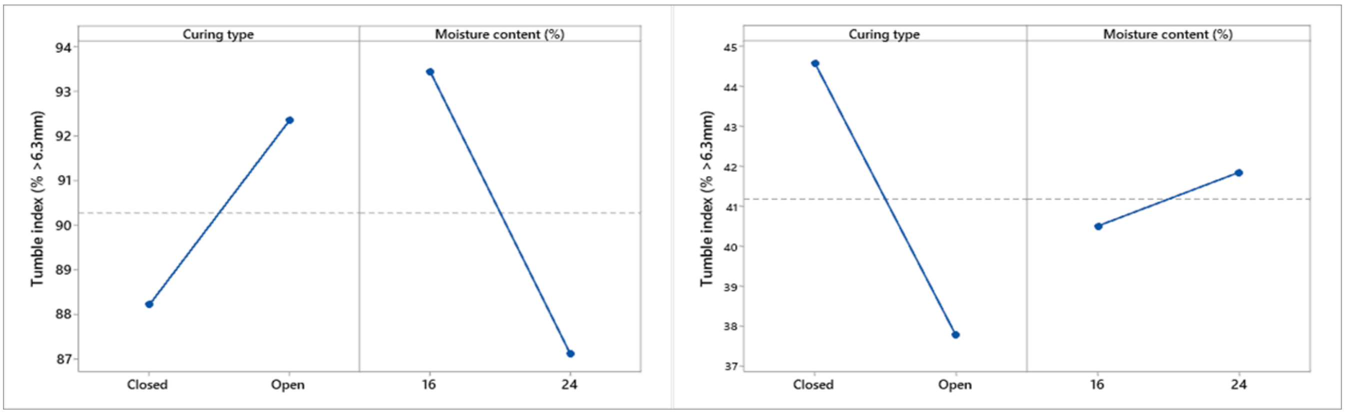

Figure 49: Main-effects plot of tumble index, left at briquette ore top size of −6.3 mm and right at a briquette ore top size of −12.5 mm

The interaction plot indicates that there no interaction exists between moisture content and curing condition on the TI at the briquette ore top size of −6.3 mm; however, there is a strong interaction at the briquette ore top size of −12.5 mm (Figure 50). This suggests that at a briquette ore top size of -12.5 mm, the TI is strongly influenced by the interaction between moisture content and curing conditions.

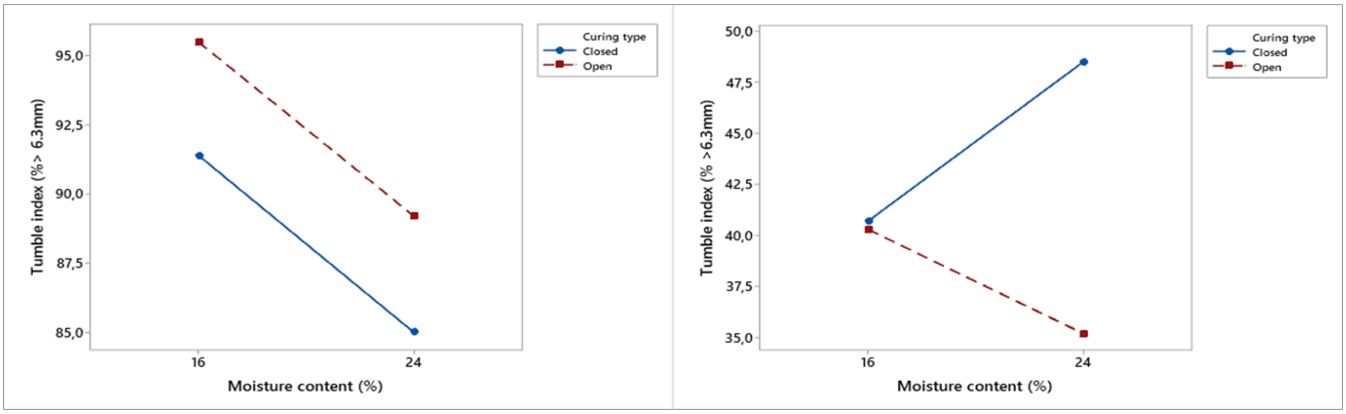

Figure 50: Interaction plot of tumble index, left at briquette ore top size of −6.3 mm and right at a briquette ore top size of −12.5 mm

The main-effects and interaction plots of the AI are illustrated in Figure 51 and Figure 52 respectively. The main-effects plots indicate that for both briquette ore top sizes, curing condition has far greater significance on the AI than the moisture content. The results indicate that the lowest AI was obtained under open curing conditions.

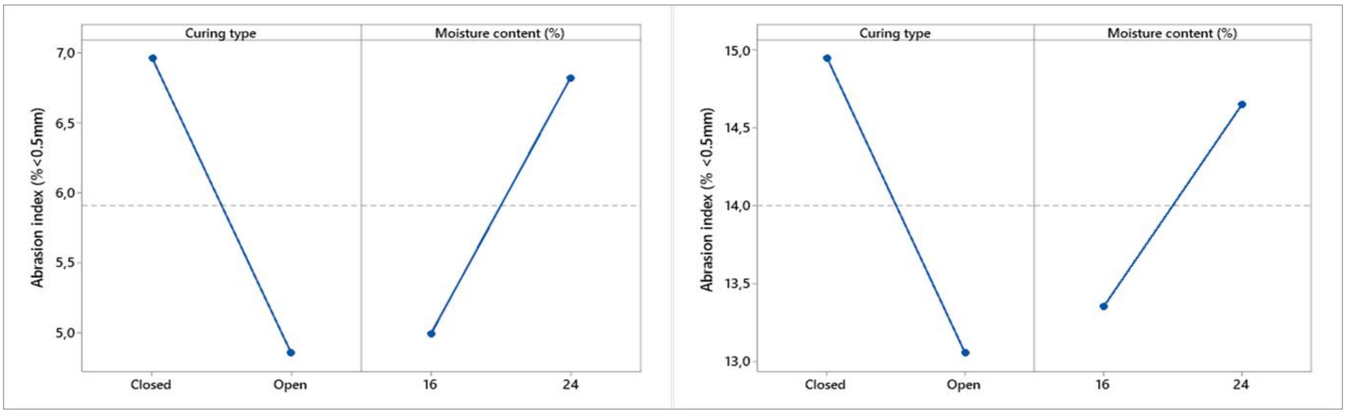

Figure 51: Main-effects plot of abrasion index, left at a briquette ore top size of −6.3 mm and right at a briquette ore top size of −12.5 mm

The interaction plots show minimal interaction between the moisture content and curing conditions, and illustrate that the AI is sensitive to moisture content under both open and closed curing conditions.

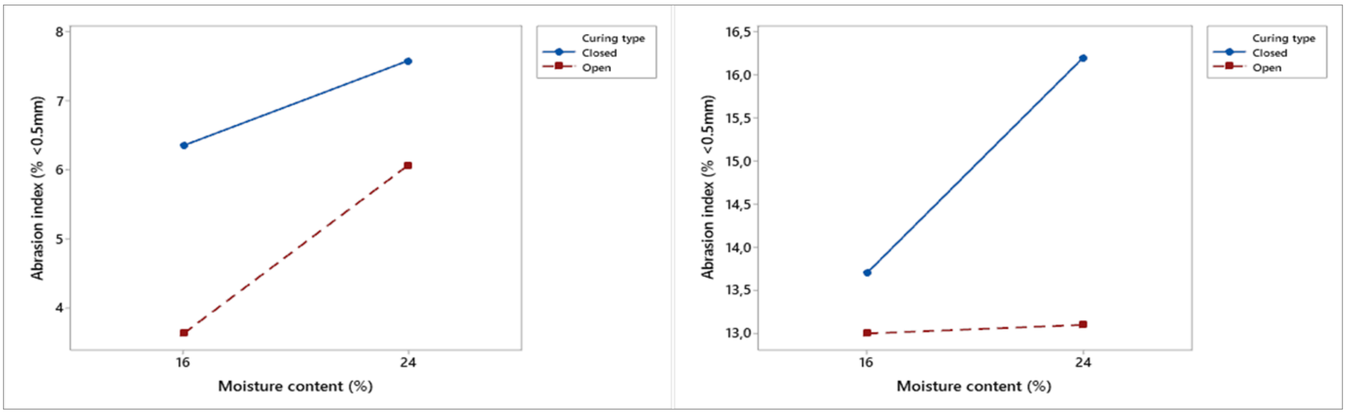

Figure 52: Interaction plot of abrasion index, left at a briquette ore top size of −6.3 mm and right at a briquette ore top size of −12.5 mm

5.3.4.Reducibility index

5.3.4.1.Degree of reduction

In the RI test, oxygen was removed from the briquettes by heating to 800°C under reducing conditions, with a Po_2 of 96.2 kPa (Section 4.8, Table 18). The temperature and gas profiles, and different stages in the reduction process are illustrated in Appendix 6. The mass loss per stage was recorded using a balance that was integrated into the RI furnace.

The results presented in Table 27 indicate a decrease in the degree of reduction with an increase in moisture content for both briquette top sizes.

These results indicate a similar trend to that observed by Goenka and Naik (2013), who noted a decrease in the degree of iron reduction with an increase in moisture content from 13% to 15%. Murakami et al. (2009) and Li (1999) (Section 2.3.5) also asserted that an increase in moisture content had a detrimental effect on the degree of reduction, with the latter attributing this effect to the presence of water vapour.

The percentage decrease in degree of reduction per percentage increase in moisture content was calculated according to equation 31. For open-cured briquettes with the ore top size of −6.3 mm, a 0.31% decrease in the degree of reduction was measured for a 1% increase in moisture content. This value increased to 1.14% under closed curing conditions.

Table 27: Summary of reducibility index test results

Briquette ore top size	Moisture, %	Curing condition	Average mass loss, g	Average reduction, %
−6.3 mm	16	Open	132.5	33.4
	16	closed		
	24	open	165.1	27.6
	24	Closed		
−12.5 mm	16	Open	124.0	39.9
	16	closed		
	24	open	135.0	37.5
	24	Closed		

The volume and density analysis results for the briquette ore top size of −6.3 mm indicate a correlation between the volume shrinkage (density increase), TI, and AI. The change in the density is primarily due to reduction of hematite (Fe_2O_3) to magnetite (Fe_3O_4). A volume shrinkage of 24.8% and density increase of 11.9% were recorded for a moisture content of 16%; these values were 32.2% and 30.4%, respectively, for 24% moisture (Appendix 5). The results indicate a similar trend to those reported by Chen (2019), who observed a volume shrinkage and density increase on reduction of hematite to magnetite at1456^{o}C. Setiawan et al. (2022) concluded that the volume shrinkage is dependent on reduction temperature and reaction time, and is closely related to thermal history and degrees of reduction and metallization. Wang (2018) stated that the volume shrinkage increased with increasing reduction temperature.

The main-effects plots and interaction plots are illustrated in Figure 53 and Figure 54 respectively. The main-effects plots indicate that moisture content has a far greater significance on the degree of reduction than the curing condition for the briquette ore top size of −6.3 mm (Figure 53). For the briquette ore top size of −12.5 mm, however, curing conditions have a far greater impact on the degree of reduction than moisture content.

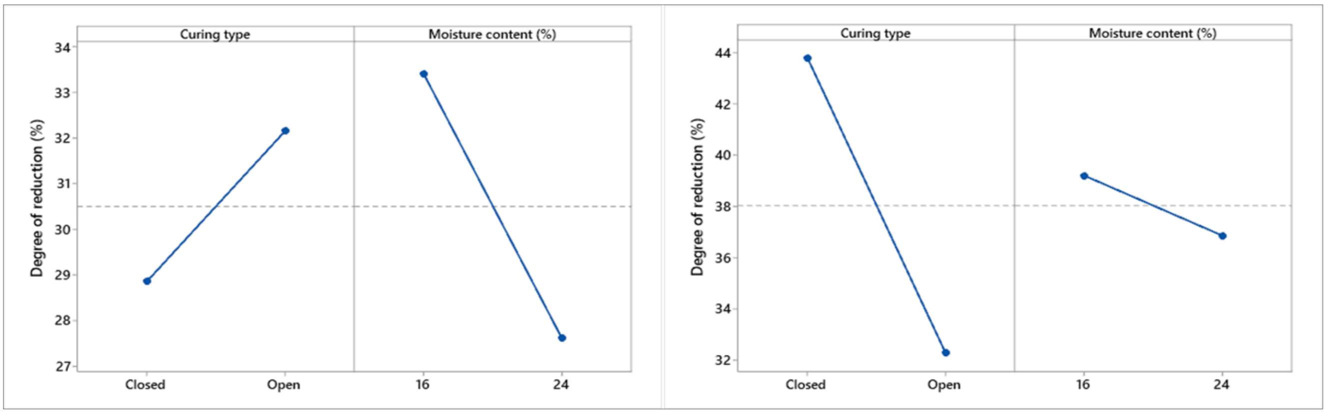

Figure 53: Main-effects plot of degree of reduction, left at a briquette ore top size of −6.3 mm and right at a briquette ore top size of −12.5 mm

The interaction plots indicate that an interaction exists between moisture content and curing conditions on the degree of reduction for both briquette compositions, with the maximum degree of reduction obtained at a moisture content of 16% (Figure 54).

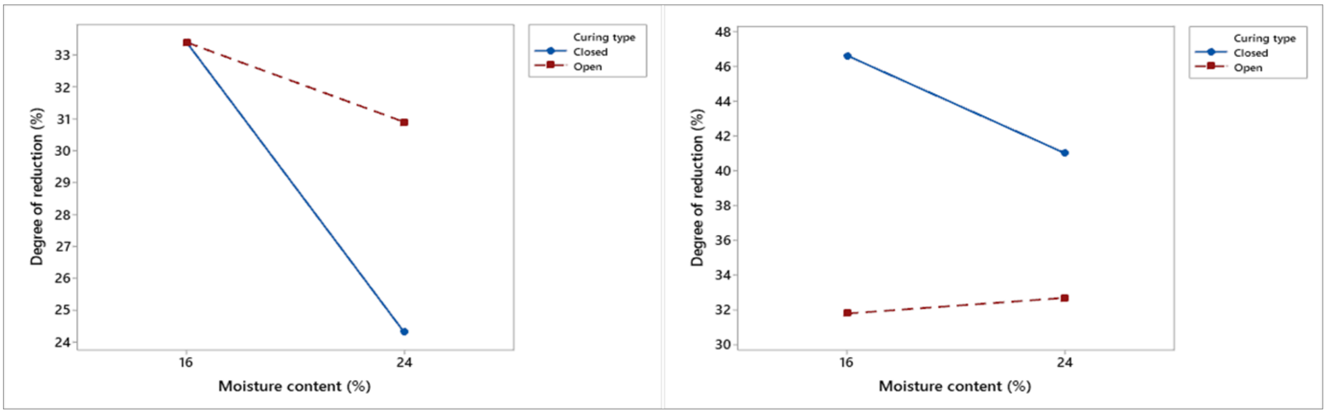

Figure 54: Interaction plot of degree of reduction, left at a briquette ore top size of −6.3 mm and right at a briquette ore top size of −12.5 mm

5.3.4.2.Chemical and mineralogical analysis

XRF analyses indicated that the briquettes produced at the ore top size of −6.3 mm contained an average of 2.72 mass% NiO, 42.3 mass% SiO_2, and 27.0 mass% Fe_2O_3 on completion of the reducibility index tests (Table 28). The calculated analyses gave average values of 3.04 mass% NiO, 53.2 mass% SiO_2, and 31.0 mass% Fe_2O_3.

The corresponding XRF analyses of the briquettes with ore top size of −12.5 mm gave 2.31 mass% NiO, 46.6 mass% SiO_2, and 18.5 mass% Fe_2O_3 (Table 28). Detailed XRF analyses are presented in Appendix 6.

Table 28: X-ray fluorescence analyses of reduced briquette samples

Briquette ore top size	Description	Component (mass %)							
		NiO	SiO_2	Fe_2O_3	Al_2O_3	MgO	Cr_2O_3	MnO	LOI
−6.3 mm	Assay	2.72	42.3	27.0	4.58	20.8	1.30	0.42	−0.85
	Calc.	3.04	53.2	31.0	5.91	27.4	1.53	0.52	-
−12.5 mm	Assay	2.31	46.6	18.5	2.95	27.6	0.92	0.27	−0.45
	Calc.	2.49	57.1	18.4	3.45	37.2	0.87	0.48	-

Quantitative XRD results indicated that the briquettes of ore top size of −6.3 mm consisted primarily of enstatite ($Mg_{1.50}Fe_{0.49}Si_2O_6$) (25.7%) and forsterite ($Mg_{1.82}Fe_{0.18}SiO_4$) (28.9%) on completion of the RI test (Table 29). Additional phases included diospide ($Ca_{0.92}(Mg_{0.53}Fe_{0.41}Al_{0.14})Si_2O_6$), hornblende ($Ca_{1.71}Na_{0.46}(Mg_{3.44}Fe_{1.72}Al_{1.10})Si_{6.90}O_{22}(OH)_2$), magnetite ($Fe_3O_4$), and quartz ($SiO_2$).

For the briquette ore top size of −12.5 mm, quantitative XRD results confirmed the thermal decomposition of lizardite into enstatite and forsterite during the RI (the feed contained 18.0 mass% lizardite). On completion of the RI test, the briquettes comprised an average of 42.3% forsterite, 18.5% amorphous phase, 16.5% enstatite, and 7.76% magnetite (Table 29). The results further confirmed the conversion of hematite to magnetite. Detailed quantitative XRD results are presented in Appendix 6. The product phases are largely in accordance with expectations based on prior work, as discussed in Section 2.6.10.

Table 29: X-ray diffraction analysis results for reduced briquettes

Briquette ore top size	Mineral (mass%)						
	Amorphous	Diopside	Enstatite	Forsterite	Hornblende	Magnetite	Quartz
−6.3 mm	26.6	6.17	25.7	28.9	3.84	3.21	5.62
−12.5 mm	18.5	-	16.5	42.3	5.40	7.76	9.50

EDS and X-ray elemental mapping analyses were conducted on the reduced briquettes. The observed phases included enstatite, forsterite, hornblende, magnetite, and quartz. Wustite was also observed for the briquette ore top size of −12.5 mm, suggesting that it was present in trace quantities because it was not detected by quantitative XRD analysis. The BEI and X-ray elemental maps analyses are given in Appendix 6.

The EDS mineral compositions of the reduced briquettes also indicate that these silicate phases (diopside, enstatite, and forsterite) contained iron, nickel, and magnesium. This observation is in agreement with result reported by Yang et al. (2019), who suggested that that these elements coexist in a silicate lattice to form a solid solution.

Rhamdhani et al. (2009) conducted EDS analyses on reduced nickel laterite ores, confirming the presence of nickel in forsterite, magnetite, and enstatite, which is in agreement with the results of the current study. Results for the briquette ore top size of −12.5 mm showed that iron was contained primarily in magnetite and wustite.

EDS analysis of the quartz revealed that the average composition closely corresponded to its stoichiometric composition for both briquette types. X-ray mapping illustrated that trace amounts of other oxides in the quartz were primarily due to inclusions of other minerals or to liquid infillings in cavities within the quartz.

Cr-spinel was also observed in both reduced briquette types. This confirmed results of Selivanov et al. I2020), who also detected impurities of Cr-spinel in a reduced sample. EDS analyses and stoichiometries of the major phases identified in the briquette samples are presented in Appendix 6.

5.3.5.Decrepitation index test results

At the briquette ore top size of −6.3 mm, the results indicate an increase in DI with an increase in moisture content, under both open and closed curing conditions. Under open curing conditions, DI values of 0.28% and 0.47% were reported for 16% and 24% moisture contents, respectively (Table 30). The corresponding DI values under closed curing conditions were 0.37% and 0.74%, respectively (Table 30). The presence of moisture is linked to decrepitation of the particles. In general, a high DI is undesirable because it indicates a higher degree of fines and dust formation, which negatively impact charge permeability.

The likelihood of disintegration of briquettes and formation of fines increased with an increase in moisture content. At 16% moisture, an average mass disintegration (mass% of −0.5 mm particles) of 0.09% was reported; this value increased to 0.16% at 24% moisture, indicating a 43.8% increase in fines generation.

In studying the behaviour of briquettes manufactured from the Azul and Urucum deposits in Brazil, Faria et al. (2010) concluded that ores with higher moisture content exhibited higher decrepitation intensity than those with lower moisture content.

At the briquette ore top size of −12.5 mm, the results indicated a marginal decrease in DI with moisture content: an average DI of 2.34% was reported for 16% moisture, which decreased to 1.96% for 24% moisture. The likelihood of disintegration of briquettes, resulting in the formation of fines, decreased marginally with an increase in moisture content. Average mass disintegrations (mass% −0.5 mm) of 0.36% and 0.26% were measured for 16% and 24% moisture contents, respectively, indicating a 28.6% decrease in the generation of fines. Detailed DI test results are presented in Appendix 7.

Table 30: Decrepitation index test results

Briquette ore top size −6.3 mm				
Moisture, %	Curing condition	Decrepitation index, % < 6.3 mm	Briquette mass disintegration,	
			% < 3.15 mm	% < 0.5 mm
16	Open	0.28	0.19	0.09
16	Closed	0.37	0.23	0.09
Average		**0.33**	**0.21**	**0.09**
24	Open	0.47	0.28	0.14
24	Closed	0.74	0.47	0.18
Average		**0.61**	**0.38**	**0.16**
Briquette ore top size −12.5 mm				
Moisture, %	Curing condition	Decrepitation index, % < 6.3 mm	Briquette mass disintegration,	
			% < 3.15 mm	% < 0.5 mm
16	Open	2.24	1.26	0.4
16	Closed	2.44	0.85	0.31
Average		**2.34**	**1.06**	**0.36**
24	Open	2.56	1.14	0.3
24	Closed	1.35	0.71	0.22
Average		**1.96**	**0.93**	**0.26**

The main-effects and interaction plots of the decrepitation index are illustrated in Figure 55 and Figure 56. The main-effects plots indicate that for the briquette ore top size of −6.3 mm, moisture content had a greater significance on the DI than the curing condition; the opposite was true for the briquette ore top size of −12.5 mm.

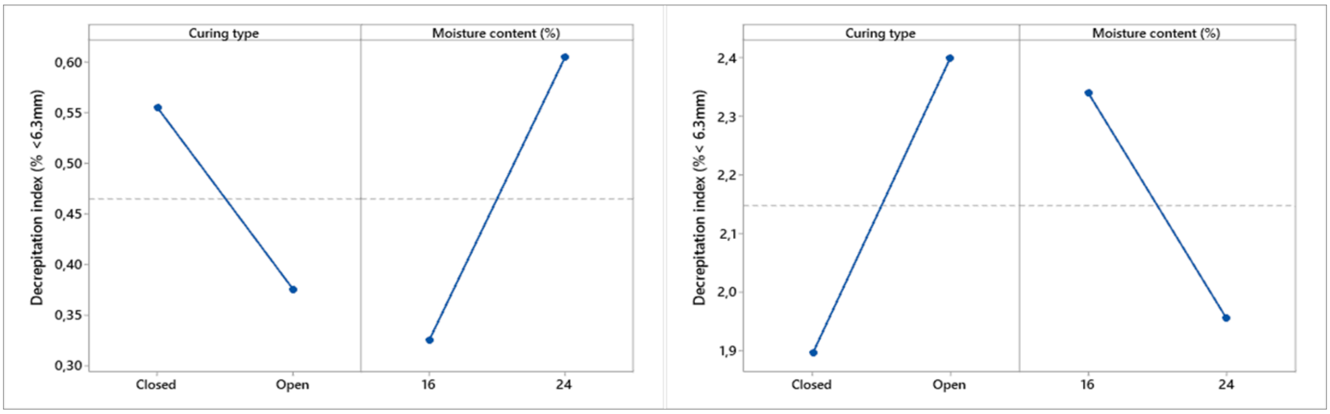

Figure 55: Main-effects plot of decrepitation index, left at a briquette ore top size of −6.3 mm and right at a briquette ore top size of −12.5 mm

The interaction plots show an interaction between moisture content and curing condition on the DI. For the briquette ore top size of −6.3 mm, a lower DI was obtained at 16% moisture under open curing conditions; in contrast, for the briquette ore top size of −12.5 mm, a lower DI was obtained at 24% moisture content under closed curing conditions (Figure 56).

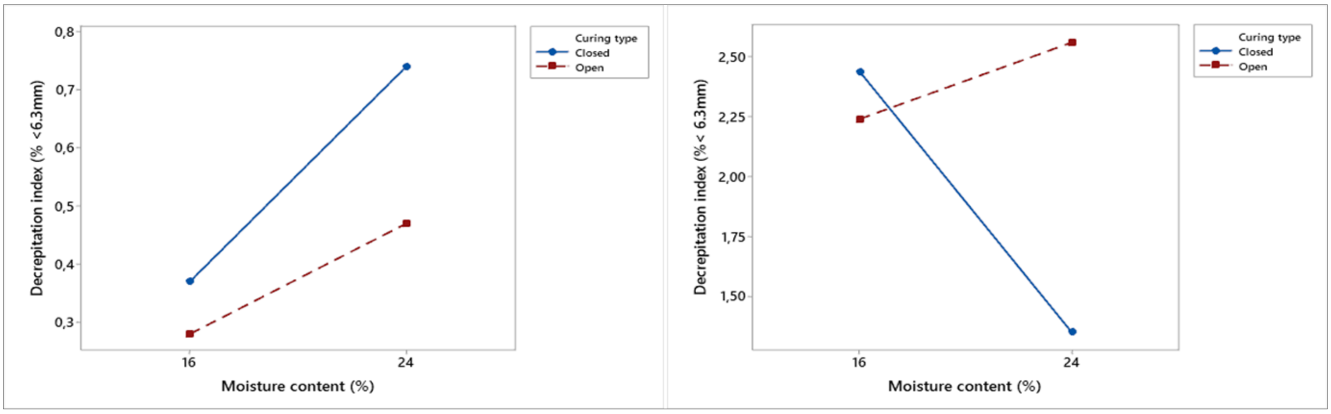

Figure 56: Interaction plot of decrepitation index, left at a briquette ore top size of −6.3 mm and right at a briquette ore top size of −12.5 mm

5.3.5.1.Quantitative XRD analysis

Lizardite decomposes into forsterite and enstatite on heating (Section 2.6.5). Lizardite has a density of 2.55 g/cm^3, while those of enstatite and forsterite are 3.20 g/cm^3 and 3.33 g/cm^3, respectively. The transformation of lizardite to enstatite and forsterite is accompanied by a change in density. The change in density induces stress in specific regions, leading to formation of cracks; disintegration of briquettes is increased by the presence of cracks.

Quantitative XRD results for the feed indicated an average 18.8 mass% lizardite at the ore top size of −6.3 mm and 18.0 mass% lizardite for the top size of −12.5 mm. Quantitative XRD analysis carried out on completion of the DI tests indicated averages of 4.80 mass% and 5.20 mass% lizardite, respectively (Table 31).

Thermal decomposition of lizardite is in accordance with the findings by Selivanov et al. (2020), with the results showing an average 74.5 mass% decrease in lizardite for the briquette ore top size of −6.3 mm and 71.1 mass% decrease for the briquette ore top size of −12.5 mm. These results suggests that the degree of thermal decomposition of lizardite is also a function of the available lizardite at inception and that the higher the initial lizardite content, the greater is the degree of the thermal decomposition. Quantitative XRD analysis results for the briquettes on completion of the DI tests are presented in Appendix 7.

Table 31: Quantitative X-ray diffraction analysis of briquettes after decrepitation index test

Mineral, mass %		
Mineral	Briquette ore top size −6.3 mm	Briquette ore top size −12.5 mm
Amorphous	43.5	36.4
Clinochlore	7.00	8.98
Enstatite	12.5	8.68
Forsterite	4.38	10.0
Hematite	6.08	4.08
Hornblende	4.63	5.98
Lizardite	4.80	5.20
Quartz	5.73	8.03
Talc	11.6	12.8

5.3.6. Reduction disintegration index results

The zone in which reduction of hematite (Fe_2O_3) to magnetite (Fe_3O_4) commences along the shaft of a furnace is referred to as the low-temperature reduction zone. Disintegration of material in this zone of the furnace shaft is primarily attributed to crack initiation and propagation, as a consequence of the volume change associated with the reduction (Lu, 2015). The RDI gives a measure of the fines generated when the burden is reduced in this zone of the furnace.

A summary of the RDI results is presented in Table 32; detailed results are presented in Appendix 8. Three RDI were calculated: $RDI_{+6.3mm}$, $RDI_{-3.15mm}$, and $RDI_{-0.5mm}$. The results indicate that with an increase in the briquette ore top size, briquette disintegration increased. Coarser particles are more prone to defects and cracks, and can serve as stress concentrators, increasing the likelihood of deterioration of the briquette during reduction.

Table 32: Reduction disintegration test results

Briquette ore top size −6.3 mm				
Moisture, %	Curing condition	Reduction disintegration index,		
		RDI$_{+6.3\ mm}$	**RDI$_{-3.15mm}$**	**RDI$_{-0.5\ mm}$**
16	Open	97.6	2.24	1.59
16	Closed	96.9	2.93	1.93
Average		**97.3**	**2.59**	**1.76**
24	Open	96.9	3.03	2.54
24	Closed	92.4	6.54	4.11
Average		**94.7**	**4.79**	**3.33**
Briquette ore top size −12.5 mm				
Moisture, %	Curing condition	Reduction disintegration index,		
		RDI$_{+6.3\ mm}$	**RDI$_{-3.15mm}$**	**RDI$_{-0.5\ mm}$**
16	Open	79.8	14.4	7
16	Closed	78.3	14.3	6.53
Average		**79.1**	**14.4**	**6.77**
24	Open	69.4	16.9	6.35
24	Closed	72.7	17.7	7.8
Average		**71.1**	**17.3**	**7.08**

Quantitative XRD analysis conducted on the briquettes following the RDI tests confirmed conversion of hematite to magnetite. For the briquette ore top sizes of −6.3 mm and −12.5 mm, averages of 8.64 and 5.05 mass% magnetite formed during the reduction test, respectively. These results confirm the phenomenon reported by Lu (2015), who attributed the disintegration of particles to this reaction. Quantitative XRD analysis results are presented in Appendix 8.

The main-effects and interaction plots are presented in Figure 57 to Figure 59 and Figure 60 to Figure 62, respectively. The main-effects plots of RDI$_{+6.3mm}$ indicate that for the briquette ore top size of −6.3 mm, the impacts of moisture content and curing condition on the RDI are comparable; however, for the briquette ore top size of −12.5 mm, the moisture content has a far greater impact on the RDI.

The main-effects plots of RDI$_{-0.5mm}$ indicate that for the briquette ore top size of −6.3 mm, moisture content has the most prominent impact. For the briquette ore top size of −12.5 mm, however, curing conditions have a greater impact on the RDI. The main-effects plot further indicates that for the briquette ore top size of −6.3 mm, the minimum RDI (RDI$_{-0.5mm}$) was obtained at a moisture content of 16%, while for the briquette ore top size of −12.5 mm, RDI$_{-0.5mm}$ was obtained under open curing conditions.

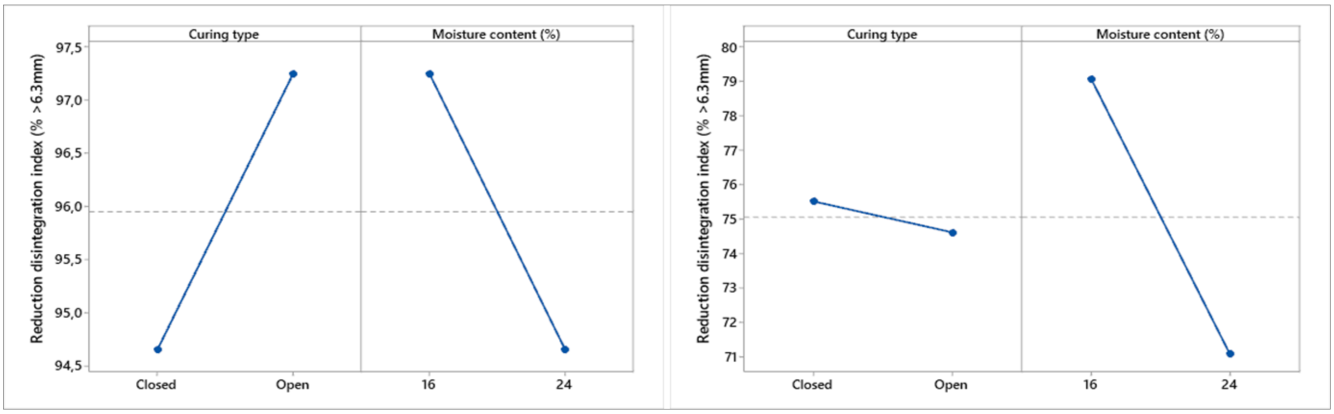

Figure 57: Main-effects plot of RDI$_{+6.3mm}$, left at a briquette ore top size of −6.3 mm and right at a briquette ore top size of −12.5 mm

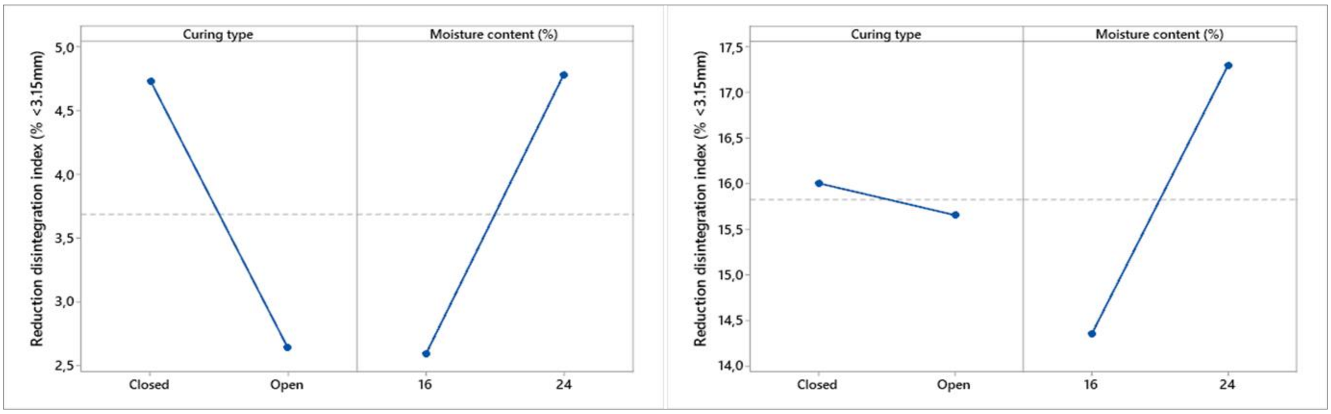

Figure 58: Main-effects plot of RDI$_{-3.15mm}$, left at a briquette ore top size of −6.3 mm and right at a briquette ore top size of −12.5 mm

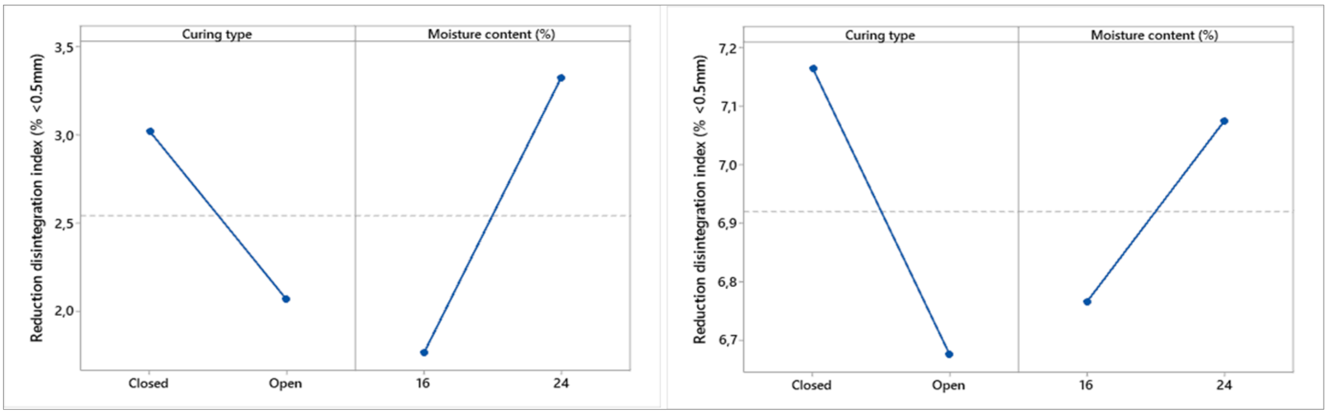

Figure 59: Main-effects plot of RDI$_{-0.5mm}$, left at a briquette ore top size of −6.3 mm and right at a briquette ore top size of −12.5 mm

The interaction plots (Figure 60 to Figure 62 show that there is an interaction between moisture content and curing conditions on the RDI. The optimum RDI$_{+6.3mm}$ was obtained at a moisture content of 16% under open curing conditions for both briquette types. For both briquette types, RDI$_{-0.5mm}$ was obtained at a moisture content of 16% under open curing conditions. Appendix 8 presents the main-effects and interaction plots for RDI$_{-3.15mm}$.

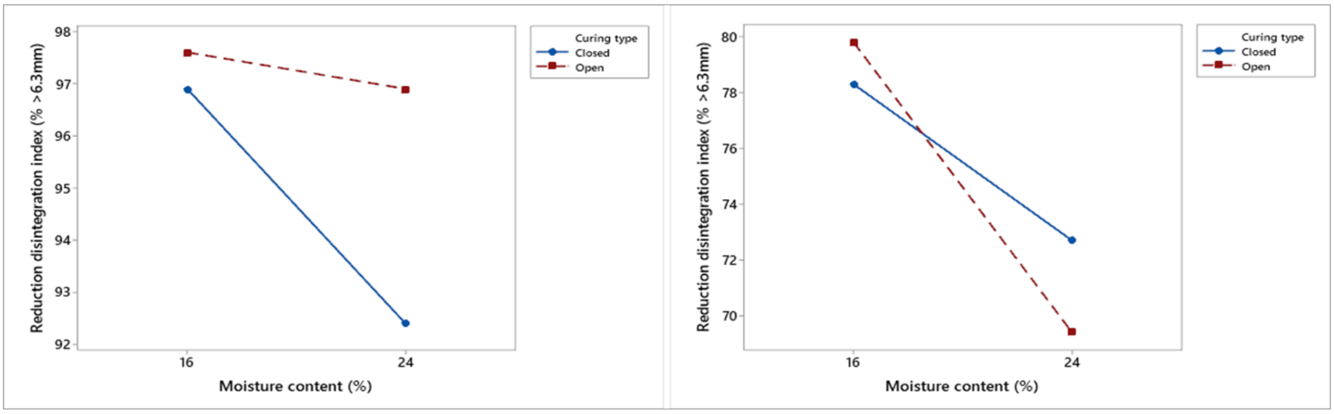

Figure 60: Interaction plot of RDI$_{+6.3mm}$, left at a briquette ore top size of −6.3 mm and right at a briquette ore top size of −12.5 mm

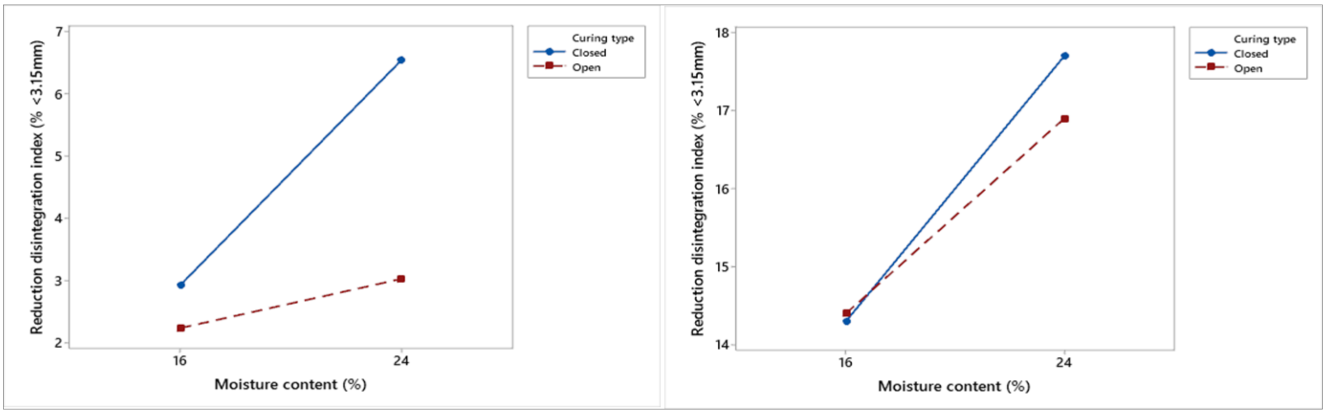

Figure 61: Interaction plot of RDI$_{-3.15mm}$, left at a briquette ore top size of −6.3 mm and right at a briquette ore top size of −12.5 mm

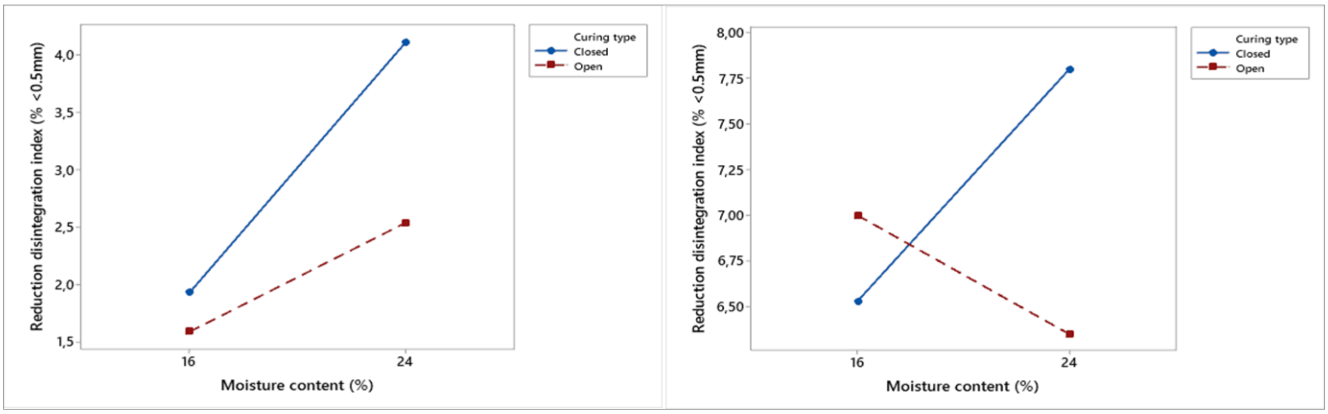

Figure 62: Interaction plot of RDI$_{-0.5mm}$, left at a briquette ore top size of −6.3 mm and right at a briquette ore top size of −12.5 mm

5.3.7.Linder furnace test results

5.3.7.1.Disintegration index

Linder furnace tests were conducted to simulate conditions in a rotary kiln. The objective was to evaluate the disintegration of briquettes when tumbled, heated, calcined, and reduced. Figure 63 illustrates the briquettes after Linder furnace testing. The briquettes disintegrated completely at a top size of −12.5 mm, generating significant amounts of fines.


(a)

(b)

Figure 63: Top size (a) −6.3 mm and (b) −12.5 mm briquettes after Linder furnace test

Disintegration of the briquettes, resulting in the generation of fines (mass% −0.5 mm), increased with briquette ore top size (Table 33). These findings are similar to those observed by Rojas Arias et al. (2018), who reported that disintegration increased with an increase in particle size when a sample was subjected to Linder reactor conditions.

An increase in briquette disintegration with an increase in moisture content was also noted. These results suggest that although moisture can act as a binding agent, excessive moisture may weaken bonds between the particles in the briquette, thereby leading to higher degree of disintegration. It may be inferred that higher moisture content could lead to a higher degree of swelling, which could cause greater porosity, making the briquettes more prone to disintegration and leading to excessive fines generation. For the briquette ore top size of −12.5 mm, under open curing conditions and a moisture content of 16%, 27.5 mass% exhibited a particle size > 6.3 mm; under closed curing conditions, this value was 23.3 mass%. The results indicate a greater degree of disintegration for this briquette ore top size. Detailed results are presented in Appendix 9.

Table 33: Summary of Linder furnace tests briquette mass disintegration

Briquette ore top size	Moisture, %	Curing condition	Average mass disintegration index, %		
			+6.3 mm	−3.15 mm	−0.5 mm
−6.3 mm	16	Open	95.3	4.5	3.8
	16	Closed			
	24	Open	70.3	21.4	11.3
	24	Closed			
−12.5 mm	16	Open	25.4	50.3	25.1
	16	Closed			
	24	Open	30.3	45.5	19.8
	24	Closed			

A comparative analysis of the PSD of the briquettes after the Linder furnace tests was conducted for the briquette ore top size of −6.3 mm with those reported by Anglo American (Value-In-Use). The results, presented in Table 34, showed averages of 96.1 mass% +10 mm and 2.93 mass% −0.5 mm. Standard deviations were calculated for each particle size classes. According to the empirical rule, 95% of all observations in a data set should fall within two standard deviations (Stdev) of the mean. In this case, the standard deviations ranged from 0.13–1.45, which implies that the results from the current study are comparable with those obtained from Anglo American.

Table 34: Particle size distributions of briquettes after Linder test

Screen size, mm	Current study (briquette ore top size of −6.3 mm)		Anglo American Study		Average, mass%	Stdev
	16% moisture (Open cure)	16% moisture (Closed cure)	15% moisture	15% moisture (No reduction)		
10	95.7	94.2	96.7	97.6	96.1	1.45
−10+6.3	0.18	0.34	0.11	0.03	0.16	0.13
−6.3+3.15	0.3	0.33	0.13	0.04	0.2	0.14
−3.15 +0.5	0.57	0.86	0.73	0.39	0.64	0.2
−0.5	3.26	4.24	2.34	1.9	2.93	1.04

The main-effects and interaction plots of the briquette mass disintegration are presented in Figure 64 and Figure 65 and in Figure 66 and Figure 67, respectively. The main-effects plot indicates that moisture content was the most significant parameter for both briquette ore top sizes. Furthermore, curing conditions had a minimal effect on disintegration of the briquettes.

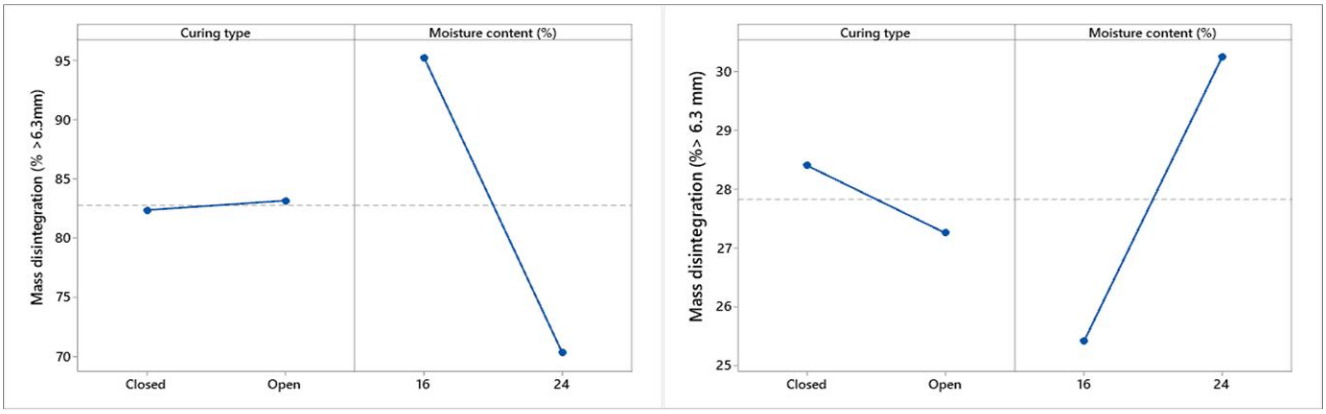

Figure 64: Main-effects plot of mass disintegration (+6.3 mm), left at a briquette ore top size of −6.3 mm and right at a briquette ore top size of −12.5 mm

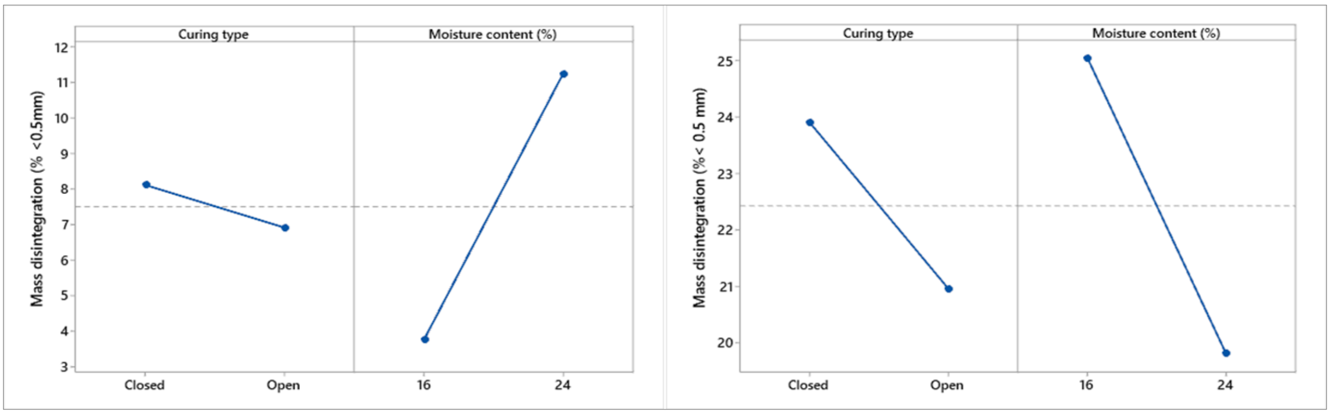

Figure 65: Main-effects plot of mass disintegration (−0.5 mm), left at a briquette ore top size of −6.3 mm and right at a briquette ore top size of −12.5 mm

For the briquette ore top size of −6.3 mm, the interaction plots indicate that no interaction exists between moisture content and curing conditions with respect to the disintegration of the briquettes (both mass% +6.3 mm and mass% −0.5 mm) however, for briquette ore top size of −12.5 mm, there was a strong interaction between these variables for both size fractions. Figure 67 shows that for the briquette ore top size of −12.5 mm, optimal conditions with regards to disintegration of briquettes can be set at a moisture content of 24% under open curing conditions.

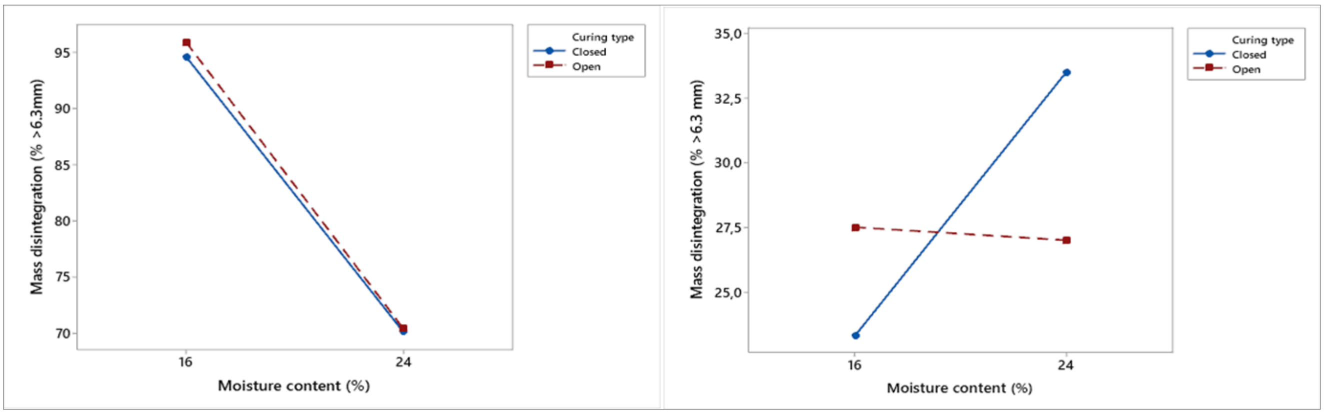

Figure 66: Interaction plot of mass disintegration (+6.3 mm), left at a briquette ore top size of −6.3 mm and right at a briquette ore top size of −12.5 mm

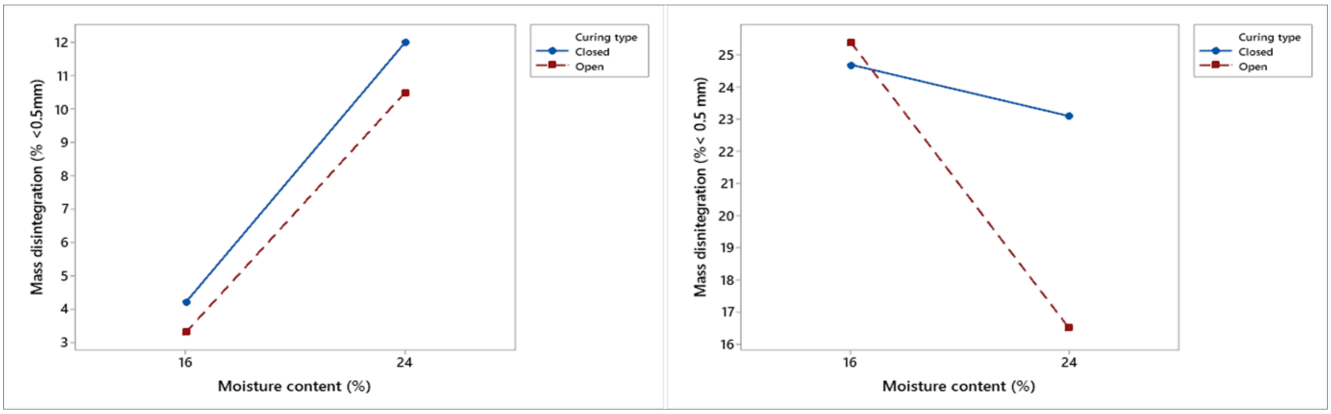

Figure 67: Interaction plot of mass disintegration (−0.5 mm), left at a briquette ore top size of −6.3 mm and right at a briquette ore top size of −12.5 mm

5.3.7.2.Compressive strength and drop number tests

Compressive strength and drop number tests were conducted on product briquettes on completion of the Linder furnace tests. These results are presented in Appendix 9. Eight compressive strength analyses were carried out for each batch of briquettes.

For the briquette ore top size of −6.3 mm, under open curing conditions at 16% moisture content, an average compressive strength of 852 N was attained with an average drop number of 12.4; for 24% moisture content, an average compressive strength of 228 N and average drop number of 1.67 were attained. These results illustrate that an increase in moisture content adversely affected the compressive strength and drop number, under both open and closed curing conditions. At 16% moisture content, the average compressive strength was 945 N and average drop number was 11.0; the respective values for 24% moisture were 188 N and 1.67. Notably, at 24% moisture content under closed curing conditions, the briquettes completely disintegrated during the Linder furnace testing.

For the briquette ore top size of −12.5 mm, the briquettes completely disintegrated in the Linder furnace test, leaving no whole briquette available for compressive strength or drop number testing.

5.3.7.3.Chemical and mineralogical analysis

Detailed XRF analyses conducted on the briquettes on completion of the Linder furnace tests are presented in Appendix 9. The briquettes of ore top size of −6.3 mm assayed averages of 2.57 mass% NiO, 42.3 mass% SiO_2, 25.7 mass% (Fe_2O_3 + Fe_3O_4), and (SiO_2)/(Al_2O_3 + (Fe_2O_3 + Fe_3O_4)) mass ratio of 1.39.

The corresponding values for the briquette ore top size of −12.5 mm were 2.23 mass% NiO, 45.9 mass% SiO_2, 16.3 mass% Fe_2O_3, and $(SiO_2)/(Al_2O_3 + Fe_2O_3)$ mass ratio of 2.43. These results are consistent with the feed ore assays, for which $(SiO_2)/(Al_2O_3 + (Fe_2O_3 + Fe_3O_4))$ ratios of 1.44 and 2.62 were obtained for feed ore top sizes of −6.3 mm and −12.5 mm, respectively. Table 35 presents a summary of the XRF analyses .

Table 35: X-ray fluorescence analyses of briquettes after Linder furnace tests

Briquette ore top size	**Component, average mass %**							
	NiO	SiO_2	Fe_2O_3	Al_2O_3	MgO	Cr_2O_3	MnO	LOI
−6.3 mm	2.57	42.3	25.7	4.68	22.0	1.20	0.42	0.16
−12.5 mm	2.23	45.9	16.3	2.65	29.7	0.76	0.23	1.36

Quantitative XRD analyses of the briquettes, presented in Table 36, indicate that they primarily consisted of enstatite, forsterite, quartz, magnetite, and hornblende.

Table 36: Quantitative X-ray diffraction analysis of briquettes after Linder furnace tests

Mineral, mass %		
Mineral	−6.3 mm	−12.5 mm
Amorphous	30.3	18.0
Diopside	6.51	-
Enstatite	19.6	12.94
Forsterite	26.6	53.1
Hornblende	4.79	4.80
Magnetite	4.56	2.71
Quartz	6.02	8.46
Hematite	1.52	-

EDS analysis and X-ray elemental mapping were conducted on the briquette samples on completion of the Linder furnace tests, the results of which are presented in Appendix 9. The observed phases from BEI were enstatite, hornblende, diopside, quartz, and forsterite.

Additionally, a Cr-spinel was observed for both briquette types. The latter accords with results presented by Rhamdhani et al. (2009). Wustite and an FeNi alloy were also observed for the briquette ore top size of −12.5 mm. These phases were not observed at the detection limit of quantitative XRD, so it may be concluded that they were present in trace amounts.
EDS analysis of the briquettes and stoichiometries of the major phases present in the briquettes after the Linder furnace tests are presented in Appendix 9.

5.4. Summary of main and interaction plots

A summary of the main-effects and interaction plots from the test programme is shown in Table 37. The results indicate that moisture content had the greatest effect on briquette properties for a top size of −6.3 mm, while curing conditions had the greatest effect for a top size of −12.5 mm.

The results indicate that for briquette ore top size of −12.5 mm, an interaction between moisture and curing conditions existed for all parameters tested. For the briquette ore top size of −6.3 mm, there was no interaction effect between moisture content and curing conditions on the briquette compressive strength, TI, and Linder furnace briquette disintegration indexes.

Table 37: Main-effect and interaction plots summary

Parameter	**Main effect**		**Interaction**	
	−6.3 mm	−12.5 mm	−6.3 mm	−12.5 mm
Compressive strength (N)	Moisture	Curing	No interaction	✓
Tumble index (% +6.3 mm)	Moisture	Curing	No interaction	✓
Abrasion index (% -0.5 mm)	Curing	Curing	✓	✓
Degree of reduction (%)	Moisture	Curing	✓	✓
Decrepitation index (% −0.5 mm)	Moisture	Curing	✓	✓
$\text{RDI}_{+6.3\text{mm}}$ (% +6.3 mm)	-	Moisture	✓	✓
$\text{RDI}_{--3.15\text{mm}}$ (% −3.15 mm)	-	Moisture	✓	✓
$\text{RDI}_{-0.5\text{mm}}$ (% −0.5 mm)	Moisture	Curing	✓	✓
Linder $_{+6.3\text{mm}}$ (% +6.3 mm)	Moisture	Moisture	No interaction	✓
Linder $_{-0.5\text{mm}}$ (% −0.5 mm)	Moisture	Moisture	No interaction	✓

5.5. Analysis of variance

The ANOVA technique was adopted to assess whether differences between the measured responses are statically significant at different factor levels. The ANOVA test criteria are presented in Section 3.7. The test statistics were as follows:

- Null hypothesis: All means are equal (measured responses, yield, compressive strength, TI, etc.);
- Alternative hypothesis: Not all means are equal;
- Significance level (α): 0.05;
- Confidence interval: 95%.

5.5.1. Green briquette compressive strength

A summary of the green briquette ANOVA results is presented in Table 38. The p-value indicates that owing to the curing conditions, the difference in the average green briquette compressive strength is not statistically significant. Owing to moisture content, the difference in average green briquette compressive strength is only statistically significant for the briquette ore top size of −6.3 mm.

Table 38: ANOVA of the green briquette compressive strength

Factor analysed	Briquette ore top size −6.3 mm	Briquette ore top size −12.5 mm
	p-value	
Effect of curing condition	0.848	0.112
Effect of moisture content	**0.034**	0.130

5.5.2. Tumble strength and abrasion index

A summary of the TI and AI ANOVA results is shown in Table 39. The p-value indicates that the difference in the AI and TI at different moisture content levels and curing conditions is not statistically significant.

Table 39: ANOVA analysis of tumble and abrasion indices

Tumble index, mass% +6.3 mm		
Factor analysed	Briquette ore top size −6.3 mm	Briquette ore top size −12.5 mm
	p-value	
Effect of curing condition	0.453	0.353
Effect of moisture content	0.163	0.572
Abrasion index, mass% −0.5 mm		
Factor analysed	Briquette ore top size −6.3 mm	Briquette ore top size −12.5 mm
	p-value	
Effect of curing condition	0.302	0.544
Effect of moisture content	0.387	0.384

5.5.3. Reducibility index

A summary of the RI test ANOVA results is presented in Table 40. The p-value indicates that the difference in the degree of reduction at different moisture content levels is not statistically significant. For the briquette ore top size of −12.5 mm, the difference in degree of reduction at different curing conditions is statistically significant.

Table 40: ANOVA of degree of reduction

Degree of reduction, %		
Factor analysed	Briquette ore top size −6.3 mm	Briquette ore top size −12.5 mm
	p-value	
Effect of curing condition	0.557	**0.055**
Effect of moisture content	0.221	0.808

5.5.4.Decrepitation index

The DI test ANOVA results are given in Table 41. The p-value indicates that the difference in the DI, mass% −3.15 mm, and mass% −0.5 mm, at different moisture content levels and curing conditions is not statistically significant for the briquette ore top size of −6.3 mm.

Table 41: ANOVA of decrepitation index

Decrepitation index, mass% −6.3 mm		
Factor analysed	Briquette ore top size −6.3 mm	Briquette ore top size −12.5 mm
	p-value	
Effect of curing condition	0.503	0.468
Effect of moisture content	0.263	0.594
Mass disintegration, mass% −3.15 mm		
Factor analysed	Briquette ore top size −6.3 mm	Briquette ore top size −12.5 mm
	p-value	
Effect of curing condition	0.507	**0.045**
Effect of moisture content	0.323	0.704
Mass disintegration (mass percentage -0.5mm)		
Factor analysed	Briquette ore top size −6.3 mm	Briquette ore top size −12.5 mm
	P-value	
Effect of curing condition	0.744	0.334
Effect of moisture content	0.073	0.255

5.5.5.Reduction disintegration index

The RDI test ANOVA results are given in Table 42. The p-value indicates that the difference in the RDI at different moisture content levels and curing conditions is not statistically significant for either briquette type.

Table 42: ANOVA of reduction disintegration index

Reduction disintegration index, mass% +6.3 mm		
Factor analysed	Briquette ore top size −6.3 mm	Briquette ore top size −12.5 mm
	p-value	
Effect of curing condition	0.455	0.346
Effect of moisture content	0.449	0.815
Reduction disintegration index, mass% −3.15 mm		
Factor analysed	Briquette ore top size −6.3 mm	Briquette ore top size −12.5 mm
	p-value	
Effect of curing condition	0.446	0.345
Effect of moisture content	0.423	0.607
Reduction disintegration index, mass% −0.5 mm		
Factor analysed	Briquette ore top size −6.3 mm	Briquette ore top size −12.5 mm
	p-value	
Effect of curing condition	0.538	0.399
Effect of moisture content	0.285	0.343

5.5.6. Linder furnace

A summary of the Linder furnace material disintegration ANOVA results is presented in Table 43. For the briquette ore top size of −6.3 mm, the p-value indicates that the difference in the mass disintegration (mass% +6.3 mm, mass% −3.15 mm, mass% −0.5 mm) at different moisture contents is statistically significant; however, the same conclusion could not be drawn for different curing conditions. The curing condition p-value is greater than the alpha value ($P > \alpha$), indicating that the differences in the mass disintegration for all size fractions at different curing conditions is not statistically significant.

For the briquette ore top size of −12.5 mm, the ANOVA indicates that the difference in the mass disintegration at different curing conditions is not statistically significant. With the exception of the mass% −0.5 mm, the difference in material disintegration is not statistically significant at different curing conditions for different moisture contents.

Table 43: ANOVA of Linder furnace test

Mass disintegration, mass% +6.3 mm		
Factor analysed	Briquette ore top size −6.3 mm	Briquette ore top size −12.5 mm
	p-value	
Effect of curing condition	0.968	0.563
Effect of moisture content	**0.012**	0.377
Mass disintegration, mass% −3.15 mm		
Factor analysed	Briquette ore top size −6.3 mm	Briquette ore top size −12.5 mm
	p-value	
Effect of curing condition	0.936	0.605
Effect of moisture content	**0.003**	0.266
Mass disintegration, mass% −0.5 mm		
Factor analysed	Briquette ore top size −6.3 mm	Briquette ore top size −12.5 mm
	p-value	
Effect of curing condition	0.837	0.956
Effect of moisture content	**0.021**	**0.010**

5.6. Summary of results

A summary of the test programme results is presented in Table 44. For the briquette ore top size of −6.3 mm, average green briquette compressive strengths of 480 N and 155 N were measured for moisture contents of 16% and 24%, respectively. Increasing the briquette ore top size to −12.5 mm resulted in average briquette compressive strengths of 125 N and 75.9 N, respectively.

The results indicate a decrease in TI with increases in both moisture content and briquette ore top size. For the briquette ore top size of −6.3 mm, average TI of 93.5% and 87.6% were reported for moisture contents of 16% and 24%, respectively; for the briquette ore top size of −12.5 mm, the respective values are 40.5% and 41.9%.

An average AI of 5.91% was measured for the briquette ore top size of −6.3 mm; this value increased to 14.0% for the briquette ore top size of −12.5 mm, which is an average 136.8% increase in AI. An increase in AI with briquette ore top size has a detrimental effect on permeability.

For the briquette ore top size of −6.3 mm, average degrees of reduction of 33.4% and 27.6% were reported for 16% and 24% moisture content, respectively, which represents a 17.4% decrease. For the briquette ore top size of −12.5 mm, the average degrees of reduction were 39.2% and 36.9% for 16% and 24% moisture contents, which is a 5.86% decrease. These results indicate that optimal degree of reduction was obtained for the briquette ore top size of −12.5 mm.

The results suggest that briquettes produced at an ore top size of −12.5 mm have marginally higher porosity, which allows for improved gas and temperature permeability. Density analyses indicated a marginally lower density for the briquette ore top size of −12.5 mm (2.357 g/cm^3), which further supports the suggestion that the porosity was marginally higher in these briquettes, resulting in marginally higher reduction. Considering the PSD analyses and reduction results suggests that the presence of finer particles adversely affected gas permeability, thereby leading to a decrease in the degree of reduction.

An increase in moisture content was associated with an increase in the DI for both briquette types. Increasing the briquette ore top size from −6.3 mm to −12.5 mm had a detrimental effect on the RDI (RDI$_{+6.3mm}$, RDI$_{-3.15mm}$ and RDI$_{-0.5mm}$).

For briquette ore top sizes of −6.3 mm and −12.5 mm, average RDI$_{+6.3mm}$ of 96.0% and 75.1% were reported, respectively, representing a 21.8% decrease with an increase in the top size. Disintegration of briquettes, resulting in the formation of fine particles, also increased with an increase in the briquette ore top size: For the briquette ore top sizes of −6.3 mm and−12.5 mm, average RDI$_{-0.5mm}$ of 2.54% and 6.92%, respectively, were measured.

The Linder furnace test results indicated that increasing the briquette ore top size from −6.3 mm to −12.5 mm had a detrimental effect on the mass disintegration and generation of fines. For the briquette ore top size of −6.3 mm, an average mass disintegration (mass% −0.5 mm) of 7.50% was reported; the corresponding value for the briquette ore top size of −12.5 mm was 22.4%.

Table 44: Summary of test programme results

Briquette description (average responses)				
Parameter	Briquette ore top size: −6.3 mm		Briquette ore top size: −12.5 mm	
	Moisture content		Moisture content	
	16%	24%	16%	24%
Average briquette yield (%)	85.2	67.7	88.4	78.2
Compressive strength (N)	480	155	125	75.9
Tumble index (% +6.3 mm)	93.5	87.6	40.5	41.9
Abrasion index (% −0.5 mm)	4.99	6.83	13.4	14.7
Degree of reduction (%)	33.4	27.6	39.9	37.5
Decrepitation index (% −0.5 mm)	0.33	0.61	2.34	1.96
$\text{RDI}_{+6.3\text{mm}}$ (% +6.3 mm)	97.3	94.7	79.1	71.1
$\text{RDI}_{-3.15\text{mm}}$ (% −3.15 mm)	2.59	4.79	14.4	17.3
$\text{RDI}_{-0.5\text{mm}}$ (% −0.5 mm)	1.76	3.33	6.77	7.08
$\text{Linder}_{+6.3\text{mm}}$ (% +6.3 mm)	95.3	70.3	25.4	30.3
$\text{Linder}_{-3.15\text{mm}}$ (% −3.15 mm)	4.46	21.4	50.3	45.5
$\text{Linder}_{-0.5\text{mm}}$ (% −0.5 mm)	3.75	11.3	25.1	19.8

6. Conclusion

The purpose of this study was to evaluate the performance of briquettes as potential feed into the electric arc furnaces at the Barro Alto operation. The study considered three key parameters in evaluating the performance of briquettes: moisture content (16% and 24%), curing conditions (open and closed), and PSD of the feed to the briquetting process (−6.3 mm and −12.5 mm). This study complements the results of pilot-plant campaign tests undertaken by Anglo American at the Value-In-Use facility in Pretoria, South Africa. Briquette performance was evaluated using ISO tests for TI, AI, RI DI, and RDI, and the Anglo American Value-In-Use in-house standard Linder furnace test, which simulates conditions in a rotary kiln.

Some important considerations in the move towards briquetting at the Barro Alto operation are the increase in nameplate capacity, lower electricity consumption, and improved process safety and stability.

A bulk sample from Barro Alto mine was made available for the test programme. The sample was identified as a saprolitic laterite containing 2.03 mass% NiO and 17.2 mass% Fe_2O_3. The main mineral constituents were identified as serpentine (lizardite), olivine (forsterite), and amphibole (hornblende).

RI testing showed a decrease in the degree of reduction with an increase in moisture content for both briquette types. The results suggest that the presence of water vapour has a detrimental effect on the degree of reduction. An increase in the degree of reduction was also observed with an increase in briquette ore top size, the −6.3 mm top size comprised a greater degree (19.1%) of fine particles (−0.5 mm) than the −12.5 mm top size (15.2%).

As moisture content and briquette ore top size increased, there was a decrease in TI. For the briquette ore top size of −6.3 mm, the average TI were 93.5% and 87.6% for moisture contents of 16% and 24%, respectively. With the larger briquette ore top size of −12.5 mm, the average TI were 40.5% and 41.9% for moisture contents of 16% and 24%, respectively.

Additionally, the study found that for the briquette ore top size of −6.3 mm, the average AI was 5.91%, which increased to 14.0% for the briquette ore top size of −12.5 mm. This increase in AI has a detrimental effect on permeability.

The DI, RDI, and Linder furnace decrepitation index all showed an increase in briquette disintegration for the briquette ore top size of −12.5 mm, suggesting that coarser particles lead to weaker bonds, making the briquettes more susceptible to breakage.

The conditions that yielded briquettes with highest structural integrity were obtained for an ore top size of −6.3 mm at 16% moisture content under open curing conditions. The highest degree of reduction was obtained for the briquette top size of −12.5 mm at a moisture content of 16% under closed curing conditions. The results obtained for briquettes with an ore top size of −6.3 mm, a moisture content of 16%, and open curing conditions are comparable to those obtained by Anglo American (Value-In-Use) during their pilot-plant campaign.

The ANOVA largely indicated that the different measured responses for different curing conditions and moisture contents are not statistically significant, at the set test statistic.

Recommendations from the findings are based on the relative precedence of the parameters in the operation. Where process safety and stability take precedence, it is recommended to produce briquettes with an ore top size of −6.3 mm and moisture content of 16% under open curing conditions. Green briquette compressive strength results revealed that an increase in moisture content led to a deterioration in compressive strength for both briquette types. These results affirm those of numerous literature studies, which attribute this to a reduction in the surface energy due to physical absorption.

7. Future Work

Having completed the test programme, the ANOVA indicated that difference in the measured responses at briquette ore top sizes of −6.3 mm and −12.5 mm were not statistically significant, based on the test statiscis selected. These results require interpretation in conjunction with sensitivity analysis of plant data. It is therefore recommended that a sensitivity analysis be conducted to indicate the relative sensitivity of the process parameters (moisture content, curing condition, top size) and tolerance limits of each parameter.

8. References

Anglo American, 2009, *Anglo American analyst visit 2009*, from https://www.angloamerican.com/~/media/Files/A/Anglo-American-Group v5/PLC/media/presentations/2009pres/barro_alto_visit/barro_alto_visit.pdf

Anglo American, 2022, *Climate change report, 2022*, from https://www.angloamerican.com/~/media/Files/A/Anglo-American-Group-v5/PLC/investors/annual-reporting/2022/climate-change-report-2022.pdf

Antony, J., 2014, 'A systematic methodology for design of experiments' in J. Antony, *Design of experiments for engineers and scientists*, 2nd edn, pp. 33–50, Elsevier, Edinburgh.

Aslam, M., 2020, 'Introducing Grubbs's test for detecting outliers under neutrosophic statistics – An application to medical data', *Journal of King Saud University - Science*, 32(6), 2696–2700.

Barnes, V.E., 1930, 'Changes in hornblende at about 800°C'. *Journal of the Mineralogical Society of America*, 15(9), 393–417.

Barros de Oliveira, S.M., Trescases, J.J. & Melfi, A.J. 1992, 'Lateritic nickel deposits of Brazi', *Mineralium Deposita*, 27(2), 137–146, from https://doi.org/10.1007/bf00197099

Bolaños-Benítez, V., Van Hullebusch, E.D., Birck, J.-L., Garnier, J., Lens, P.N.L., Tharaud, M., Quantin, C. & Sivry, Y., 2021, 'Chromium mobility in ultramafic areas affected by mining activities in Barro Alto massif, Brazil: An isotopic study', *Chemical Geology*, 561, 120, from https://doi.org/10.1016/j.chemgeo.2020.120000

Brosig, D., Safe, P., Russell, M., Arévalo, J., Kiyan, C., Rodrigues, M. & Miranda, M., 2023, 'Decarbonization at the Anglo-American Barro Alto smelter through implementation of the ecombustible technology', in *Proceedings of the 61st Conference of Metallurgists, COM 2022*, Springer eBooks, Cham, pp. 939–948, from https://doi.org/10.1007/978-3-031-17425-4_104

Brujin, W., 2019, *Brazil: Minas-Rio and nickel: Bulks seminar and site visit, Brisbane*, from https://www.angloamerican.com/~/media/Files/A/Anglo-American-Group/PLC/media/presentations/2019pres/minas-rio-and-nickel.pdf

Cardoso, D. das D. de P., Soares, C.M.A., Souza, M.B. de L.D., Azevedo, M. da S.P. de, Martins, R.M.B., Queiróz, D.A. de O., Brito, W.M.E.D. de, Munford, V. & Rácz, M.L., 2003, ‘Epidemiological features of rotavirus infection in Goiânia, Goiás, Brazil, from 1986 to 2000’, *Memórias do Instituto Oswaldo Cruz*, 98(1), 25–29, from https://doi.org/10.1590/S0074-02762003000100004

Chen, Z., Qu, Y., Zeilstra, C., Van der Stel, J., Sietsma, J. & Yang, Y., 2019, ‘Prediction of density and volume variation of hematite ore particles during in-flight melting and reduction’, *Journal of Iron and Steel Research International*, 26(12), 1285–1294, from https://doi.org/10.1007/s42243-019-00265-3

Cho, M. & Fawcett, J.J., 1986, ‘A kinetic study of clinochlore and its high temperature equivalent forsterite-cordierite-spinel at 2 kbar water pressure’, *American Mineralogist*, 71, 68–77.

Crundwell, F., Moats, M.S., Ramachandran, V., Robinson, T.G. & Davenport, W.G. 2011, *Extractive metallurgy of nickel, cobalt and platinum group metals*, Elsevier, Amsterdam.

Da Silva, A.L., De Oliveira, A.H. & Fernandes, M.L.S., 2011, ‘Influence of preferred orientation of minerals in the mineralogical identification process by x-ray diffraction’, in International Atomic Energy Agency, *International Nuclear Atlantic Conference - INAC 2011.* Associação Brasileira de Energia Nuclear – ABEN, pp. 1–11.

Dalvi, A., Bacon, W.G. & Osborne, R., 2004, ‘The past and the future of nickel laterites’, in *Proceedings of the PDAC 2004 International Convention, Trade Show and Investors Exchange*, 7–10 March 2004, pp.1–27.

De Angelis, S.H., Larsen, J., Coombs, M., Dunn, A. & Hayden, L., 2015, ‘Amphibole reaction rims as a record of pre-eruptive magmatic heating: An experimental approach’, *Earth and Planetary Science Letters*, 426, 235–245, from https://doi.org/10.1016/j.epsl.2015.06.051

Deer, W.A., Howie, R.A. & Zussman, J., 1992, *An introduction to the rock-forming minerals*, 2nd edn., Longman Scientific & Technical, Harlow.

Drzymała, Z., 1993, *Industrial briquetting: Fundamentals and methods,* Elsevier, Amsterdam.

Efimchenko, V.S., Barkovskii, N.V., Fedotov, V.K., Meletov, K.P., Chernyak, V.M. & Khryapin, K.I., 2019, 'Destruction of fayalite and formation of iron and iron hydride at high hydrogen pressures', *Physics and Chemistry of Minerals*, 46(8), 743–749, from https://doi.org/10.1007/s00269-019-01035-z

Eisele, T.C. & Kawatra, S.K., 2003, 'A review of binders in iron ore pelletization', *Mineral Processing and Extractive Metallurgy Review*, 24(1), 1–90, from https://doi.org/10.1080/08827500306896

Elliott, R., Pickles, C.A. & Forster, J. 2016, 'Thermodynamics of the reduction roasting of nickeliferous laterite ores', *Journal of Minerals and Materials Characterization and Engineering*, 04(06), 320–346, from https://doi.org/10.4236/jmmce.2016.46028

Faria, G.L., Vianna, N.C.S., Jannotti, N., Vieira, C.B. & Da Silva, A.F.G., 2010, 'Decrepitation of Brazilian manganese lump ores', in A.Vartiainen (ed.), *Proceedings of the Twelfth International Ferroalloys Congress: Sustainable Future*, Helsinki, Finland, June 6–10, 2010, pp. 449–456.

Fisher, E.A., 1923, 'Some factors affecting the evaporation of water from soil', *The Journal of Agricultural Science*, 13(2), 121–143, from https://doi.org/10.1017/s0021859600003270

Gidigasu, M.D., 1976, *Laterite soil engineering: Pedogenesis and engineering principles*, Elsevier, Amsterdam.

Gleeson, S.A., Herrington, R.J., Durango, J., Velasquez, C.A. & Koll, G., 2004, 'The mineralogy and geochemistry of the Cerro Matoso S.A. Ni laterite deposit, Montelibano, Colombia', *Economic Geology*, 99(6), 1197–1213, from https://doi.org/10.2113/gsecongeo.99.6.1197

Goenka, M. & Naik, A., 2013, 'Effect of size distribution and water content on properties of iron ore pellets', B Tech thesis, National Institute of Technology, Rourkela, India, from http://ethesis.nitrkl.ac.in/4902/

Goupy, J.L., 1993, *Methods for experimental design: Principles and applications for physicists and chemists*, transl. C.O. Parkes, Elsevier, Amsterdam.

Graham, W.A.P., 1926, 'Variations in the chemical composition of hornblende from different types of igneous rocks', *American Mineralogist*, 11(5), 118–123.

Halt, J.A. & Kawatra, S.K., 2014, ‘Review of organic binders for iron ore concentrate agglomeration’, *Mining, Metallurgy & Exploration*, 31(2), 73–94, from https://doi.org/10.1007/bf03402417

Han, J. & Zhou, Z., 2013, ‘Dynamics of soil water evaporation during soil drying: laboratory experiment and numerical analysis’, *The Scientific World Journal*, 2013, Article ID 240280, from https://doi.org/10.1155/2013/240280

Iljana, M., 2017, ‘Iron ore pellet properties under simulated blast furnace conditions: Investigation on reducibility, swelling and softening’, Doctoral thesis, Faculty of Technology, University of Oulu, Finland, pp.1–87.

International Nickel Study Group, 2022, *World nickel factbook 2021*, INSG, Lisbon, Portugal, from https://insg.org/wp-content/uploads/2022/02/publist_The-World-Nickel-Factbook-2021.pdf

Janwong, A., 2012, ‘The agglomeration of nickel laterite ore’, Doctoral thesis, Department of Metallurgical Engineering, University of Utah, United Sates of America, pp.26–34.

Kaliyan, N. & Vance Morey, R., 2009, ‘Factors affecting strength and durability of densified biomass products’, *Biomass and Bioenergy*, 33(3), 337–359, from https://doi.org/10.1016/j.biombioe.2008.08.005

Kleinebudde, P. & Knop, K. 2007, ‘Direct pelletization of pharmaceutical pellets in fluid-bed processes’ in A. Salman, M. Hounslow & J. Seville (eds.), *Granulation*, pp. 780–810, Elsevier, Düsseldorf.

Koerner, R.M. & MacDougall, J.A., 1983, *Elements II briquetting and agglomeration*, The Institute for Briquetting and Agglomeration, Erie, PA.

Kozu, S., Yoshiki, B. & Kani, K. 1926, ‘Note on the study of the transformation of common hornblende into basaltic hornblende at 750°C', *Science Reports of the Tohoku Imperial University: Mineralogy, Petrology, Economic Geology*, 3(2), 143–159.

Kurunov, I. and Aitber Bizhanov ,2018, ‘Features of Stiff Vacuum Extrusion as a Method of Briquetting Natural and Anthropogenic Raw Materials’, Topics in mining, metallurgy and materials engineering, pp.23–68, from doi:https://doi.org/10.1007/978-3-319-72712-7_2.

Larssen, T.A. & Tangstad, M., 2022, ‘Effect of moisture, hydrogen, and water–gas shift reaction on the prereduction behavior of Comilog and Nchwaning manganese ores’, *Metallurgical and Materials Transactions B*, 53(4), 2104–2116, from https://doi.org/10.1007/s11663-022-02511-8

Li, S., 1999, ‘Study of nickeliferrous laterite reduction’, Master’s dissertation, Faculty of Engineering, McMaster University, Hamilton, ON.

Li, Y., Zang, Y., Xiong, Y., Qiu, D., Wang, C., Yan, L. & Yu, Y., 2022, ‘Effect of briquetting pressure on the properties, reduction behavior, and reduction kinetics of cold-bonded briquette prepared from return fines of sinter’, *Metallurgical and Materials Transactions B*, 54(1), 355–369, from https://doi.org/10.1007/s11663-022-02696-y

Lima, F.G., Haraguchi, M., Pfister, J.A., Guimarães, V.Y., Andrade, D.D., Ribeiro, C.S., Costa, G.L., Araújo, A.R. & Fioravanti, M.C., 2012, ‘Weather and plant age affect the levels of steroidal saponin and Pithomyces chartarum spores in Brachiaria grass’, *International Journal of Poisonous Plant Research*, 2(1), 45–53.

Lu, X., Guo, E., Yuan, Q., Pan, C. & Liu, M., 2013, ‘New method to produce FeNi nuggets from low grade ore by semi-molten reduction’, in *The Thirteenth International Ferroalloys Congress Efficient Technologies in Ferroalloy Industry*, Alamaty, Kazakhstan, pp. 223–228

Liu, X., Liu, X. & Hu, Y., 2014, ‘Investigation of the thermal decomposition of talc’, *Clays and Clay Minerals*, 62(2), 137–144, from https://doi.org/10.1346/ccmn.2014.0620206

Lu, L. (ed.), 2015, *Iron ore: Mineralogy, processing and environmental sustainability*, Woodhead Publishing, Cambridge.

Mc Dougall, I., 2013, ‘Chapter 4: Ferroalloys processing equipment’, in M. Gasik (ed.), *Handbook of ferroalloys: Theory and technology*, pp. 83–138, Elsevier, from http://dx.doi.org/10.1016/B978-0-08-097753-9.00004-6

Moreira Alves, T. & De Souza Sales, P.C., 2002, ‘Barro Alto preliminary mine closure plan’, viewed 1 November 2023, from https://brasil.angloamerican.com/~/media/Files/A/Anglo-American-Group-v5/Brazil/sustentabilidade/plano-de-fechamento-de-mina-de-barro-alto-2022.pdf

Murakami, T., Nishimura, T. & Kasai, E., 2009, ‘Lowering reduction temperature of iron ore and carbon composite by using ores with high combined water content’, *ISIJ International*, 49 (11), 1686–1693, from https://doi.org/10.2355/isijinternational.49.1686

Nheta, W., Portia Lubisi, T. & Jeli, E., 2018, ‘Effect of different binders on mechanical properties of iron flotation concentrate briquettes’, *Materials Today: Proceedings*, 5(1), 294–301, from https://doi.org/10.1016/j.matpr.2017.11.085

Oxley, A., Smith, M.E. & Caceres, O., 2016, ‘Why heap leach nickel laterites?’ *Minerals Engineering*, 88, 53–60, from https://doi.org/10.1016/j.mineng.2015.09.018

Peckner, D. & Bernstein, I.M., 1977, *Handbook of stainless steels*, McGraw-Hill, New York, NY.

Pichler, H. & Schmitt-Riegraf, C., 1997, *Rock-forming minerals in thin section*, 2nd edn., Springer, Dordrecht, from https://doi.org/10.1007/978-94-009-1443-8

Pietsch, W.B., 2008, *Agglomeration processes: Phenomena, technologies, equipment,* Wiley-VCH, Weinheim, Germany.

Pyatina, T., Ronne, A., Sugama, T. & Trabits, G., 2018, ‘Self-repairing properties of OPC clinker/natural zeolite blend in water and alkali carbonate environments at 270°C’, *Advances in Cement Research*, 30(1), 8–23, from http://dx.doi.org/10.1680/jadcr.16.00136

Qiu, G.Y. & Ben-Asher, J., 2010, ‘Experimental determination of soil evaporation stages with soil surface temperature’, *Soil Science Society of America Journal*, 74(1), 13–22, fom https://doi.org/10.2136/sssaj2008.0135

Ratié, G., Garnier, J., Calmels, D., Vantelon, D., Guimarães, E.D., Monvoisin, G., Nouet, J., Ponzevera, E. & Quantin, C., 2018, ‘Nickel distribution and isotopic fractionation in a Brazilian lateritic regolith: Coupling Ni isotopes and Ni K-edge XANES’, *Geochimica et Cosmochimica Acta*, 230, 137–154, from https://doi.org/10.1016/j.gca.2018.03.026

Rhamdhani, M.A., Hayes, P.C. & Jak, E., 2009, ‘Nickel laterite Part 1 – microstructure and phase characterisations during reduction roasting and leaching’, *Mineral Processing and Extractive Metallurgy: Transactions of the InstitutionsofMining and Metallurgy*, 118(3), 129–145, from https://doi.org/10.1179/174328509x431391

Rojas Arias, N., Perez Villamil, F.R. & Arango Patermina, H.J., 2018, ‘Effect of particle size in the reduction of lateritic Ni ore in a Linder reactor’, *Revista ION*, 31(1), 97–104, from https://doi.org/10.18273/revion.v31n1-2018015

Rosenbusch, H., 2018, *Mikroskopische Physiographie der Mineralien und Gesteine*, (reprint), Forgotten Books, London, UK.

Satyananda, P., Kumar, A. & Rayasam, V., 2017, ‘The effect of particle size on green pellet properties of iron ore fines’, *Journal of Mining and Metallurgy A: Mining*, 53(1), 31–41, from https://doi.org/10.5937/jmma1701031s

Schneider, C., 1891, ‘XXXIV. Zur Kenntniss basaltischer Hornblenden’, *Zeitschrift für Kristallographie - Crystalline Materials*, 18(1–6), 579–584, from https://doi.org/10.1524/zkri.1891.18.1.579

Selivanov, E.N., Sergeeva, S.V. & Gulyaeva, R.I., 2020, ‘Thermal properties of high-magnesia oxidized nickel ore’, *Materials Science Forum*, 989, 461–467, from https://doi.org/10.4028/www.scientific.net/msf.989.461

Setiawan, A., Ermawati, I., Anggraini, F., Abidin, F., Hapid, A., Kawigraha, A., Harjanto, S. & Rhamdhani, M.A., 2022, ‘Volume shrinkage during carbothermic reduction of low-grade iron ore containing goethite and coal composite’, *Sains Malaysiana*, 51(5), 1511–1524.

Smyth, J.R., 1974, ‘Experimental study on the polymorphism of enstatite’, *American Mineralogist*, 59(3-4), 345–352.

Souihi, N., 2014, ‘Multivariate synergies in pharmaceutical roll compaction: The quality influence of raw materials and process parameters by design of experiments’, Doctoral thesis, Department of Chemistry, Umeå University, Sweden.

Sun, B., Yu, J., Tahmasebi, A. & Han, Y., 2014, ‘An experimental study on binderless briquetting of Chinese lignite: Effects of briquetting conditions’, *Fuel Processing Technology*, 124, 243–248, from https://doi.org/10.1016/j.fuproc.2014.03.013

Vale, 2023, ‘Vale begins load tests in the first iron ore briquette plant in Brazil’, *Vale Now Press*, 31 August 2023, viewed 7 November 2023, from https://www.vale.com/w/vale-begins-load-tests-in-the-first-iron-ore-briquette-plant-in-brazil

Van Eeckhout, E.M., 1976, ‘The mechanisms of strength reduction due to moisture in coal mine shales’, *International Journal of Rock Mechanics and Mining Sciences & Geomechanics Abstracts*, 13(2), 61–67, from https://doi.org/10.1016/0148-9062(76)90705-1

Vining, K.R., Khosa, J. & Sparrow, G.J., 2017, ‘Briquetting conditions for Australian hematite-goethite iron ore fines’, *ISIJ International*, 57(9), 1517–1523, from https://doi.org/10.2355/isijinternational.isijint-2017-052

Wang, G., Wang, J. & Xue, Q., 2018, ‘Kinetics of the volume shrinkage of a magnetite/carbon composite pellet during solid-state carbothermic reduction’, *Metals*, 8(12), 1050, from https://doi.org/10.3390/met8121050

Weber, D. and Schroder, K. (2002). Planning, Design/Development, Manufacturing, Assembling and after Sales Services of Coal Refining Plants, Coaling Plant for Power Stations, Potash Granulating Plants.

Xue, Y., Zhu, D., Pan, J., Guo, Z., Tian, H., Li, G., Huang, Q., Pan, L. & Huang, X., 2022, ‘Significant influence of self-possessed moisture of limonitic nickel laterite on sintering performance and its action mechanism’, *Journal of Iron and Steel Research International*, 29(9), 1368–1380, from https://doi.org/10.1007/s42243-021-00691-2

Yang, J., Zhang, G., Ostrovski, O. & Jahanshahi, S., 2019, ‘Selective reduction of an Australian garnieritic laterite ore’, *Minerals Engineering*, 131, 79–89, from https://doi.org/10.1016/j.mineng.2018.10.018

Appendix 1: X-Ray Fluorescence Analysis

Feed samples

Table 45: X-ray fluorescence analysis of feed ore samples

	Component, mass %		
	Run-of-mine	Feed ore top size −6.3 mm	Feed ore top size −12.5 mm
SiO_2	41.6	37.6	44.2
TiO_2	0.05	0.07	0.03
Al_2O_3	2.80	4.18	2.67
Fe_2O_3	17.2	21.9	14.2
MnO	0.26	0.37	0.22
MgO	23.0	19.4	28.8
CaO	0.64	0.60	-
Na_2O	0.00	< 0.01	-
K2O	0.02	0.03	0.02
Cr_2O_3	0.81	1.08	0.67
CuO	0.00	< 0.01	0.02
NiO	2.03	2.15	1.93
V_2O_5	0.01	0.01	0.0
ZrO_2	0.00	0.01	-
P_2O_5	0.01	0.01	-
Co_3O_4	-	0.08	0.05
ZnO	-	0.03	0.01
MoO_3	-	< 0.01	-
BaO	-	0.18	-
WO_3	-	-	0.02
LOI*	11.0	12.4	11.1
TOTAL	99.5	100	100

*** LOI: loss on ignition**

X-ray fluorescence analysis of different size fractions of run-of-mine sample

Table 46: X-ray fluorescence analysis of different size fractions

Fraction	Component, mass%																	
	SiO_2	**Al_2O_3**	**MgO**	**P_2O_5**	**Fe_2O_3**	**CaO**	**TiO_2**	**V_2O_5**	**Cr_2O_3**	**K_2O**	**MnO**	**NiO**	**CuO**	**Co_3O_4**	**BaO**	**PbO**	**Sr**	**ZnO**	**LOI**
26.5 mm	51.6	1.12	25.2	< 0.005	8.5	0.60	0.01	< 0.005	0.47	< 0.005	0.10	1.44	< 0.005	0.02	< 0.005	< 0.005	< 0.005	0.01	10.9
19 mm	42.9	1.41	29.6	< 0.005	9.7	1.06	0.02	< 0.005	0.47	< 0.005	0.11	1.60	< 0.005	0.02	< 0.005	< 0.005	< 0.005	0.01	13.1
13.2 mm	43.8	1.46	27.9	< 0.005	10.7	0.54	0.02	< 0.005	0.51	< 0.005	0.12	1.74	<0.005	0.02	< 0.005	< 0.005	< 0.005	0.01	13.1
9.5 mm	42.5	1.70	28.3	< 0.005	10.6	0.69	0.03	< 0.005	0.58	< 0.005	0.26	1.78	< 0.005	0.06	0.014	< 0.005	< 0.005	0.01	13.5
6.7 mm	40.8	2.21	25.7	< 0.005	14.1	0.70	0.03	< 0.005	0.71	< 0.005	0.19	1.91	< 0.005	0.04	< 0.005	< 0.005	< 0.005	0.02	13.6
4.75 mm	38.9	2.75	22.9	< 0.005	17.8	0.71	0.05	0.009	0.85	< 0.005	0.27	2.09	0.015	0.06	0.010	< 0.005	< 0.005	0.02	13.6
3.35 mm	38.3	3.31	20.5	< 0.005	19.8	0.61	0.06	0.009	0.96	< 0.005	0.30	2.15	0.008	0.06	0.010	< 0.005	< 0.005	0.03	13.9
2.36 mm	37.2	3.59	18.9	< 0.005	21.6	0.65	0.06	0.009	1.04	< 0.005	0.33	2.24	0.009	0.06	0.010	0.007	< 0.005	0.03	14.2
1.7 mm	36.1	3.86	17.3	< 0.005	23.8	0.62	0.08	0.011	1.10	< 0.005	0.38	2.34	< 0.005	0.07	0.016	0.009	< 0.005	0.04	14.3
1.18 mm	35.8	4.06	16.8	< 0.005	24.5	0.62	0.08	0.011	1.12	< 0.005	0.38	2.36	< 0.005	0.07	0.012	0.007	< 0.005	0.04	14.1
850 µm	35.5	4.10	16.3	< 0.005	25.2	0.61	0.09	0.013	1.10	< 0.005	0.39	2.38	< 0.005	0.07	0.014	< 0.005	< 0.005	0.04	14.1
600 µm	35.5	4.09	16.3	< 0.005	25.1	0.65	0.09	0.011	1.14	< 0.005	0.40	2.38	< 0.005	0.07	0.015	< 0.005	< 0.005	0.04	14.2
425 µm	35.7	4.11	16.6	< 0.005	24.8	0.63	0.08	0.011	1.16	< 0.005	0.40	2.39	< 0.005	0.07	0.014	< 0.005	< 0.005	0.03	14.1
300 µm	35.8	4.15	16.9	< 0.005	24.1	0.59	0.08	0.011	1.34	< 0.005	0.40	2.39	< 0.005	0.08	0.014	< 0.005	< 0.005	0.04	14.1
250 µm	35.6	4.28	17.1	< 0.005	23.6	0.60	0.08	0.013	1.63	< 0.005	0.41	2.37	< 0.005	0.08	0.013	0.007	< 0.005	0.04	14.1
212 µm	35.7	4.37	17.5	< 0.005	22.9	0.70	0.08	0.013	1.70	< 0.005	0.39	2.31	< 0.005	0.07	0.011	< 0.005	< 0.005	0.04	14.2
150 µm	35.6	4.45	17.7	< 0.005	22.7	0.71	0.08	0.013	1.80	< 0.005	0.39	2.29	< 0.005	0.07	0.012	< 0.005	< 0.005	0.04	14.2
106 µm	36.5	4.04	18.3	< 0.005	21.9	0.74	0.07	0.011	1.49	< 0.005	0.38	2.28	< 0.005	0.07	0.011	< 0.005	< 0.005	0.04	14.2
75 µm	36.3	4.41	18.2	< 0.005	22.5	0.87	0.08	0.013	1.64	< 0.005	0.37	2.23	< 0.005	0.07	0.011	< 0.005	< 0.005	0.04	13.3
53 µm	36.1	4.08	18.2	< 0.005	23.5	0.86	0.08	0.013	1.20	< 0.005	0.36	2.33	< 0.005	0.07	0.011	< 0.005	< 0.005	0.04	13.2
45 µm	35.4	3.76	16.9	< 0.005	25.0	0.80	0.08	0.011	0.74	< 0.005	0.34	2.50	< 0.005	0.06	0.012	< 0.005	< 0.005	0.04	14.3
25 µm	34.0	3.60	15.8	< 0.005	27.0	0.74	0.09	0.011	0.63	< 0.005	0.33	2.52	0.014	0.06	0.014	0.005	< 0.005	0.05	15.1
< 25 µm	35.0	3.97	16.8	< 0.005	26.2	0.88	0.09	0.011	0.93	< 0.005	0.35	2.37	< 0.006	0.06	0.011	0.008	< 0.005	0.04	13.2

Appendix 2: Back-scattered Electron Image Analysis and X-Ray Mapping of Feed Sample

Run-of-mine

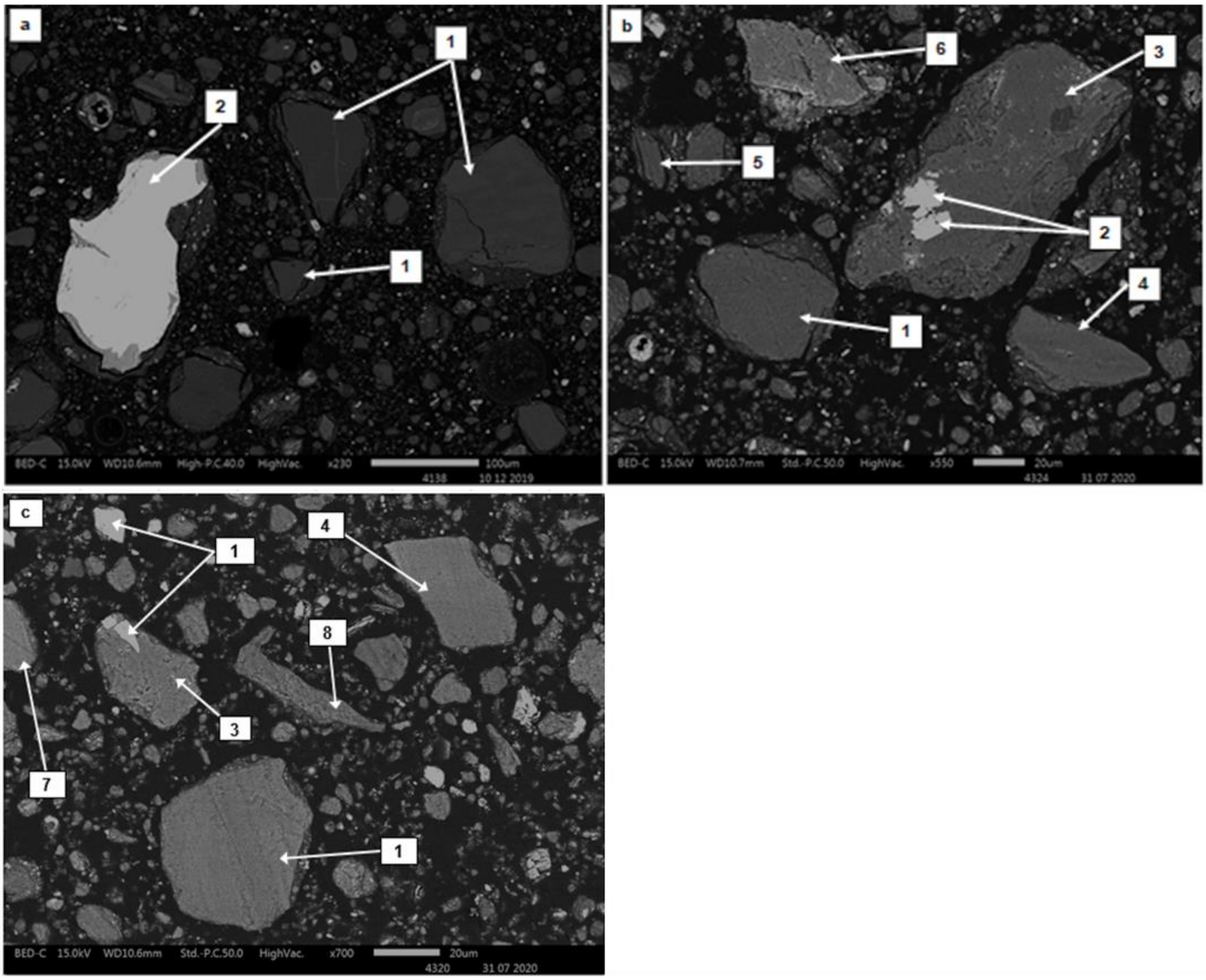

Figure 68: Back-scattered electron images of plant feed: (a) 100 µm; (b) 20 µm; (c) 10 µm, where (1) forsterite; (2) iron oxide; (3) quartz; (4) enstatite; (5) talc; (6) hornblende; (7) lizardite; (8) chlorite

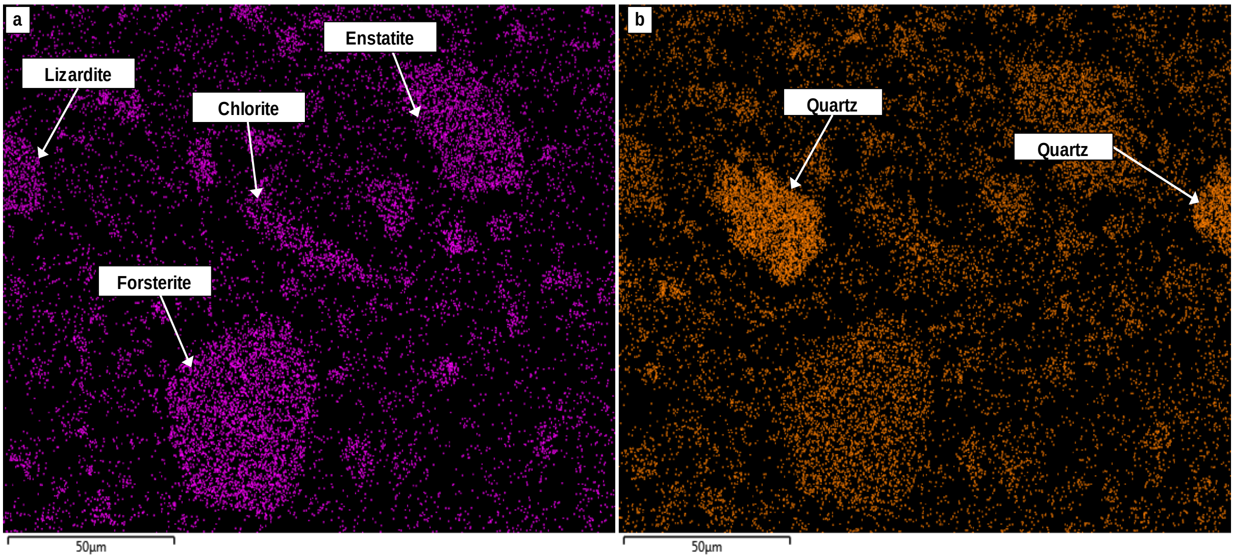

Figure 69: X-ray maps of major elements present in plant feed: (a) Mg, (b) Si (Figure 68(c))

Feed ore top size −6.3 mm

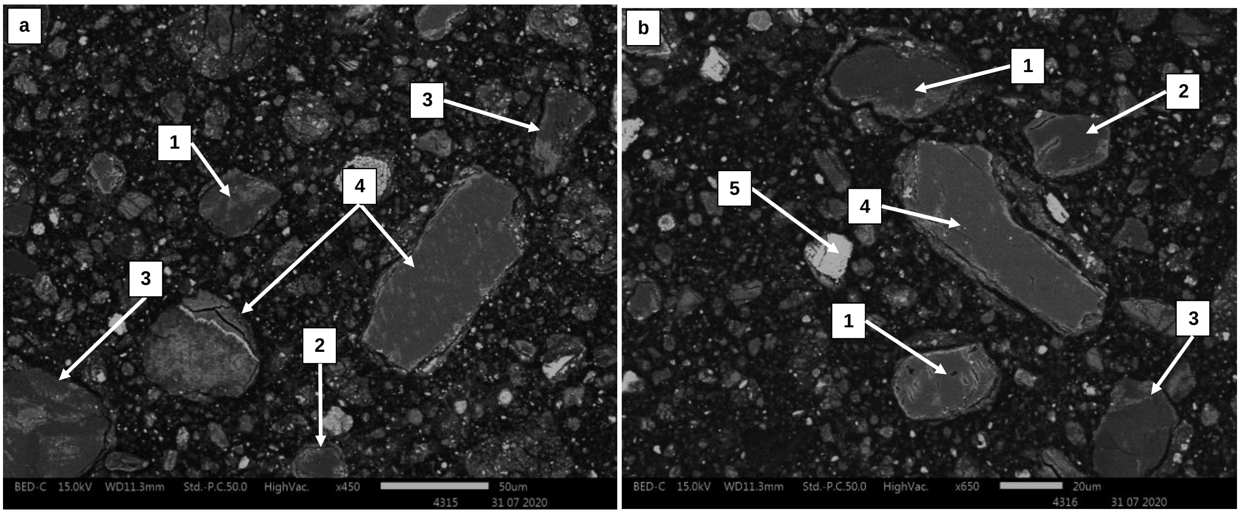

Figure 70: Back-scattered electron images of −6.3 mm fraction: (a) 50 µm and (b) 20 µm, where (1) forsterite; (2) quartz; (3) lizardite; (4) hornblende; (5) iron oxide

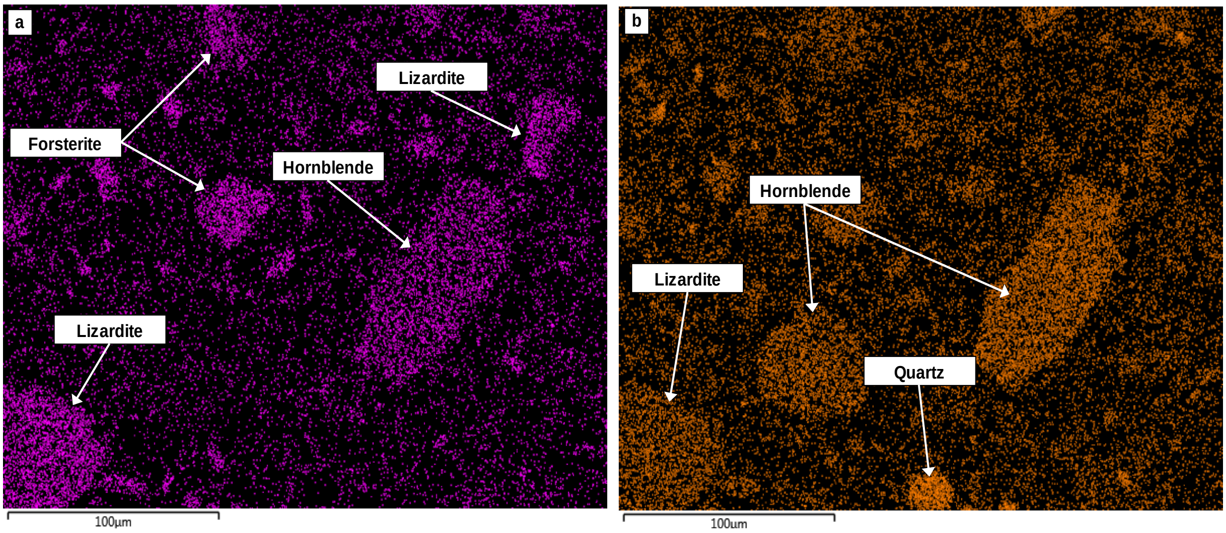

Figure 71: X-ray maps of major elements present in −6.3 mm fraction; (a) Mg, (b) Si (Figure 87(a))

Feed ore top size −12.5 mm

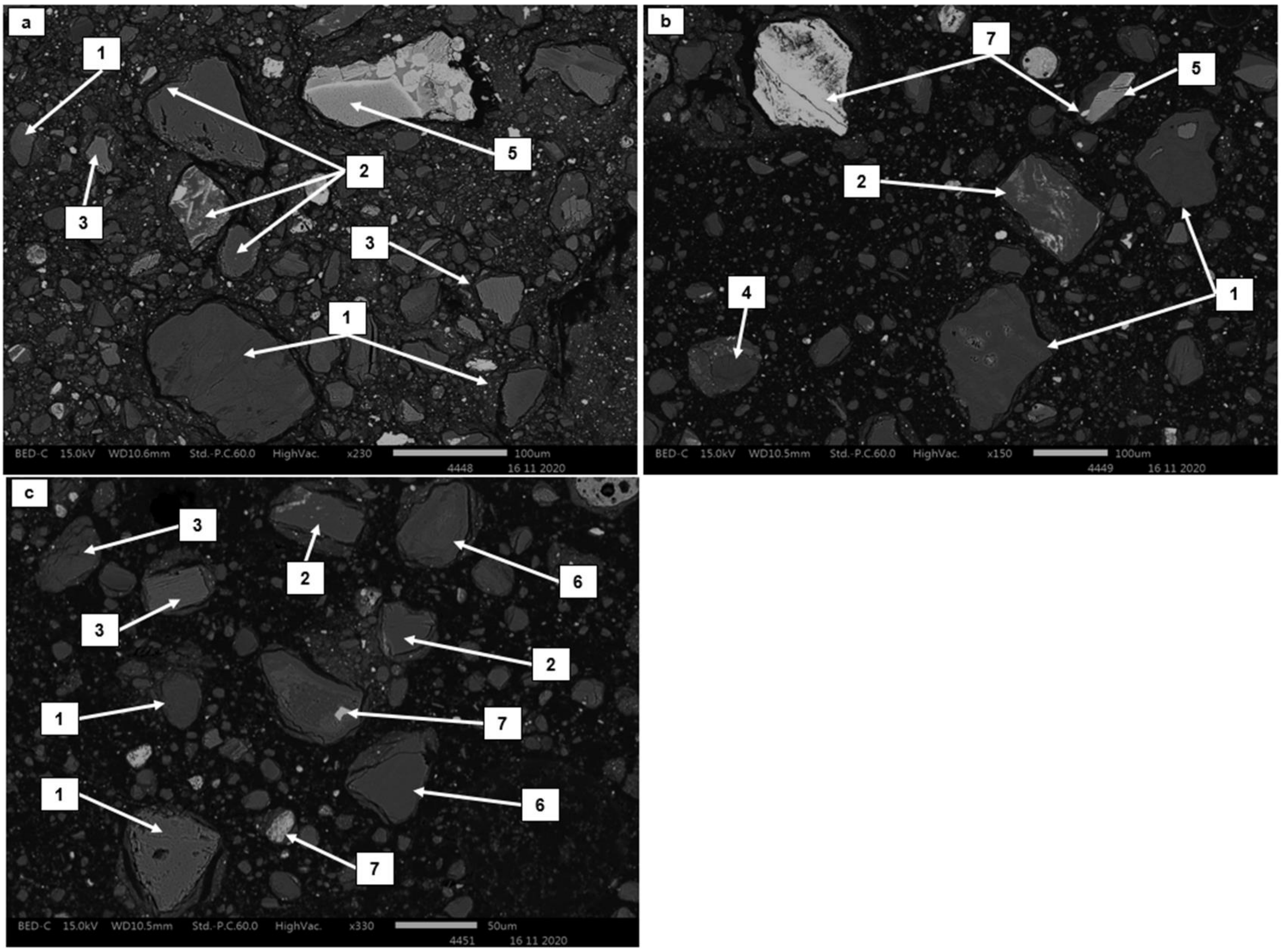

Figure 72: Back-scattered electron images of a portion of −12.5 mm fraction: (1) forsterite; (2) quartz; (3) hornblende; (4) chlorite; (5) spinel; (6) enstatite; (7) hematite

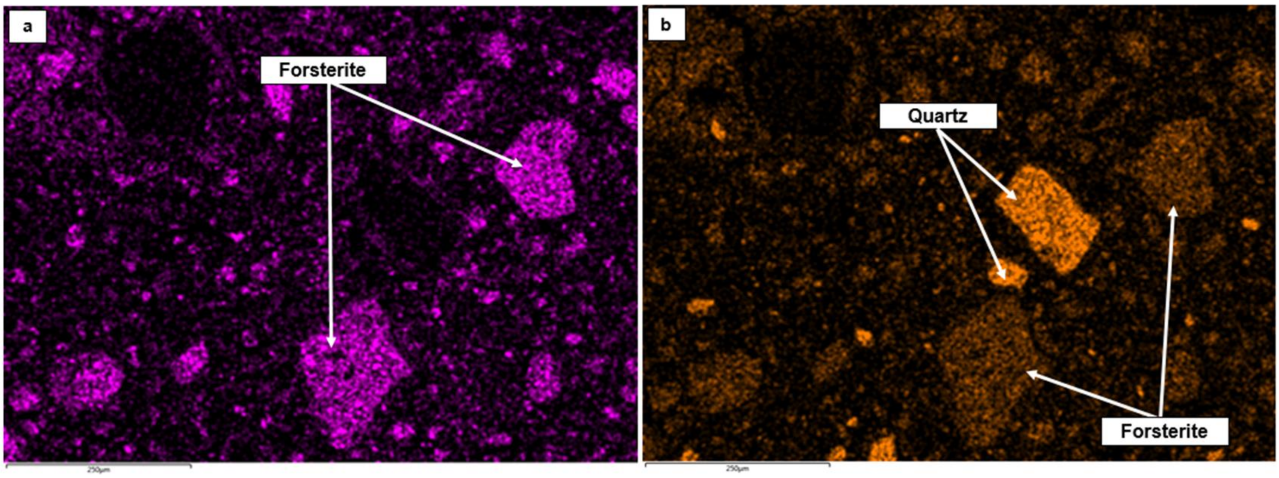

Figure 73: X-ray maps of major elements present in −12.5 mm fraction: (a) Mg; (b) Si (Figure 72(b))

Appendix 3: Energy-Dispersive Spectroscopy and Stoichiometric Analysis of Phases Present in Feeds

Run-of-mine

Table 47: Energy-dispersive spectroscopy compositions of major phases found in run-of-mine sample

Element →	**O**		**Mg**		**Al**		**Si**		**Fe**		**Ni**		**Stoichiometry**
Phase ↓	mass%	at%	mass%	at%	mass%	at%	mass%	at%	mass%	at%	mass%	at%	
Chlorite	48.7	60.9	22.8	19.8	7.06	5.02	15.8	10.9	3.38	1.90	1.44	0.51	$(Mg_{11.1}Al_{2.81}Fe_{1.06}Ca_{0.50}Ni_{0.29})Si_{6.09}O_{34.1}$
Enstatite	44.8	59.6	21.2	17.1	0.80	0.63	23.0	18.9	7.27	3.27	2.88	0.55	$(Mg_{0.85}Fe_{0.16}Al_{0.03}Ni_{0.03})Si_{0.95}O_{2.98}$
Forsterite	44.9	58.3	26.8	23.9	0.46	0.35	21.6	15.3	5.31	1.98	1.27	0.45	$(Mg_{1.67}Fe_{0.14}Ni_{0.03})Si_{1.07}O_{4.08}$
Hornblende	45.6	60.3	12.4	8.80	6.08	3.55	22.4	17.2	2.79	4.01	-	-	$Na_{0.52}Ca_{1.79}(Mg_{3.46}Fe_{1.58}Al_{1.40}Cr_{0.1})Si_{6.76}O_{23.7}$
Iron oxide	31.0	60.1	0.8	0.98	4.64	5.075	1.07	1.15	65.77	36.80	1.52	0.76	$(Fe_{2.53}Al_{0.35}Mn_{0.14}Si_{0.1}Mg_{0.07}Cr_{0.06}Ni_{0.05})O_3$
Lizardite	45.6	60.3	22.7	20.9	1.03	0.82	20.4	15.0	7.93	2.71	2.56	1.32	$(Mg_{2.93}Fe_{0.38}Ni_{0.18}Al_{0.11})Si_{2.10}O_{8.44}$
Quartz	52.1	66.2	1.90	1.58	0.88	0.66	44.1	31.9	2.02	0.74	-	-	$Si_{0.96}O_{2.0}$
Talc	46.8	61.3	20.9	16.3	1.24	0.95	26.2	20.2	4.64	1.21	-	-	$(Mg_{3.09}Fe_{0.23}Al_{0.18}Ca_{0.02})Si_{3.84}O_{11.64}$

Table 48: Energy-dispersive spectroscopy composition of amorphous phase in run-of-mine sample

Component, mass%												
MgO	SiO_2	Fe_2O_3	Al_2O_3	NiO	Cr_2O_3	K_2O	CaO	MnO	TiO_2	V_2O_5	P_2O_5	**Total**
18.8	38.5	34.0	0.62	4.13	3.24	0.09	0.09	0.22	0.22	0.04	0.04	**100**

Feed ore top size −6.3 mm

Table 49: Energy-dispersive spectroscopy compositions of major phases in −6.3 mm feed

Element →	**O**		**Mg**		**Al**		**Si**		**Fe**		**Ni**		**Stoichiometry**
Phases ↓	mass%	at%	mass%	at%	mass%	at%	mass%	at%	mass%	at%	mass%	at%	
Chlorite	48.6	64.0	22.8	19.7	5.24	3.10	15.62	9.80	5.53	1.98	2.21	1.80	$(Mg_{11}Al_{1.74}Fe_{1.11}Ni_{1.01})Si_{5.49}O_{35.8}$
Enstatite	46.1	59.8	25.7	16.5	0.81	1.66	21.4	18.0	5.43	2.87	-	-	$(Mg_{0.83}Fe_{0.14}Al_{0.08})Si_{0.90}O_{2.99}$
Forsterite	44.7	58.2	28.4	24.3	-	-	20.4	15.1	6.27	2.34	1.22	0.44	$(Mg_{1.70}Fe_{0.16})Si_{1.06}O_{4.07}$
Hornblende	45.6	60.3	12.7	5.70	2.96	22.8	22.8	18.2	2.52	2.69	-	-	$Na_{0.58}K_{0.06}Ca_{1.57}(Mg_{3.97}Fe_{1.05}Al_{1.16})Si_{7.12}O_{23.6}$
Iron oxide (hematite+ magnetite)	32.0	59.3	6.13	7.10	1.29	1.44	2.79	3.01	57.5	30.4	2.50	1.28	$(Fe_{1.59}Mg_{0.36}Si_{0.15}Ni_{0.06}Cr_{0.04})O_{2.97}$ $/(Fe_{2.09}Mg_{0.49}Si_{0.21}Al_{0.10}Ni_{0.09}Cr_{0.06})O_{4.08}$
Lizardite	44.3	58.8	24.5	21.4	0.51	0.40	21.0	15.9	8.49	3.24	1.50	0.54	$(Mg_{3.00}Fe_{0.45}Ni_{0.08}Al_{0.06})Si_{2.20}O_{8.23}$
Quartz	51.9	66.4	0.35	0.31	0.19	0.15	43.9	31.9	4.10	1.60	-	-	$Si_{0.96}O_{1.99}$

Table 50: Composition of amorphous phase in −6.3 mm feed

Component, mass%																	
MgO	SiO_2	Fe_2O_3	Al_2O_3	NiO	Cr_2O_3	K_2O	CaO	MnO	TiO_2	V_2O_5	P_2O_5	NaO	ZrO_2	Co_3O_4	ZnO	BaO	**Total**
18.1	30.5	33.3	8.23	3.91	2.40	0.09	0.68	1.14	0.22	0.03	0.03	0.46	0.031	0.2	0.1	0.55	**100**

Feed ore top size −12.5 mm

Table 51: Energy-dispersive spectroscopy compositions of major phases in −12.5 mm feed

Elements →	**O**		**Mg**		**Al**		**Si**		**Fe**		**Ni**		**Stoichiometry**
Phases ↓	mass%	at%	mass%	at%	mass %	at%	mass%	at%	mass%	at%	mass %	at%	
Chlorite	48.5	60.4	23.4	19.2	3.70	1.68	18.3	13.0	4.75	1.69	1.37	0.47	$(Mg_{10.7}Al_{2.95}Fe_{0.95}Ni_{0.26})Si_{7.26}O_{33.8}$
Enstatite	45.3	59.2	22.8	15.7	-	-	24.8	19.5	5.43	3.05	1.72	2.54	$(Mg_{0.79}Fe_{0.15}Ni_{0.13})Si_{0.97}O_{2.96}$
Forsterite	44.3	58.0	27.1	24.1	-	-	21.5	15.2	6.31	2.37	1.32	0.48	$(Mg_{1.69}Fe_{0.17}Ni_{0.03})Si_{1.06}O_{4.06}$
Hornblende	44.0	59.9	10.5	10.9	4.34	3.50	23.1	17.1	6.54	3.26	2.52	1.02	$(Na_{0.68}K_{0.05})Ca_{1.37}(Mg_{4.26}Fe_{1.28}Al_{1.37}Ni_{0.4}Mn_{0.07})Si_{6.73}O_{23.5}$
Hematite	24.7	51.7	4.23	5.24	3.88	4.64	1.91	2.10	67.9	41.3	1.95	0.98	$(Fe_{2.07}Mg_{0.26}Al_{0.23}Cr_{0.20}Si_{0.11}Ni_{0.05})O_{2.58}$
Lizardite	44.3	58.4	25.2	21.8	-	-	22.3	16.7	5.90	2.24	2.37	0.85	$(Mg_{3.06}Fe_{0.31}Ni_{0.12})Si_{2.34}O_{8.17}$
Quartz	52.5	66.4	0.49	0.40	-	-	42.1	32.8	1.65	0.66	-	-	$Si_{0.99}O_{1.99}$
Talc	46.4	60.0	20.4	17.4	1.65	1.27	26.2	19.3	4.94	1.83	-	-	$(Mg_{3.31}Fe_{0.35}Al_{0.24}Ca_{0.11})Si_{3.67}O_{11.40}$

Table 52: Energy-dispersive spectroscopy composition of amorphous phase in −12.5 mm feed

Component, mass%															
MgO	SiO_2	Fe_2O_3	Al_2O_3	NiO	Cr_2O_3	K_2O	CaO	MnO	TiO_2	NaO	ZnO	CuO	WO_3	Co_3O_4	**Total**
44.4	25.4	21.7	2.60	1.97	1.72	0.06	1.00	0.63	0.09	0.09	0.03	0.06	0.063	0.2	**100**

Table 53: Energy-dispersive spectroscopy composition of spinel mineral in −12.5 mm feed

Element →	**Stoichiometry**	**O**		**Mg**		**Al**		**Fe**		**Cr**	
Mineral group		mass%	at%	mass%	at%	mass%	at%	mass%	at%	mass%	at%
Spinel	$(Mg_{0.87}Fe^{2+}_{0.13})(Al_{1.38}Cr_{0.32}Fe^{3+}_{0.15})O_{4.14}$	40.6	57.4	13.1	12.0	22.4	19.1	9.36	3.85	10.3	4.60

Appendix 4: Green Briquette Results

Green briquette compressive strength

Table 54: Green briquette compressive strength and yield at top size of −6.3 mm

Moisture, %	Curing condition	Density, g/cm^3	Average drop number		Average compressive strength, N	
			Individual test	Moisture specific	Individual test	Moisture specific
16	Open	2.751	20.4	19.1	522	430
16	Closed	2.832	17.8		339	
24	Open	2.421	12.8	11.1	81	94
24	Closed	2.511	9.40		107	

Table 55: Green briquette compressive strength and yield at top size of −12.5 mm

Moisture, %	Curing condition	Density, g/cm^3	Average drop number		Average compressive strength, N	
			Individual test	Moisture specific	Individual test	Moisture specific
16	Open	2.455	3	2.6	92.7	86.1
16	Closed	2.255	2.2		79.4	
24	Open	2.41	1.75	1.63	90.1	77.5
24	Closed	2.357	1.50		65	

Appendix 5: Tumble Index and Abrasion Index Test Results

Tumble strength and abrasion index

Table 56: Tumble and abrasion index results at a briquette ore top size of −6.3 mm

Moisture, %	Curing condition	TI % > 6.3 mm	Average TI Moisture specific	AI % < 0.5 mm	Average AI Moisture specific
16	Open	95.5	93.4	3.63	4.99
16	Closed	91.4		6.35	
24	Open	89.2	87.1	6.07	6.82
24	Closed	85		7.58	

Table 57: Tumble and abrasion index results at briquette ore top size of −12.5 mm

Moisture, %	Curing condition	TI % > 6.3 mm	Average TI Moisture specific	AI % < 0.5 mm	Average AI Moisture specific
16	Open	40.3	40.5	13	13.4
16	Closed	40.7		13.7	
24	Open	35.2	41.9	13.1	14.7
24	Closed	48.5		16.2	

Density and volume analysis

Table 58: Density and volume analysis results at a briquette ore top size of −6.3 mm

Moisture, %	Curing condition	Green briquette		RI briquette*		Average, %	
		Volume, cm^3	Density, g/cm^3	Volume, cm^3	Density, g/cm^3	Volume shrinkage	Density increase
16	Open	7.29	2.75	5.31	3.16	24.8	11.9
16	Closed	7.10	2.83	5.51	3.08		
24	Open	7.81	2.42	5.05	3.36	32.2	30.4
24	Closed	7.60	2.51	5.39	3.07		

*RI: Reproducibility index

Appendix 6: Reducibility Index

Temperature and gas profiles

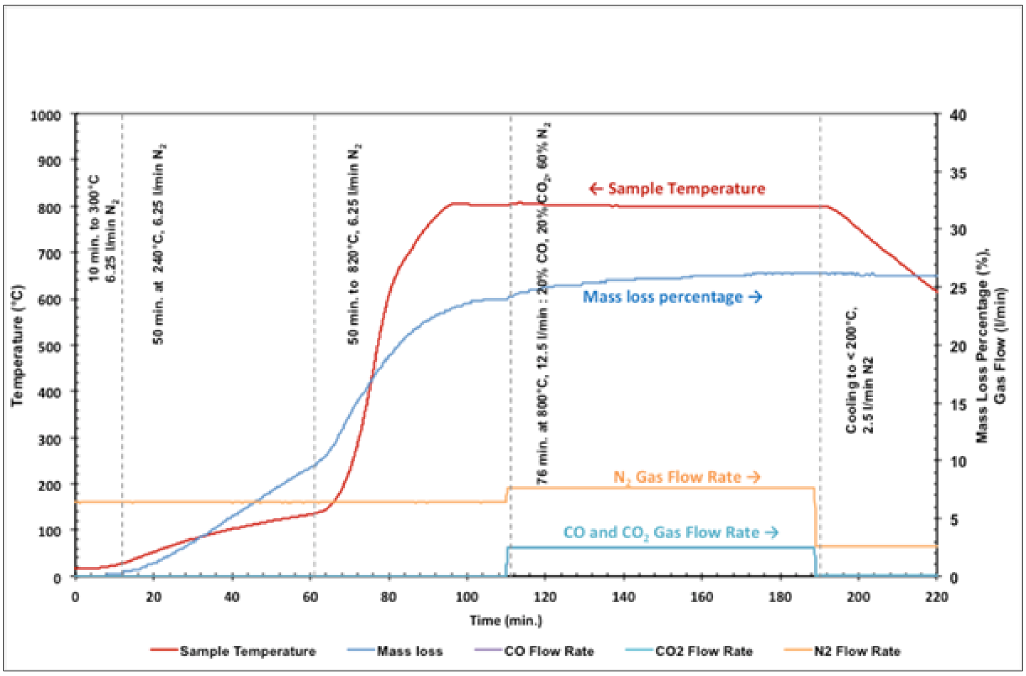

Figure 74: Reproducibility index test of briquettes produced from ore top size −6.3 mm, 16% moisture content, open curing conditions

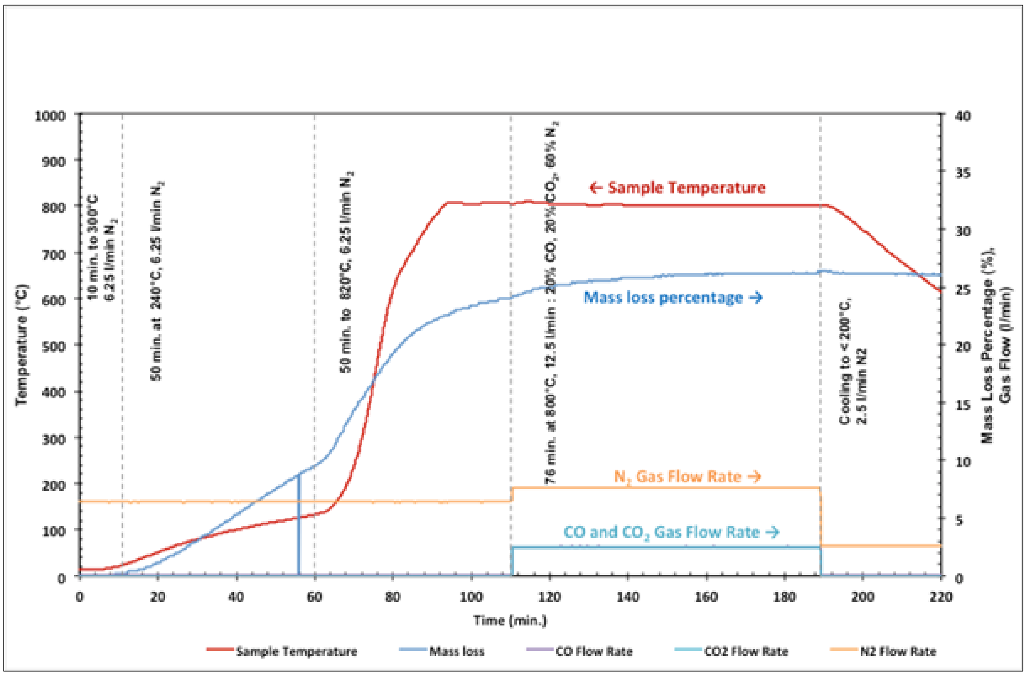

Figure 75: Reducibility index test of briquettes produced from ore top size −6.3 mm, 16% moisture content, closed curing conditions

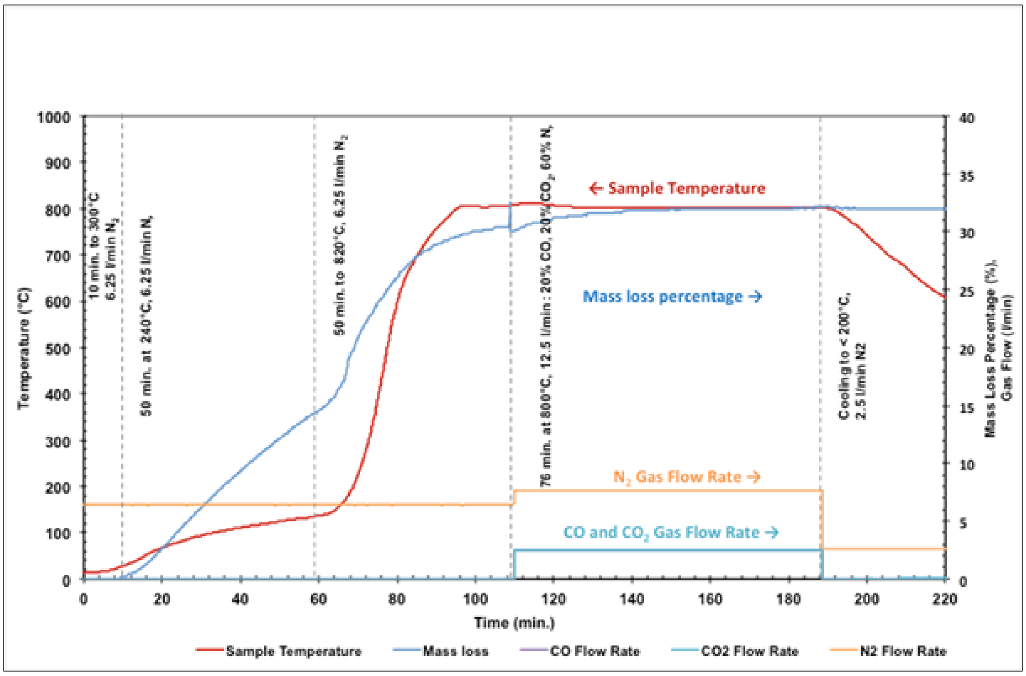

Figure 76: Reducibility index test of briquettes produced from ore top size −6.3 mm, 24% moisture content, open curing conditions

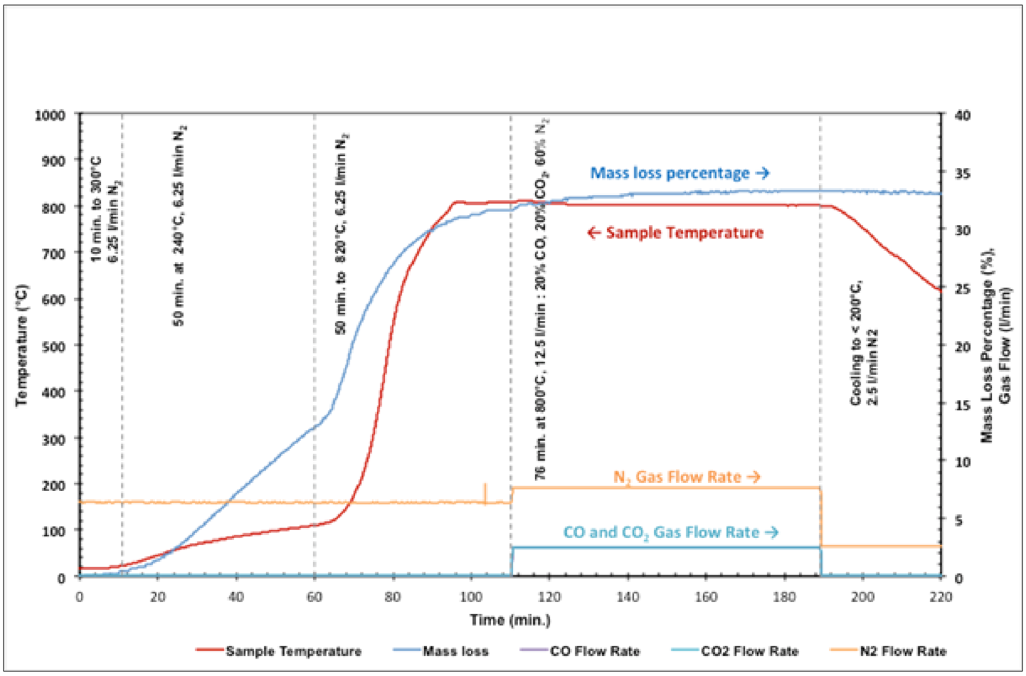

Figure 77: Reducibility index test of briquettes produced from ore top size −6.3 mm, 24% moisture content, closed curing conditions

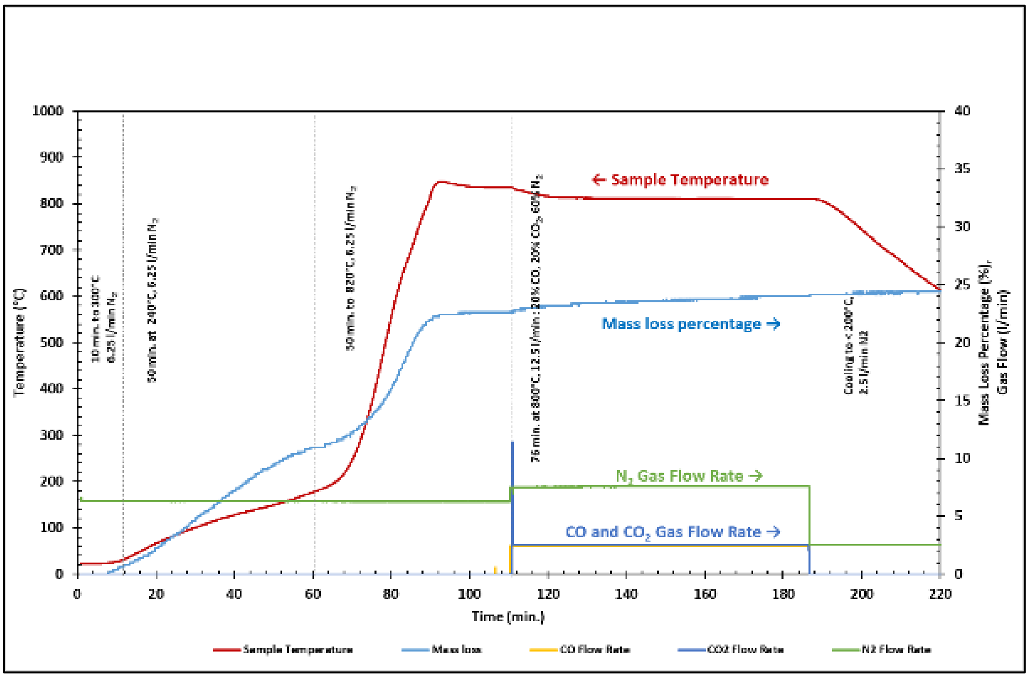

Figure 78: Reducibility index test of briquettes produced from ore top size −12.5 mm, 16% moisture content, open curing conditions

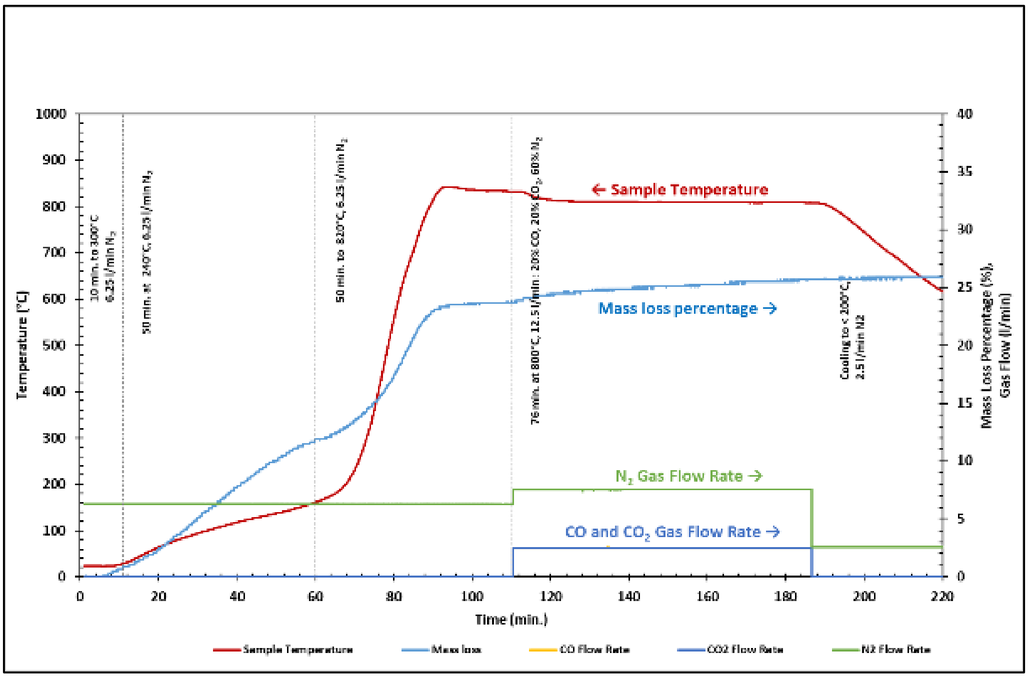

Figure 79: Reducibility index test of briquettes produced from ore top size −12.5 mm, 16% moisture content, closed curing conditions

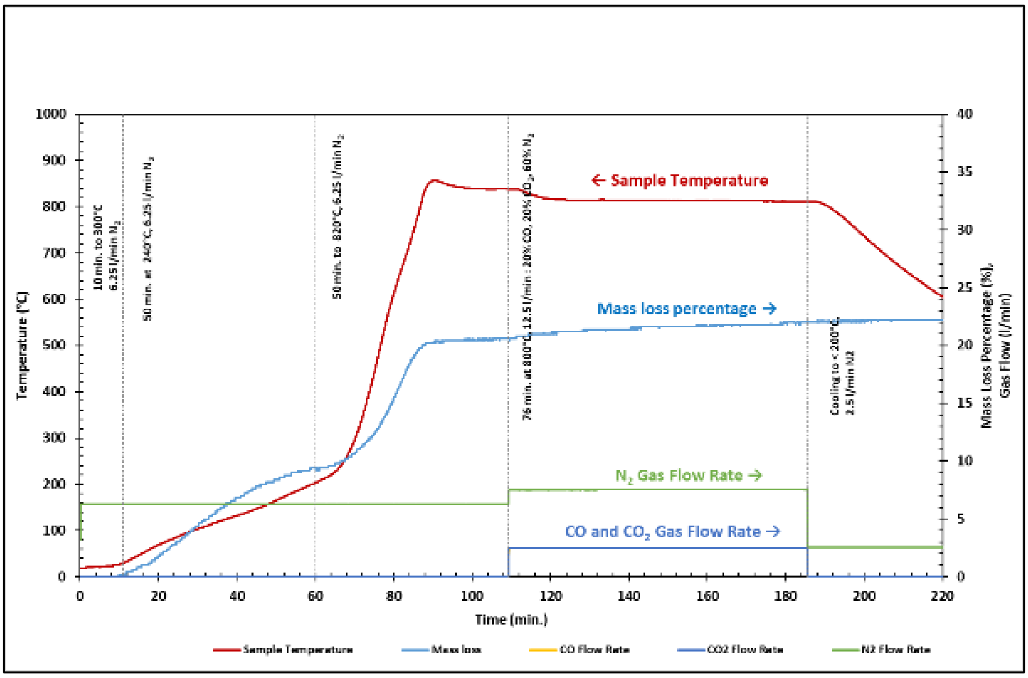

Figure 80: Reducibility index test of briquettes produced from ore top size −12.5 mm, 24% moisture content, open curing conditions

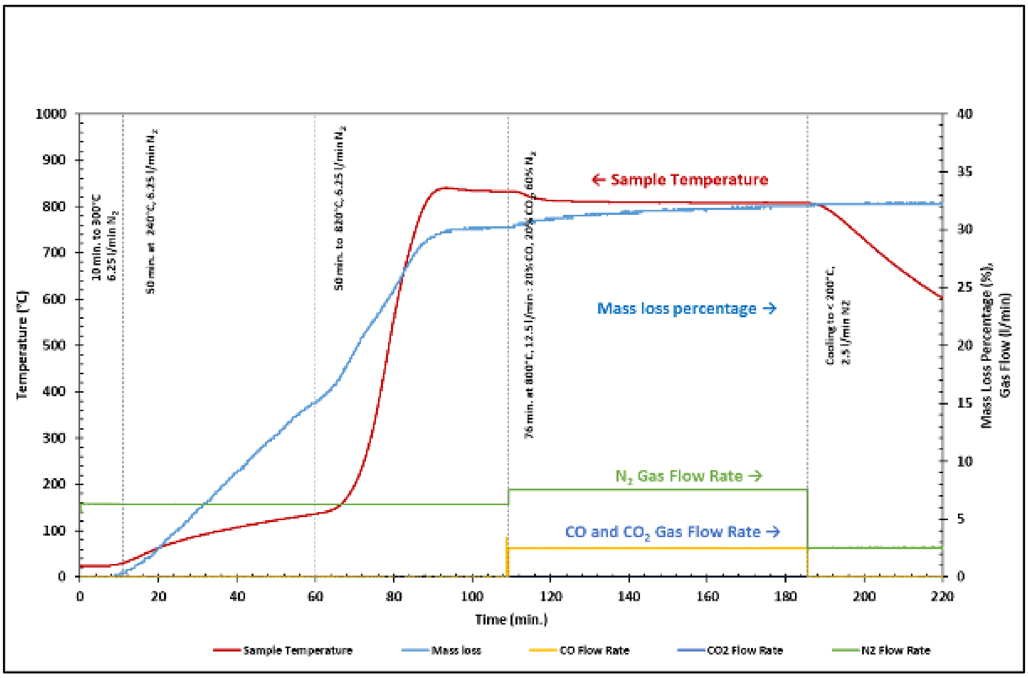

Figure 81: Reducibility index test of briquettes produced from ore top size −12.5 mm, 24% moisture content, closed curing conditions

Degree of reduction analysis

Table 59: Reduction analysis of briquettes produced from ore top size of −6.3 mm

Sample ID	Mass loss per stage, g				Reduction, %
	Drying	Calcine	Reduction	Total*	
16% Open curing	48.9	73.00	11.00	132.90	33.40
16% Closed curing	48.4	72.60	11.00	132.00	33.40
24% Open curing	76	77.00	10.20	163.20	30.90
24% Closed curing	65	94.00	8.00	167.00	24.30

*Total = ∑ Drying, Calcine, Reduction

Table 60: Reduction analysis of briquettes produced from ore top size of −12.5 mm

Sample ID	Mass loss per stage, g				Reduction, %
	Drying	Calcine	Reduction	Total*	
16% Open curing	55	58.00	7.00	120.00	32.80
16% Closed curing	58.5	60.00	10.00	128.00	46.90
24% Open curing	47	56.00	7.00	110.00	32.80
24% Closed curing	75	76.00	9.00	160.00	42.20

*Total = ∑ Drying, Calcine, Reduction

X-ray fluorescence analysis

Table 61: X-ray fluorescence analysis of briquettes produced from ore top size of −6.3 mm

Component, mass %				
	16% Open curing	16% Closed curing	24% Open curing	24% Closed curing
SiO_2	42.2	42.5	42.3	42.2
Al_2O_3	4.63	4.59	4.49	4.60
Fe_2O_3	26.7	27.0	27.0	27.1
TiO_2	0.09	0.09	0.08	0.09
CaO	0.74	0.79	0.67	0.69
MgO	21.1	20.5	20.8	20.7
K_2O	< 0.05	<0.05	< 0.05	< 0.05
MnO	0.41	0.42	0.42	0.42
P	< 0.05	< 0.05	< 0.05	< 0.05
BaO	0.01	0.01	0.01	0.01
Co_3O_4	0.08	0.08	0.08	0.08
Cr_2O_3	1.35	1.32	1.26	1.29
CuO	< 0.005	< 0.005	< 0.005	< 0.005
NiO	2.69	2.68	2.74	2.76
PbO	< 0.005	< 0.005	< 0.005	0.01
Sr	< 0.005	< 0.005	< 0.005	< 0.005
V_2O_5	0.01	0.01	0.01	0.01
ZnO	0.04	0.04	0.04	0.04
LOI	−0.85	−0.59	−0.85	−1.09

Table 62: X-ray fluorescence analysis of briquettes produced from ore top size of −12.5 mm

Component, mass %				
	16% Open curing	16% Closed curing	24% Open curing	24% Closed curing
SiO_2	46.7	47.7	47.8	44.1
Al_2O_3	2.73	2.71	2.68	3.68
Fe_2O_3	17.2	17.3	16.9	22.5
TiO_2	0.05	0.04	0.04	0.06
CaO	0.80	0.74	0.62	0.72
MgO	29.1	28.1	28.5	24.9
K_2O	< 0.05	< 0.05	< 0.05	< 0.05
MnO	0.25	0.23	0.24	0.35
P	< 0.05	< 0.05	< 0.05	<0.05
BaO	0.01	0.01	0.01	0.01
Co_3O_4	0.05	0.04	0.04	0.06
Cr_2O_3	0.90	0.83	0.83	1.10
CuO	< 0.005	< 0.005	< 0.005	< 0.005
NiO	2.22	2.24	2.29	2.50
PbO	< 0.005	< 0.005	0.01	< 0.005
Sr	< 0.005	< 0.005	< 0.005	< 0.005
V_2O_5	0.01	0.01	0.01	0.01
ZnO	0.02	0.02	0.02	0.03
LOI	−0.31	−0.41	−0.29	−0.81

X-ray diffraction analysis

Table 63: X-ray diffraction analysis of briquette produced from ore top size of −6.3 mm

Phase ID	Mineral mass, %			
	16 % Moisture		24% Moisture	
	Open curing	Closed curing	Open curing	Closed curing
Amorphous	13.6	26.7	28.9	37.3
Diopside	8.38	5.52	6.61	4.16
Enstatite	28.4	29.2	24.4	20.7
Forsterite	36.2	27.5	28.6	23.2
Hornblende	4.56	3.48	2.55	4.75
Magnetite	3.50	1.71	3.62	4.00
Quartz	5.44	5.81	5.34	5.87

Table 64: X-ray diffraction analysis of briquette produced from ore top size of −12.5 mm

Phase ID	Mineral mass, %			
	16 % Moisture		24% Moisture	
	Open curing	Closed curing	Open curing	Closed curing
Amorphous	23.5	20.3	15.6	14.5
Enstatite	12.0	16.5	22.0	15.6
Forsterite	40.6	44.3	37.2	47.2
Hornblende	7.00	3.20	5.60	5.80
Magnetite	6.57	8.20	6.60	9.68
Quartz	10.3	7.50	13.0	7.20

Back-scattered electron imaging and X-ray mapping analysis

Briquette Ore Top Size −6.3 mm

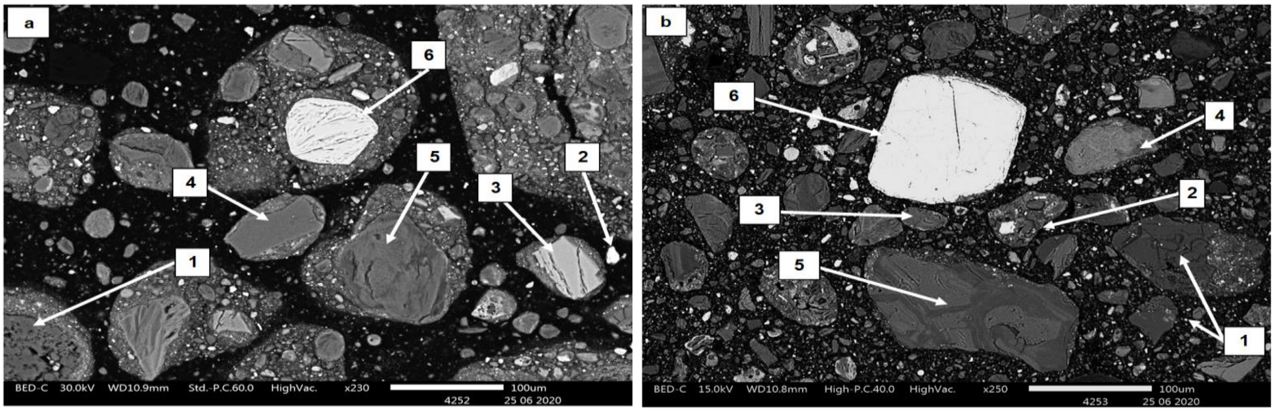

Figure 82: Back-scattered electron imaging of reduced briquettes: (a) 16% moisture content under open curing, (b) 16% moisture content under closed curing, where (1) quartz; (2) magnetite; (3) hornblende; (4) diopside; (5) forsterite; (6) spinel mineral; (7) enstatite

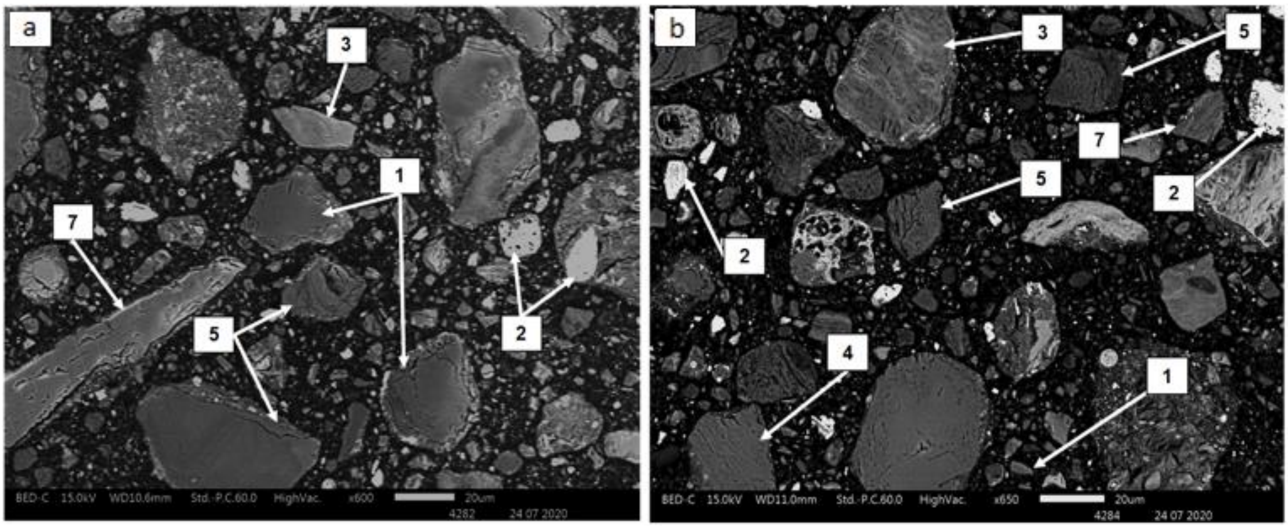

Figure 83: Back-scattered electron imaging of reduced briquettes: (a) 24% moisture content under open curing, (b) 24% moisture content under closed curing, where (1) quartz; (2) magnetite; (3) hornblende; (4) diopside; (5) forsterite; (6) spinel mineral; (7) enstatite

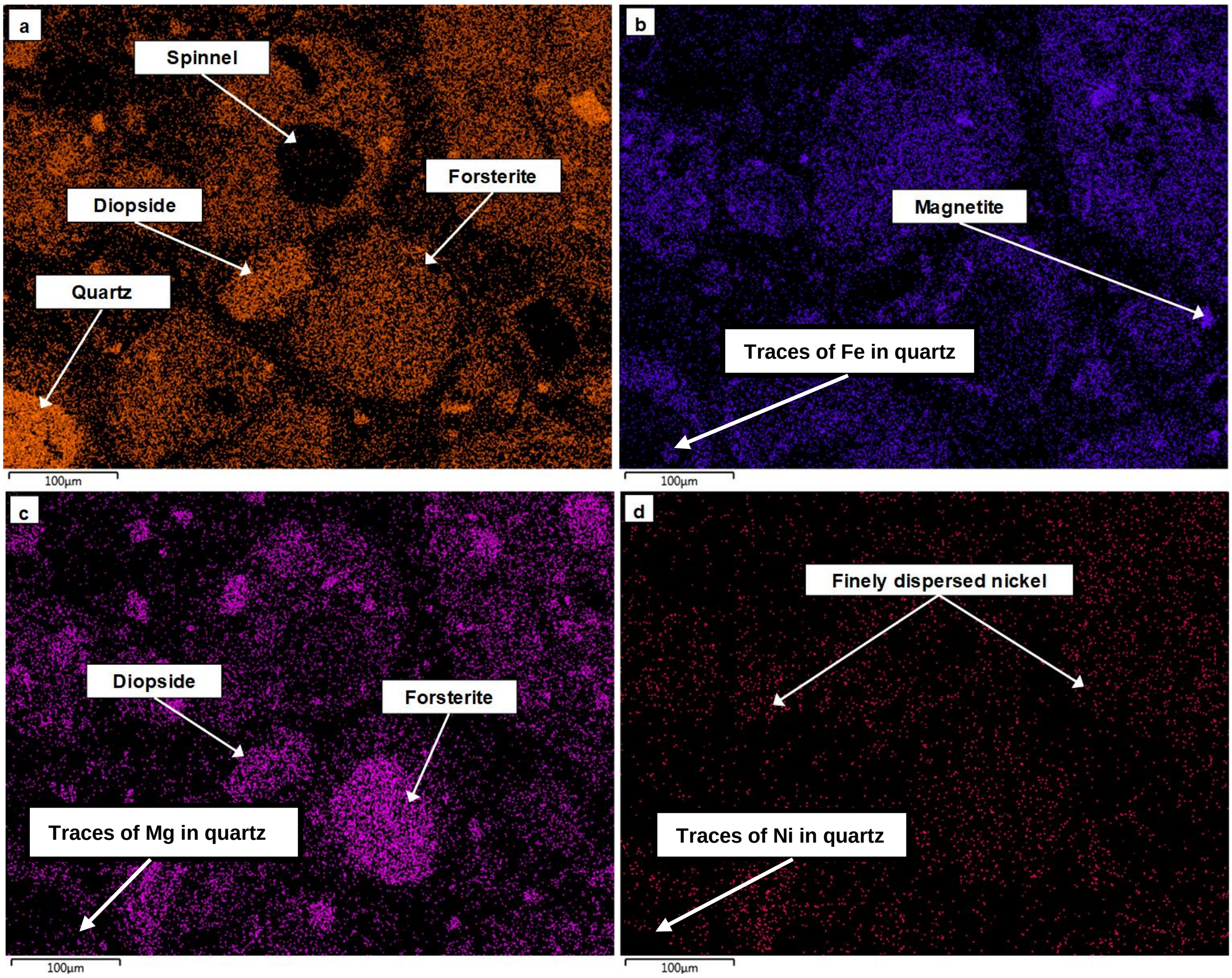

Figure 84: X-ray mapping analysis of major elements present in briquettes after reducibility index test: 16% moisture content under open curing conditions: (a) Si; (b) Fe; (c) Mg; (d) Ni; (e) Al (BEI in Figure 82(a))

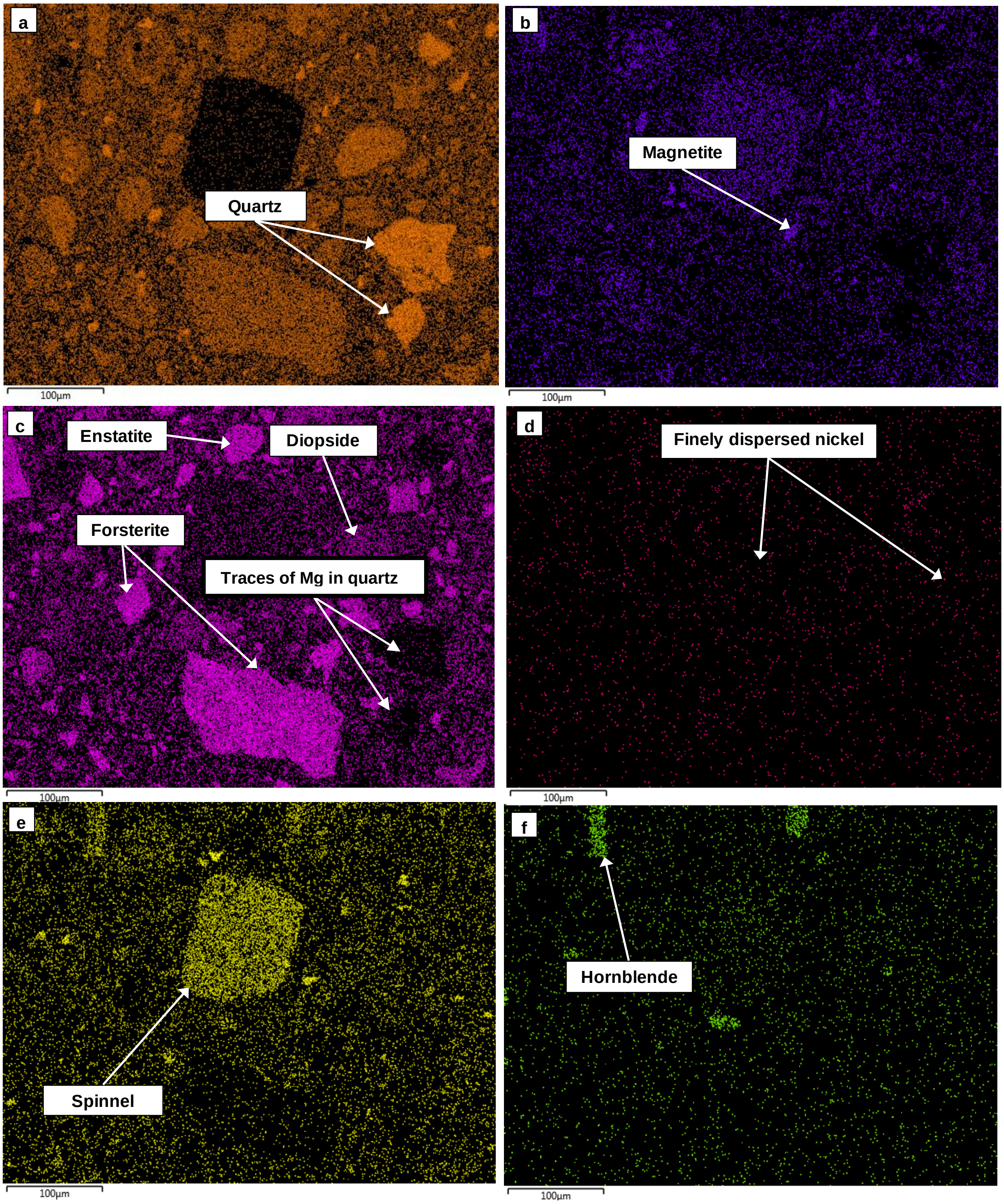

Figure 85: X-ray mapping analysis of major elements present in briquettes after reducibility index testing: 24% moisture content under open curing conditions: (a) Si; (b) Fe; (c) Mg; (d) Ni; (e) Al; (f) Ca (BEI in Figure 82(b))

Briquette Ore Top Size −12.5 mm

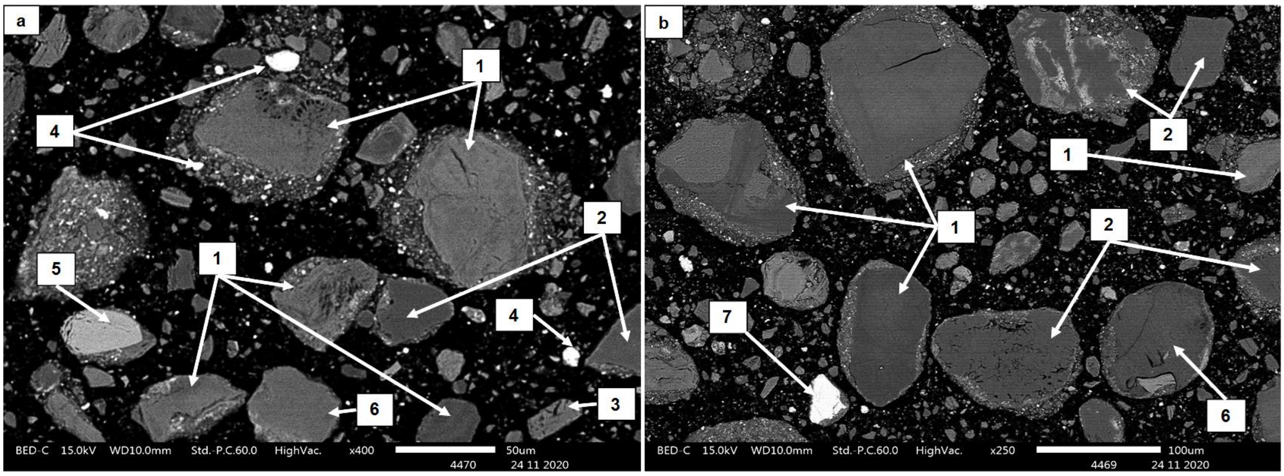

Figure 86: Back-scattered electron imaging of reduced briquettes at 16% moisture content under closed curing conditions: (1) forsterite; (2) quartz; (3) hornblende; (4) magnetite; (5) spinel; (6) enstatite; (7) wustite

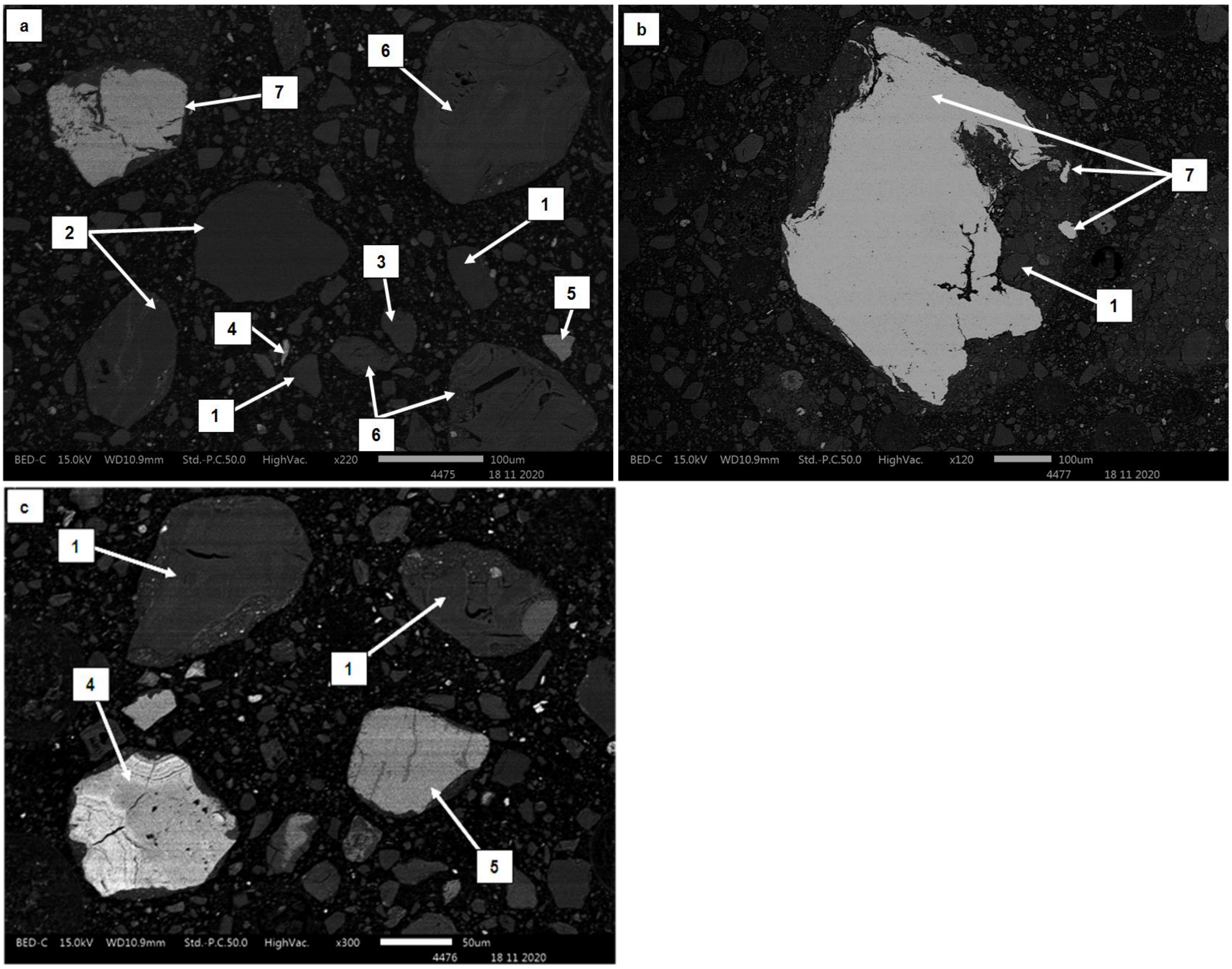

Figure 87: Back-scattered electron imaging of reduced briquettes at 16% moisture content under open curing conditions: (1) forsterite; (2) 1quartz; (3) hornblende; (4) magnetite; (5) spinel; (6) enstatite; (7) wustite

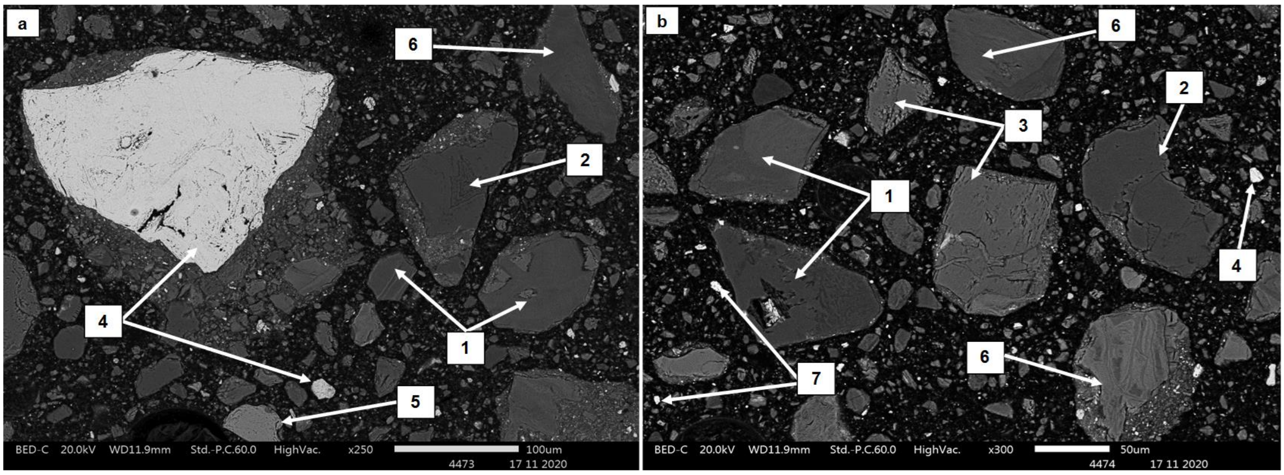

Figure 88: Back-scattered electron imaging of reduced briquettes at 24% moisture content under open curing conditions: (1) forsterite; (2) quartz; (3) hornblende; (4) magnetite; (5) spinel; (6) enstatite; (7) wustite

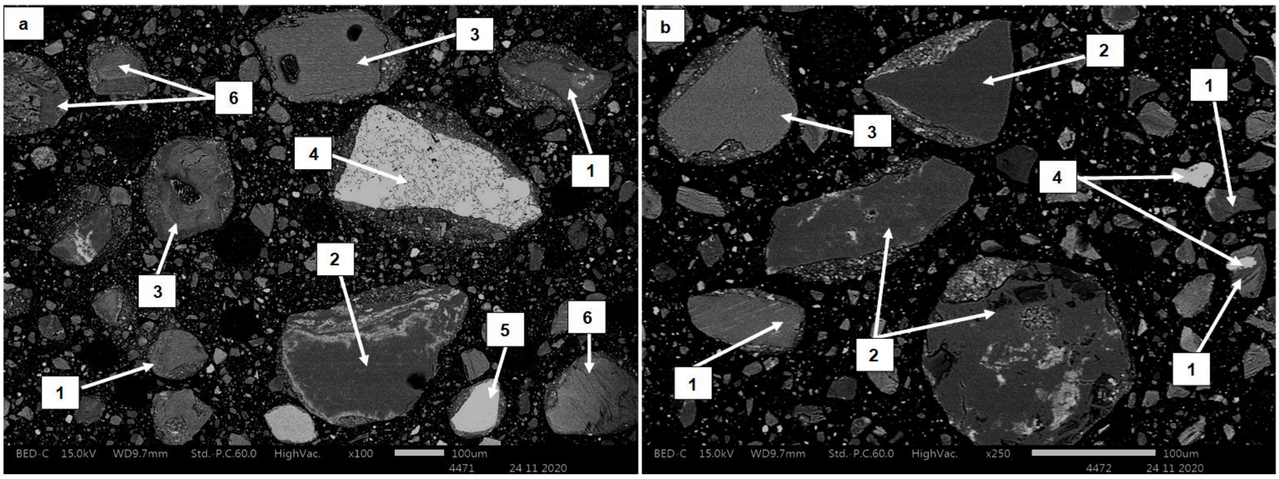

Figure 89: Back-scattered electron imaging of reduced briquettes at 24% moisture content under closed curing conditions: (1) forsterite; (2) quartz; (3) hornblende; (4) magnetite; (5) spinel; (6) enstatite

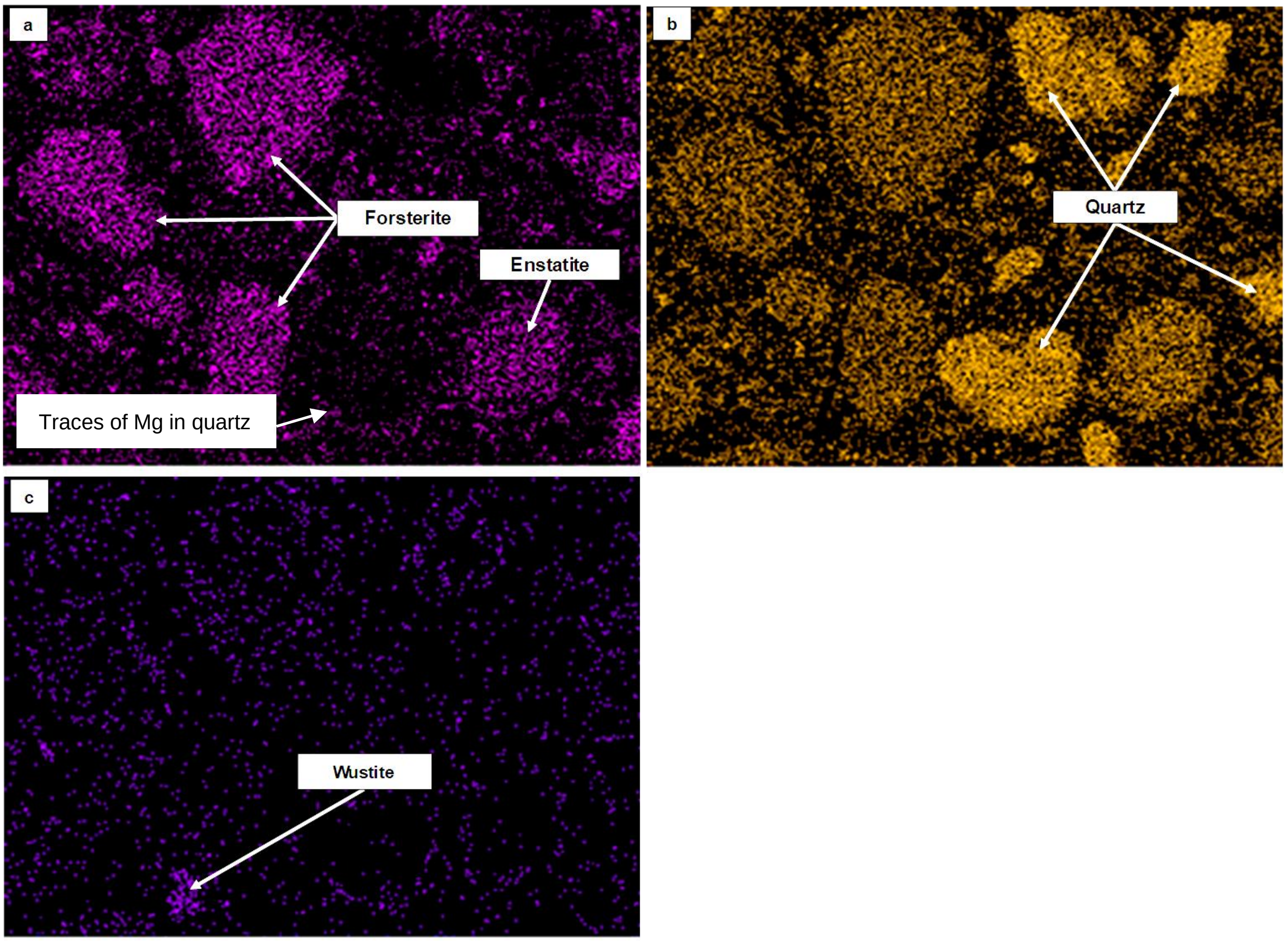

Figure 90: X-ray mapping analysis of major elements present in reduced briquettes at 16% moisture content under closed curing conditions: (a) Mg; (b) Si; (c) Fe (BEI in Figure 86(b))

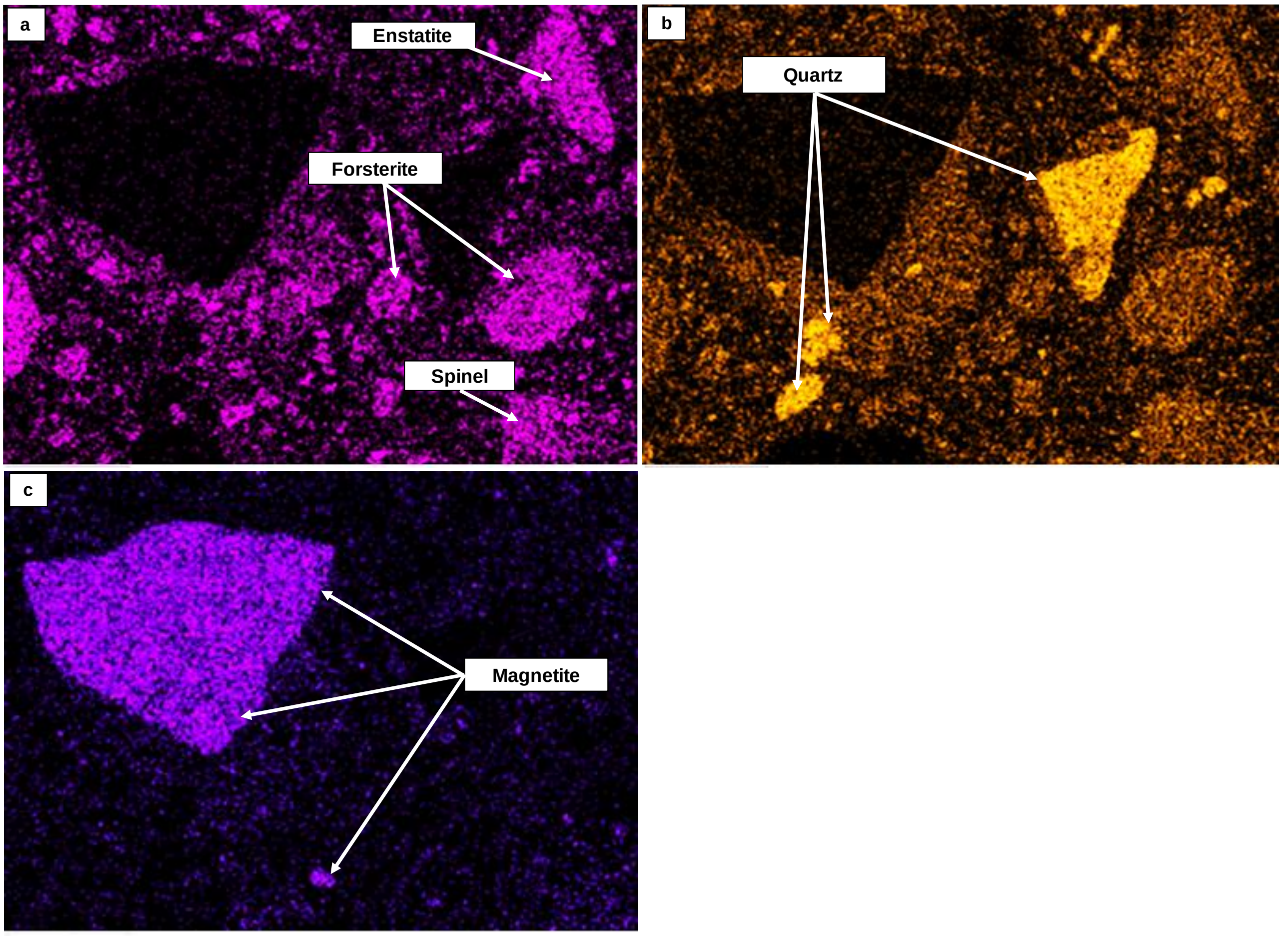

Figure 91:X-ray mapping analysis of major elements present in reduced briquettes at 24% moisture content under open curing conditions: (a) Mg; (b) Si; (c) Fe (BEI in Figure 88(a))

Energy-dispersive spectroscopy and stoichiometric analysis

Briquette Ore Top Size −6.3 mm

Table 65: Energy-dispersive spectroscopy compositions of major phases in reduced briquettes at 16% moisture under open curing conditions

Element →	**O**		**Mg**		**Al**		**Si**		**Fe**		**Ni**		**Stoichiometry**
Phase ↓	mass%	at%	mass%	at%	mass%	at%	mass%	at%	mass%	at%	mass%	at%	
Diopside	48.8	63.3	12.6	4.80	3.94	3.03	22.7	18.8	1.86	0.69	0.13	0.04	$Ca_{0.90}(Mg_{0.51}Fe_{0.07}Al_{0.32}Na_{0.07}Cr_{0.03}Ti_{0.01}Ni_{0.004})Si_{2.01}O_{6.79}$
Enstatite	44.3	57.5	27.7	16.1	-	-	22.9	21.1	3.89	4.45	1.17	0.83	$(Mg_{0.81}Fe_{0.22}Ni_{0.04})Si_{1.05}O_{2.88}$
Forsterite	44.3	58.0	26.5	22.8	0.28	0.22	22.0	16.4	5.92	2.22	0.94	0.34	$(Mg_{1.60}Fe_{0.16}Al_{0.02}Ni_{0.02})Si_{1.15}O_{4.06}$
Hornblende	49.3	63.0	14.4	12.0	0.30	0.23	18.5	15.7	5.28	3.47	-	-	$Na_{0.40}Ca_{1.84}(Mg_{4.72}Fe_{1.36}Al_{0.09})Si_{6.17}O_{24.8}$
Iron Oxide	26.9	54.6	-	-	1.43	1.72	3.54	4.09	64.8	37.6	1.17	0.65	$(Fe_{2.63}Si_{0.29}Al_{0.12}Mn_{0.07}Ni_{0.05}Cr_{0.02})O_{3.82}$
Quartz	56.0	69.2	-	-	-	-	43.5	30.6	0.45	0.16	-	-	$Si_{0.92}O_{2.08}$

Table 66: Energy-dispersive spectroscopy compositions of major phases in reduced briquettes at 16% moisture under closed curing conditions

Element →	**O**		**Mg**		**Al**		**Si**		**Fe**		**Ni**		**Stoichiometry**
Phase ↓	mass%	at%	mass%	at%	mass%	at%	mass%	at%	mass%	at%	mass%	at%	
Diopside	47.4	60.3	7.98	7.13	1.20	0.75	24.1	21.8	10.9	5.58	0.98	0.36	$Ca_{0.41}(Mg_{0.76}Fe_{0.60}Al_{0.08}Ni_{0.04})Si_{2.33}O_{6.46}$
Enstatite	46.0	58.7	19.6	14.5	-	-	27.7	23.6	5.79	3.16	0.87	0.31	$(Mg_{1.10}Fe_{0.20}Ni_{0.03})Si_{1.76}O_{2.94}$
Forsterite	45.0	58.4	28.7	24.6	-	-	19.6	14.5	5.54	2.16	0.66	0.26	$(Mg_{1.72}Fe_{0.15}Ni_{0.02})Si_{1.02}O_{4.09}$
Hornblende	48.1	62.7	12.5	10.7	4.54	3.51	22.3	16.5	2.19	0.82	-	-	$Na_{0.37}Ca_{1.71}(Mg_{4.22}Fe_{0.32}Al_{1.38}Cr_{0.32})Si_{6.50}O_{22.6}(O)_2$
Iron Oxide	27.4	56.7	-	-	-	-	0.25	0.29	72.4	43.0	-	-	$(Fe_{3.01}Si_{0.02})O_{3.97}$
Quartz	54.4	68.2	0.27	0.22	-	-	43.9	31.4	0.56	0.21	-	-	$Si_{0.94}O_{2.05}$

Table 67: Energy-dispersive spectroscopy compositions of major phases in reduced briquettes at 24% moisture content under open curing conditions

Element →	**O**		**Mg**		**Al**		**Si**		**Fe**		**Ni**		**Stoichiometry**
Phase ↓	mass%	at%	mass%	at%	mass%	at%	mass%	at%	mass%	at%	mass%	at%	
Diopside	44.3	59.7	12.1	10.7	3.72	2.97	23.6	18.1	2.74	1.06	0.38	0.14	$Ca_{0.67}(Mg_{1.15}Fe_{0.11}Al_{0.32}Na_{0.07}Ni_{0.02})Si_{1.94}O_{6.40}$
Enstatite	46.1	59.6	22.4	19.1	0.84	0.64	25.3	18.6	4.96	1.84	0.65	0.23	$(Mg_{0.96}Fe_{0.09}Al_{0.03}Ni_{0.01})Si_{0.93}O_{2.98}$
Forsterite	44.6	58.0	27.7	23.7	-	-	21.6	16.0	5.30	1.98	1.16	0.41	$(Mg_{1.66}Fe_{0.14}Ni_{0.03})Si_{1.12}O_{4.06}$
Hornblende	47.1	61.6	12.5	10.8	5.50	4.27	22.6	16.8	2.23	0.84	-	-	$Na_{0.45}Ca_{1.67}(Mg_{4.24}Fe_{0.33}Al_{1.68}Cr_{0.09})Si_{6.61}O_{24.2}$
Iron Oxide	25.6	52.4	1.86	2.45	1.85	2.15	3.51	3.97	67.8	40.2	-	-	$(Fe_{2.81}Si_{0.28}Mg_{0.17}Al_{0.15})O_{3.67}$
Quartz	52.5	66.4	0.77	0.64	-	-	45.5	32.8	1.03	0.38	-	-	$Si_{0.98}O_{1.99}$

Table 68: Energy-dispersive spectroscopy compositions of major phases in reduced briquettes at 24% moisture content under closed curing conditions

Element →	**O**		**Mg**		**Al**		**Si**		**Fe**		**Ni**		**Stoichiometry**
Phase ↓	mass%	at%	mass%	at%	mass%	at%	mass%	at%	mass%	at%	mass%	at%	
Diopside	42.0	58.4	12.6	7.49	2.58	1.88	25.3	20.4	5.06	3.89	-	-	$Ca_{0.85}(Mg_{0.80}Fe_{0.42}Al_{0.20})Si_{2.19}O_{6.26}$
Enstatite	44.1	58.0	21.0	15.7	0.86	0.67	26.1	22.6	7.32	2.76	0.67	0.24	$(Mg_{0.79}Fe_{0.14}Al_{0.03}Ni_{0.01})Si_{1.13}O_{2.90}$
Forsterite	44.6	58.0	27.7	23.7	-	-	21.6	16.0	5.05	1.88	1.04	0.37	$(Mg_{1.66}Fe_{0.13}Ni_{0.03})Si_{1.12}O_{4.06}$
Hornblende	43.7	61.7	10.94	8.20	3.33	2.26	23.6	19.4	15.0	6.89	2.10	0.81	$Na_{0.22}Ca_{0.1}(Mg_{3.21}Fe_{2.70}Al_{0.89}Ni_{0.32}Cr_{0.09})Si_{7.60}O_{24.2}$
Iron Oxide	27.7	54.1	1.69	2.1	1.71	2.07	6.34	6.83	60.7	34.4	2.75	1.39	$(Fe_{2.41}Si_{0.48}Al_{0.14}Mg_{0.14}Ni_{0.10}Cr_{0.03})O_{3.79}$
Quartz	52.4	66.2	0.71	0.59	-	-	45.1	32.5	1.88	0.68	-	-	$Si_{0.97}O_{1.99}$

Table 69: Energy-dispersive spectroscopy compositions of spinel minerals

Sample ID	Element →	O		Mg		Al		Fe		Cr	
	Stoichiometry	mass%	at%	mass%	at%	mass%	at%	mass%	at%	mass%	at%
16% Open cure	$(Fe_{0.64}Mg_{0.35})(Cr_{1.36}Al_{0.49})O_{4.14}$	33.9	59.2	4.32	4.96	6.73	6.97	18.4	9.21	36.1	19.4
24% Open cure	$(Fe_{0.70}Mg_{0.25})(Cr_{1.30}Al_{0.52})O_{4.24}$	34.9	60.5	3.14	3.58	7.21	7.41	20.0	9.94	34.7	18.5

Briquette Ore Top Size −12.5 mm

Table 70: Energy-dispersive spectroscopy compositions of major phases in reduced briquette at 16% moisture under open curing conditions

Element →	**O**		**Mg**		**Al**		**Si**		**Fe**		**Ni**		**Stoichiometry**
Phase ↓	mass%	at%	mass%	at%	mass%	at%	mass%	at%	mass%	at%	mass%	at%	
Enstatite	45.2	59.3	22.0	17.1	-	-	21.3	20.3	9.93	3.80	-	-	$(Mg_{0.86}Fe_{0.24}Ca_{0.19})Si_{1.01}O_{2.96}$
Forsterite	44.2	58.1	26.4	22.9	-	-	21.5	16.1	7.43	2.80	3.11	1.14	$(Mg_{1.60}Fe_{0.20}Ni_{0.08})Si_{1.13}O_{4.07}$
Hornblende	46.4	60.6	13.7	10.9	4.40	3.40	26.1	20.3	-	-	-	-	$Na_{0.55}Ca_{2.03}(Mg_{4.28}Fe_{1.67}Al_{1.33})Si_{7.99}O_{23.8}$
Magnetite	27.9	56.2	4.10	5.18	6.52	7.29	5.75	6.33	60.9	32.1			$(Fe_{2.24}Al_{0.51}Si_{0.36})O_{3.93}$
Quartz	52.6	65.8	-	-	-	-	46.2	32.9	-	-	-	-	$Si_{0.99}O_{1.97}$
Wustite	22.3	50.0	-	-	-	-	-	-	77.7	50.0	-	-	FeO

Table 71: Energy-dispersive spectroscopy compositions of major phases in reduced briquette at 16% moisture under close curing conditions

Element →	**O**		**Mg**		**Al**		**Si**		**Fe**		**Ni**		**Stoichiometry**
Phase ↓	mass%	at%	mass%	at%	mass%	at%	mass%	at%	mass%	at%	mass%	at%	
Enstatite	46.7	60.1	22.1	16.9	-	-	26.6	19.5	3.34	3.15	1.32	0.46	$(Mg_{0.84}Fe_{0.16}Ni_{0.02})Si_{0.97}O_{3.00}$
Forsterite	44.6	58.3	27.1	23.3	-	-	21.3	15.9	6.45	2.42	1.62	0.59	$(Mg_{1.63}Fe_{0.17}Ni_{0.04})Si_{1.11}O_{4.08}$
Hornblende	45.8	60.2	16.1	14.4	3.50	2.20	20.1	15.6	2.17	1.99	-	-	$Na_{0.63}Ca_{1.12}(Mg_{5.67}Fe_{0.78}Al_{0.86})Si_{6.13}O_{23.6}$
Magnetite	25.7	52.8	1.49	2.01	1.60	1.94	3.95	4.61	66.1	38.9	3.25	1.82	$(Fe_{2.72}Si_{0.32}Al_{0.14}Mg_{0.14}Cr_{0.11})O_{3.70}$
Quartz	53.0	66.6	1.17	0.96	-	-	46.1	33.0	1.77	0.64	-	-	$Si_{0.99}O_{2.00}$
Wustite	22.9	50.6	0.71	1.03	-	-	0.76	0.95	75.3	47.6	-	-	$Fe_{0.95}O_{1.01}$

Table 72: Energy-dispersive spectroscopy compositions of major phases in reduced briquette at 24% moisture content under open curing conditions

Element →	O		Mg		Al		Si		Fe		Ni		Stoichiometry
Phase ↓	mass%	at%	mass%	at%	mass%	at%	mass%	at%	mass%	at%	mass%	at%	
Enstatite	44.2	58.3	25.2	21.9	-	-	22.1	16.6	6.52	2.46	2.19	0.79	$(Mg_{1.09}Fe_{0.12}Ni_{0.04}Ca_{0.01})Si_{0.83}O_{2.92}$
Forsterite	44.3	57.9	27.3	23.5	1.35	1.08	21.3	15.8	6.20	2.33	1.11	0.40	$(Mg_{1.64}Fe_{0.16}Al_{0.08}Ni_{0.03}Mn_{0.01})Si_{1.11}O_{4.06}$
Hornblende	42.8	60.0	11.1	10.2	2.64	2.15	24.2	19.1	15.0	6.59	1.22	0.50	$Ca_{1.21}(Mg_{4.00}Fe_{2.59}Al_{2.47}Ni_{0.20}Cr_{0.13}Mn_{0.10})Si_{5.71}O_{23.6}$
Magnetite	25.8	52.7	1.75	2.33	1.80	2.19	3.44	4.00	65.9	38.7	1.57	0.87	$(Fe_{2.71}Si_{0.28}Al_{0.15})O_{3.69}$
Quartz	52.7	66.4	0.75	0.63	-	-	45.7	32.8	2.00	0.74	0.47	0.17	$(Si_{0.99}Fe_{0.02}Mg_{0.02})O_{1.99}$
Wustite	23.4	50.9	1.33	1.91	-	-	1.61	1.98	73.6	45.8	-	-	$Fe_{0.92}O_{1.02}$

Table 73: Energy-dispersive spectroscopy compositions of major phases in reduced briquette at 24% moisture content under close curing conditions

Element →	O		Mg		Al		Si		Fe		Ni		Stoichiometry
Phase ↓	mass%	at%	mass%	at%	mass%	at%	mass%	at%	mass%	at%	mass%	at%	
Enstatite	44.7	58.6	24.8	17.2	-	-	22.9	21.4	6.97	2.62			$(Mg_{0.86}Fe_{0.13}Ni_{0.03}Ca_{0.02})Si_{1.07}O_{2.93}$
Forsterite	43.8	57.9	26.3	22.8	3.03	2.37	20.9	15.7	6.70	2.54	2.51	0.91	$(Mg_{1.60}Fe_{0.18}Ni_{0.06})Si_{1.01}O_{4.05}$
Hornblende	44.7	59.6	17.3	12.0	2.94	2.50	23.8	19.3	6.5	3.52	1.94	0.74	$Na_{0.34}Ca_{1.22}(Mg_{4.89}Fe_{1.48}Al_{2.21}Ni_{0.29})Si_{6.32}O_{23.4}$
Magnetite	24.1	53.5	3.59	4.80	-	-	2.87	3.26	68.2	40.3	9.02	2.76	$(Fe_{2.82}Mg_{0.34}Si_{0.23}Al_{0.21}Cr_{0.07})O_{3.74}$
Quartz	52.2	66.3	0.79	0.66	-	-	45.1	32.6	3.39	1.26	-	-	$(Si_{0.98}Fe_{0.04}Mg_{0.02})O_{1.99}$
Wustite	22.3	50.0							77.7	50.0			FeO

Table 74: Energy-dispersive spectroscopy compositions of spinel phases in reduced briquettes

Element →	O		Mg		Al		Si		Fe		Cr		Stoichiometry
Sample ID	mass%	at%	mass%	at%	mass%	at%	mass%	at%	mass%	at%	mass%	at%	
16% Open cure	36.0	57.3	7.61	7.83	14.9	13.7	17.2	15.3	17.7	8.17	24.9	11.1	$(Mg_{0.55}Fe_{0.57})(Al_{0.96}Cr_{0.89})O_{4.01}$
16% Close cure	39.4	57.1	10.2	9.76	26.5	22.8	-	-	11.0	4.58	12.9	5.75	$(Mg_{0.68}Fe_{0.32})(Al_{1.59}Cr_{0.40})O_{4.00}$
24% Open cure	37.4	57.2	8.81	8.87	21.3	19.3	-	-	12.5	5.48	18.7	8.79	$(Mg_{0.62}Fe_{0.38})(Al_{1.35}Cr_{0.62})O_{4.01}$
24% Close cure	37.2	57.0	9.11	9.20	20.1	18.3	-	-	12.8	5.62	20.9	9.87	$(Mg_{0.64}Fe_{0.39})(Al_{1.28}Cr_{0.69})O_{3.99}$

Appendix 7: Decrepitation Index

Briquette decrepitation index

Table 75: Decrepitation index test results at briquette ore top size of −6.3 mm

Moisture, %	Curing condition	Decrepitation index, % −6.3 mm	Mass disintegration, % −3.15 mm	% −0.5 mm
16	Open	0.28	0.19	0.09
16	Closed	0.37	0.23	0.09
24	Open	0.47	0.28	0.14
24	Closed	0.74	0.47	0.18

Table 76: Decrepitation index test results at briquette ore top size of −12.5 mm

Moisture, %	Curing condition	Decrepitation index, % −6.3 mm	Mass disintegration, % −3.15 mm	% −0.5 mm
16	Open	2.24	1.26	0.40
16	Closed	2.44	0.85	0.31
24	Open	2.56	1.14	0.3
24	Closed	1.35	0.71	0.22

Quantitative X-ray diffraction analysis

Table 77: X-ray diffraction analysis of briquettes after decrepitation index test at briquette ore top size −6.3 mm

Phase ID	Mineral mass, %			
	16 % Moisture		24% Moisture	
	Open curing	Closed curing	Open curing	Closed curing
Amorphous	36.5	46.8	44.5	46
Clinochlore	6.1	7.8	7	7.1
Enstatite	16.8	8.5	12.9	11.8
Forsterite	3.6	5.8	4.6	3.5
Hematite	7.3	4.8	6.1	6.1
Hornblende	5.3	3.8	4.4	5.0
Lizardite	5.8	5.4	4.2	3.8
Quartz	5.8	6.7	5.2	5.2
Talc	12.8	10.6	11.2	11.6

Table 78: X-ray diffraction analysis of the briquettes after decrepitation index test at briquette ore top size −12.5 mm

Phase ID	Mineral mass, %			
	16 % Moisture		24% Moisture	
	Open curing	Closed curing	Open curing	Closed curing
Amorphous	41	36.8	35	32.7
Clinochlore	6.3	9.7	10.4	9.5
Enstatite	5.7	8.2	4	16.8
Forsterite	14	7.7	12.4	5.8
Hematite	4.2	3.1	3.6	5.4
Hornblende	6.3	6.9	5.8	4.9
Lizardite	2.9	6.8	4.9	6.2
Quartz	9.3	6.7	9.5	6.6
Talc	10.5	14.2	14.4	12.1

Appendix 8: Reduction Disintegration

Briquette disintegration index

Table 79: Reduction disintegration index test results at briquette ore top size −6.3 mm

Moisture, %	Curing condition	Reduction disintegration index, % +6.3 mm	% −3.15 mm	% −0.5 mm
16	Open	97.6	2.24	1.59
16	Closed	96.9	2.93	1.93
24	Open	96.9	3.03	2.54
24	Closed	92.4	6.54	4.11

Table 80: Reduction disintegration index test results at briquette ore top size −12.5 mm

Moisture, %	Curing condition	Reduction disintegration index, % +6.3 mm	% −3.15 mm	% −0.5 mm
16	Open	79.8	14.4	7
16	Closed	78.3	14.3	6.53
24	Open	69.4	16.9	6.35
24	Closed	72.7	17.7	7.80

Quantitative X-ray diffraction analysis

Table 81: X-ray diffraction analysis at briquette ore top size −6.3 mm

Phase ID	Mineral mass, % 16 % Moisture Open curing	16 % Moisture Closed curing	24% Moisture Open curing	24% Moisture Closed curing
Amorphous	27.5	34.6	45.5	35.2
Clinochlore	7.89	6.17	5.42	5.74
Diopside	1.39	1.71	1.29	1.77
Enstatite	11	7.65	7.96	8.47
Forsterite	6.25	4.96	4.25	4.92
Hornblende	6.13	4.91	3	4.24
Lizardite	16.9	16.8	13.9	17.5
Magnetite	8.28	9.08	8.69	8.5
Quartz	8.72	8.22	5.92	7.86
Talc	5.85	5.85	4.06	5.77

Table 82: X-ray diffraction analysis at briquette ore top size −12.5 mm

Phase ID	Mineral mass, %			
	16 % Moisture		24% Moisture	
	Open curing	Closed curing	Open curing	Closed curing
Amorphous	27.2	25.9	19.1	23.3
Chlorite	15.4	13.7	16.6	14.4
Enstatite	4.6	6.3	5	7.7
Hornblende	2.8	2.1	3.6	2
Lizardite	20.3	23.1	22.5	24.3
Magnetite	4.7	5.4	5.5	4.6
Quartz	7.3	8.8	8.7	6.9
Talc	17.1	14.7	19.1	16.8

Appendix 9: Linder Furnace Test Results

Briquette disintegration index

Table 83: Disintegration index at briquette ore top size of −6.3 mm

Moisture, %	Curing condition	Mass disintegration, % +6.3 mm	% −3.15 mm	% −0.5 mm
16	Open	95.9	3.83	3.26
16	Closed	94.6	5.09	4.24
24	Open	70.4	20.9	10.5
24	Closed	70.1	21.8	12.00

Table 84: Disintegration index at briquette ore top size of −12.5 mm

Moisture, %	Curing condition	Mass disintegration, % +6.3 mm	% −3.15 mm	% −0.5 mm
16	Open	27.5	49.2	25.4
16	Closed	23.3	51.3	24.7
24	Open	27	46.8	16.5
24	Closed	33.5	44.1	23.10

Compressive strength

Table 85: Compressive strength and drop number test results at briquette ore top size −6.3 mm

Moisture, %	Curing condition	Average compressive strength, N	Average drop number
16	Open	852	12.4
16	Closed	1038	9.6
24	Open	228	1.67
24	Closed	147	-

X-ray fluorescence analysis

Table 86: X-ray fluorescence analysis at briquette ore top size −6.3 mm

	Component, mass%			
	16% Open curing	**16% Closed curing**	**24% Open curing**	**24% Closed curing**
NiO	2.54	2.57	2.6	2.58
SiO_2	42.3	42.5	42	42.2
Fe_2O_3	25.6	25.5	25.9	25.6
Al_2O_3	4.66	4.62	4.73	4.7
MgO	22	22.1	21.6	22.1
Na_2O	< 0.01	< 0.01	< 0.01	< 0.01
P_2O_5	0.03	0.02	0.02	0.02
K_2O	0.04	0.05	0.04	0.04
CaO	0.68	0.66	0.69	0.69
TiO_2	0.07	0.07	0.08	0.08
V_2O_5	0.01	0.01	0.01	0.01
Cr_2O_3	1.24	1.17	1.18	1.21
MnO	0.41	0.42	0.43	0.43
CuO	< 0.01	< 0.01	< 0.01	< 0.01
ZrO_2	0.01	0.02	0.01	0.01
Co_3O_4	0.09	0.09	0.09	0.09
ZnO	0.03	0.03	0.03	0.03
MoO_3	< 0.01	< 0.01	< 0.01	0.02
BaO	0.25	0.2	0.19	0.24
PbO	-	-	-0.01	-
SrO	-	-	-	< 0.01
Cs_2O	-	-	-	< 0.01
SO_3	-	-	-	0.01
Nb_2O_5	-	-	-	0.01
LOI	0	0.09	0.44	0.1
TOTAL	99.91	99.94	99.94	99.95

Table 87: X-ray fluorescence analysis at briquette ore top size −12.5 mm

	Component, mass%			
	16% Open curing	16% Closed curing	24% Open curing	24% Closed curing
SiO_2	45.9	45.9	45.9	46
Al_2O_3	2.69	2.65	2.67	2.58
MgO	29.7	29.6	29.9	29.7
Na_2O	< 0.01	< 0.01	< 0.01	< 0.01
P_2O_5	0.02	0.01	0	0.01
Fe_2O_3	16.3	16.3	16.2	16.3
K_2O	0.02	0.02	0.02	0.02
CaO	0.64	0.64	0.65	0.64
TiO_2	0.02	0.02	0.02	0.02
V_2O_5	< 0.01	0.01	< 0.01	< 0.01
Cr_2O_3	0.77	0.76	0.77	0.74
MnO	0.23	0.22	0.23	0.22
NiO	2.29	2.19	2.23	2.19
CuO	< 0.01	< 0.01	< 0.01	< 0.01
ZrO_2	< 0.01	< 0.01	< 0.01	< 0.01
S	< 0.01	< 0.01	< 0.01	< 0.01
Co_3O_4	0.05	0.05	0.05	0.05
ZnO	0.02	0.02	0.02	0.02
Ag_2O	0.06	< 0.01	< 0.01	0.04
TeO2	< 0.01	< 0.01	< 0.01	< 0.01
ThO_2	< 0.01	0.05	0.05	< 0.01
Nb_2O_5	0.02	0.04	0.04	0.02
LOI	1.22	1.55	1.24	1.44
TOTAL	99.97	99.97	99.95	99.96

Quantitative X-ray diffraction analysis

Table 88: X-ray diffraction analysis of briquettes at ore top size −6.3 mm

Phase ID	Mineral mass, %			
	16% moisture		24% moisture	
	Open curing	Closed curing	Open curing	Closed curing
Amorphous	35.3	16.1	29.6	40.2
Diopside	3.77	6.92	6.74	8.61
Enstatite	11.1	29.7	24.3	13.6
Forsterite	28	30.5	25.4	22.6
Hornblende	4.86	3.97	4.62	5.69
Magnetite	5.88	4.8	3.97	3.57
Quartz	6.48	6.66	5.15	5.78
Hematite	4.6	1.3	0.19	-

Table 89: X-ray diffraction analysis of briquettes at ore top size −12.5 mm

Phase ID	Mineral mass, %			
	16% moisture		24% moisture	
	Open curing	Closed curing	Open curing	Closed curing
Amorphous	15.2	12.1	20.6	24.1
Enstatite	17.1	7.52	19.1	8.02
Forsterite	49.6	60.4	50	52.3
Hornblende	6.06	6.38	2.08	4.67
Magnetite	2.84	2.86	2.27	2.86
Quartz	9.12	10.7	5.98	8.05

Back-scattered electron imaging and X-ray mapping analysis

Briquette ore top size −6.3 mm

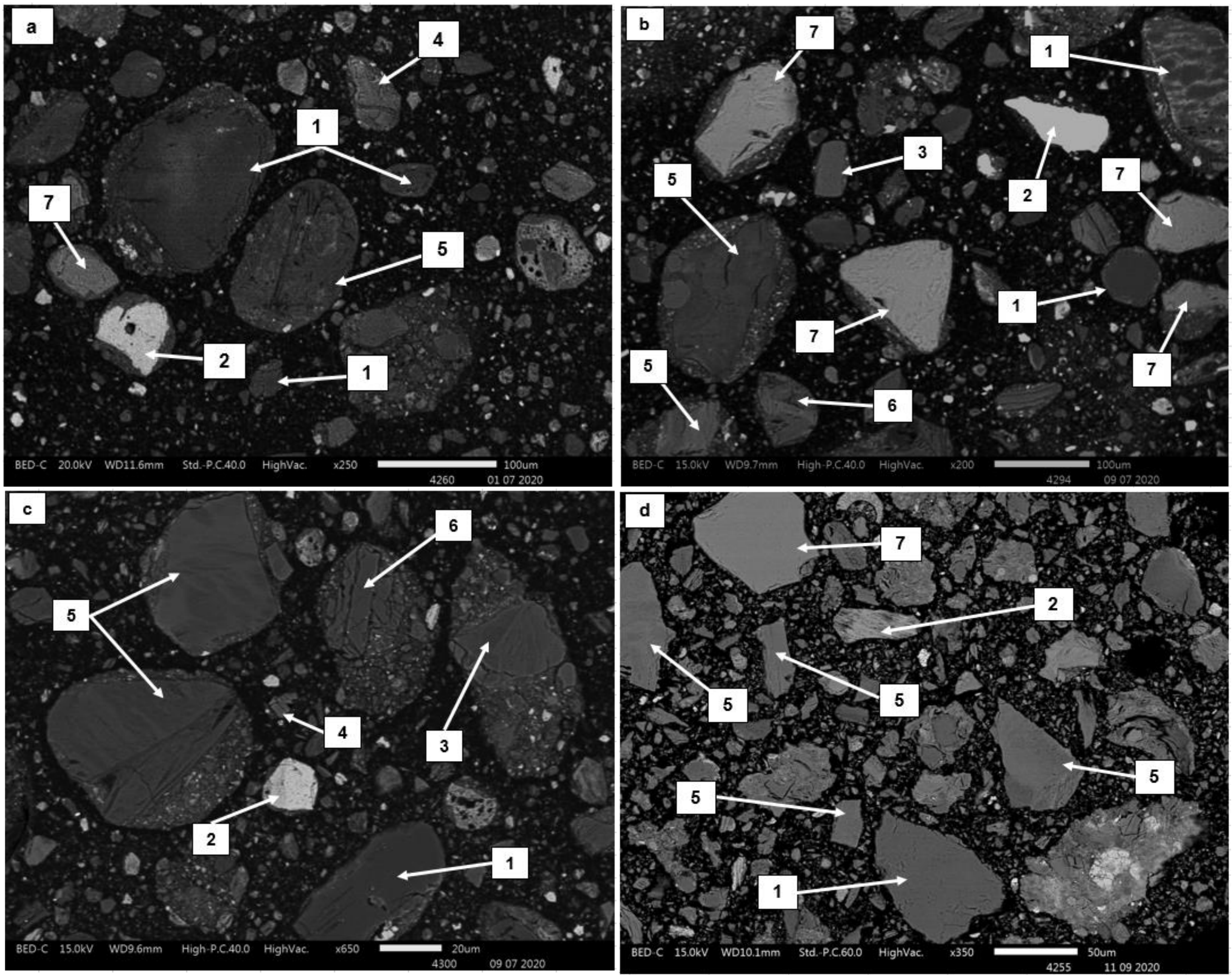

Figure 92: Back-scattered electron imaging of minerals and phases present in briquettes after Linder furnace test: (a)16% H_2O open curing; (b) 16% H_2O closed curing; (c) 24% H_2O open curing; (d) 24% H_2O closed curing, where (1) quartz; (2) iron oxide; (3) hornblende; (4) diopside; (5) forsterite; (6) enstatite; (7) spinel

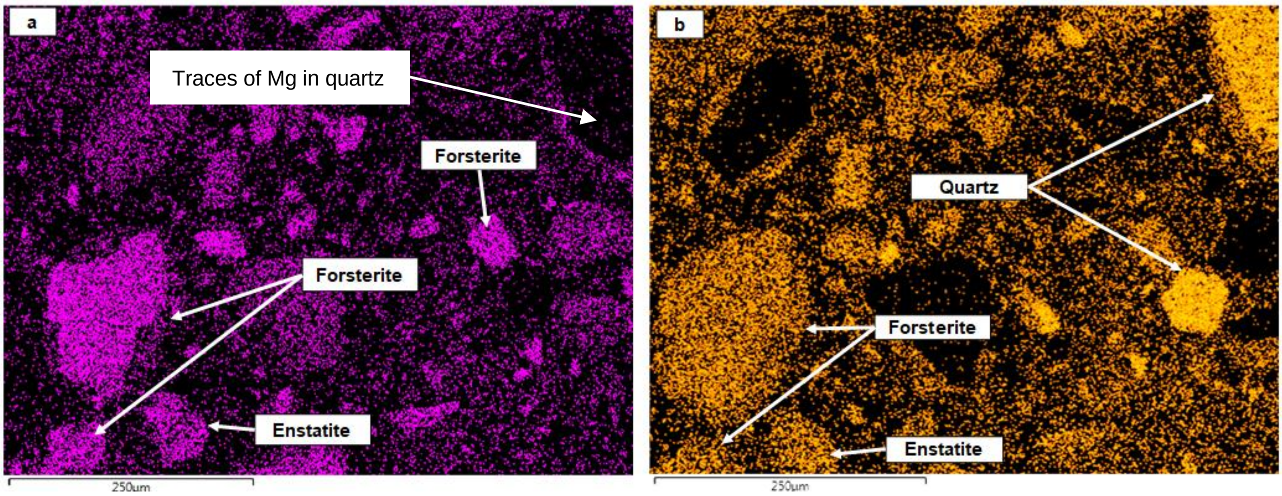

Figure 93: Major elemental distribution mapping analysis of briquette after Linder testing at 16% moisture content under closed curing conditions: (a) Mg; (b) Si (BEI in Figure 92(b))

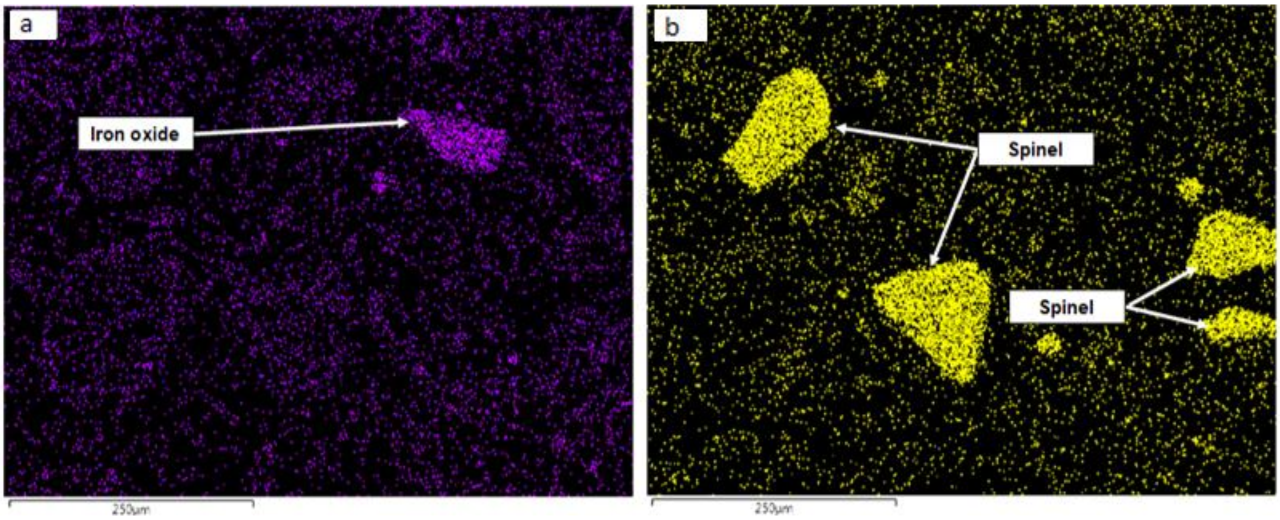

Figure 94: Major elemental distribution mapping analysis of briquette after Linder testing at 16% moisture content under closed curing conditions: (a) Fe; (b) Al (BEI in Figure 92(b))

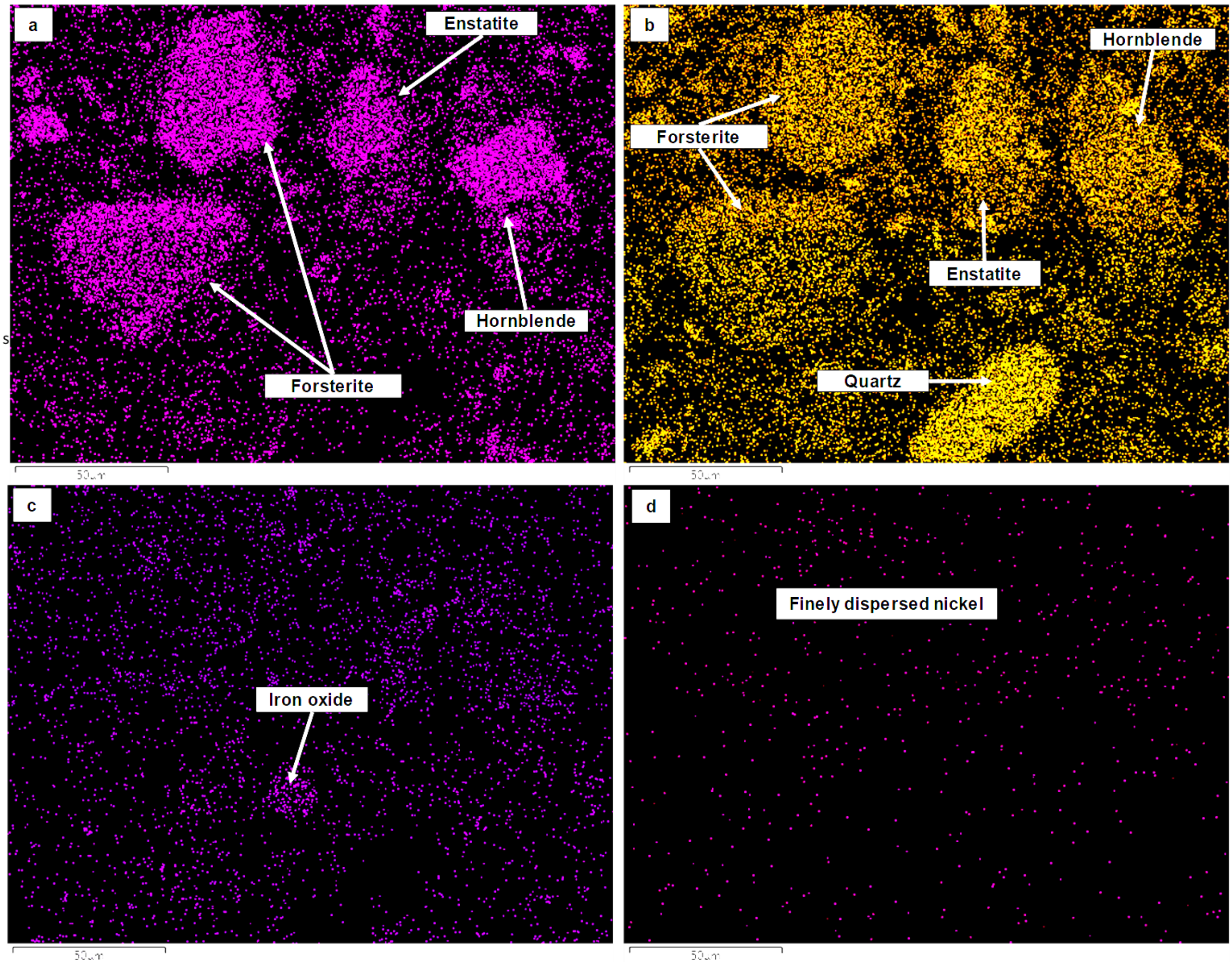

Figure 95: Major elemental distribution mapping analysis of briquettes after Linder testing at 24% moisture content under open curing conditions: (a) Mg; (b) Si; (c) Fe; (d) Ni (BEI in Figure 92(c))

Briquette ore top size −12.5 mm

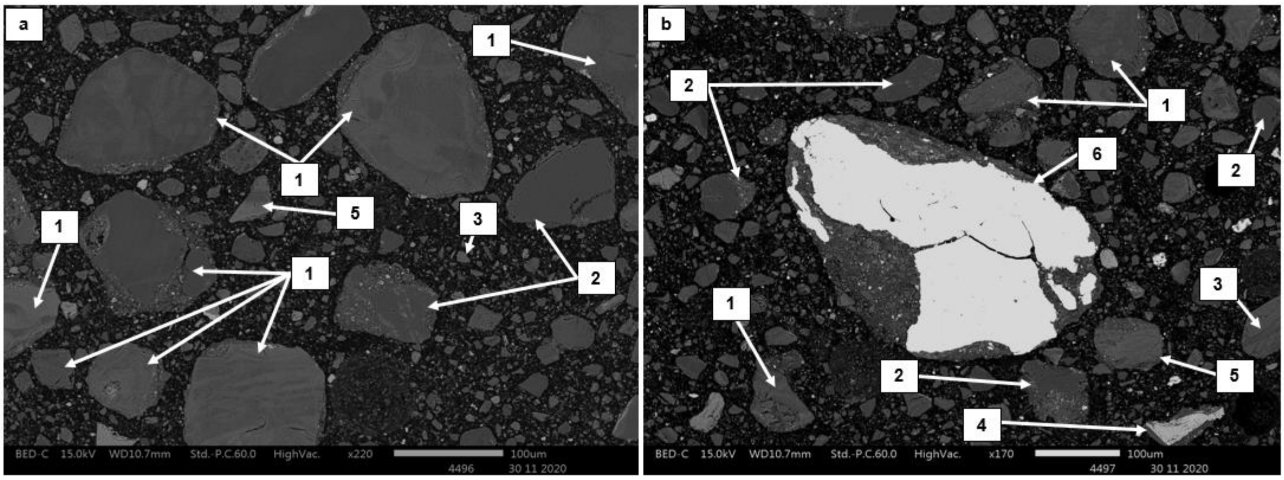

Figure 96: Back-scattered electron imaging of briquettes after Linder furnace test at 16% moisture content under open curing conditions: (1) forsterite; (2) quartz; (3) hornblende; (4) spinel; (5) enstatite; (6) FeNi alloy

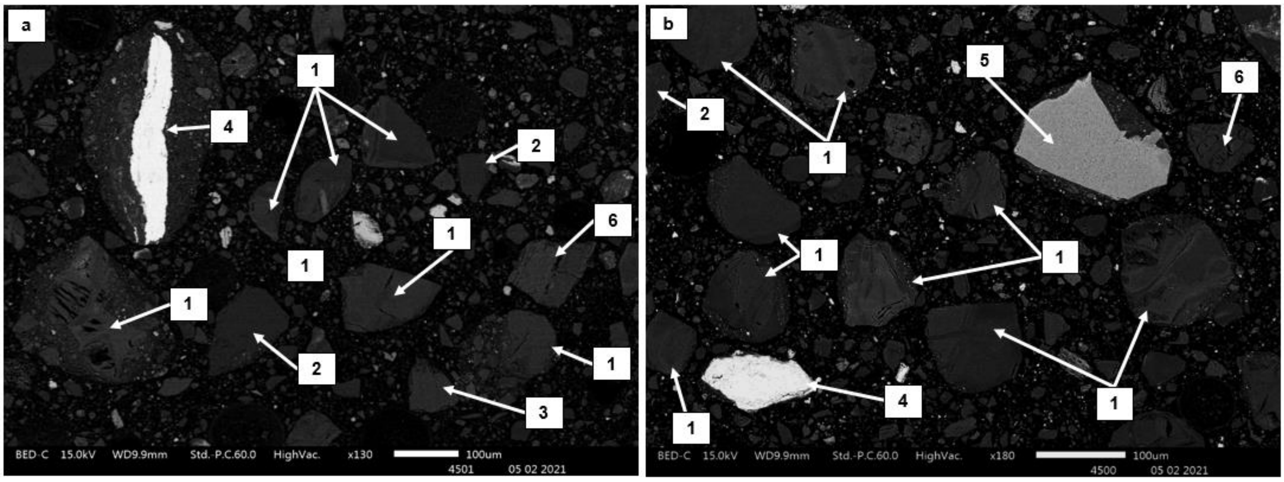

Figure 97: Back-scattered electron imaging of briquettes after Linder furnace test at 16% moisture content under closed curing conditions: (1) forsterite; (2) quartz; (3) hornblende; (4) magnetite; (5) spinel; (6) enstatite

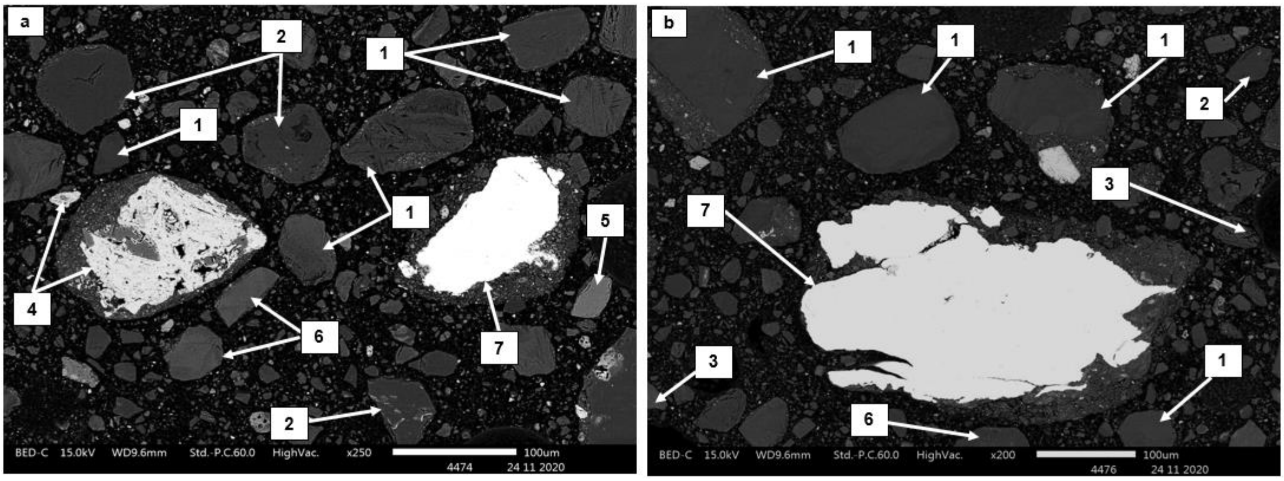

Figure 98: Back-scattered electron imaging of briquettes after Linder furnace test at 24% moisture content under open curing conditions: (1) forsterite; (2) quartz; (3) hornblende; (4) magnetite; (5) spinel; (6) enstatite; (7) FeNi alloy

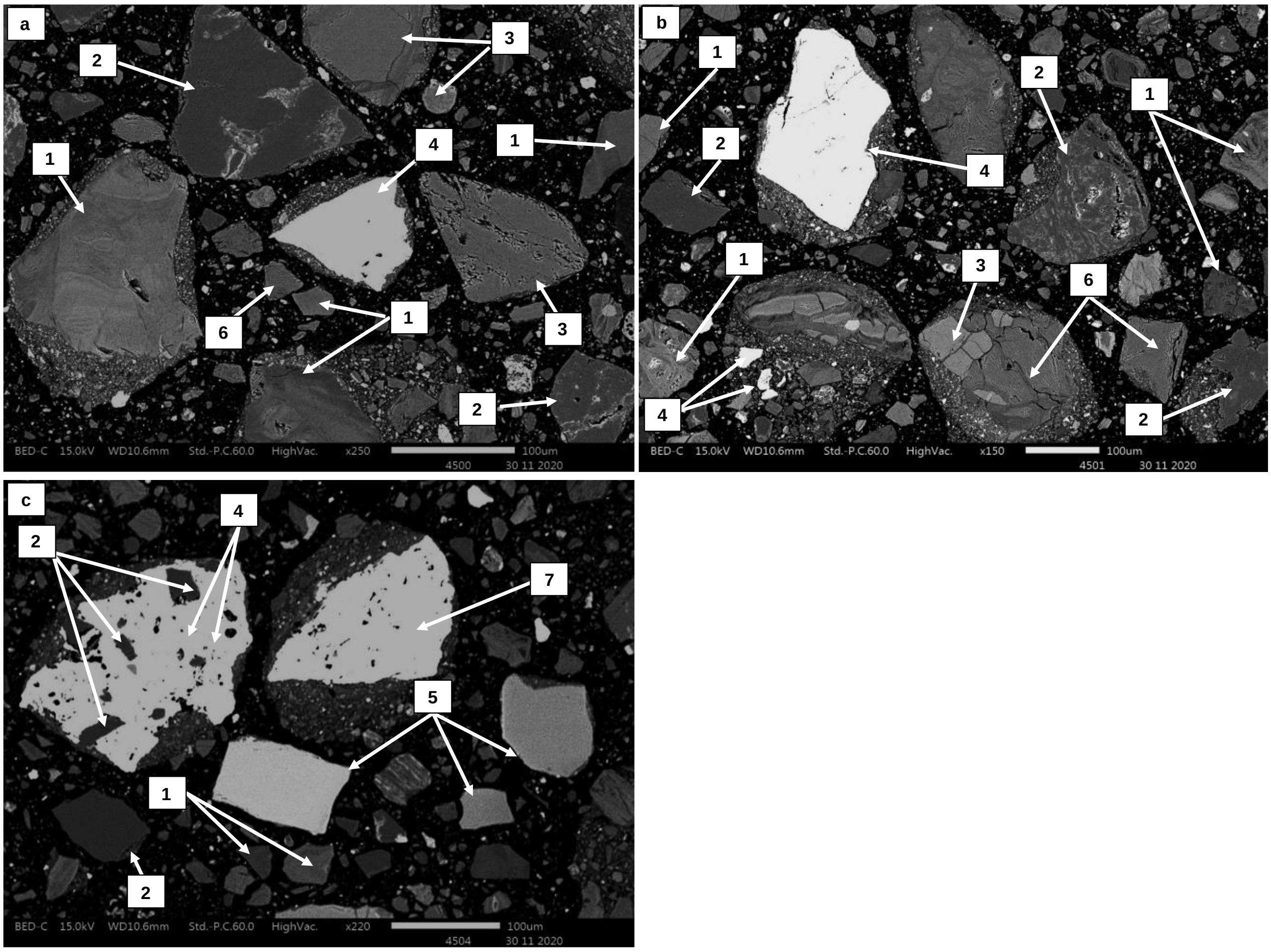

Figure 99: Back-scattered electron imaging of briquettes after Linder furnace testing at 24% moisture content under closed curing conditions: (1) forsterite; (2) quartz; (3) hornblende; (4) magnetite; (5) spinel; (6) enstatite; (7) wustite

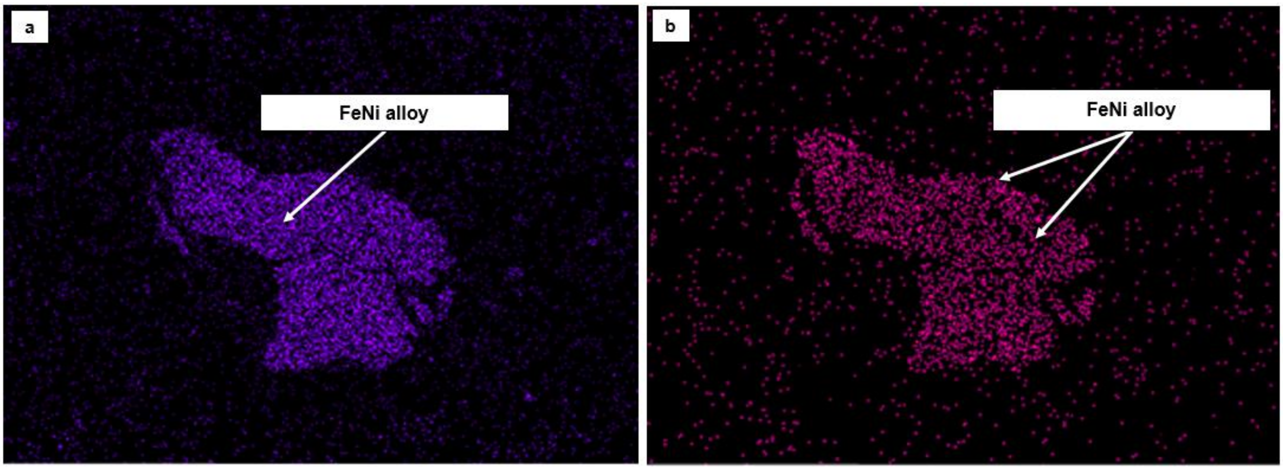

Figure 100: X-ray mapping analysis of major elements present in briquettes after Linder furnace test at 16% moisture content under open curing conditions: (a) Fe; (b) Ni (BEI in Figure 96(b))

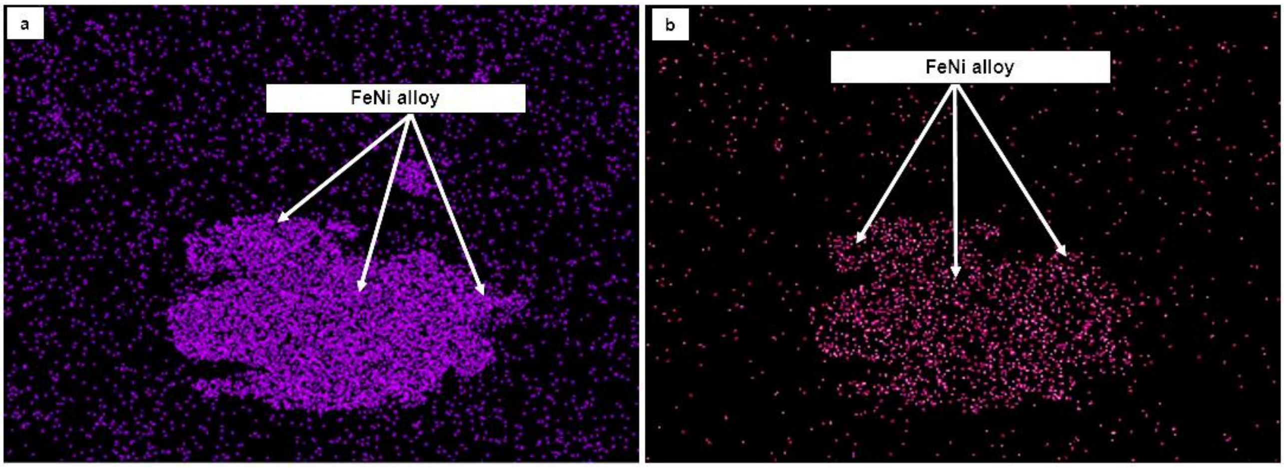

Figure 101: X-ray mapping analysis of major elements present in briquettes after Linder furnace test at 24% moisture content under open curing conditions: (a) Fe; (b) Ni (BEI in Figure 98(b))

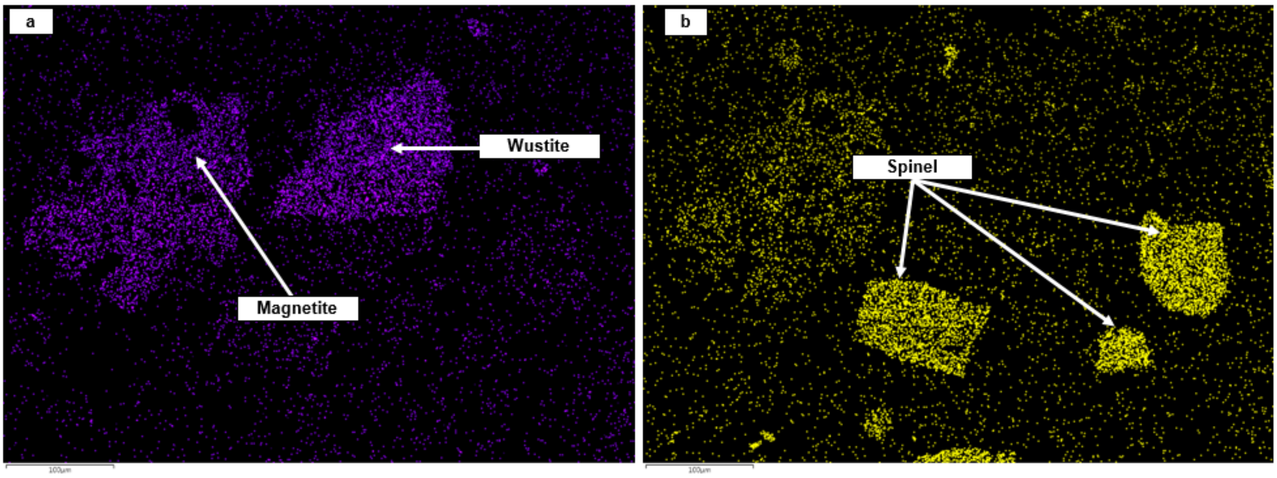

Figure 102: X-ray mapping analysis of major elements present in briquettes after Linder furnace test at 24% moisture content under closed curing conditions: (a) Fe; (b) Cr (BEI in Figure 99(c))

Energy-dispersive spectroscopy and stoichiometric analysis

Briquette ore top size −6.3 mm

Table 90: Energy-dispersive spectroscopy composition of major phases in briquettes at 16% moisture content under open curing conditions after Linder furnace testing

Element →	**O**		**Mg**		**Al**		**Si**		**Fe**		**Ni**		**Stoichiometry**
Phase ↓	mass%	at%	mass%	at%	mass%	at%	mass%	at%	mass%	at%	mass%	at%	
Diopside	45.2	54.6	8.40	6.60	3.50	2.48	21.0	19.2	12.00	10.68	-	-	$Ca_{0.79}(Mg_{0.71}Fe_{1.15}Al_{0.27})Si_{2.06}O_{5.86}$
Enstatite	48.3	61.6	20.7	17.3	1.15	0.60	25.3	18.8	4.60	1.68	-	-	$(Mg_{0.87}Fe_{0.0}8Al_{0.03})Si_{0.94}O_{3.08}$
Forsterite	48.4	61.6	25.5	21.5	-	-	21.1	15.1	4.97	1.82	-	-	$(Mg_{1.50}Fe_{0.13})Si_{1.06}O_{4.30}$
Hornblende	46.1	61.4	13.2	9.87	4.26	2.71	21.1	16.5	5.89	3.50	-	-	$Na_{1.11}Ca_{1.35}(Mg_{3.92}Fe_{1.39}Al_{1.08}Cr_{0.15})Si_{6.57}O_{24.2}$
Iron oxide	39.0	64.9	-	-	9.21	8.97	1.32	1.55	43.4	20.8	1.32	0.43	$(Fe_{1.04}Al_{0.45}Cr_{0.18}Ni_{0.02})O_{3.24}$
Quartz	55.2	68.3	0.82	0.68	-	-	44.5	31.4	-	-	-	-	$Si_{0.94}O_{2.05}$

Table 91: Energy-dispersive spectroscopy compositions of major phases in briquettes at 16% moisture content under closed curing conditions after Linder furnace testing

Element →	**O**		**Mg**		**Al**		**Si**		**Fe**		**Ni**		**Stoichiometry**
Phase ↓	mass%	at%	mass%	at%	mass%	at%	mass%	at%	mass%	at%	mass%	at%	
Diopside	45.6	59.9	9.42	8.14	2.04	1.59	25.2	18.9	6.96	2.62	-	-	$Ca_{0.95}(Mg_{0.87}Fe_{0.28}Al_{0.17})Si_{2.02}O_{6.43}$
Enstatite	45.6	59.5	22.1	19.0	0.48	0.37	25.2	18.7	5.17	1.93	1.21	0.43	$(Mg_{0.95}Fe_{0.10}Al_{0.02}Ni_{0.02})Si_{0.94}O_{2.97}$
Forsterite	44.4	58.2	26.7	23.0	-	-	21.8	16.2	5.97	2.24			$(Mg_{1.61}Fe_{0.16}Ni_{0.07})Si_{1.13}O_{4.06}$
Hornblende	45.5	60.1	13.8	12.01	3.66	2.86	22.1	16.9	3.73	2.65	-	-	$Na_{0.26}Ca_{1.85}(Mg_{4.78}Al_{1.14}Fe_{1.05}Cr_{0.26})Si_{6.70}O_{23.9}$
Iron oxide	29.7	58.9	0.82	1.07	-	-	0.56	0.63	66.9	38.0	1.53	0.83	$(Fe_{1.90}Mg_{0.05}Ca_{0.04}Si_{0.03})O_{2.94}$
Quartz	52.4	66.5	-	-	-	-	45.6	32.9	1.51	0.55	-	-	$Si_{0.98}O_{1.99}$

Table 92: Energy-dispersive spectroscopy compositions of major phases in briquettes at 24% moisture content under open curing conditions after Linder

Element →	**O**		**Mg**		**Al**		**Si**		**Fe**		**Ni**		**Stoichiometry**
Phase ↓	mass%	at%	mass%	at%	mass%	at%	mass%	at%	mass%	at%	mass%	at%	
Diopside	44.2	56.0	8.8	5.50	4.03	1.80	22.3	19.2	8.75	9.50	-	-	$Ca_{0.81}(Mg_{1.18}Fe_{0.57}Al_{0.13})Si_{1.92}O_{5.79}$
Enstatite	46.2	59.8	21.3	18.1	1.12	0.86	26.1	19.2	5.35	1.99	-	-	$(Mg_{0.91}Fe_{0.10}Al_{0.04})Si_{0.96}O_{2.99}$
Forsterite	43.9	58.1	25.6	22.3	0.62	0.48	21.3	16.1	7.31	2.77	1.63	0.59	$(Mg_{1.56}Fe_{0.19}Ni_{0.04}Al_{0.02})Si_{1.12}O_{4.06}$
Hornblende	48.2	62.5	14.5	9.10	3.72	2.50	22.7	18.9	5.70	3.74	-	-	$Ca_{1.26}(Mg_{3.62}Fe_{1.49}Ca_{1.26}Al_{0.99}Cr_{0.07})Si_{7.50}O_{24.9}$
Iron oxide	24.2	51.5	-	-	2.73	3.45	0.98	1.18	72.1	43.9	-	-	$(Fe_{3.07}Al_{0.24}Si_{0.08})O_{3.60}$
Quartz	52.8	66.5	-	-	-	-	46.1	33.1	1.09	0.39	-	-	$Si_{0.99}O_{2.00}$

Table 93: Energy-dispersive spectroscopy compositions of major phases in briquettes at 24% moisture content under closed curing conditions after Linder furnace testing

Elements →	**O**		**Mg**		**Al**		**Si**		**Fe**		**Ni**		**Stoichiometry**
Phases ↓	mass%	at%	mass%	at%	mass%	at%	mass%	at%	mass%	at%	mass%	at%	
Diopside	43.2	56.0	6.90	5.87	1.92	1.50	21.5	18.5	14.8	9.40	-	-	$Ca_{0.93}(Mg_{0.63}Fe_{1.01}Al_{0.16})Si_{1.99}O_{6.01}$
Enstatite	46.3	60.9	16.4	14.2	0.36	0.28	25.9	19.8	6.12	2.62	5.10	2.24	$(Mg_{0.71}Fe_{0.13}Al_{0.01}Ni_{0.11})Si_{0.99}O_{3.04}$
Forsterite	46.8	60.5	26.0	22.1	-	-	19.8	14.6	6.17	2.29	2.44	0.88	$(Mg_{1.55}Fe_{0.16}Ni_{0.06})Si_{1.02}O_{4.23}$
Hornblende	45.1	59.9	12.9	11.2	5.08	4.00	23.9	18.0	2.17	0.83	-	-	$Na_{0.40}Ca_{1.85}(Mg_{4.47}Fe_{0.33}Al_{1.59}Cr_{0.17})Si_{7.16}O_{23.8}$
Iron oxide	33.8	58.6	2.31	2.63	1.41	1.45	12.4	12.3	48.3	24.0	-	-	$(Fe_{1.20}Si_{0.62}Mg_{0.13}Cr_{0.05})O_{2.93}$
Quartz	56.7	69.6	-	-	-	-	43.4	30.4	-	-	-	-	$Si_{0.91}O_{2.10}$

Table 94: Energy-dispersive spectroscopy compositions of spinel mineral after Linder furnace testing

Element →	**O**		**Mg**		**Al**		**Fe**		**Cr**		**Stoichiometry**
Sample ID ↓	mass%	at%	mass%	at%	mass%	at%	mass%	at%	mass%	at%	
16% Open cure	44.6	62.7	8.43	8.06	22.9	18.9	9.64	3.89	14.5	6.49	$(Mg_{0.56}Fe_{0.27})(Al_{1.32}Cr_{0.45})O_{4.39}$
16% Closed cure	39.9	57.1	11.1	10.5	27.3	23.1	9.51	3.90	12.2	5.36	$(Mg_{0.73}Fe_{0.27})(Al_{1.62}Cr_{0.38})O_{4.0}$
24% Closed cure	42.9	60.4	10.80	10.01	24.4	20.4	9.15	3.69	12.8	5.54	$(Mg_{0.70}Fe_{0.26})(Al_{1.43}Cr_{0.39})O_{4.23}$

Briquette ore top size −12.5 mm

Table 95: Energy-dispersive spectroscopy compositions of major phases in briquettes after Linder furnace test at 16% moisture content under open curing conditions

Element →	**O**		**Mg**		**Al**		**Si**		**Fe**		**Ni**		**Stoichiometry**
Phase ↓	mass%	at%	mass%	at%	mass%	at%	mass%	at%	mass%	at%	mass%	at%	
Enstatite	45.2	59.2	22.8	17.7	-	-	24.7	20.2	5.37	1.89	3.48	1.26	$(Mg_{0.89}Fe0.10Ni_{0.06})Si_{1.01}O_{2.96}$
FeNi alloy	22.2	50.1	-	-	-	-	-	-	58.8	38.1	18.9	11.7	
Forsterite	44.4	58.4	26.0	22.5	-	-	21.3	16.0	6.78	2.57	1.94	0.70	$(Mg_{1.58}Fe_{0.18}Ni_{0.05})Si_{1.12}O_{4.09}$
Hornblende	41.5	58.9	11.9	10.9	2.33	4.32	20.7	17.3	10.8	4.55	1.44	0.5	$Ca_{3.19}(Mg_{4.30}Fe_{1.79}Al_{1.70}Ni_{0.2}Cr_{0.12})Si_{6.11}O_{23.1}$
Magnetite	26.6	53.3	-	-	4.78	5.68	2.55	2.91	63.3	36.4	-	-	$(Fe_{2.55}Al_{0.40}Si_{0.20}Cr_{0.12})O_{3.73}$
Quartz	53.2	66.9	0.74	0.57	-	-	45.5	32.6	1.76	0.65	-	-	$Si_{0.98}O_{2.01}$
Wustite	22.3	50.0	-	-	-	-	-	-	77.7	50.0	-	-	FeO

Table 96: Energy-dispersive spectroscopy compositions of major phases in briquettes after Linder furnace test at 16% moisture content under closed curing conditions

Element →	**O**		**Mg**		**Al**		**Si**		**Fe**		**Ni**		**Stoichiometry**
Phase ↓	mass%	at%	mass%	at%	mass%	at%	mass%	at%	mass%	at%	mass%	at%	
Enstatite	44.9	59.4	20.8	16.7	2.72	2.14	23.6	18.9	7.68	3.14	4.32	1.59	$(Mg_{0.84}Fe_{0.16}Ca_{0.14}Al_{0.11}Ni_{0.08})Si_{0.94}O_{2.97}$
FeNi alloy	22.0	50.0	-	-	-	-	-	-	57.5	37.4	20.5	12.7	
Forsterite	44.5	58.4	26.0	23.0	-	-	21.9	15.9	6.85	2.58	-	-	$(Mg_{1.61}Fe_{0.18}Ni_{0.06})Si_{1.11}O_{4.09}$
Hornblende	44.7	60.2	15.0	11.8	4.21	3.32	23.1	18.3	9.5	4.12	5.19	1.92	$Ca_{1.89}Na_{0.92}(Mg_{4.63}Fe_{1.62}Al_{2.81}Ni_{0.75})Si_{6.10}O_{23.6}$
Magnetite	28.5	56.7	0.47	0.62	4.16	4.90	4.09	4.63	64.8	36.9	-	-	$(Fe_{2.58}Cr_{0.38}Al_{0.34}Si_{0.32}Mg_{0.04}Mn_{0.04})O_{3.97}$
Quartz	53.1	66.6	0.45	0.37	-	-	46.5	33.2	1.63	0.60	-	-	$Si_{0.97}O_{1.99}$
Wustite	23.0	50.2			1.80	0.97	2.30	0.88	73.0	47.9	0.00	0.00	$(Fe_{0.96}Al_{0.02}Si_{0.02})O_{1.00}$

Table 97: Energy-dispersive spectroscopy compositions of major phases in briquettes after Linder furnace test at 24% moisture content under open curing conditions

Element →	O		Mg		Al		Si		Fe		Ni		Stoichiometry
Phase ↓	mass%	at%	mass%	at%	mass%	at%	mass%	at%	mass%	at%	mass%	at%	
Enstatite	43.8	58.6	22.8	16.7	-	-	22.7	20.5	7.04	2.71	4.88	1.81	$(Mg_{0.84}Fe_{0.14}Ni_{0.09})Si_{1.03}O_{2.93}$
FeNi alloy	22.1	50.0	-	-	-	-	-	-	58.6	38.1	19.3	11.9	
Forsterite	43.9	58.0	26.2	23.0	-	-	21.4	15.8	6.80	2.57	2.37	0.86	$(Mg_{1.61}Fe_{0.18}Ni_{0.06})Si_{1.11}O_{4.06}$
Hornblende	45.3	60.2	14.7	11.5	7.07	5.48	24.0	18.2	5.43	3.10	-	-	$Ca_{1.90}(Mg_{4.51}Fe_{1.22}Al_{2.15}Cr_{0.06})Si_{7.16}O_{23.6}$
Magnetite	24.7	51.9	-	-	2.23	2.77	1.90	2.28	69.9	42.2	1.51	0.85	$(Fe_{2.95}Al_{0.19}Si_{0.13}Cr_{0.04})O_{3.64}$
Quartz	52.4	66.2	1.86	2.08	-	-	44.9	32.3	1.91	0.70	-	-	$Si_{0.97}O_{1.99}$
Wustite	23.6	50.9	2.03	2.91	1.50	1.90	2.02	2.45	73.1	45.1	-	-	$(Fe_{0.90}Mg_{0.05}Ca_{0.03})O_{1.02}$

Table 98: Energy-dispersive spectroscopy compositions of major phases in briquettes after Linder furnace test at 24% moisture content under closed curing conditions

Element →	O		Mg		Al		Si		Fe		Ni		Stoichiometry
Phase ↓	mass%	at%	mass%	at%	mass%	at%	mass%	at%	mass%	at%	mass%	at%	
Enstatite	45.7	59.4	22.9	17.6	-	-	25.3	20.7	5.62	2.10	2.76	0.99	$(Mg_{0.83}Fe_{0.10}Ni_{0.05}Ca_{0.01})Si_{0.96}O_{2.77}$
FeNi alloy	22.1	50.0	-	-	-	-	-	-	58.0	37.7	19.9	12.3	
Forsterite	44.1	58.1	26.1	22.9	-	-	21.5	15.9	6.84	2.59	2.00	0.73	$(Mg_{1.60}Fe_{0.18}Ni_{0.05}Cr_{0.02})Si_{1.11}O_{4.06}$
Hornblende	45.2	60.2	13.3	11.4	3.51	2.78	25.3	19.2	2.62	1.00	-	-	$Ca_{2.04}(Mg_{4.47}Fe_{0.39}Al_{1.09}Cr_{0.12})Si_{7.56}O_{23.7}$
Magnetite	27.0	53.3	5.83	7.7	5.47	6.36	3.28	3.67	61.0	34.7	2.54	1.37	$(Fe_{2.43}Mg_{0.54}Al_{0.45}Si_{0.26}Cr_{0.11}Ni_{0.10})O_{3.73}$
Quartz	52.6	66.6	0.31	0.26	-	-	45.4	32.7	1.51	0.55	-	-	$Si_{0.98}O_{2.00}$
Wustite	22.4	50.1	-	-	-	-			77.5	49.8	-	-	FeO

Table 99: EDS compositions of spinel minerals present in briquettes after Linder furnace tests

Element →	O		Mg		Al		Fe		Cr		Stoichiometry
Sample ID↓	mass%	at%	mass%	at%	mass%	at%	mass%	at%	mass%	at%	
16% Open cure	36.2	57.0	8.07	8.18	18.3	16.6	14.5	6.70	22.9	11.5	$(Mg_{0.57}Fe_{0.47})(Al_{1.16}Cr_{0.80})O_{3.99}$
16% Closed cure	39.0	57.4	10.2	9.84	24.1	20.9	10.9	4.65	15.5	7.11	$(Mg_{0.69}Fe_{0.33})(Al_{1.47}Cr_{0.50})O_{4.02}$
24% Open cure	38.8	57.1	10.0	9.70	24.8	21.6	11.5	4.85	14.9	6.7	$(Mg_{0.68}Fe_{0.34})(Al_{1.51}Cr_{0.47})O_{4.00}$
24% Closed cure	36.8	57.1	8.19	8.14	19.8	17.5	14.0	6.54	21.2	10.8	$(Mg_{0.57}Fe_{0.46})(Al_{1.23}Cr_{0.75})O_{3.99}$

Appendix 10: Results Comparison

Table 100: Comparison of test programme results at briquette ore top sizes of −6.3 mm and −12.5 mm and the pilot-plant conditions as determined by Anglo American (Value-In-Use)

Test type	Parameter	ISO	Pilot campaign	Briquette ore top size	
				−6.3 mm	−12.5 mm
				16% moisture content	
				Open curing	Closed curing
Green briquette	Compressive strength (N)	ISO-4700	350–620	522–578	93–257
Reducibility index	Reduction (%)	ISO-4695	39.3–42.2	33.4	46.9
	Compressive strength (N)		370– 779	934	-
	Drop number		4–10.7	22.6	-
	TI (% > 6.3 mm)		95.5–96.2	95.5	40.7
	AI (% −0.5 mm)		2.93–3.57	3.63	13.7
Reduction disintegration index	RDI (%−0.5 mm)	ISO-4696-1	1.42–6.02	1.59	6.53
	RDI (%−3.15 mm)		1.60–8.95	2.24	14.3
Decrepitating index	DI (% −3.15 mm)	ISO-8371	0.083–0.22	0.23	0.85
Rotary kiln simulation	Mass% −3.15 mm	Non-standard test	2.67–5.6	3.83	51.3

Declaration on plagiarism

UNIVERSITY OF PRETORIA

Faculty of Engineering, the Built Environment and Information Technology

Department of Materials Science and Metallurgical Engineering

The University places great emphasis upon integrity and ethical conduct in the preparation of all written work submitted for academic evaluation.

While academic staff teach you about systems of referring and how to avoid plagiarism, you too have a responsibility in this regard. If you are at any stage uncertain as to what is required, you should speak to your lecturer before any written work is submitted.

You are guilty of plagiarism if you copy something from a book, article or website without acknowledging the source and pass it off as your own. In effect you are stealing something that belongs to someone else. This is not only the case when you copy work word-by-word (verbatim), but also when you submit someone else's work in a slightly altered form (paraphrase) or use a line of argument without acknowledging it. You are not allowed to use another student's past written work. You are also not allowed to let anybody copy your work with the intention of passing it off as his/her work.

Students who commit plagiarism will lose all credits obtained in the plagiarised work. The matter may also be referred to the Disciplinary Committee (Students) for a ruling. Plagiarism is regarded as a serious contravention of the University's rules and can lead to expulsion from the University.

No written work will be accepted unless the declaration has been completed and attached.

I (full names): Johnny Obakeng Mogalanyane__

Student number: u04338502

Topic of work: Evaluation of the Performance of Briquettes as Potential Feed Material to the Rotary Kiln Electric Furnace at Barro Alto, Brazil

Declaration

1. I understand what plagiarism is and am aware of the University's policy in this regard.
2. I declare that this report is my own original work. Where other people's work has been used (from a printed source, internet or any other source), this has been properly acknowledged and referenced in accordance with departmental requirements.
3. I have not used another student's past written work to hand in as my own.
4. I have not allowed, and will not allow, anyone to copy my work with the intention of passing it off as his or her own work.

Signature ______________________________